Preparation of Metal Electrode Materials and Absorber Layers for Flexible PV Application

A Thesis Submitted to The University of Manchester for The Degree of Doctor of Philosophy in The Faculty of Natural Sciences

2019

Thamer Alraddadi

Department of Chemistry, The University of Manchester, Oxford Road
Manchester, M13 9PL

Table of contents

Words: 36,586

List of Figures

.

List of Tables

Abstract

With the rapid growth of electronic technologies, the demand for portable electronic devices is increasing. Therefore, chemists and materials researchers are exploring and developing new materials and fabrication processes to produce highly flexible, fully portable, and low-cost electronic devices. The work presented here involved the synthesis of copper, bismuth sulfide, and lead sulfide nanoparticles, as well as the deposition of lead sulfide on cellulose substrate.

Several copper(II) amino carboxylic acid complexes; namely glycine (Gly), L-alanine (L-Ala), L-valine (L-Val) and picolinic acid (Pic) have been synthesised and characterised. The complexes were used as precursors for the preparation of copper nanostructure by solid-state reaction under nitrogen at three different temperatures 350, 400 and 450 °C, respectively. Also, hot injection method at 270 °C in oleylamine has been used to synthesise Cu NPs at different times such as 10, 30 and 60 min. The copper nanostructures were characterised by powder X-ray diffraction, Raman spectrum and scanning electron microscopy.

Bismuth (III) xanthate complexes with formula $[Bi(S_2COR)_4][N(C_2H_5)_4)]$ where R = methyl, ethyl, n-propyl, iso-propyl, n-butyl, iso-butyl, pentyl and n-hexyl, were synthesised. The X-ray single crystal structures of these complexes and their thermal decomposition have been studied. Bi_2S_3 nanocrystals with flake-like shape morphology were obtained from the thermolysis of $[Bi(S_2COR)_4(N(C_2H_5)_4)]$ where R = ethyl, n-propyl, n-butyl and n-hexyl at three different temperatures 250, 300 and 350 °C under nitrogen.

Lead(II) alky xanthate complexes where alky are ethyl, n-propyl, n-butyl and n-hexyl have been synthesised, characterised and used as single-source precursors for the deposition of lead sulfide nanoparticles on two types of cellulose substrates (filter paper and cotton yarn) at 200 °C under nitrogen. Cubic morphology of PbS has been obtained with different size. The decrease of the particle size by increasing the length of alkyl chain result in the increased bandgap of lead sulfide deposited on cellulose substrate.

Declaration

I declare that no portion of the work referred to in this thesis has been submitted in support of an application for another degree or qualification of this or any other university or other institute of learning.

Copyright Statement

i. The author of this thesis (including any appendices and/or schedules to this thesis) owns certain copyright or related rights in it (the “Copyright”) and s/he has given The University of Manchester certain rights to use such Copyright, including for administrative purposes.

ii. Copies of this thesis, either in full or in extracts and whether in hard or electronic copy, may be made only in accordance with the Copyright, Designs and Patents Act 1988 (as amended) and regulations issued under it or, where appropriate, in accordance with licensing agreements which the University has from time to time. This page must form part of any such copies made.

iii. The ownership of certain Copyright, patents, designs, trademarks and other intellectual property (the “Intellectual Property”) and any reproductions of copyright works in the thesis, for example graphs and tables (“Reproductions”), which may be described in this thesis, may not be owned by the author and may be owned by third parties. Such Intellectual Property and Reproductions cannot and must not be made available for use without the prior written permission of the owner(s) of the relevant Intellectual Property and/or Reproductions.

iv. Further information on the conditions under which disclosure, publication and commercialisation of this thesis, the Copyright and any Intellectual Property and/or Reproductions described in it may take place is available in the University IP Policy (see http://documents.manchester.ac.uk/DocuInfo.aspx?DocID=24420), in any relevant Thesis restriction declarations deposited in the University Library, The University Library’s regulations (see http://www.library.manchester.ac.uk/about/regulations/) and in The University’s policy on Presentation of Theses.

Acknowledgement

First of all, I would like to express my gratitude and appreciation for the invaluable guidance and support of my supervisor professor Paul O'Brien. This work would not have been possible without his excellent knowledge, encouragement and continuous advice and support. I will be forever grateful for him.

I would also like to thank Dr David J. Lewis for providing guidance and feedback throughout my study journey. He introduces me to the field of materials chemistry and solar cell, which are fundamental part of this thesis. I would also express my gratitude to David Collision for providing his assistance and guidance for writing the thesis. Also, thanks to Dr Firoz Alam, and Dr Paul Dr McNaughter for their guidance and useful advice. I thank all my colleagues during the PhD journey. I am also very grateful to the technical staff in the department of chemistry and materials for their support. Also, special thanks to the ministry of higher education represented by Jeddah University for awarding me my PhD scholarship. I would also like to thank my family for their encouragement and support.

Abbreviations

0D	0-Dimensional
1D	1- Dimensional
2D	2-Dimensional
PV	Photovoltaics
AACVD	Aerosol-Assisted Chemical Vapour Deposition
Bu	Butyl
CdTe	Cadmium Telluride
CIGS	Copper Indium Gallium Diselenide
CTAB	Cetyltrimethylammonium Bromide
CTE	Coefficient of Thermal Expansion
CZTS	Copper Zinc Tin Sulphide
DDAB	Dodecylammonium Bromide
DMF	Dimethylmethanamide
EDX	Energy Dispersive X-ray Spectroscopy
Eg	Energy Gap
EG	Ethylene glycol
Et	Ethyl
FF	fill factor
GHG	Greenhouse Gases
HTMT	Hexamethylenetetramine
^{i}Pr	ISO Propyl
I_{SC}	Circuit Current
NPs	Nanoparticles

OMA	Oleylamine
PCE	Power Conversion Efficiency
Pr	Propyl
PVP	Polyvinylpyrrolidone
p-XRD	Powder X-ray Diffraction
SQ	Shockley–Quessier
STC	Stander Test Conditions
SEM	Scanning Electron Microscope
SSP	Single Source precursor
TAA	Thioacetamide
TFTs	Thin-Film Transistors
Tg	Glass Transition Temperature
TOP	tri-*n*-octylphosphine
TOPO	tri-*n*-octylphosphine oxide
V_{OC}	Circuit Voltage

Chapter 1. Introduction

1.1. Classification of solids

Solid materials can be categorized with a consideration of the conductivity into three different types, including conductors, semiconductors, and insulators Figure 1.1. The difference between these kinds of solid materials is explained clearly by the band theory, which stands on the idea that in the isolated atom, the electrons usually occupy only specific orbitals corresponding to its energy levels. When two atoms are brought together into a molecule, their atomic orbitals merge to form pairs of molecular orbitals arranged slightly higher and slightly lower in energy than each original level. A solid material consists of large numbers of atoms, each atomic orbital splits into a very large number of levels and so close together in energy to the extent that the separation between those levels will be very small which can be described as continuum region of the energy or band of allowed levels. In the case of conductors, the energy band consist of different energy levels which are overlapping together to the degree that the separation between those levels is unattainable. On the other hand, in the case of insulators and semiconductors, the energy band split to two levels. The higher occupied band is called the valence band, and the lowest unoccupied is called the conduction band, the between bands termed as the bandgap. Insulators have a wider bandgap. However, semiconductors have an energy gap, which is narrow enough to allow the electrons to move from the valence to the conduction band under any excitation conditions, such as high temperatures.

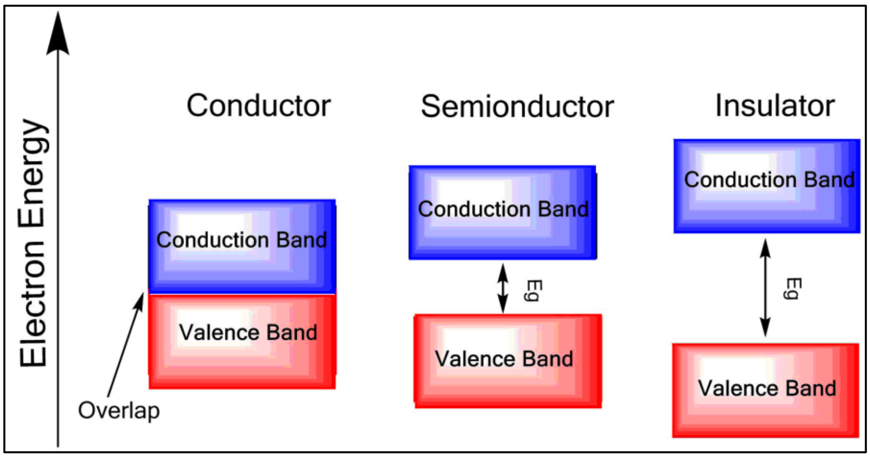

Figure 1.1 Diagram illustrating the band structure of insulators, semiconductors, and conductors.

1.2. Semiconductors

In general, the expression of semiconductor used to describe a material with conductivity between 10^{-8} to 10^{4} Ω cm^{-1}. The metals have conductivity in the range of 10^{4} and 10^{8} Ω cm^{-1}, whereas those of insulators are less than 10^{-8} Ω cm^{-1}. Another possible way to distinguish semiconductor from other materials is through the density of free carriers. Semiconductors have a carrier density that lies between metals insulators.

Table 1-1 Physical properties of different types of solids.[1]

Type of solid	***The conductivities*** **σ (cm^{-1})**	***Energy gap (eV)***	***Carried density n (cm^{-3})***
Metal	10^{5}- 10^{10}	No energy gap	10^{22}
Semiconductor	10^{-9}-10^{2}	$0 < E_G < 4$	$<10^{17}$
Insulator	$<10^{2}$	$E_G \geq 4$	<1

In the semiconductor material, the lower energy level (valence band) is fully occupied by electrons while the higher energy level (conduction band) is empty. At low temperature, the electron doesn’t have enough energy to promote to from valence band to higher energy level. However, at a higher temperature, the electron gains enough energy to jump from lower energy level to conduction band leaving a hole in the valence band. Semiconductor materials are classified according to whether they have a direct bandgap or an indirect bandgap. The difference between them is based on the physical quantity term called the k-vector or wave vector, which is related to a momentum vector associated with electrons in a crystal lattice. The difference between direct and indirect bandgap Semiconductors can be explained clearly regarding diagrams of energy vs *k* Figure 1.2. If the gap between the maximum energy level of the valence band and the minimum energy level of the conduction band equal to k-vectors it is called direct bandgap, if not equal to k-vectors it is called indirect band gab. In the direct bandgap materials, the electron can absorb or emit photons directly because the energy needed to move the electron between the conduction band and the valence band has the same value of the crystal momentum of electrons. Direct bandgap materials are optically active because of the probability of electron-hole recombination is very high and fast the recombination usually occurs within 10^{-8} to 10^{-10} sec. Therefore, direct semiconductor materials are suitable materials for the fabrication of PV device. In the case of indirect gap semiconductor materials, the electron cannot combine with a hole until a phonon with required energy and momentum is available.. The excess energy from electron-hole recombination is dissipated in the crystal lattice as a heat. As result, the probability of recombination is weak and slow, the recombination usually occurs within 10^{-2} to 10^{-3} sec; therefor these materials are not suitable for light sources.

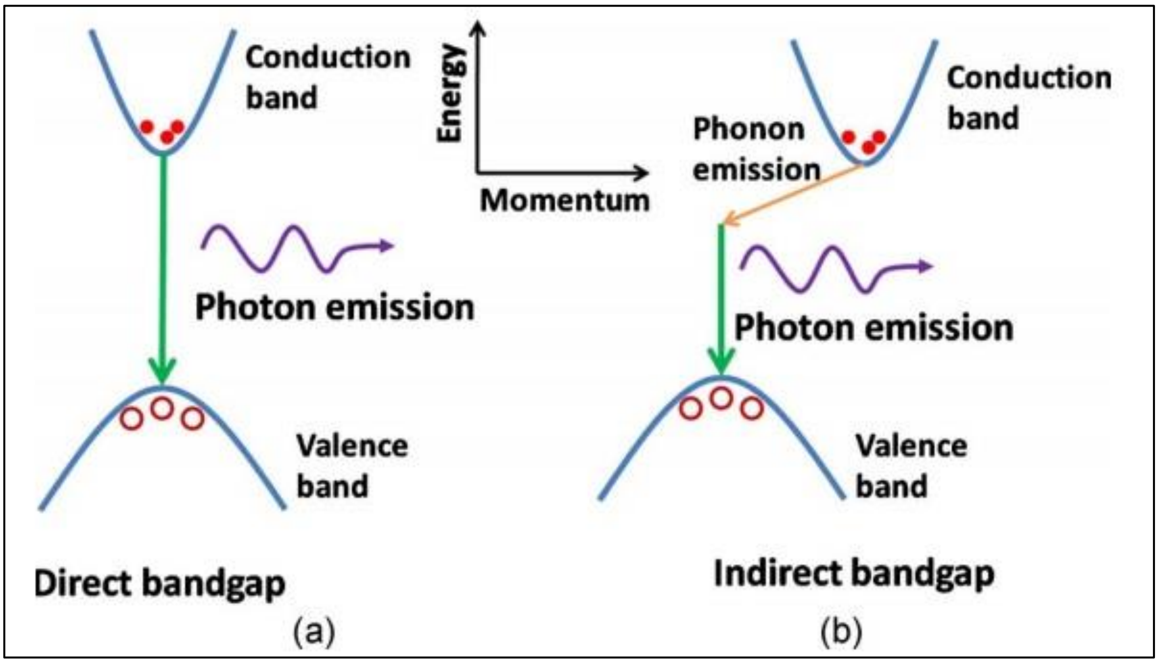

Figure 1.2 The difference between (a) direct bandgap and (b) indirect bandgap.

In the nanocrystalline semiconductor, two factors are responsible for the variation in behaviour of semiconductor from the bulky materials, the high surface/volume ratio and the size of the particles. In bulk semiconductors, a small band gap separates the valence band from the conduction band, and movement from the earlier to the latter can be achieved by thermal or optical excitation. When the scale of semiconductor particles is too small to be comparable to the wavelength of electron, the quantum confinement effect is observed. In this case, the energy levels at the band edge becoming discrete spacing between levels similar to those found metals resulting in changing the optoelectronic, mechanical, magnetic and physicochemical properties. For example, Figure 1.3. shows the bandgap of nanoparticles with diameters of 2–6 nm is increased due to the quantum size effect compared with the bulk semiconductor, and it leads to different fluorescent colours reflecting small differences in the particle size.

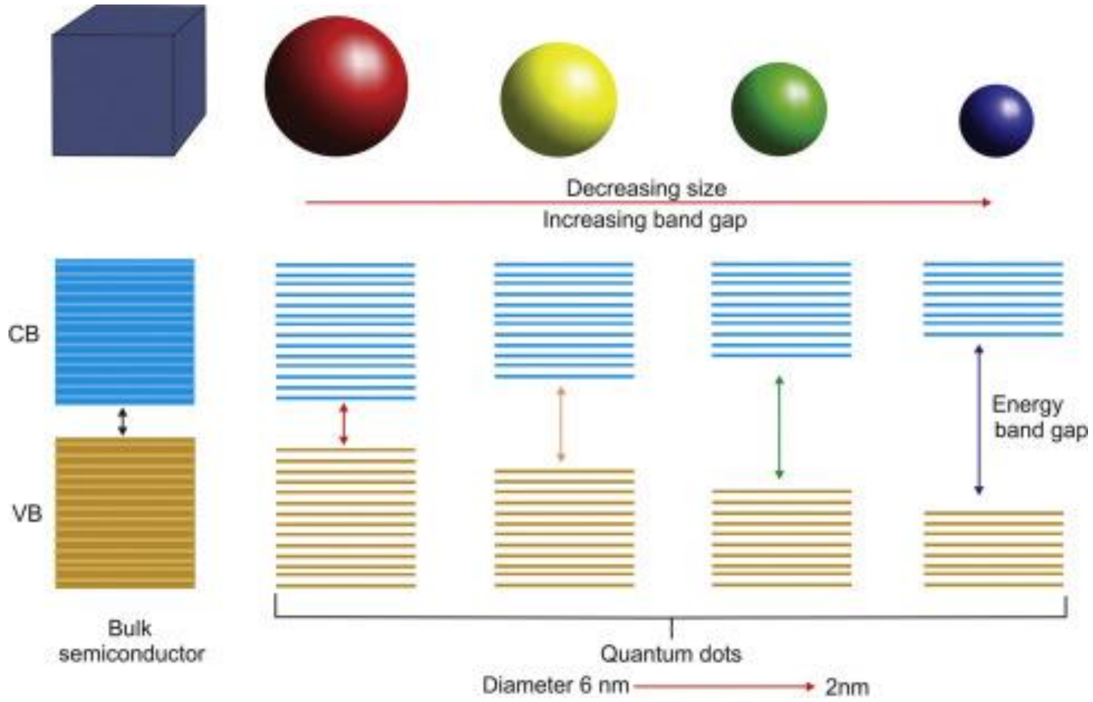

Figure 1.3 Energy band variation in quantum dots as the size is varied. Reproduced from ref.2. Copyright 2018 with permission from Elsevier.

1.3. Metal chalcogenide semiconductor

1.3.1. Bismuth sulfide (Bi_2S_3)

Bismuth sulfide is a relatively nontoxic n-type semiconductor material; it has an orthorhombic crystal structure Figure 1.4. Bulk crystalline Bi_2S_3 possesses a direct bandgap with energy between 1.30 eV and 1.70 eV that is close to optimal for PV solar cells. The variations of the bandgap value could be associated with stoichiometry variations and/or quantum confinement effects resulting from the reducing the size.[3] Bi_2S_3 has a large visible-light absorption coefficient (10^5 cm^{-1}).[3, 4] Bismuth sulfide has been subjected to research for possible applications such as solar cells,[5, 6] sensors,[7-9] thermoelectric cooler devices,[10-12] hydrogen storage,[13, 14] medical contrast agent,[15, 16] biomolecule detector,[17] and cancer therapy.[18] Various approaches have been employed for the preparation of Bi_2S_3 nanoparticles and thin films including; colloidal methods,[19, 20] solvothermal,[21] hydrothermal,[22, 23] and single-source routes.[24-29]

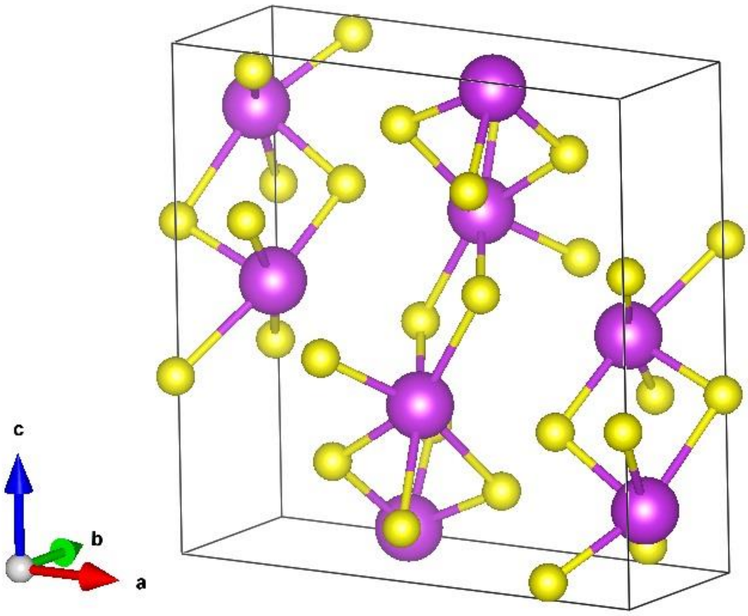

Figure 1.4 Orthorhombic bismuth sulfide with space group *Pnma*, a = 11.345(Å), b = 3.994(Å) and c = 11.193, and $\alpha = \beta = \gamma = 90°$.[4]

The synthesis method and preparation parameters like reaction time and temperature, solvent, and precursor have a significant effect on the size and aspect ratio of the Bi_2S_3 product, which can be utilized to modify the morphology of this useful material on the nanoscale level.[30, 31] Zhang *et al.*[13] developed a simple and low-temperature (below 180 °C) hydrothermal method using bismuth (III) nitrate as bismuth source and L-cysteine as sulfur source and morphology-directing molecule to synthesise Bi_2S_3 nanostructures. Different Bi_2S_3 morphologies such as nanoflakes, flowerlike shape and nanorod were obtained by changing the reaction conditions including temperature, the concentration of L-cysteine and pH of the solution. For example, mixed flowerlike patterns and well-arranged nanorods with an average size of 50 nm were obtained at pH =1. Increasing the pH value to 11 while other conditions remained unchanged, led to the formation of nanorods with diameter between 60-80 nm.

Also, Miniach *et al.*[32] investigated the effect of the solvent system on the morphology of Bi_2S_3 nanoparticles utilizing the solvothermal technique. They managed to control the shape of bismuth sulfide NPs by altering the solvent system mixtures. For example, sphere-like particles with an average size between 100–300 nm were obtained in water at 150 °C after 24 h. The use of ethylene glycol/water (1:1, v/v) mixtures promoted the formation of high uniform Bi_2S_3 nanospheres with diameters ranging from 50 to 90 nm under the same reaction parameters. The mixtures of butyldiglycol/water (1:1, v/v) led to the plate-like shaped Bi_2S_3 nanoparticles. Lu *et al.*[22] demonstrated free surfactants hydrothermal technique to synthesise Bi_2S_3 nanorod with length ranges from 2 to 5 µm, and a diameter range from 10 to 30 nm at 180 °C after 12 h reaction time.

Moreover, Liang *et al.*[30] reported the synthesis of Bi_2S_3 nanobelts via solvothermal method at 150 °C temperature and 6 hours reaction time. Thiourea and Bi_2O_3 were used as sulfur and bismuth source, respectively and ethylene glycol (EG) as a solvent with an assistant of polyvinyl pyrrolidone (PVP). Increasing the reaction temperature to 200 °C results into changing the morphology to nanorods with the length of 2 µm and an average diameter of 200 nm. Lou *et al.*[30] reported the synthesis of Bi_2S_3 nanorod using Bi(III) di-n-octyl-dithiophosphates $Bi[S_2P\text{-}(OC_8H_{17})_2]_3$ as single-source precursors via a solvothermal method. The single-source precursors mixed with oleyamine and heat at various reaction temperatures, 140, 160 and 180 °C. Nanorod-like Bi_2S_3 crystals with lengths of 250-450 nm and an average diameter of 21 nm have been obtained at 140 °C. Increase the temperatures to 160 °C resulted in the formation of Bi_2S_3 nanorods with lengths of 300-550 nm and an average diameter of 11 nm. While Bi_2S_3 nanorods produce at 180 °C has a small size as 8 nm and lengths of 300-600 nm. Arumugam *et al.*[33] report the synthesis of Bi_2S_3 nanorods with an average length of 450 nm and average diameter of 127 nm via solvothermal approach using a mixture of bismuth nitrate, thiourea, citric acid and cetyltrimethylammonium in dimethylformamide (DMF) solvent at 180°C for 24 h.

Also, a great deal of control over the size and the morphology of Bi_2S_3 nanostructures was achieved by Díaz-Cruz *et al.*[34] using different synthesis conditions such as solvents, reaction temperatures and bismuth salts during microwave solution method. Table **1-2** outlines the morphologies obtained at different reaction conditions. They concluded that the in microwave-assisted solution method; the morphology of Bi_2S_3 could be changed by controlling the reaction kinetics during the growth process. Two essential factors affect the reaction kinetics. Firstly, the dissociation of bismuth sources in the solvent, the bismuth source with rapid dissociation led to the fast formation of polycrystalline nuclei of Bi_2S_3.

The subsequent crystal growth is carried out at the outer surface of the nuclei to produce orthorhombic “spines” on the nuclei. On the other hand, the slow dissociation of bismuth sources led to reducing the growth rate of Bi_2S_3 crystals. As a result, the Bi_2S_3 crystals grow slowly and separately into orthorhombic fibres. Another important factor is the heating capacity of the solvent in a microwave. A solvent that absorbs high microwave radiation will generate more heat inside the reactor. Consequently, changing the type of solvent under the same synthesis conditions result in modification of the morphology of the final product.

Figure **1.5** shows the different morphology obtained at different reaction conditions used by Díaz-Cruz et al.

Table 1-2 Som of the reaction conditions and results from Díaz-Cruz *et al.* experiment, ethylene glycol (EG), dimethyl formamide (DMF).[34]

Bismuth + Sulfer sources	Solvent	Temp (°C)	Size		Morphology	Figure
			Length (µm)	Diameter (nm)		
$BiCl_3$ + Thiourea	EG	100	1.2-2.0	46-74	Fibers	Figure 1.5.a
	EG	140	1.2-4.4	40-105	Fibers	Figure 1.5.b
	EG	170	1.4-5.91	30-430	Fibers	Figure 1.5.c
	DMF	100	-	-	-	-
	DMF	140	0.7-2.0	70-200	Rods	Figure 1.5.h & i
$Bi(NO_3)_3$ + Thiourea	EG	100	2.0-3.3	26-54	Hedgehog	Figure 1.5.e
	EG	170	1.5-3.2	38-112	Hedgehog	Figure 1.5d
	DMF	100	3.6-4.8	13-40	Hedgehog	Figure 1.5.f

Table 1-2 (continued)

DMF	100	1.4-2.5	26-54	Flowers	Figure 1.5.g
H_2O(pH=1)	170	-	97-270	Flowers	Figure 1.5.j
H_2O(pH=13)	170	0.13-0.5	35-120	Rods	

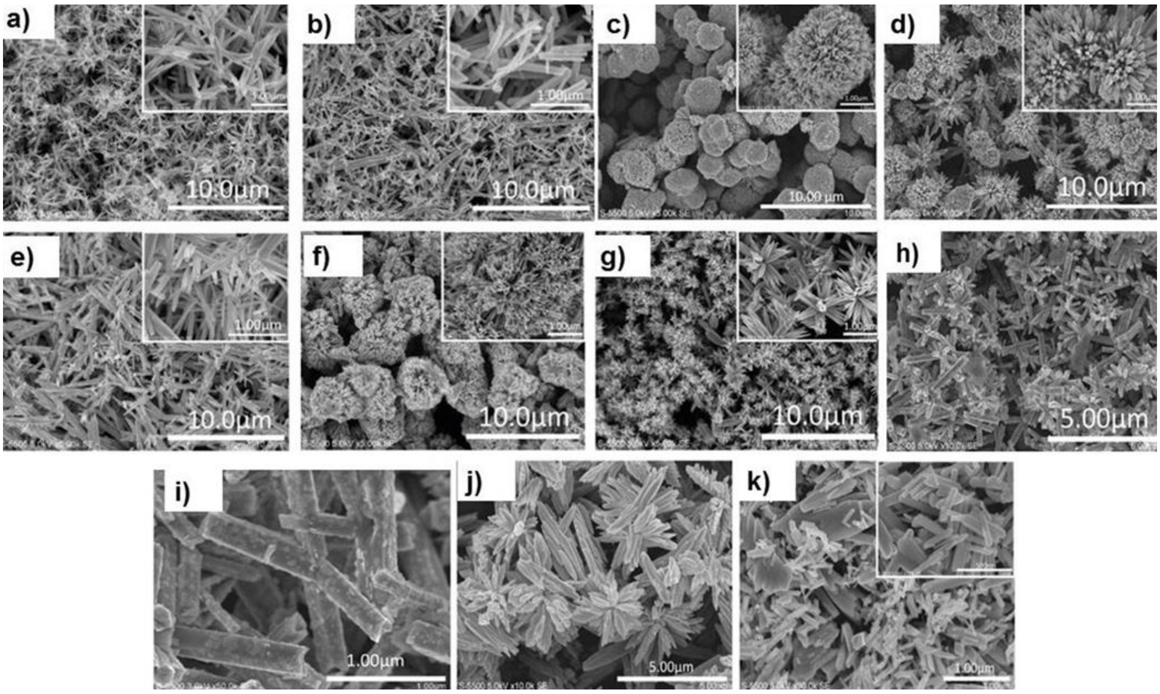

Figure 1.5 SEM micrographs of Bi_2S_3 synthesised via microwave assisted different reaction condition using thiourea as the source of sulfur. Nanofibers synthesised with $BiCl_3$ in EG solvent at different reaction temperatures: a) 100 °C and b) 140 °C, hedgehog-like shape Bi_2S_3 synthesised with $Bi(NO_3)_3$ in EG at c)100°C, and d) 170°C, e) nanofibers synthesised with $BiCl_3$ in EG solvent at170°C, f) and g) Bi_2S_3 products synthesised with $Bi(NO_3)_3$ in DMF solvent at 100°C using different concentrations of Bi and S sources 0.05 M and 0.25 M; and (b) 0.005 M and 0.025 M, respectively, h) and i) Bi_2S_3 nanorods obtained from $BiCl_3$ and TU in DMF solvent at 140 °C, h) and i) are Bi_2S_3 nanorods prepared with $BiCl_3$ in DMF solvent at 14 °C. Bi_2S_3 products obtained from $Bi(NO_3)_3$ in water at 170 °C with (j) pH = 1 and (k) pH = 13.Reproduced from ref.34. Copyright 2017 with permission from Elsevier.

Bismuth sulfide has been widely used as absorber layer on many PV device. For example, Liao *et al.* reported the growth of Bismuth sulfide (Bi_2S_3) nanorods, 37.2 nm in length and 6.1 nm in width, using the solution process method, at 130 °C for 30 min. The as-synthesized nanorods were blended with poly(3-hexylthiophene) (P3HT) to form bulk heterojunction hybrid film.[35] Also, Mock *et al.* used (Bi_2S_3) nanoparticle layer in combination with (P3HT) as an organic-inorganic planar heterojunction solar cell.[36] Brooks *et al.,* described the construction of inorganic-organic solar cells by spin-coating (P3HT) solutions atop the Bi_2S_3 nanowire networks.[37] MacLachlan *et al.* noted the fabrication of solution-processed nontoxic mesoporous (Bi_2S_3) structures via the thermal decomposition of a thin film composed of a bismuth xanthate single source precursor. The porous (Bi_2S_3) films were infiltrated with the hole conductor (P3HT) to generate Bi_2S_3/P3HT heterojunction devices.[38]

1.3.2. Lead sulfide (PbS)

Lead sulfide Figure 1.6 is an important IV−VI semiconductor. The PbS has a direct narrow-bandgap of 0.41 eV at room temperature with large size excitation 18 nm.[39, 40] This narrow bandgap allows absorption from visible to the infrared spectrum. The extraordinary third-order nonlinear optical properties associated with PbS nanoparticles makes them useful for various range of applications including; optical switches, biosensors, drug delivery, fire alarm sensors and infrared optoelectronic devices.[41-46]

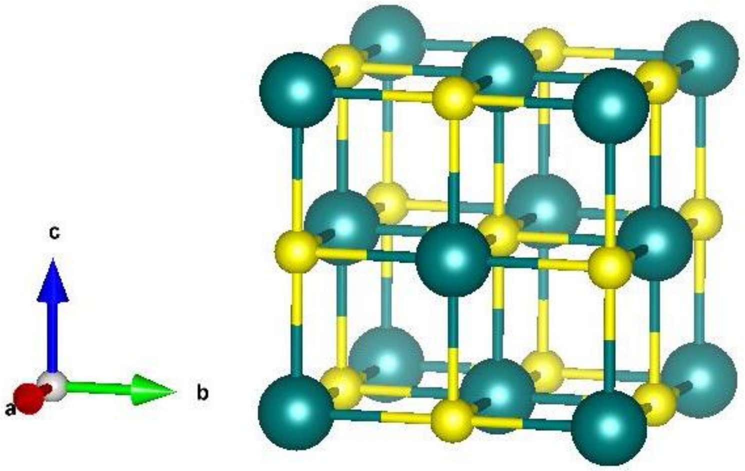

Figure 1.6 Cubic lead sulfide with space group Fm3m, a=b=c=5.93(Å), and α=β=γ=90°. [47]

Various methods have been proposed for the preparation of PbS nanoparticles with different morphologies and sizes; these methods include microwave heating,[48, 49] ultrasonic irradiation,[50] decomposition of single-source precursor,[51-55] colloidal solutions,[56,57] hydrothermal,[58,59] and self-assembly.[60] The size of PbS produced is influenced by the synthesis methods used as well as the reaction parameters, solvent and capping agents. For example, Ding *et al.* described a procedure for the synthesis of PbS with various morphologies, such as cubes, dendrites, stars, and wires, via a facile hydrothermal method with the assistant of capping agents like hexamethylenetetramine (HMT) and cetyltrimethylammonium bromide (CTAB), Figure 1.12 a & c.[58] Zhao *et al.* demonstrated a low temperature (40 °C) and fast (40 min) ultrasonic method using lead acetate trihydrate, thioacetamide (TAA), and nitrilotriacetic acid as lead and sulfur precursors respectively, to prepare dendritic-like lead sulfide nanocrystals without any surfactant, Figure 1.7b.[50] Flower-like morphology was synthesised via microwave thermolysis of lead diethyldithiocarbamate in ethylenediamine, Figure 1.7 d.[53] Wang *et al.* reported the growth of Pbs nanotubes by room temperature ultra-sonication of $Pb(CH_3COO)_2{\cdot}3H_2O$ and thiourea in ethanol, Figure 1.7 e.[61] A biomolecule-assisted method has been used to synthesise a flower-like PbS nanocrystals, Figure 1.7 f.[62]

PbS has been extensively used as absorber layer. For instent, Hansen *et al.* presented a water phase synthesis method for lead sulfide colloidal quantum dots, and their use as light absorber (dye) in a dye-sensitized solar cell (DSSC).[63] Göde *et al.*, reported the fabrication of ITO/CdS/PbS/Ag solar cell structures, where the window layers, cadmium sulfide (CdS) thin film deposited via the chemical bath deposition (CBD) method, while absorption layers, lead sulfide (PbS) thin film were deposited on ITO substrates at room temperature using the successive ionic layer absorption and reaction (SILAR) technique.[64] Tulsani *et al.* developed a simple and highly compatible optical ultraviolet ozone (UVO) treatment approach to alter the electronic properties of PbS- 1,2 ethanedithiol (EDT) layer and implement it in enhancing the solar cell performances.[65] Yeon *et al.*, described a scalable, low cost, and less toxic synthesis method for the construction of double absorber PbS/CdS heterojunction solar cells.[66]

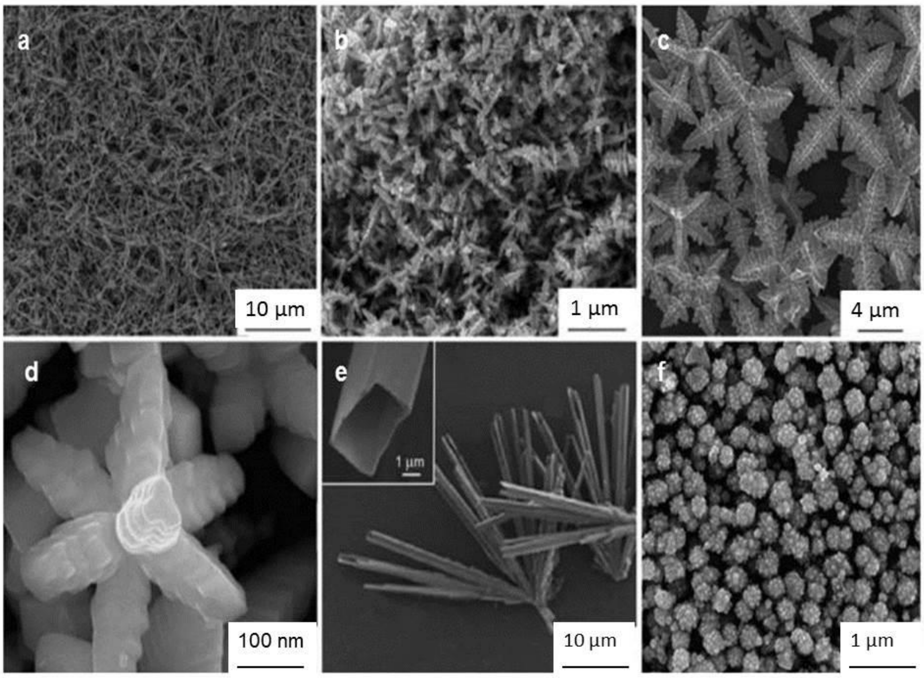

Figure 1.7 SEM images of lead sulfide nanostructured with different morphology; a) nanowires, reproduced from ref.58. Copyright 2009 with permission from Elsevier. b) dendrites, reproduced from ref.50. Copyright 2007 with permission from Elsevier. c) stars, reproduced from ref.58. Copyright 2009 with permission from Elsevier. d) flower like structure, reproduced from ref.53. Copyright 2009 with permission from Elsevier. e) nanotubes, reproduced from ref.61. Copyright 2006 with permission from Elsevier. f) flower like structure , reproduced from ref.62. Copyright 2009 with permission from Elsevier.

1.4. Definitions of nanomaterial

Nano derives from the Greek word “nanos” which means dwarf, and nowadays this phrase is used as a prefix that means billionth. It’s usually combined with the metric system as a measurement unit. The term nanotechnology refers to the part of the technology that is interested in this study, synthesis, development and application of any materials or devices and with processes that take place in the nanometre range.[67] A nanomaterial is often described as any solid material that demonstrates significantly different properties from both molecular and bulk material on account of it having at least one dimension in this range (usually 100 nm).

According to this definition, nanomaterials can be classified in different categories considering the dimensionality (height, width and length) of material. For instance, if the entire dimensions of the nanomaterial are in nano range than it is called a nanoparticle or zero-dimensional (0D). Additionally, if the nanoparticle structure was in a well-organized arrangement of atoms (or ions), it is called nanocrystals. While the term `quantum dots' or `artificial atoms' is used to describe tiny particles that have a diameter in the range of 2-10 nm.[68] Moreover, the term `cluster' is used to describe small nanoparticles with sizes of less than 1 nm. Another type of nanomaterial is termed as one-dimensional (1D), which is used to describe the material that has at least one dimension not at the nanoscale where the other two are in nanoscale. Ideal examples of this type are nanorods and nanowires. The third class called two-dimensional objects (2D) is used to express the nano objects that have two dimensions not in nanometre range and the third dimensions in nano range, such as nanodisc.

1.5. Synthesis of nanomaterials

Several approaches for the preparation of nanomaterials are listed in Figure 1.8. Two techniques have been used in the preparation of such materials. The first is the top-down method; in this process, the solid substance is broken down into smaller particles. The second is the bottom-up approach; where the formation of nanoparticles starts from atoms or molecules and building up the nanostructures. Top-down fabrication techniques enable nanoparticles to be synthesised on a large scale. However, there is limited control over the size of the particles, and consequently, the properties of resulting products. On the other hand, bottom-up approaches have enabled the preparation of chemically homogeneous nanocrystals with controlled particle size.[69]

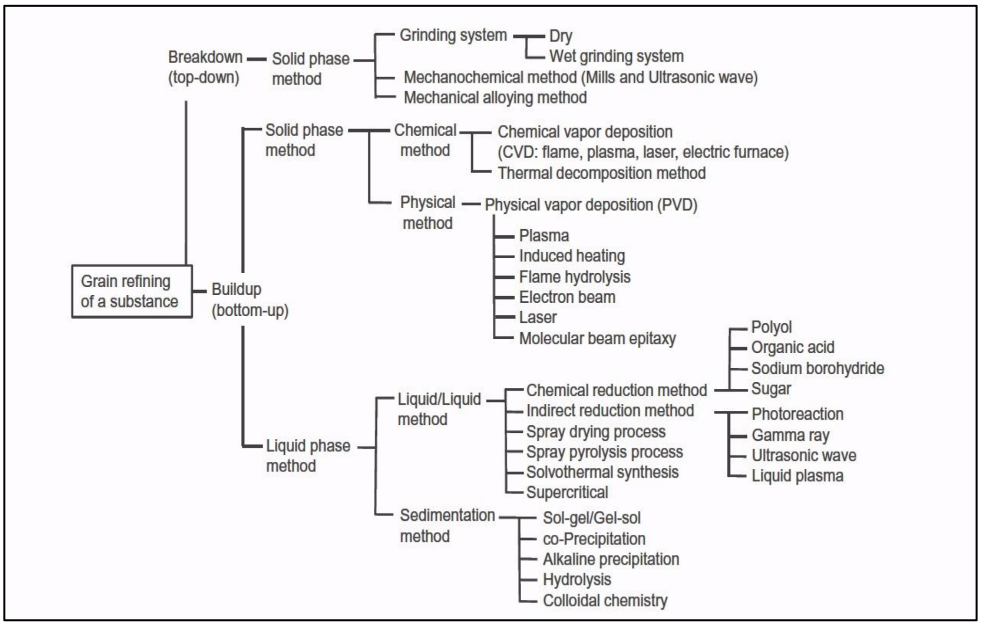

Figure 1.8 Methods used for the preparation of nanomaterials. Copyright © 2013 Wiley-VCH Verlag GmbH & Co. KGaA. [70]

1.6. Method for preparation of metal sulfide nanoparticles

Nanostructured materials are receiving increasing interest in recent years due to their unique physical and chemical properties and potential applications in nanoscale devices. A wide range of synthetic techniques have been reported for the preparation of semiconductor nanoparticle.

1.6.1. The hot-injection method

This method involved the injection of the precursor solutions into a heated solvent under an inert atmosphere. The high boiling solvent allows the mixture to react at high temperature and also serves as a stabilizing agent. The main advantage of this method lies in the use of non-ionic precursors in high-boiling organic solvents, which offers a potential control of the growth rate. This methodology has been used for the synthesis of high quality metal and metal sulfide nanoparticles, such as Au, Pd, Pt, PbS, Ag_2S and Bi_2S_3[56, 71-75] Bawendi *et al.*[76] reported the synthesis of monodisperse and highly crystalline nanoparticles of CdSe, CdS, and CdTe using this method. In a typical preparation, a solution of chalcogen precursor and dimethylcadmium were mixed in tri-*n*-octylphosphine (TOP) and injected into hot tri-*n*-octylphosphine oxide (TOPO) at temperatures ranging between 120 °C – 250 °C. Al-Shakban *et al.*[77] synthesised Cu_xS nanorods using a series of copper(I) xanthates as single source precursors $[(PPh_3)_2Cu(S_2COR)]$ (R = isobutyl, 2-methoxyethyl, 2-ethoxyethyl, 1-methoxy-2-propyl, 3-methoxy-1-butyl, and 3-methoxy-3-methyl-1-butyl) by hot injection technique in oleylamine at 260 °C for 5 second and 60 min. They noted that short reaction times lead to the formation of $Cu_{1.74S}S$ nanorods, while at longer reaction times aggregated Cu_2S is formed. However, the use of high boiling point solvents could be a disadvantage from economic and environmental points of view.

1.6.2. Solid-State Reaction

This technique is achieved by pyrolysis of a precursor to bring about its decomposition at high temperature, it`s often carried out under an inert condition. The simplicity of this method makes the scale-up process easier than most other technique. Melt reactions are solvent-free methods: this gives the solid-reaction technique an environmental and economic advantage over other approaches such as heating-up and injection which usually use high boiling point solvents. Another interesting feature of melt reactions is that the by-products produced during the reaction can act as capping agent, which play an important role in the size and the shape of particles formed. The melt approach has been successfully used in the preparation of metals, metal oxides, and metal chalcogenide nanomaterials,[78] with a broad range of morphologies including spheres,[79, 80] nanorods,[24, 72, 73] nanowires,[24, 83, 84] and nanodisks.[82, 85]

1.6.3. Single source precursor

A single source precursor contains all elements that are required in the preparation of the target compound at the correct ratio. The use of single-source precursors was first reported by Stegerwald group.[86] There are several advantages of using single-molecular precursors over other existing methods. For instance,

- The use of single-source method in the preparation of nanoparticles helps to avoid the need for volatile, toxic and/or pyrophoric precursors.
- Some nanoparticles of group II-VI and III-V are air and moisture sensitive. All synthesis of precursor is carried out under inert conditions, with the resulting being air and moisture stable.
- Less chance of impurities introduced to the nanoparticle products.

1.6.3.1. (Dialkyldithiocarbamato) metal complexes

The first report on the synthesis of metal dithiocarbamates [$M(S_2CNRR)_n$] was in 1965 by Kupchik and Calabretta.[87] Since that time; the dithiocarbamate complexes have reserved considerable interest because of high stability[88] and the relatively low thermal decomposition temperature. Another interesting advantage is the ability of this ligand to bond the metal with three different coordination modes which are monodentate, bidentate and chelating ligand Figure 1.9.[89]

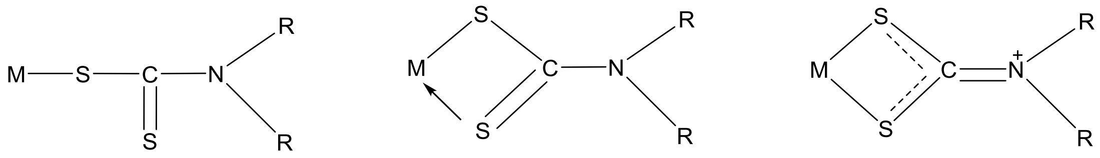

(1) (2) (3)

Figure 1.9 The coordination modes of dithiocarbamate groups (1) monodentate, (2) asymmetric bidentate, and (3) symmetric bidentate. Reproduced from ref.89. Copyright 1981, with permission from Pergamon, Ltd.

Metal dithiocarbamate complexes usually synthesised in two steps; the synthesis of ligand and that the reaction of a metal salt with the prepared ligand. Dithiocarbamate ligands are synthesised by the reaction between primary or secondary dialkyl amine and carbon disulfide with potassium or sodium hydroxide as follows:

$$R_2NH + KOH \longrightarrow R_2NK + H_2O \qquad \text{(scheme 1.1)}$$

$$R_2NK + CS_2 \longrightarrow S_2CNR_2K \qquad \text{(scheme 1.2)}$$

$$2S_2CNR_2K_{(aq)} + M^{2+}_{(aq)} \longrightarrow M(S_2CNR_2)_{2(s)} + 2K^{+}_{(aq)} \qquad \text{(scheme 1.3)}$$

There have been several studies reporting the use of dithiocarbamate for the growth of metal sulfide nanomaterials especially Bi_2S_3 and PbS.[51-51, 90-93] For example, Kun group reported the synthesis of $(Bi_{1-x}Sb_x)_2S_3$ for thermal decomposition of bismuth and antimony piperidinedithiocarbamates in oleylamine.[28] They also noted the deposition of Bi_2S_3 thin films using heterocyclic bismuth (III) dithiocarbamato complexes.[29] Onwudiwe *et al.* investigated the influence of the precursor on the size and the morphology of the PbS nanoparticles prepared in ethylene glycol by microwave irradiation method.[94] lead sulfide nanorods with length and average diameter of 33 nm were obtained from complex of Pb(II)bis(*N*-ethyl-*N*-phenyldithiocarbamate). However, the use of complex Pb(II)bis(*N*-

butyl-*N*-phenyldithiocarbamate as single source-precursor led to the formation of non-uniform cube-like shape with 150 nm as average length. Trindade *et al.* reported the synthesis of cubic PbS nanoparticles using lead(II) isopropyldithiocarbamato by hot injection method in toluene and tri-n-octylphosphine oxide (TOPO) at two different temperatures; 100 and 150 °C. They observed that the reaction temperature has a strong effect on the size and the morphology of the products, most of crystallites products at 100 °C were round in shape and in the quantum size range (6.3±1.4 nm). On the other hand, the PbS nanoparticles prepared at 150 °C consist of larger and square-like nanocrystal with average size of 85 ± 23 nm.[95] Trindade *et al.* obtained nanofibers with an average of 6 nm from the refluxing of $Bi[(S_2CN)(C_6H_{13})]_3$ in hot ethylene glycol at 132 °C after 2 h.[96] Chauhan *et al.* investigated the influence of solvents like ethylene glycol, n-octadecylamine and dodecanethiol on the morphology of bismuth sulfide NPs from Bi(III) 4-hydroxypiperdine dithiocarbamate as single-source precursor single. They indicated the formation of an agglomerated rods from the thermal decomposition of the precursor at 550 °C for 6 h under argon. On the other hand, in these capping agent-assisted syntheses, the dimensions of the rods become smaller. In the case of using hot (250 °C) ethylene glycol, the length of nanorods were 400-600 nm with an average diameter between 20–30 nm. The use of hot (200 °C) n-octadecylamine led to the formation of nanorods with 200–300 nm length and 20–25 nm in diameter, where the use of hot (170 °C) dodecanethiol helps to reduce the length to 100–150 nm long and the diameter to 10–20 nm.[97]

1.6.3.2. (O-alkyldithiocarbomato) metal complexes

Metal xanthates with the chemical formula $[M(S_2COR)_n]$ have been used widely in the preparation of metal sulfide nanoparticles because of their lower decomposition temperatures.[98, 99] Xanthates are organized in three famous forms;[100] and other three rare structures which are formed from the interaction between the metal and oxygen or while bimetallic bond happens between sulfur atoms or sulfur and oxygen atoms.[101]   Figure 1.10.

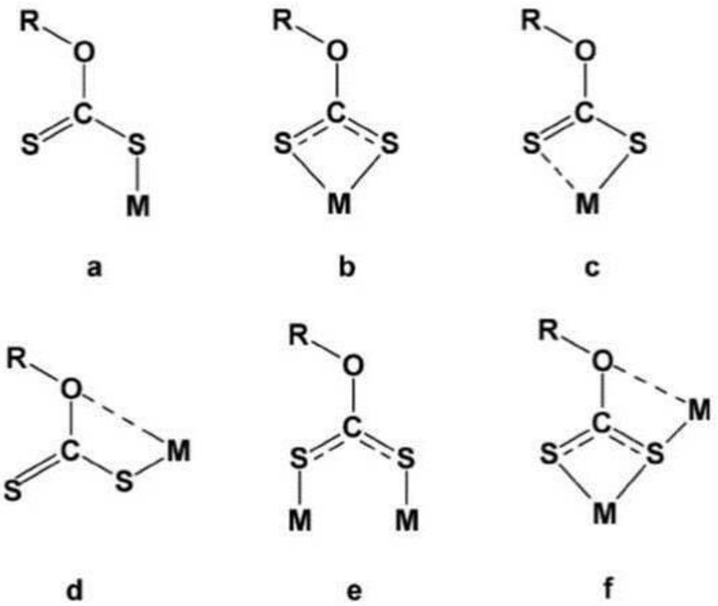

Figure 1.10 Different classification of xanthate ligands (a) monodentate, (b) isobidentate and (c) anisobidentate, and three more rare forms (d, e, f). Reproduced from ref.101. Copyright 2003 with permission from Elsevier B.V.

Metal xanthate complexes can be prepared by two steps; the synthesis of xanthate ligand, followed by the reaction of a metal salt with the prepared ligand. Xanthate ligands are synthesied from the reaction between potassium or sodium hydroxide, alcohol and carbon disulphide. Metal xanthate produces from the reaction of a metal salt and a solution of potassium or sodium alkylxanthate as follows:

$$\mathrm{ROH + KOH \longrightarrow RO^{-}K^{+} + H_2O} \qquad \text{(scheme 1.4)}$$

$$\mathrm{RO^{-}K^{+} + CS_2 \longrightarrow S_2COR^{-}\,K^{+}} \qquad \text{(scheme 1.5)}$$

$$\mathrm{2S_2COR^{-}\,K^{+}_{(aq)} + M^{2+}_{(aq)} \longrightarrow M(S_2COR)_{2(s)} + 2K^{+}_{(aq)}} \qquad \text{(scheme 1.6)}$$

.

Metal xanthate complexes have attracted considerable attention for the preparation of metal sulfide nanoparticles, mostly due to the lower decomposition temperature growth compare to metal dithiocarbamato complexes. Wide ranges of methods have been reported for the synthesis of metal sulfides such as Bi_2S_3 and PbS. For example, Clark *et al.* reported the synthesis of PbS nanocubes with an average size of 40 nm from the thermal decomposition of $Pb(S_2COEt)_2$ at 350 °C via a technique called RAPET (reaction under auto-generated pressure at elevated temperatures). They also reported the use of $Pb(S_2COEt)_2$.TMEDA (tetramethylethylenediamine) as single-source precursor for the deposition of PbS film on glass by Aerosol-assisted chemical vapour deposition (AACVD) at 200 °C.[102]

McNaughter *et al.* studied the effect of precursor on the size of PbS nanoparticles using lead(II) alkylxanthates as single source precursors via melt reactions. They found that the longer alkyl chains resultied in smaller cubic nanocrystals.[103] Akhtar *et al.* reported simple and low growth temperatures method between 150–250 °C for the deposition of PbS films by (AACVD) on plastic substrates.[104] Bismuth sulfide nanorod structures were synthesised via melt reaction method at 250 °C under nitrogen for 60 min from tris(o-ethylxanthate)bismuth (III) as single-source precursors.[25] Bi_2S_3 nanorods with average diameters of 20-35 nm and were synthesised via a hydrothermal method of $Bi(S_2COR)_3$ where R=sec-butyl, with the assistant of poly vinyl pyrrolidone (PVP) at 180°C for 16 h.[105] In a comparison between lead(II) dithiocarbamate and lead(II) alkyxanthates, Lewis *et al.* investigated the influence of precursor structure on PbS−polymer hybrid films morphology. They conclude that the morphology of the PbS−polymer films is sensitive to the precursor used. For example, dithiocarbamate complexes formed inhomogeneous films containing very large PbS particles. In contrast, the xanthate complexes produce homogeneous film morphologies. They claimed that the precursor reactivity is responsible for the dramatic differences in particle size between the dithiocarbamate and xanthate complexes. The lower decomposition temperatures of xanthate complexes result in a fast nucleation burst, leading to production of a homogeneous film containing small nanocrystals. While the higher decomposition temperatures of dithiocarbamate complexes result in slow nucleation which leads to the formation of larger particles.[106]

1.7. Method for preparation of copper nanomaterials

Metal nanostructured materials such as Au, Ag, Cu, Pd and Pt have been the subject of widespread research, because of their unique electronic, catalytic, optical and magnetic properties.[107-111] The properties of metal nanostructures can be tuned by controlling their composition, size, shape, and structure.[112-115] These metal NPs have been extensively used in a broad range of applications including; biomedical,[116, 117] sensing[118, 119] and catalysis.[120] Among the noble metals, copper nanomaterials are an inexpensive conductive electrode. The synthesis of metal nanocrystals is challenging because they are easily oxidized in air and they aggregate in the absence of proper capping.[121, 122] Pedersen noted that the copper nanoparticles are, at room temperature oxidized at their surface.[123] The problems of aggregation and oxidation can be prevented by the addition of protecting agents such as polymers and organic ligands.[124-126]

Cu has been used in a wide range of applications because it offers high electrical conductivity and strong catalytic activity[127, 128] Consequently, various methods have been developed for the synthesis of monodisperse copper nanomaterials, including thermal decomposition, hot injection, chemical reduction, polyol and solvothermal method.[129-135] Togashi *et al.* described a novel procedure for the preparation of monodisperse copper NPs from the thermal decomposition of an oleylamine-coordinated Cu oxalate complex in oleylamine at lower temperature 130 °C.[136] Ye *et al.* reported self-assembly of high-quality Cu nanowires by surface ligand exchange of oleylamine and trioctylphosphine.[137] Zhang *et al.* demonstrated a self-catalytic growth of Cu nanowires in a liquid-crystalline medium of hexadecylamine (HAD) and cetyltriamoninum bromide (CTAB).[138] Additionally, Lee *et al.* illustrated a large-scale polyol technique using polyvinylpyrrolidone(PVP) as a stabilizing polymer and sodium hypophosphite as a reducing agent.[139] Also, Wei reported the synthesis of Cu nanoparticles from thermal decomposition of copper acetylacetonate in the presence of oleylamine (OMA), they noted that the addition of dodecylammonium bromide (DDAB) to the reaction media with direct the structure to obtained Cu nanorods.[140] Rajesh noted the eco-friendly green route of synthesis copper (NPs) using *Syzygium aromaticum*.[141]

Kang *et al.*, reported the fabrication of organic solar cells made with transparent Cu nanowire mesh electrode on polyethylene terephthalate (PET) substrate. Moreover, these flexible Cu mesh electrodes demonstrate the potential use of large area fabrication of such transparent metal electrode using a roll-to-roll process.[142] Chen *et al.*, developed a facile and scaled-up solution method to prepare Cu nanowire transparent conductive electrodes (TCEs) coated with poly(3,4-ethylenedioxythiophene): poly(styrenesulfonate) (PEDOT:PSS). They also investigated the use of this (TCEs) in the fabrication of flexible bulk heterojunction polymer solar cells.[143] Liu *et al.* noted the enhancement in the power conversion efficiency of an organic bulk-heterojunction solar cell when copper nanoparticles introduce to poly(3,4-thylenedioxythiophene):poly(styrenesulfonate) (PEDOT:PSS) layers.[144]

1.8. Renewable energy

Energy is essential to improved quality of life, economic and social development. Nearly 85% of planetary energy consumption depends on fossil fuels which are depletable and produce greenhouse gases and other pollutants that are harmful to the environment.[145] Only 13% of energy comes from renewable sources (biofuel and waste 9.7%, hydro 2.5% and others: solar, wind, geothermal, heat, among others 1.5%), 81% comes from fossil fuels (oil 31.7%, natural gas 21.6%, and coal 28.1%), and 4.9% nuclear power.[146] Emission of greenhouse gases was raised by 2.2% per year between 2000 and 2010, compared with 1.3% per year from 1970 to 2000.[147] Fig 10 shows the change on the demand of different energy source between 1973 and 2015.

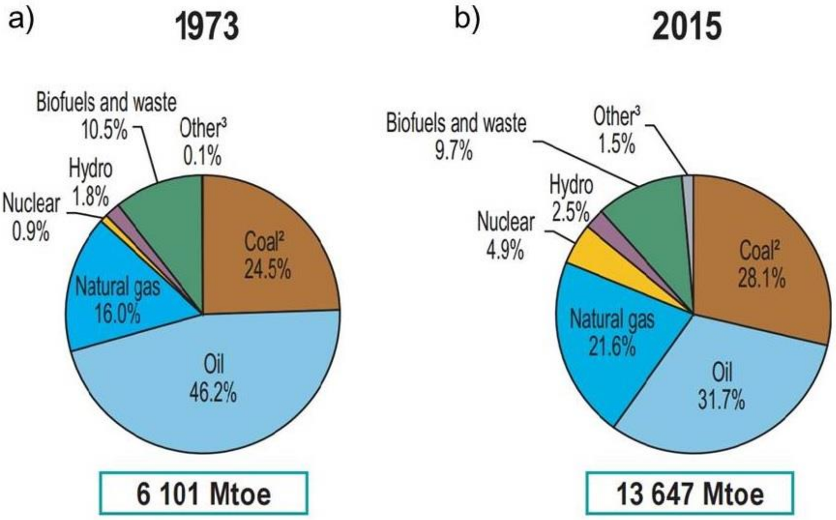

Figure 1.11 The sources of planetary primary energy supply in a) 1973 and b) 2015. Mtoe = Millions Tonnes of Oil Equivalent.[148]

Investors and scientists are focusing on the discovery of new and sustainable clean energy sources to reduce the emissions of air pollutants as well as greenhouse gases (GHG). Solar energy is the largest global sustainable energy sources which will contribute to the security of future energy supplies. It also has environmental advantages over other energy sources, since it is not producing any waste products or air pollutants.[149, 150] Solar photovoltaic (PV) technologies are at the top of the list of applications that use solar power. Resent forecast reports by Fraunhofer Institute for Solar Energy Systems (ISE) indicated that the world PV market increased by 24% between the years 2010 to 2017.

1.9. Photovoltaic Cell (PV)

A photovoltaic cell or a solar cell is a device used to converts solar radiation to electricity; this cell is usually made of semiconductor materials, and exhibits photovoltaic effect. The photovoltaic effect occurs when semiconductor materials absorb photons resulting in the excitation of electrons and leaving a hole surrounding by electrons. The p-n junction assists the electrons to move in one direction, which generates current.[151, 152] The amount of current produced is proportional to the number of absorbed photons, which implies that PV solar cells are a variable current source. The sun is a black-body emitter with the highest emission at the visible wavelengths around 500 nm. The travelling light from the sun is attenuated by the absorbing species in the atmosphere. Figure 1.12 shows the spectrum of solar emission and the optical band gaps of selected semiconductors.[153]

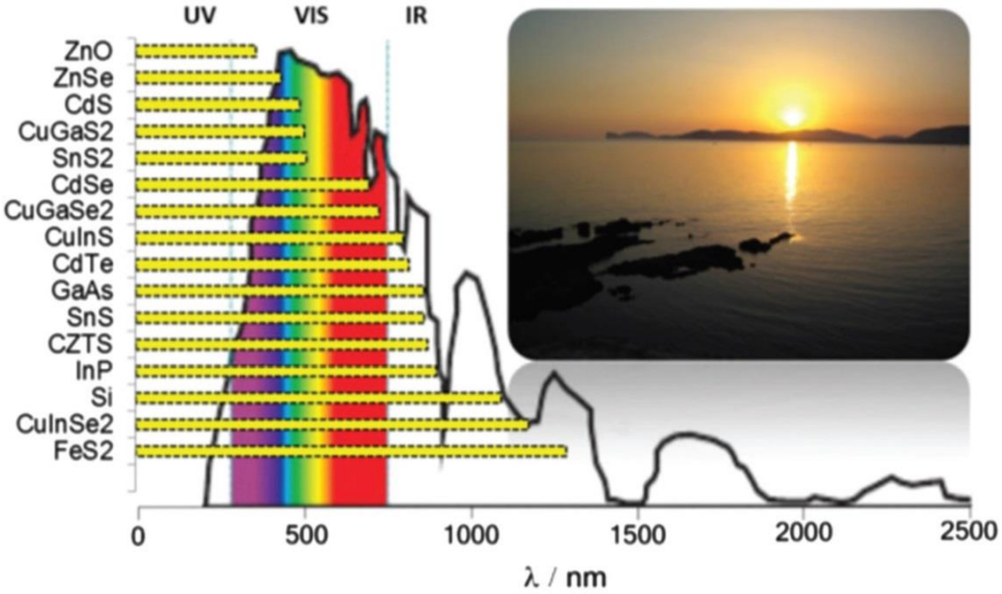

Figure 1.12 The solar emission spectrum and the optical bandgaps of some semiconductors. Reproduced from ref.153. Copyright 2014 with permission from the Partner Organisations.

A good photoactive semiconductor must have a bandgap between 1.0–1.5 eV. This is a result of the Shockley–Quessier (SQ) limit, which is the theoretical maximum efficiency for a single p-n-junction solar cell Figure **1.13**.[154]

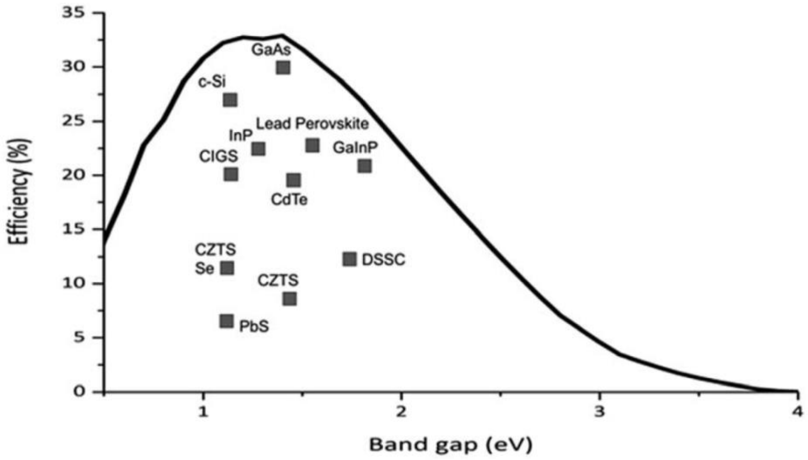

Figure 1.13 The maximum theoretical efficiency (Shockley–Quessier limit) for solar cells under AM 1.5 illumination, and the optical band gaps of a selection of photovoltaic materials. Reproduced from ref.154 . Copyright 2017 with permission from The Royal Society of Chemistry.

1.9.1. Generations of photovoltaic cells

Since the invention of solar Industry researchers are focusing on the producing cheap, low-toxic and efficient materials, that could be used in the fabrication of PV devices.Depending on the materials used, the photovoltaic technologies are classified into three generations namely first, second, and third generations.

1.9.1.1. First generations

First-generation wafer-based crystalline silicon is dominated the current market for PV device because of their high efficiency and stability, which account for 94% of the total production in 2019. However, their manufacturing process costs are, and their performance easily degrades at higher temperature conditions.

1.9.1.2. Second generations

A great amount of research has been devoted to improve the efficiency and reduce the cost of the first-generation solar cells. Introducing the thin film technology has more benfits in reducing the cost by using less material. However, those materials are not efficient as silicon. Diffrent materials have been use in the fabrication of thin-film solar cells such as cadmium sulphide (CdS), cadmium telluride (CdTe) and copper indium gallium (di)selenide (CIGS).

1.9.1.3. Third-generation photovoltaic cells

The aim of third-generation photovoltaic cells is to achieve high-efficiency devices but still use thin-film by exploring new materials with high efficiency and compatible with large-scale implementation. Besides reducing the fabrication cost. For example, Copper zinc tin sulfide (Cu_2ZnSnS_4) is a semiconductor material with a bandgap of 1.5 eV that matched with the best part of the solar spectrum. It is non-toxic, friendly to the environment and is made up of cheap materials. Another emerging material is perovskite, which has developed rapidly in the last years. The maximum power conversion efficiency (PCE) increases significantly from 3.8% in 2009 to a certified 22.1% in 2016. However, it took approximately 30 years for silicon PV devices to achieve such high efficiencies. Another procmsing candidate is quantum dot materials. A quantum dot solar cell is where quantum dots act as the absorbing layer. Semiconducting quantum dots have many advantages over traditional bulk materials such as fabrication at low-temperature, solution-processability and the ability of tuning their bandgap by varying the dots' size, which allows their absorption properties to be enhanced for PV application. Table **1-3** present the efficiency of different solar cell.

Table 1-3 Confirmed single-junction terrestrial cell and submodule efficiencies measured under the global AM1.5 spectrum (1000 W/m2) at 25°C (IEC 60904-3: 2008, ASTM G-173-03 global)[155] CIGS, $CuIn_{1-y}Ga_ySe_2$; CZTSSe, $Cu_2ZnSnS_{4-y}Se_y$; CZTS, Cu_2ZnSnS_4, Amonix; Amonix Inc, ISCAS; Institute of Semiconductors–Chinese Academy of Sciences, FirstSolar; First Solar Inc, IBM; International Business Machines, UNSW; University of

New South Wales, U.Q; Queensland University of Queensland, KRICT/ MIT; Korea Research Institute of Chemical Technology / Massachusetts Institute of Technology.

Classification	Efficiency	Institute
Si (crystalline cell)	27.6%	Amonix
GaAs (thin-film cell)	29.1	Alta Devices
CIGS (cell) (Cd-free)	23.4	ISCAS
CdTe (cell)	22.1	First Solar
CZTSSe (cell)	12.16	IBM
CZTS (cell)	10.0	UNSW
Quantum dot cell	16.6	U.Q
Perovskite (cell)	25.2	KRICT/MIT

1.10. Flexible PV devices

The first flexible solar cells were fabricated in the 1960s for space power applications.[156, 157] these cells were made of thin silicon wafers about 180µm on plastic substrate. In 1976 Wronski *et al.* reported the fabrication of a Pt/a-Si:H solar cell on stainless steel.[158]123 in the same year Staebler *et al.* successfully fabricated amorphous silicon indium tin oxide single-junction p-i-n on stainless steel.[159] Qaeed *et al.* described a low-temperature chemical method to produce indium gallium nitride nanocubes and reported the use of this material in the fabrication of flexible solar cell devices.[160] In a recent study Jo *et al*. reported a new record of efficiency 8% on thin-film solar cells made of CZTSSe on flexible Mo foil.[161] Zhang demonstrated the fabrication of flexible quantum dot PbS solar cells by introducing a layer of MgZnO nanocrystals[162] Chao *et al*. developed recently a new environmental-friendly method for the fabrication of flexible perovskite solar cells.[163]

1.11. Cellulose substrates

Cellulose is the most abundant biopolymer on the planet. Paper is an eco-friendly material made of cellulose pulp derived from wood. In fact, it is considered as one of the greatest discoveries of humankind. While paper is usually used for storing information, packaging and displaying, the possibility of using paper as a potential substrate for low-cost, flexible electronics has attracted considerable interest for many years.[164] Brody and Page proposed the first effort to use paper as a substrate for advanced applications, such as inorganic thin-film transistors (TFTs) on paper for flexible circuits.[165, 166] However, the idea of making electronics on paper did not receive much interest at that time because of the difficulty in the manufacturing process and the brittleness of the circuitry. After 30 years, Berggren renewed the interest in paper electronics, by using printing technologies and redox-active conducting polymers to fabricate simple electronic components and circuits on paper.[164, 167] The development during the last decades of manufacturing and printing technologies has increased the interest in producing flexible electronics on ether plastic and paper.

The main application of paper in electronics and optoelectronics can be divided into different categories. Firstly, on paper-type applications where is the paper used as a flexible substrate to provide mechanical support to different functional materials. The main advantage of this type is the cost savings in the device fabrication. For example, the paper is 1000 times less expensive than traditional glass substrates and is 100 times less expensive than common plastic substrates, an important factor to consider that the substrate cost represents 25–60% of total material costs in current solar modules.[168-170] Another class of applications is called electroactive paper or smart paper, where is the paper used as an active material or part of a device. However, the use of cellulose-based materials in optoelectronic applications is not straightforward. There are some challenges associated with surface roughness and porosity, which require refabricating cellulose for the intended application.

The first step in the construction of solar cells is to select a suitable substrate according to the device requirements. Glass is the most frequently-used substrate because of the high transparency, low cost and the high stability against fabrication conditions. However, the thickness, high rigidity and weight prevent the use of glass on flexible solar cells. There are some technical requirements of paper substrates to assure performance and reproducibility;

- Thermal stability: It is well known that paper is sesitve to temperature. Therefore, the glass transition temperature (Tg) of the substrates should be compatible with the maximum fabrication process temperature.

- Mechanical stability: The coefficient of thermal expansion (CTE) measures the fractional increase of length per unit rise in temperature. It is important to avoid the thermal mismatch between the substrate and deposited layers to prevent the breaking in film in the case of thermal cycling associated with the fabrication process.
- Surface smoothness: The substrate should possess an acceptable roughness to prevent any shunting issues.
- Optical transmittance; high transmittance and a high haze factor are essential properties to maximize the efficiency of solar cells.
- Chemical properties: The substrate should not release contaminants and should be inert against common chemicals.

A comparison between different flexible substrates is presented in Table 1-4.

Table 1-4 Set of morphologic properties (glass transition temperature, Tg, coefficient of thermal expansion, CTE, and water vapor transmission rate, WVTR) of different flexible solar cell materials versus glass.[171] [a] Estimated value for microcrystalline cellulose powder (~20 µm, M_n= 74 500; from Sigma-Aldrich), with 70% crystallinity index and 5% water content. [b] Test conditions [µm; °C; RH%] provide, respectively, the thickness of the material tested, the temperature, and the relative humidity. [c] Value for the 100 µm thin Corning® Willows glass.[d] Value for the bleached Kraft paper (70 gm^{-2}) from the Limerick Pulp and Paper Centre. Aluminium (Al), stainless steel (SS), Cornings glass, polyethylene naphthalate (PEN), polyethylene terephthalate (PET), polyimide (PI), and cellulose. Reproduced from ref.163. Copyright 2018, The Royal Society of Chemistry.

	Al	Corning® glass	PEN	PET	PI	Cellulose
Tg (°C)	N/A	620[172]	120[173]	70[173]	270[173]	~80[a] [174]
CTE (ppm k^{-1})	23-27	3.2-3.6	16-20	33[173]	8-20[173]	28-40
WVTR ($g\ m^{-2}\ day^{-1}$) [test conditions][b]	0.007 [9 mm; 38 °C; 90%]	7X10-6-5x10-5 [100 mm; 45–85 °C; 85%][c]	0.23–0.65 [200 mm; 70 °C; 25–80%]	1.1–11 [100 mm, 45–85 °C, 85%][c]	2.4–54 [25 mm, 23 °C, 50%]	435–1209 [120 mm, 25 °C, 33–75%][d]

In the past decade, great attention has been devoted to the use of cellulose-based materials as substrate. For example, Lamprecht *et al.* fabricated the first solar cell on a paper substrate was in 2005. The organic solar cell was supported on newspaper coated with a parylene C film as a moisture barrier, followed by a layer of ORMOCER® to improve the surface roughness.[172] Recently, Voggu *et al.* reported the first nanocrystal photovoltaic devices (PVs) made on paper. They used the spray-coating to deposit $CuInSe_2$ on paper made of pure crystalline cellulose nanofibers. The cell demonstrates excellent thermal and air-stability with efficiencies as high as 2.25%, which consider as the highest efficiency yet reported for solar cells constructed directly on paper.[173] Brody *et al.* successfully fabricated a paper PV with an efficiency of 5.0%.[171] More advanced wireless sensor paper has been proposed Damilano *et al.*[171] Different types of solar cells recently fabricated on distinct paper-based substrates are summarized in Table 1-5.

Table 1-5 Recent study on the fabrication of PV on paper. Reproduced from ref.171. Copyright 2018, The Royal Society of Chemistry.

SC type	Cellulose type	Coating / contact layer	J_{SC} (mA cm^{-2})	V_{OC} (V)	FF (%)	Efficiency (%)	Year	ref
OPV	Newspaper	Parylene + ORMOCERs	0.22	0.40	N/D	< 0.30	2005	172
	COP	Amylum film	0.10	0.39	33	0.13%	2010	174
	Gloss paper	Glue + Zn	3.64	0.59	37	1.31	2011	175
	CNF	ITO	2.41	0.38	23	<0.40	2013	176
	CNC	Ag + PEIE	7.50	0.65	54	2.70	2013	177
	CNC	Ag + PEI	7.80	0.81	64	4.00	2014	178

Table 1-5 (continued)

	Gloss paper	Glue +Zn polypropylene	10.60	0.71	55	4.10	2014	179
	CNF	Ag nanowire suspension	9.58	~0.74	N/D	3.20	2015	180
	CNC	Ag + AZO	3.50	0.90	40	1.40	2016	181
	CNF	Ag + AZO	2.00	0.70	0.30	0.50	2016	181
DSSC	Cardboard	Ni	6.70	0.68	76	1.21	2011	182
	Glass paper (used as substrate and electrolyte medium)	Pt (electrocatalytic); Ru-complex dye-loaded TiO2 (photoelectrode)	3.90	0.68	76	2.05	2012	183
	Manila paper	Ni	7.79	0.65	56	2.90	2012	184
	Carbon fiber composite	PEDOT	13.09	0.72	63	6.13	2016	185
	COP	Graphene dots + PEDOT:PSS	12.08	0.70	58	4.91	2017	186
QDPV	COP	Graphite	2.30	0.78	N/D	1.80	2016	187

Table 1-5 (continued)

Perovskite	CNF	TiO2 + Ag + TiO_2 (DMD structure)	15.37	0.86	48	6.37	2016	188
THSC	CNF	$CuInSe_2$	10.47	0.44	0.48	2.25	2017	173

1.12. Instrumentation

1.12.1. Powder X-ray diffraction

Powder X-ray diffraction (p-XRD) is a powerful, fast and non-destructive characterization technique. It provides important information about structure, phase, composition, shape, size, crystallinity, and other important features of nanoscale materials. The technique is based on constructive interference between the X-rays beam and atoms in the sample. The main components of an X-ray diffractometer are an X-ray tube, a sample holder, and an X-ray detector. When the sample is bombarded by a beam of X-rays, X-rays diffracted by layers of atoms in the sample, which obey Bragg's Law[189]:

$$(n\lambda = 2d \sin \theta) \qquad \text{(eq 1.1)}$$

where λ is the wavelength of the X-rays, *n* is the order, *d* is the spacing between adjacent crystal planes, and θ is the diffraction angle. Identification of the sample phase is often accomplished by comparing the experimental diffracted ray angles with standard reference patterns in the ICDD (International Centre for Diffraction Data) database.

One application of powder XRD is calculated the mean value of the crystal size by using the Scherrer equation:[190]

$$(D = K \lambda / \beta \cos \theta) \qquad \text{(eq 1.1)}$$

where (D) is crystalline domain size. The Scherrer constant, k, is typically considered to be 0.9, λ is the wavelength of the X-rays. β is the full width at half-maximum (FWHM) of the peak reflections, θ is diffraction angle.

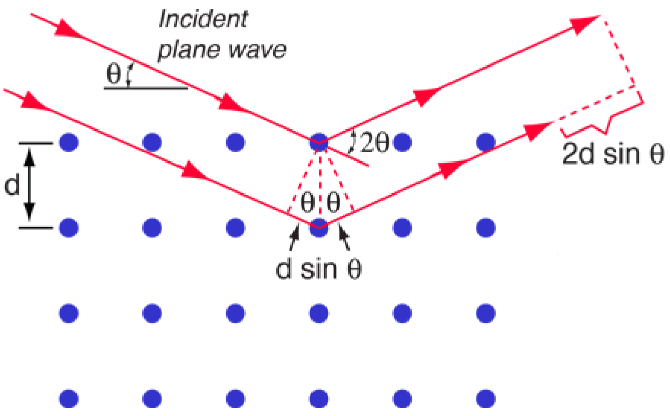

Figure 1.14 Schematic illustrationof Bragg's law.

1.12.2. Uultraviolet-visible (UV-VIS)

The optical properties of semiconductor material can be examined using the ultraviolet-visible (UV-VIS) spectroscopy. When the beam of light is irradiated the sample some part of the photons may be absorbed while remaining can be transmitted, the detector measures the ratio of light transmitted (I) through the sample where it is compared with the light incident (I_0) on the sample. For a given wavelength, the absorption (Aλ) can be calculated based on the absorbance in eq

$$A\lambda = \mathrm{Log}_{10}\,(I_0 / I) \qquad \text{(eq. 1.2)}$$

The UV-VIS spectrum of the sample is usually presented as a graph of the absorption at different wavelengths. The optical bandgap can be obtained by using a Tauc plot.[191] Typically, the x axis represents photon energy (hv) and y axis present (αhv)1/r, where α is the material's absorption coefficient and r represents the nature of the electron transition. Here, r could have different values due to the different distributions of energy levels; r equals to 0.5 for the direct allowed transition, while r equals to 2 for the indirect allowed transition

1.12.3. Raman Spectroscopy

Raman spectroscopy is a useful technique that provides a simple, fast and non-destructive analysis of both organic and inorganic materials. A Raman spectrometer consists of leaser source, sample illumination & collector system, wavelength selector and detector & data processing system. Its basically based on the principle of inelastic scattering of light with material. Whene the sample is illuminated by intense laser beam of frequency (v_o) in the UV-Visible region, the scattered laser beam is often observed in a direction perpendicular to the incident beam. The scattered beam is consists of two components: a strong elastic scattering of photons (Rayleigh scattering) which has the same frequency as the incident light (v_o), and very weak inelastic scattering (Raman scattering) that has frequency ($v_o \pm v_m$), where (v_m) is a vibrational frequency of a molecule. The ($v_o - v_m$), and ($v_o + v_m$) lines are called the Stoke and anti-Stoke lines respectively.

1.13. Aim of study

In the past two decades, the combinations of soft materials and electronic materials have been extensively investigated to achieve high flexibility of electronic devices. Materials chemistry plays essential roles in the exploring and developing new active materials, new elastic substrates, and new manufacture processes of both. An ideal solar cell is consist of three essential layers; a transparent conducting substrate, an absorber layer and metal conduct electrode. The objective of this study is to investigate the possibility of obtaining suitable, inexpensive and high-efficiency materials which could be used in the fabrication of PV devices. Therefore, we hypothesise that copper(II) aminocarboxlaic complexes could be used as precursors to produce a copper as a conductive electrode. We also believe that the metal xanthate complexes are a promising candidate for the production of binary, ternary and quaternary metal sulfide as an absorber layer. Furthermore, cellulose is an excellent choice for a flexible, inexpensive and environmental friendly substrate. The combination of these materials could be useful for the construction of a flexible solar cell.

1.14. References

1. Holger T. Grahn, Introduction to Semiconductor Physics, World Scientific publishing Co. Pte.Ltd, 1999.
2. D. Sumanth Kumar, B. Jai Kumar and H. M. Mahesh, in Synthesis of Inorganic Nanomaterials, eds. S. M. Bhagyaraj, O. S. Oluwafemi, N. Kalarikkal and S. Thomas, Woodhead Publishing, 2018, pp. 59-88.
3. M. Bernechea, Y. M. Cao and G. Konstantatos, *J. Mater. Chem. A*, 2015, **3**, 20642-20648.
4. H. Y. He and T. T. Liu, *JOM*, 2014, **66**, 979-984.
5. A. Kyono and M. Kimata, *Am. Miner.*, 2004, **89**, 932-940.
6. K. Ramasamy, M. A. Malik, N. Revaprasadu and P. O'Brien, *Chem. Mater.*, 2013, **25**, 3551-3569.
7. G. Hodes, J. Manassen and D. Cahen, *Nat*, 1976, **261**, 403-404.
8. G. Konstantatos, L. Levina, J. Tang and E. H. Sargent, *Nano Lett.*, 2008, **8**, 4002-4006.
9. H. Li, J. Yang, J. Zhang and M. Zhou, *RSC Adv.*, 2012, **2**, 6258-6261.
10. B. Sun, T. T. Feng, J. Dong, X. L. Li, X. H. Liu, J. Wu and S. Y. Ai, *CrystEngComm*, 2019, **21**, 1474-1481.
11. Q. Yang, C. G. Hu, S. X. Wang, Y. Xi and K. Y. Zhang, *J. Phys. Chem. C*, 2013, **117**, 5515-5520.
12. S. C. Liufu, L. D. Chen, Q. Yao and C. F. Wang, *Appl. Phys. Lett.*, 2007, **90**, 112-106.
13. B. Zhang, X. Ye, W. Hou, Y. Zhao and Y. Xie, *J. Phys. Chem. B*, 2006, **110**, 8978-8985.
14. Q. T. Wang, X. B. Wang, W. J. Lou and J. C. Hao, *New J. Chem.*, 2010, **34**, 1930-1935.
15. A. Rajaee, S. Wang and L. Y. Zhao, *Pol. J. Med. Phys. Eng.*, 2019, **25**, 79-85.
16. O. Rabin, J. M. Perez, J. Grimm, G. Wojtkiewicz and R. Weissleder, *Nat. Mater.*, 2006, **5**, 118-122.
17. L. Cademartiri, F. Scotognella, P. G. O'Brien, B. V. Lotsch, J. Thomson, S. Petrov, N. P. Kherani and G. A. Ozin, *Nano Lett.*, 2009, **9**, 1482-1486.
18. H. Zhang, G. Chen, B. Yu, Y. Shen and H. Cong, *ACS Appl. Bio. Mater.*, 2019.

19. E. Miniach and G. Gryglewicz, *J. Mater. Sci.*, 2018, **53**, 16511-16523.

20. Z. J. Wang, S. C. Qu, X. B. Zeng, J. P. Liu, F. R. Tan, L. Jin and Z. G. Wang, *Appl. Surf. Sci.*, 2010, **257**, 423-428.

21. X. Y. Ma, L. Liu, W. L. Mo, H. Liu, H. Z. Kou and Y. Wang, *J. Cryst. Growth*, 2007, **306**, 159-165.

22. J. Lu, Q. Han, X. Yang, L. Lu and X. Wang, *Mater. Lett.*, 2007, **61**, 3425-3428.

23. J. Wang and Y. Li, *Mater. Chem. Phys.*, 2004, **87**, 420-423.

24. M. B. Sigman and B. A. Korgel, *Chem. Mater.*, 2005, **17**, 1655-1660.

25. L. Tian, H. Yao Tan and J. J. Vittal, *Cryst. Growth Des.*, 2007, **8**, 734-738.

26. T. Alqahtani, M. D. Khan, D. J. Kelly, S. J. Haigh, D. J. Lewis and P. O’Brien, *J. Mater. Chem. C*, 2018, **6**, 12652-12659.

27. M. D. Khan, M. Akhtar, M. A. Malik, N. Revaprasadu and P. O'Brien, *ChemistrySelect*, 2018, **3**, 2943-2950.

28. W. N. Kun, P. D. McNaughter, L. D. Nyamen, B. F. Spencer, P. O'Brien, P. T. Ndifon and N. Revaprasadu, *RSC Adv.*, 2019, **9**, 15836-15844.

29. W. N. Kun, S. Mlowe, L. D. Nyamen, M. P. Akerman, P. O'Brien, P. T. Ndifon and N. Revaprasadu, *Polyhedron*, 2018, **154**, 173-181.

30. K. Q. Liang, C. G. Wang, X. J. Xu, J. C. Leng and H. Ma, *Phys. Lett. A*, 2017, **381**, 652-657.

31. W. J. Lou, M. Chen, X. B. Wang and W. M. Liu, *Chem. Mater.*, 2007, **19**, 872-878.

32. E. Miniach and G. Gryglewicz, *J. Mater. Sci.*, 2018, **53**, 16511-16523.

33. J. Arumugam, A. D. Raj, A. A. Irudayaraj and M. Thambidurai, *Mater. Lett.*, 2018, **220**, 28-31.

34. E. B. Díaz-Cruz, O. A. Castelo-González, C. Martínez-Alonso, Z. Montiel-González, M. C. Arenas-Arrocena and H. Hu, *Mater. Sci. Semicond. Process.*, 2018, **75**, 311-318.

35. H. C. Liao, M. C. Wu, M. H. Jao, C. M. Chuang, Y. F. Chen and W. F. Su, *Crystengcomm*, 2012, **14**, 3645-3652.

36. J. Mock, B. Klingebiel, D. Schillings, M. Nuys, J. Flohre, S. Wang, T. Kirchartz and R. Carius, *Phys Rev Mater*, 2019, **3**, 105406.

37. L. Whittaker-Brooks, J. Gao, A. K. Hailey, C. R. Thomas, N. Yao and Y. L. Loo, *Jo. Mater. Chem. C*, 2015, **3**, 2686-2692.

38. A. J. MacLachlan, F. T. O'Mahony, A. L. Sudlow, M. S. Hill, K. C. Molloy, J. Nelson and S. A. Haque, *Chemphyschem*, 2014, **15**, 1019-1023.
39. A. Parveen, S. Agrawal and A. Azam, *Opt. Mater.*, 2018, **76**, 21-27.
40. R. Dalven, *Infrared Phys.Technol.*, 1969, **9**, 141-184.
41. K. W. Johnston, A. G. Pattantyus-Abraham, J. P. Clifford, S. H. Myrskog, D. D. MacNeil, L. Levina and E. H. Sargent, *Appl. Phys. Lett.*, 2008, **92**, 151115.
42. S. A. McDonald, G. Konstantatos, S. Zhang, P. W. Cyr, E. J. Klem, L. Levina and E. H. Sargent, *Nat. Mater.*, 2005, **4**, 138-142.
43. S. F. Wang, F. Gu and M. K. Lu, *Langmuir*, 2006, **22**, 398-401.
44. J. Sun, M. Q. Zhu, K. Fu, N. Lewinski and R. A. Drezek, *Int. J. Nanomedicine*, 2007, **2**, 235-240.
45. T. Mandal, G. Piburn, V. Stavila, I. Rusakova, T. Ould-Ely, A. C. Colson and K. H. Whitmire, *Chem. Mater.*, 2011, **23**, 4158-4169.
46. M. Uchida, M. L. Flenniken, M. Allen, D. A. Willits, B. E. Crowley, S. Brumfield, A. F. Willis, L. Jackiw, M. Jutila, M. J. Young and T. Douglas, *J. Am. Chem. Soc.*, 2006, **128**, 16626-16633.
47. L. S. Ramsdell, *Am. Mineral.*, 1925, **10**, 281-304.
48. J. Q. Sun, X. P. Shen, L. J. Guo, K. M. Chen and Q. Liu, *Physica E*, 2009, **41**, 1527-1532.
49. Y. Zhao, X. H. Liao, J. M. Hong and J. J. Zhu, *Mater. Chem. Phys.*, 2004, **87**, 149-153.
50. P. T. Zhao, G. Chen, Y. Hu, X. L. He, K. Wu, Y. Cheng and K. X. Huang, *J. Cryst. Growth*, 2007, **303**, 632-637.
51. T. Trindade, P. OBrien, X. M. Zhang and M. Motevalli, *J. Mater. Chem.*, 1997, **7**, 1011-1016.
52. M. Afzaal, K. Ellwood, N. L. Pickett, P. O'Brien, J. Raftery and J. Waters, *J. Mater. Chem.*, 2004, **14**, 1310-1315.
53. J. Akhtar, M. A. Malik, P. O'Brien and M. Helliwell, *J. Mater. Chem.*, 2010, **20**, 6116-6124.
54. I. Jen-La Plante, T. W. Zeid, P. Yang and T. Mokari, *J. Mater. Chem.*, 2010, **20**, 6612-6617.

55. T. P. Duan, W. J. Lou, X. B. Wang and Q. J. Xue, *Colloids Surf., A*, 2007, **310**, 86-93.

56. M. A. Hines and G. D. Scholes, *Adv. Mater.*, 2003, **15**, 1844-1849.

57. M. Corricelli, D. Altamura, L. De Caro, A. Guagliardi, A. Falqui, A. Genovese, A. Agostiano, C. Giannini, M. Striccoli and M. L. Curri, *CrystEngComm*, 2011, **13**, 3988-3997.

58. B. Ding, M. M. Shi, F. Chen, R. J. Zhou, M. Deng, M. Wang and H. Z. Chen, *J. Cryst. Growth*, 2009, **311**, 1533-1538.

59. M. Salavati-Niasari and D. Ghanbari, *Particuology*, 2012, **10**, 628-633.

60. A. Querejeta-Fernandez, J. C. Hernandez-Garrido, H. Yang, Y. Zhou, A. Varela, M. Parras, J. J. Calvino-Gamez, J. M. Gonzalez-Calbet, P. F. Green and N. A. Kotov, *ACS Nano*, 2012, **6**, 3800-3812.

61. W. X. Wang, Q. Li, M. Li, H. Lin and L. J. Hong, *J. Cryst. Growth*, 2007, **299**, 17-21.

62. J. Jiao, X. Liu, W. Gao, C. Wang, H. Feng, X. Zhao and L. Chen, *Solid State Sci.*, 2009, **11**, 976-981.

63. K. R. Hansen, J. R. Peterson, A. Perego, M. Shelley, C. R. Olsen, L. D. Perez, H. L. Hogg, R. K. Watt and J. S. Colton, *Appl. Nanosci*, 2018, **8**, 1687-1699.

64. F. Gode and S. Unlu, *Mater. Sci. Semicond. Process.*, 2019, **90**, 92-100.

65. S. R. Tulsani and A. K. Rath, *J. Colloid Interface Sci.*, 2018, **522**, 120-125.

66. D. H. Yeon, B. C. Mohanty, C. Y. Lee, S. M. Lee and Y. S. Cho, *ACS Omega*, 2017, **2**, 4894-4899.

67. S. P. Gubin, Y. A. Koksharov, G. Khomutov and G. Y. e. Yurkov, *Russ. Chem. Rev.*, 2005, **74**, 489-520.

68. K. Wang and A. Balandin, *Optics of Nanostructured Mater.*, 2001, 515-550.

69. J. Park, J. Joo, S. G. Kwon, Y. Jang and T. Hyeon, *Angew. Chem. Int. Ed.*, 2007, **46**, 4630-4660.

70. S. Horikoshi and N. Serpone, *Microwaves in Nanoparticle Synthesis*, 2013, 1-24.

71. S. Peng, Y. M. Lee, C. Wang, H. F. Yin, S. Dai and S. H. Sun, *Nano Res.*, 2008, **1**, 229-234.

72. W. Zhou, J. Wu and H. Yang, *Nano Lett.*, 2013, **13**, 2870-2874.

73. M. Kluenker, B. M. Connolly, D. M. Marolf, M. N. Tahir, K. Korschelt, P. Simon, U. Kohler, S. Plana-Ruiz, B. Barton, M. Panthofer, U. Kolb and W. Tremel, *Inorg. Chem.*, 2018, **57**, 13640-13652.
74. P. Jiang, Z. Q. Tian, C. N. Zhu, Z. L. Zhang and D. W. Pang, *Chem. Mater.*, 2012, **24**, 3-5.
75. H. B. Li, D. Chen, L. L. Li, F. Q. Tang, L. Zhang and J. Ren, *CrystEngComm*, 2010, **12**, 1127-1133.
76. C. B. Murray, D. J. Norris and M. G. Bawendi, *J. Am. Chem. Soc.*, 1993, **115**, 8706-8715.
77. M. Al-Shakban, P. D. Matthews, G. Deogratias, P. D. McNaughter, J. Raftery, I. Vitorica-Yrezabal, E. B. Mubofu and P. O'Brien, *Inorg. Chem.*, 2017, **56**, 9247-9254.
78. E. Lewis, S. Haigh and P. O'Brien, *J. Mater. Chem. A*, 2014, **2**, 570-580.
79. M. Lazell and P. O'Brien, *Chem. Commun.*, 1999, 2041-2042.
80. K. Abe, T. Hanada, Y. Yoshida, N. Tanigaki, H. Takiguchi, H. Nagasawa, M. Nakamoto, T. Yamaguchi and K. Yase, *Thin Solid Films*, 1998, **327**, 524-527.
81. T. H. Larsen, M. Sigman, A. Ghezelbash, R. C. Doty and B. A. Korgel, *J. Am. Chem. Soc.*, 2003, **125**, 5638-5639.
82. M. B. Sigman, Jr., A. Ghezelbash, T. Hanrath, A. E. Saunders, F. Lee and B. A. Korgel, *J. Am. Chem. Soc.*, 2003, **125**, 16050-16057.
83. L. Chen, Y. B. Chen and L. M. Wu, *J. Am. Chem. Soc.*, 2004, **126**, 16334-16335.
84. J. Chen, L. Chen and L. M. Wu, *Inorg. Chem.*, 2007, **46**, 8038-8043.
85. Y. B. Chen, L. Chen and L. M. Wu, *Inorg. Chem.*, 2005, **44**, 9817-9822.
86. J. G. Brennan, T. Siegrist, P. J. Carroll, S. M. Stuczynski, L. E. Brus and M. L. Steigerwald, *J. Am. Chem. Soc.*, 1989, **111**, 4141-4143.
87. E. J. Kupchik and P. J. Calabretta, *Inorg. Chem.*, 1965, **4**, 973-978.
88. M. L. Riekkola, T. Pakkanen and L. Niinisto, *Acta Chem. Scand.*, 1983, **37**, 807-816.
89. C. P. Sharma, N. Kumar, M. C. Khandpal, S. Chandra and V. G. Bhide, *J. Inorg. Nucl. Chem.*, 1981, **43**, 923-930.
90. O. C. Monteiro, H. I. S. Nogueira, T. Trindade and M. Motevalli, *Chem. Mater.*, 2001, **13**, 2103-2111.
91. S. M. Lee, Y. W. Jun, S. N. Cho and J. Cheon, *J. Am. Chem. Soc.*, 2002, **124**, 11244-11245.

92. A. C. Fabretti, A. Giusti, C. Preti, G. Tosi and P. Zannini, *Polyhedron*, 1986, **5**, 871-875.

93. E. Sathiyaraj and S. Thirumaran, *Spectrochim. Acta, Part A*, 2012, **97**, 575-581.

94. D. C. Onwudiwe, *Heliyon*, 2019, **5**, 1-17.

95. T. Trindade, P. O'Brien, X.-m. Zhang and M. Motevalli, *J. Mater. Chem.*, 1997, **7**, 1011-1016.

96. O. C. Monteiro and T. Trindade, *J. Mater. Sci. Lett.*, 2000, **19**, 859-861.

97. R. Chauhan, J. Chaturvedi, M. Trivedi, J. Singh, K. C. Molloy, G. Kociok-Kohn, D. P. Amalnerkar and A. Kumar, *Inorg. Chem. Acta*, 2015, **430**, 168-175.

98. C. P. Sharma, N. Kumar, M. C. Khandpal, S. Chandra and V. G. Bhide, *J. Inorg. Nucl. Chem.*, 1981, **43**, 923-930.

99. D. Barreca, A. Gasparotto, C. Maragno and E. Tondello, *J. Electrochem. Soc.*, 2004, **151**, G428-G435.

100. M. Shankaranarayana and C. Patel, *Can. J. Chem.*, 1961, **39**, 1633-1637.

101. J. S. Casas, A. Castiñeiras, I. Haiduc, A. n. Sánchez, R. F. Semeniuc and J. Sordo, *J. Mol. Struct.*, 2003, **656**, 225-230.

102. J. M. Clark, G. Kociok-Kohn, N. J. Harnett, M. S. Hill, R. Hill, K. C. Molloy, H. Saponia, D. Stanton and A. Sudlow, *Dalton Trans*, 2011, **40**, 6893-6900

103. P. D. McNaughter, S. A. Saah, M. Akhtar, K. Abdulwahab, M. A. Malik, J. Raftery, J. A. Awudza and P. O'Brien, *Dalton Trans*, 2016, **45**, 16345-16353.

104. J. Akhtar, M. Afzaal, M. A. Vincent, N. A. Burton, I. H. Hillier and P. O'Brien, *Chem. Commun.*, 2011, **47**, 1991-1993.

105. Q. F. Han, J. Chen, X. J. Yang, L. Lu and X. Wang, *J. Phys. Chem. C*, 2007, **111**, 14072-14077.

106. E. A. Lewis, P. D. McNaughter, Z. J. Yin, Y. Q. Chen, J. R. Brent, S. A. Saah, J. Raftery, J. A. M. Awudza, M. A. Malik, P. O'Brien and S. J. Haigh, *Chem. Mater.*, 2015, **27**, 2127-2136.

107. L. Brus, *Acc. Chem. Res.*, 2008, **41**, 1742-1749.

108. L. Zhang, W. X. Niu and G. B. Xu, *Nano Today*, 2012, **7**, 586-605.

109. C. Zhu, D. Du, A. Eychmuller and Y. Lin, *Chem. Rev.*, 2015, **115**, 8896-8943.

110. P. K. Jain, X. Huang, I. H. El-Sayed and M. A. El-Sayed, *Acc. Chem. Res.*, 2008, **41**, 1578-1586.

111. M. Nasrollahzadeh, A. Zahraei, A. Ehsani and M. Khalaj, *Rsc Adv.*, 2014, **4**, 20351-20357.

112. S. Yu, R. Wen, H. Wang, Y. Zha, L. Qiu, B. Li, W. Xue and D. Ma, *Chem. Mater.*, 2019.

113. A. F. Melo, A. Hassan, L. J. Macedo, I. Osica, L. K. Shrestha, Q. Ji, O. N. Oliveira Jr, J. Henzie, K. Ariga and F. N. Crespilho, *ACS Appl. Mater. Interfaces*, 2019, **11**, 18053-18061.

114. N. Zhao, L. Yan, X. Zhao, X. Chen, A. Li, D. Zheng, X. Zhou, X. Dai and F. J. Xu, *Chem. Rev.*, 2019, **119**, 1666-1762.

115. S. Wang, J. Yin, H. Wei, K. Huang, L.-M. Liu and H. Wu, *ACS Appl. Energy Mater.*, 2018, **2**, 468-476.

116. M. Hu, J. Chen, Z. Y. Li, L. Au, G. V. Hartland, X. Li, M. Marquez and Y. Xia, *Chem. Soc. Rev.*, 2006, **35**, 1084-1094.

117. S. E. Skrabalak, J. Chen, L. Au, X. Lu, X. Li and Y. Xia, *Adv. Mater.*, 2007, **19**, 3177-3184.

118. P. Alivisatos, *Nat. Biotechnol.*, 2004, **22**, 47-52.

119. J. P. Camden, J. A. Dieringer, J. Zhao and R. P. Van Duyne, *Acc. Chem. Res.*, 2008, **41**, 1653-1661.

120. B. Lim, M. Jiang, P. H. Camargo, E. C. Cho, J. Tao, X. Lu, Y. Zhu and Y. Xia, *Sci.*, 2009, **324**, 1302-1305.

121. M. Salavati-Niasari, N. Mir and F. Davar, *Appl. Surf. Sci.*, 2010, **256**, 4003-4008.

122. F. Davar, Z. Fereshteh and M. Salavati-Niasari, *J. Alloys Compd.*, 2009, **476**, 797-801.

123. D. B. Pedersen, S. Wang and S. H. Liang, *J. Phys. Chem. C*, 2008, **112**, 8819-8826.

124. R. M. Crooks, M. Zhao, L. Sun, V. Chechik and L. K. Yeung, *Acc. Chem. Res.*, 2001, **34**, 181-190.

125. L. Balogh and D. A. Tomalia, *J. Am. Chem. Soc.*, 1998, **120**, 7355-7356.

126. D. Mott, J. Galkowski, L. Wang, J. Luo and C. J. Zhong, *Langmuir*, 2007, **23**, 5740-5745.

127. M. B. Gawande, A. Goswami, F. X. Felpin, T. Asefa, X. Huang, R. Silva, X. Zou, R. Zboril and R. S. Varma, *Chem. Rev.*, 2016, **116**, 3722-3811.

128. M. Kanzaki, Y. Kawaguchi and H. Kawasaki, *ACS Appl. Mater. Interfaces*, 2017, **9**, 20852-20858.

129. A. H. Shaik and J. Chakraborty, *Rsc Adv.*, 2015, **5**, 85974-85977.

130. B. K. Park, S. Jeong, D. Kim, J. Moon, S. Lim and J. S. Kim, *J. Colloid Interface Sci.*, 2007, **311**, 417-424.

131. S. Uk Son, I. Kyu Park, J. Park and T. Hyeon, *Chem. Commun.*, 2004, 778-779.

132. L. I. Hung, C. K. Tsung, W. Huang and P. Yang, *Adv. Mater.*, 2010, **22**, 1910-1914.

133. H. Z. Guo, X. Liu, Q. S. Xie, L. S. Wang, D. L. Peng, P. S. Branco and M. B. Gawande, *Rsc Adv.*, 2013, **3**, 19812-19815.

134. W. Li, D. H. Zhang and Z. Sun, *J. Phys. Chem. A*, 2014, **118**, 9801-9810.

135. H. J. Yang, S. Y. He, H. L. Chen and H. Y. Tuan, *Chem. Mater.*, 2014, **26**, 1785-1793.

136. T. Togashi, M. Nakayama, A. Hashimoto, M. Ishizaki, K. Kanaizuka and M. Kurihara, *Dalton Trans*, 2018, **47**, 5342-5347.

137. E. Ye, S. Y. Zhang, S. Liu and M. Y. Han, *Chem. Eur. J.*, 2011, **17**, 3074-3077.

138. Y. Zhang, J. Guo, D. Xu, Y. Sun and F. Yan, *Langmuir*, 2018, **34**, 3884-3893.

139. Y. Lee, J. R. Choi, K. J. Lee, N. E. Stott and D. Kim, *Nanotechnology*, 2008, **19**, 415604.

140. Y. H. Wei, S. Chen, B. Kowalczyk, S. Huda, T. P. Gray and B. A. Grzybowski, *J. Phys. Chem. C*, 2010, **114**, 15612-15616.

141. K. M. Rajesh, B. Ajitha, Y. A. K. Reddy, Y. Suneetha and P. S. Reddy, *Optik*, 2018, **154**, 593-600.

142. M.-G. Kang, H. Joon Park, S. Hyun Ahn and L. Jay Guo, *Sol. Energy Mater. Sol. Cells*, 2010, **94**, 1179-1184.

143. J. Chen, W. Zhou, J. Chen, Y. Fan, Z. Zhang, Z. Huang, X. Feng, B. Mi, Y. Ma and W. Huang, *Nano Research*, 2014, **8**, 1017-1025.

144. Z. Liu, S. Y. Lee and E.-C. Lee, *Appl. Phys. Lett.*, 2014, **105**, 223306.

145. The Intergovernmental Panel on Climate Change, *Climate Change 2007 The Physical Science Basis*, Cambridge University Press, New York, 2007.

146. M. R. Borges Neto, P. C. M. Carvalho, J. O. B. Carioca and F. J. F. Canafístula, *Energy Policy*, 2010, **38**, 4497-4506.

147. M. Hosenuzzaman, N. A. Rahim, J. Selvaraj, M. Hasanuzzaman, A. B. M. A. Malek and A. Nahar, *Renewable & Sustainable Energy Reviews*, 2015, **41**, 284-297.
148. International Energy Agency, *Key World Energy Statistics 2017*, International Energy Agency, 2017.
149. P. Moriarty and D. Honnery, *Renewable Sustainable Energy Rev*, 2012, **16**, 244-252.
150. P. M. Voroshilov, C. R. Simovski, P. A. Belov and A. S. Shalin, *J. Appl. Phys.*, 2015, **117**, 203101.
151. V. V. Tyagi, N. A. A. Rahim, N. A. Rahim and J. A. L. Selvaraj, *Renewable Sustainable Energy Rev*, 2013, **20**, 443-461.
152. B. Parida, S. Iniyan and R. Goic, *Renewable & Sustainable Energy Reviews*, 2011, **15**, 1625-1636.
153. D. J. Lewis, P. Kevin, O. Bakr, C. A. Muryn, M. A. Malik and P. O'Brien, *Inorg. Chem. Frontiers*, 2014, **1**, 577-598.
154. P. D. Matthews, P. D. McNaughter, D. J. Lewis and P. O'Brien, *Chem. Sci.*, 2017, **8**, 4177-4187.
155. M. A. Green, Y. Hishikawa, E. D. Dunlop, D. H. Levi, J. Hohl-Ebinger, M. Yoshita and A. W. Y. Ho-Baillie, *Prog. in Photovoltaics*, 2019, **27**, 3-12.
156. R. L. Crabb and F. C. Treble, *Nat.*, 1967, **213**, 1223.
157. K. A. Ray, *IEEE Trans. Aerosp. Electron. Syst.*, 1967, **AES-3**, 107-115.
158. C. R. Wronski, D. E. Carlson and R. E. Daniel, *Appl. Phys. Lett.*, 1976, **29**, 602-605.
159. D. L. Staebler, R. S. Crandall and R. Williams, *Appl. Phys. Lett.*, 1981, **39**, 733-735.
160. M. A. Qaeed, K. Ibrahim, K. M. Saron, M. A. Ahmed and N. K. Allam, *ACS Appl. Mater. Interfaces*, 2014, **6**, 9925-9931.
161. E. Jo, M. G. Gang, H. Shim, M. P. Suryawanshi, U. V. Ghorpade and J. H. Kim, *ACS Appl. Mater. Interfaces*, 2019.
162. X. Zhang, P. K. Santra, L. Tian, M. B. Johansson, H. Rensmo and E. M. J. Johansson, *ACS Nano*, 2017, **11**, 8478-8487.M. Berggren, D. Nilsson and N. D. Robinson, *Nat Mater*, 2007, **6**, 3-5.
163. L. Chao, Y. Xia, B. Li, G. Xing, Y. Chen and W. Huang, *Chem*, 2019, **5**, 995-1006.
164. M. Berggren, D. Nilsson and N. D. Robinson, *Nat Mater*, 2007, **6**, 3-5.
165. W. S. Bacon, *Pop Sci*, 1968, **193**, 124-125.
166. T. P. Brody, *IEEE Trans. Electron Devices*, 1984, **31**, 1614-1628.

167. P. Andersson, D. Nilsson, P. O. Svensson, M. Chen, A. Malmström, T. Remonen, T. Kugler and M. Berggren, *Adv. Mater.*, 2002, **14**, 1460-1464.

168. D. Tobjörk and R. Österbacka, *Adv. Mater.*, 2011, **23**, 1935-1961.

169. K. Zweibel, *Sol. Energy Mater. Sol. Cells*, 2000, **63**, 375-386.

170. J. Kalowekamo and E. Baker, *Solar Energy*, 2009, **83**, 1224-1231.

171. A. T. Vicente, A. Araujo, M. J. Mendes, D. Nunes, M. J. Oliveira, O. Sanchez-Sobrado, M. P. Ferreira, H. Aguas, E. Fortunato and R. Martins, *J. Mater. Chem. C*, 2018, **6**, 3143-3181.

172. B. Lamprecht, R. Thunauer, M. Ostermann, G. Jakopic and G. Leising, *Phys. Status Solidi A*, 2005, **202**, R50-R52.

173. V. R. Voggu, J. Sham, S. Pfeffer, J. Pate, L. Fillip, T. B. Harvey, R. M. Brown and B. A. Korgel, *ACS Energy Lett*, 2017, **2**, 574-581.

174. F. Wang, Z. J. Chen, L. X. Xiao, B. Qu and Q. H. Gong, *Sol. Energy Mater. Sol. Cells*, 2010, **94**, 1270-1274.

175. A. Hubler, B. Trnovec, T. Zillger, M. Ali, N. Wetzold, M. Mingebach, A. Wagenpfahl, C. Deibel and V. Dyakonov, *Adv. Energy Mater.*, 2011, **1**, 1018-1022.

176. L. B. Hu, G. Y. Zheng, J. Yao, N. A. Liu, B. Weil, M. Eskilsson, E. Karabulut, Z. C. Ruan, S. H. Fan, J. T. Bloking, M. D. McGehee, L. Wagberg and Y. Cui, *Energy Environ. Sci.*, 2013, **6**, 513-518.

177. Y. Zhou, C. Fuentes-Hernandez, T. M. Khan, J. C. Liu, J. Hsu, J. W. Shim, A. Dindar, J. P. Youngblood, R. J. Moon and B. Kippelen, *Sci. Rep*, 2013, **3**, 1-5.

178. Y. H. Zhou, T. M. Khan, J. C. Liu, C. Fuentes-Hernandez, J. W. Shim, E. Najafabadi, J. P. Youngblood, R. J. Moon and B. Kippelen, *Org. Electron.*, 2014, **15**, 661-666.

179. L. Leonat, M. S. White, E. D. Glowacki, M. C. Scharber, T. Zillger, J. Ruhling, A. Hubler and N. S. Sariciftci, *J. Phys. Chem. C*, 2014, **118**, 16813-16817.

180. M. Nogi, M. Karakawa, N. Komoda, H. Yagyu and T. T. Nge, *Sci Rep*, 2015, **5**, 1-7.

181. S. V. Costa, P. Pingel, S. Janietz and A. F. Nogueira, *J. Appl. Polym. Sci.*, 2016, **133,** 1-6.

182. B. Wang and L. L. Kerr, *Sol. Energy Mater. Sol. Cells*, 2011, **95**, 2531-2535.

183. S. I. Cha, Y. Kim, K. H. Hwang, Y. J. Shin, S. H. Seo and D. Y. Lee, *Energy Environ. Sci.*, 2012, **5**, 6071-6075.

184. K. Fan, T. Y. Peng, J. N. Chen, X. H. Zhang and R. J. Li, *J. Mater. Chem.*, 2012, **22**, 16121-16126.

185. B. Anothumakkool, I. Agrawal, S. N. Bhange, R. Soni, O. Game, S. B. Ogale and S. Kurungot, *ACS Appl. Mater. Interfaces*, 2016, **8**, 553-562.

186. C. P. Lee, K. Y. Lai, C. A. Lin, C. T. Li, K. C. Ho, C. I. Wu, S. P. Lau and J. H. He, *Nano Energy*, 2017, **36**, 260-267.

187. M. Dasari, P. R. Rajasekaran, R. Iyer and P. Kohli, *J. Mater. Res.*, 2016, **31**, 2578-2589.

188. M. H. Jung, N. M. Park and S.Y. Lee, *Sol. Energy*, 2016, **139**, 458-466.

189. M. Hart, *J. Cryst. Growth*, 1981, **55**, 409-427.

190. C. F. Holder and R. E. Schaak, *ACS Nano*, 2019, **13**, 7359-7365.

191. B. D. Viezbicke, S. Patel, B. E. Davis and D. P. Birnie, *Phys. Status Solidi B Basic Res.*, 2015, **252**, 1700-1710.

Chapter 2. The synthesis of copper nanoparticles from the thermal decomposition of aminocarboxylate copper(II) complexes.

2.1. Introduction

Copper nanoparticles (NPs) have received significant research attention because it offers catalytic activity, optical properties and high electrical conductivity.[1-3] However, the synthetic methods for Cu NPs are difficult especially in reducing Cu(II) or Cu(I) to Cu(0) in ambient air.[4] Cu NPs have been prepared by solution-based techniques including chemical reduction, solvothermal, and hot injection methods. [5-8]

A series of copper(II) complexes with different ligands; glycine, L-alanine, L-valine and picolinic acid have been synthesised. The formation of copper nanoparticles from the thermal decomposition of aminocarboxylate copper(II) complexes in the solid-state reaction was investigated at three different reaction temperatures 350,400 and 450 °C. The thermal decomposition of synthesised copper(II) complexes in hot oleylamine at 270 °C under nitrogen for three different times were studied as well. The main goal of this work is to prepare copper nanoparticles from the pyrolysis of a copper (II) complex. The metallic copper could be useful in the fabrication of a solar cell as a transparent conductive electrode.

2.2. Author distribution

In this work, the project idea provided by Paul O’Brien and all the experimental work was done in his laboratory. The synthesis and characterise of copper (II) glycine complex and the preparation of CuNPs by solid state-reaction and hot injection was carried out by Grace A. Kinuda. I synthesised and characterised the copper(II) complex with L-alanine, L-valine and picolinic and the formation of CuNPs. Ali Bakly has done the scanning electron microscope (SEM) images of the Cu nanoparticles prepared from the thermal decomposition of copper (II) glycine complex. David Collison and David Lewis edited the draft.

2.3. References

1. V. Abhinav K, V. K. Rao R, P. S. Karthik and S. P. Singh, *RSC Adv*, 2015, **5**, 63985-64030.
2. G. H. Chan, J. Zhao, E. M. Hicks, G. C. Schatz and R. P. Van Duyne, *Nano Lett.*, 2007, **7**, 1947-1952.
3. M. B. Gawande, A. Goswami, F. X. Felpin, T. Asefa, X. Huang, R. Silva, X. Zou, R. Zboril and R. S. Varma, *Chem. Rev.*, 2016, **116**, 3722-3811.
4. M. Luo, A. Ruditskiy, H. C. Peng, J. Tao, L. Figueroa-Cosme, Z. K. He and Y. N. Xia, *Adv. Funct. Mater.*, 2016, **26**, 1209-1216.
5. A. H. Shaik and J. Chakraborty, *RSC Adv*, 2015, **5**, 85974-85977.
6. B. K. Park, S. Jeong, D. Kim, J. Moon, S. Lim and J. S. Kim, *J. Colloid Interface Sci.*, 2007, **311**, 417-424.
7. S. Uk Son, I. Kyu Park, J. Park and T. Hyeon, *Chem. Commun.*, 2004, 778-779.
8. H. J. Yang, S. Y. He, H. L. Chen and H. Y. Tuan, *Chem. Mater.*, 2014, **26**, 1785-1793.

2.4. Manuscript 1: Direct Synthesis of Nanostructured Copper Metal from Thermal Decomposition of Aminocarboxylate Copper(II) Complexes

Thamer S Alraddadi[a], Grace A. Kinunda[b], Egid Mubofu[b], Ali Bakly[c], Paul O'Brien[a,c] and David J. Lewis[c*]

2.4.1. Abstract

This work reports the synthesis of copper(II) complexes derived from four different amino carboxylic pro-ligands; glycine (Gly), L-alanine (L-Ala), L-valine (L-Val) and picolinic acid (Pic) and their use as molecular precursors for the synthesis of nanostructured copper powders and nanoparticles. Either by direct heating of the copper aminoacid complexes in inert atmospheres or thermolysis of the same complexes in solution with oleylamine leads to products that were characterized by powder X-ray diffraction and SEM. In all cases, elemental copper was produced that contains nanoscale crystallites. The new route shown here produces metallic nanostructured copper that circumvents traditional top-down (e.g. milling) and bottom-up (e.g. colloidal synthesis) techniques. For copper powders, this is a significant processing advantage, because the removal of an insulating ligand shell potentially allows superior electrical conductivity.

---

[a]School of Chemistry and [c]School of Materials, The University of Manchester, Oxford Road, Manchester M13 9PL, UK.

[b]Chemistry Department, University of Dar es Salaam, P.O. Box 35061, Dar es Salaam, Tanzania.

*Corresponding author: david.lewis-4@manchester.ac.uk ; Tel: +44 (0)1613063561.

2.4.2. Introduction

Metal nanoparticles (NPs) have attracted considerable attention because of the potential applications in chemical engineering, catalytic applications and medical sciences,[1, 2] as they demonstrate interesting characteristics including electronic, magnetic, thermal, optical and sensing functionalities.[3-7] Methods for preparing metal nanoparticles have been widely reviewed.[8-17] These include the thermal decomposition of precursors, which is inexpensive, rapid and requires moderate reaction conditions and can produce high-quality crystalline products as a single polymorph.[18]

The preparation of some metal nanoparticles is often challenging because of surface oxidation of the particles. This can be prevented by using a suitable surfactant to protect the outer surface and prevent agglomeration of particles.[19] The surfactant can also be used as a controller of the particle growth. Octadecylamine (ODA) has been widely reported as a solvent, surfactant and reducing agent for the preparation of different metals, metal oxides and bimetallic nanocrystals.[20] Oleylamine (OAm) is an example of a surfactant with a long-chain primary alkylamine, which can also be used as a capping agent for nanoparticle synthesis. OAm is inexpensive and it is also liquid at room temperature, which can simplify handling.[21] However, the inclusion of capping ligands can stymie the extraction of electronic charge from materials and solventless routes towards materials have been designed to circumvent this.

Among various metal nanoparticles, copper nanoparticles (CuNPs) have attracted attention because they display interesting features, such as excellent electrical conductivity, low electrochemical migration performance, high melting point, good solderability, antibacterial properties and antifungal activity.[22, 23] Inexpensive and earth-abundant Cu nanomaterials are attractive for a wide range of applications, such as catalysis, chemical and electronic sensors, printable conducting films and inks, biotechnology, and magnetic storage media.[24-38]

Copper amino carboxylic acid complexes have received considerable attention; it can be used in various types of applications such as biochemistry, antibacterial agent fabrication and nutritive supplies.[39, 40] Also it can functions as a chelating ligand with copper(II) cation, as it contains two donor atoms capable of providing tow pairs of electrons one from the nitrogen atom of the amine group and another one from the oxygen of the carboxylic acid group.[41-43] The simplest amino acid is glycine that has two isomers *cis* and trans,[44] which contains a single carbon molecule attached to an amino and a carboxyl functional groups.[45] Another important amino carboxylic is picolinic acid (pyridine -2- carboxylic acid); it also has two donor atoms, the nitrogen from the pyridine and the oxygen of the carboxylic acid group.[46, 47] A wide range of studies have been reported on the synthesis and characterization of metal amino carboxylic acid complexes.[48-56] The synthesis of those complexes is easy, inexpensive and environmentally friendly. Copper(II) glycine has been used as a precursor to prepare copper-based nanostructures. For example, Gao *et al.* reported the calcination of a copper(II) glycine at 600 °C under inert atmosphere (N_2) or in air to prepare Cu/carbon and copper oxide nanostructures, respectively.[57] They also noted that products possess significant antibacterial and photocatalytic activities.

The synthesis of Cu NPs has been achieved *via* several methods, including metal salt reduction, thermal decomposition, microwave heating, polyol methods, solvothermal methods, radiation methods, laser ablation and thermal and sonochemical reduction.[58-61] Ramyadevi *et al*. reported the synthesis of copper nanoparticles from copper acetate hydrate dissolved in ethylene glycol (EG) as the solvent to avoid the oxidation and aggregation of the nanoparticles and the use of Tween 80 (polyoxyethylene-(80)-sorbitan monooleate) as a medium for nanoparticle growth as well as a stabilizing agent.[62] In another study Ye and co-workers described an easy and scalable method to prepare Cu nanowires with 50 nm diameter using CuCl as precursor and oleylamine as solvent at 200 °C.[63] The Togashi group reported the synthesis of monodisperse Cu nanoparticles via the thermal decomposition of an oleylamine-coordinated Cu oxalate complex at different temperature between 200 and 260 °C.[64] Baig *al et.* reported the synthesis of nano ferrite-glutathione-copper (nano-FGT-Cu) and the potential use as a recyclable heterogeneous Cu catalyst for azide-alkyne-cycloaddition (AAC).[65]

We believe that there are many factors which contribute to the quality of Cu NPs including; reaction conditions, methods and precursors. In addition to the surface oxidation of the Cu particles, carbon contamination is another important challenge associated with the synthesis of Cu nanoparticles, especially with the pyrolysis of organic precursors either in the solid-state or by thermal decomposition on solvent. For example, The Haase *et al.* presented a one-step route for the synthesis of carbon-coated copper nanowires ranged between 100-200 nm by thermal decomposition of copper(II)–acetylacetonate at 400 °C under vacuum.[66]

This paper reports the synthesis and the characterisation of copper complexes; *cis*–[Cu(gly)$_2$.H$_2$O] (**1**), *trans*–[Cu(L-Ala)$_2$] (**2**), *cis*–[Cu(L-Val)$_2$ .H$_2$O] (**3**), and *trans*–[Cu(pic)$_2$] (**4**). The pyrolysis of these complexes at three different temperatures (350, 400, 450°C) in nitrogen atmosphere for 60 min was carried out to investigate the possibility of using these precursors to obtain a large scale of pure copper metallic nanostructure, Thermolysis of the same complexes in oleylamine (OAm) using a hot injection method at different reaction times is also evaluated.

2.4.3. Experimental

2.4.3.1. Chemicals

Chemicals and solvents used in these experiments were purchased from Sigma-Aldrich or Fisher and were used without further purification.

2.4.3.2. Instrumentation

Elemental analysis and thermogravimetric analysis (TGA) were performed by the microanalytical laboratory at the University of Manchester, utilizing a Thermo Scientific Flash 2000 Organic Elemental Analyzer and a Seiko SSC/S200 TGA-DSC using a heating rate of 10 °C/ min from room temperature to 600 °C under nitrogen atmosphere. Fourier Transform Infrared (FT-IR) spectrum were recorded using a Thermo Scientific Nicolet iS5 FT-IR Spectrometer in the range 500-4000 cm^{-1}. Powder X-ray diffraction (*p*-XRD) patterns were measured using a Bruker AXSD diffractometer using CuKα source (λ = 1.5406 Å) and scanned between 5° and 100° 2θ with a step size of 0.0167°. Scanning Electron Microscopy (SEM) images were obtained using either a Tescan Mira3 SEM or a Zeiss EVO 50 SEM.

2.4.3.3. Precursors synthesis

2.4.3.3.1. *Synthesis of cis*–[Cu(Gly)$_2$.H$_2$O] (1)

The titled compound was prepared using a literature procedure with minor modifications.[67] Briefly, (4.0 g, 20 mmol) of copper(II) acetate monohydrate was dissolved in hot distilled water (150 mL). Glycine (3.0 g, 40 mmol) dissolved in 100 mL hot water was added to the copper(II) solution. The mixture was stirred at 70 °C for 3 h. The resulting blue solution was cooled and the blue solid that formed was collected using suction filtration to give blue powder of the title compound. Yield 3.5 g, 76%; melting point = 285-290 °C. Analysis Calc. for $C_4H_{10}N_2O_5Cu$: C, 20.91; H, 4.36; N, 12.20; Cu, 27.67%. Found: C, 21.22; H, 4.26; N, 12.09; Cu, 27.14. FT-IR (ν_{max} /cm^{-1}): 3260 (br), 1585 (s), 1432 (w), 1378 (s), 1328 (m), 1149 (s), 1061 (s), 947 (w) and 914 (s). Repored literature values; FT-IR (ν_{max} /cm^{-1}): 1578 (s), 457 (s) and 378 (m).

2.4.3.3.2. Synthesis of trans–[Cu(L-Ala)$_2$] (2)

Complex (2) was prepared according to a published method.[68] L-alanine (3.9 g, 40.0 mmol) was dissolved in water/acetone (9:1 v/v 50 ml). To this solution was added a solution of copper(II) chloride dihydrate (3.4 g, 20 mmol) in water/acetone (9:1 v/v 50 ml).The reaction mixture was stirred for 3h at room temperature and the obtained precipitates were filter off. Blue crystal. Yield 3.1 g, 67%; melting point = 305-310 °C. Calc. for $C_6H_{12}N_2O_4Cu$: C, 30.05; H, 5.05; N, 11.69; Cu, 26.70%. Found: C, 30.31; H, 5.03; N, 11.61; Cu, 26.50. FT-IR ($\nu_{max/}$ cm^{-1}): 3277 (s), 3233 (s), 1615 (s), 1462 (w), 1350 (s), 1338 (s), 1143(s), 1026 (s), 947 (w) and 925 (s). Repored literature values;   FT-IR ($\nu_{max/}$ cm^{-1}): 3284 (s), 3159 (s), 1627 (s) and 1585 (s).

2.4.3.3.3. Synthesis of cis–[Cu(L-Val)$_2$ .H$_2$O] (3)

Complexe (**3**) was synthesised analogously to (**1**). L-valine (3.9 g, 40.0 mmol) was dissolved in water/acetone (9:1 v/v 50 ml). To this solution was added a solution of copper(II) chloride dihydrate (4.7 g, 20 mmol) in water/acetone (9:1 v/v 50 ml). Blue powder. Yield 4.2 g, 66%; melting point = 295-300 °C. Calc. for $C_{10}H_{22}N_2O_5Cu$: C, 38.25; H, 7.07; N, 8.93; Cu, 20.26%. Found: C, 38.36; H, 6.95; N, 8.93; Cu, 20.14. FT-IR ($\nu_{max/}$ cm^{-1}): 3260 (br), 3156 (s), 2876 (w), 1607 (s), 1581 (s), 1463 (w), 1378 (s), 1325 (m), 1179 (s), 1087 (s), 974 (w) and 906 (s). Repored literature values; FT-IR ($\nu_{max/}$ cm^{-1}): 3284 (br), 3156 (s), 2967 (s), 2877 (s), 1627 (s) and 1585 (w).

2.4.3.3.4. Synthesis of trans–[Cu(pic)$_2$] (4)

The synthesis of the complex (**4**) was carried out according to the reported method.[69] A solution of picolinic acid (4.9 g, 40 mmol) in 50 mL of ethanol was added to a stirred solution of NaOH (1.6 g, 40 mmol) in 50 mL of distilled water. To this solution was added dropwise a solution of $CuCl_2.2H_2O$ (4.8 g, 20 mmol) in 200 mL of ethanol/water (3:1 *v/v*) at room temperature. After stirring for 45 min, the resulting blue-green solution was filtered. Blue crystals were obtained after nine days from the filtrate. These were filtered off, washed with diethyl ether and dried under vacuum. Yield 3.0 g, 63%; melting point = 295-300 °C. Calc. for $C_{12}H_8N_2O_4Cu$: C, 46.28; N, 8.98; Cu, 20.78%. Found: C, 46.51; N, 9.05; Cu, 20.52%. FT-IR (ν_{max} /cm^{-1}): 1636 (s), 1380 (w), 690 (s) and 660 (w). Repored literature values; FT-IR ($\nu_{max/}$ cm^{-1}): 1629 (s), 1374 (s) and 764 (m).

2.4.3.4. Synthesis of copper powders from complexes (1-4)

Crystalline Cu was prepared by the thermal decomposition of complexes (**1-4**). 0.2 g of each complex was placed in a ceramic crucible and heated at three different temperatures (350, 400, 450 °C) under nitrogen for 60 minutes. The sample was allowed to cool down to room temperature in the furnace. The reddish-brown powders obtained were collected for further analysis.

2.4.3.5. Synthesis of copper nanoparticles from complexes (1-4)

In a 250 mL three-necked flask oleylamine (15 mL) was heated to 270 °C under nitrogen gas flow for 30 min and 0.3 g of copper precursor in oleylamine (5 mL) was added via a syringe to the hot reaction medium. After a period of time (10, 30 or 60 min) the reaction was quenched by the addition of 2-propanol (50 mL), resulting in the formation of a flocculent precipitate. The precipitate was isolated by centrifugation, washed with methanol (3 × 60 mL) and dispersed in acetone to give brown crystalline Cu. The same procedure was applied to all complexes (**1-4**).

2.4.4. Results and Discussion

Complexes (**1-4**) were synthesised according to published procedures. Metal salts were mixed with pro-ligands in a molar ratio 1:2 that gave the metal di-amino acid complexes Figure 2.1. The crystal structures of these complexes have been studied previously, and all characterisation data in this experiment matched with those previously reported.[50, 68-70] The complexes produced were soluble in water but insoluble in less polar solvents like ethanol and acetone.

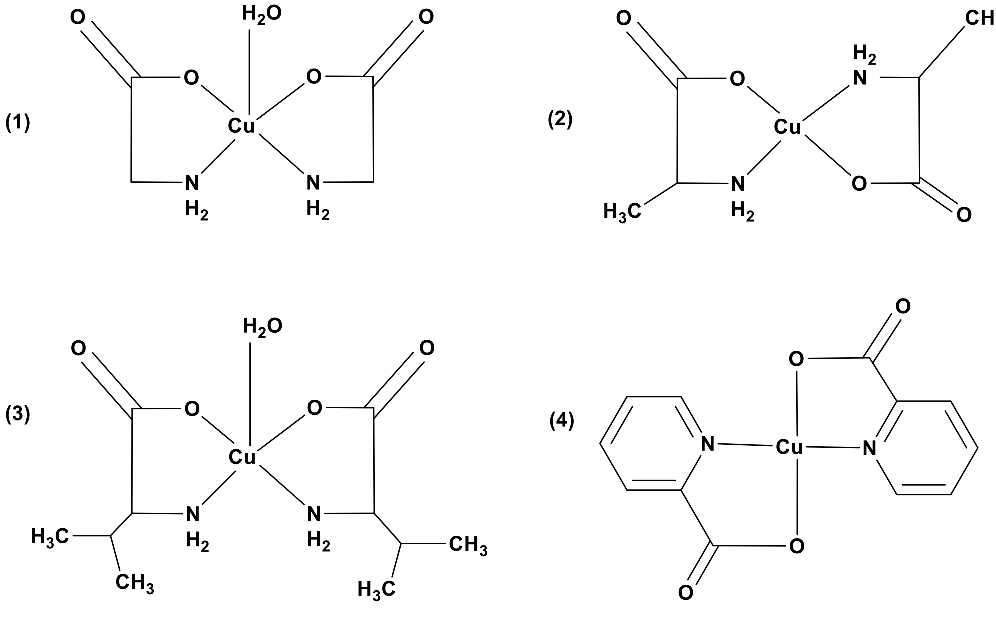

Figure 2.1 The chemical structure of copper complexes (**1**) glycine, (**2**) alanine, (**3**) valine and (**4**) picolinic acid.

Thermal decomposition of complexes (**1-4**) was examined by thermogravimetric analysis (TGA), under an inert atmosphere of nitrogen gas in the temperature range 40-400 °C (Figure **2.2**). Complexes (**1**) and (**3**) show identical two-step weight loss profiles. The first mass loss is caused by the liberation of water molecules in the range 75—130 °C with an experimental percentage mass loss of 7.5% and 6.2% respectively. This correlates well with the theoretical values of 7.8% and 5.7% for complexes (**1**) and (**3**) respectively. The release of water of crystallisation has been previously reported in the literature.[70] The second decomposition step in the range of 250 to 310 °C corresponds to the elimination of two equivalents of ligand. Complexes (**2**) and (**4**) show a single decomposition step between 260-320 °C. The final weight percentage of residue (Table.S.2-1) indicates the conversion to CuO for complexes (**1**), (**2**) and (**4**), whereas for complex (3) the final weight measured suggests the formation of metallic copper since the experiment final residue mass is matched with the calculated value for Cu^0.

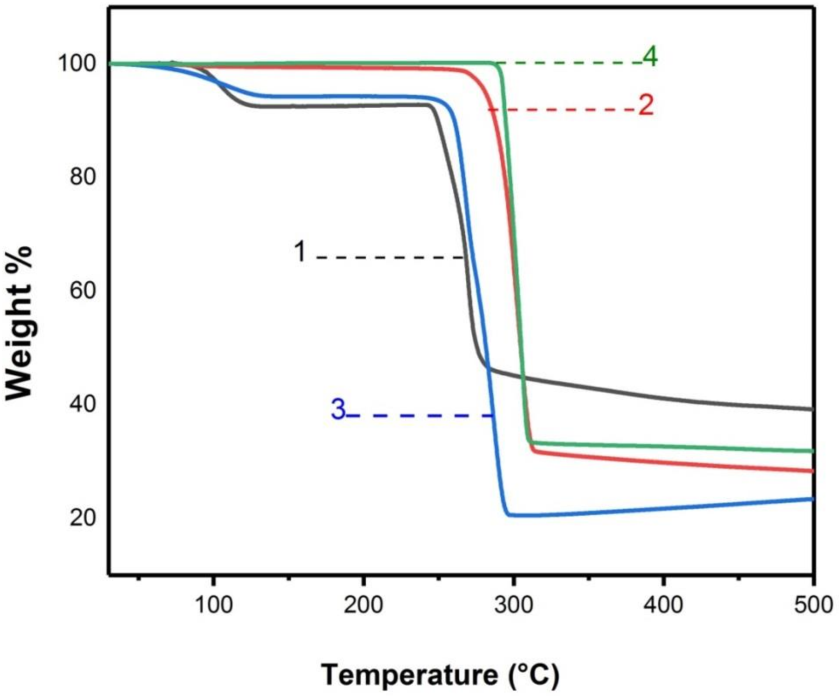

Figure 2.2 Thermogravimetric analysis (TGA) of complexes under nitrogen with heating rate of 10 °C/min, (1) *cis*–[$Cu(gly)_2.H_2O$], (2) *trans*–[$Cu(L\text{-}Aln)_2$], (3) *cis*–[$Cu(L\text{-}Val)_2 .H_2O$], (4) *trans*–[$Cu(pic)_2$].

By heating each of the copper(II) amino acid or picolinic acid complexes in the solid-state in the range 350-450 °C under nitrogen, powders were produced in every case. The *p*-XRD patterns of these powders are shown in (Figure 2.3). In all cases, the powder diffraction patterns from thermal decomposition of complexes (**1-4**) matched well with that of cubic elemental copper (Cu^0, PDF no. 00-004-0836). Diffraction peaks observed at $2\theta = 43.08°$, 50.27°, 73.89°, 89.60° and 95.00° correspond to the (111), (200), (220), (331) and (222) planes of cubic Cu respectively. No impurity peaks are observed in the *p*-XRD diffraction pattern for, from example, common contaminants such as copper oxides. (e.g CuO, Cu_2O) Similarly, when thermal decomposition of complexes (**1-4**) is performed in a boiling solution of oleylamine, the products obtained are similar Figure **2.5**. The crystallite size of the powder was calculated using the full width at half maximum (FWHM) of reflection peak at (111) reflection of Cu using the Debye–Scherrer formula.[71]

$$(D = K \lambda / \beta \cos \theta)$$

In general, all powders produced were found to have nanostructured crystallite domains with minimum length scales ranging from around 50 to 150 nm. In the solid-state reaction increasing the temperature resulted in an increment in the crystallite size of the CuNPs produced from complexes

1 and **4.** The crystallite size of CuNPs produced from complex **3** shows decreasing in the crystallite size with the increment of the reaction temperature. The crystallite size of complex **2** was decreased when the temperature increased to 400 °C, further increment in the reaction temperature result in the increasing of the crystallite size, Figure 2.4 and Table S.2-2. On the other hand, all CuNPs derived from the thermal decomposition of complexes **1-4** in hot solution shown an increment of crystallite size with increasing the reaction time Figure 2.6 and Table S.2-3.

On average, different particle sizes were observed with different reaction times and temperatures, but, there was no trend apparent. This suggests that the reaction is potentially under some form of thermodynamic control as the products tend to show no trend despite variation of reaction conditions and complex structure. The implication is that the thermolysis reaction is potentially robust and tolerant to a range of conditions which ultimately is an attractive feature for processing.

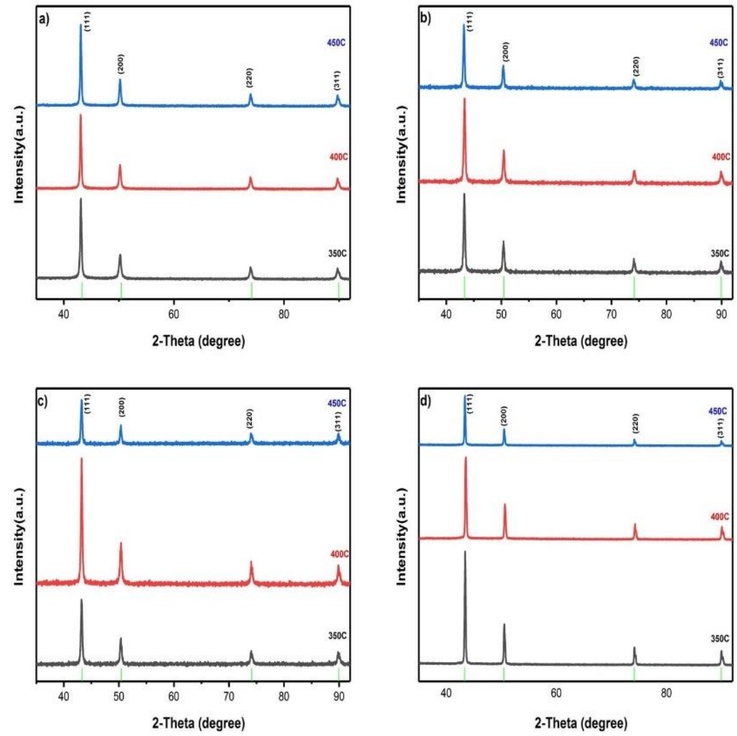

Figure 2.3 XRD pattern of nanoparticles derived from the thermal decomposition of; (a) *cis*–[Cu(gly)$_2$.H$_2$O] (b) *trans*–[Cu(L-Ala)$_2$] (C) *cis*–[Cu(L-Val)$_2$ .H$_2$O] (d) *trans*–[Cu(pic)$_2$], grown for 1 h at different temperatures, standard patterns for cubic Cu (PDF no.00-004-0836).

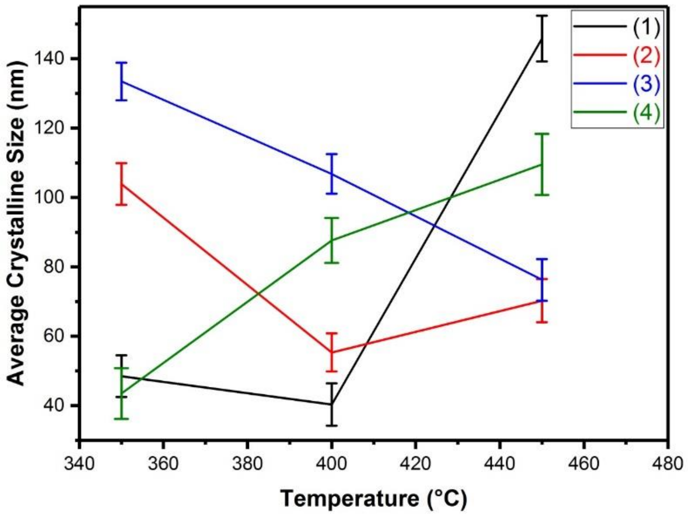

Figure 2.4 Crystallite size of the Cu prepared from the thermal decomposition of complexes (1-4) against temperature.

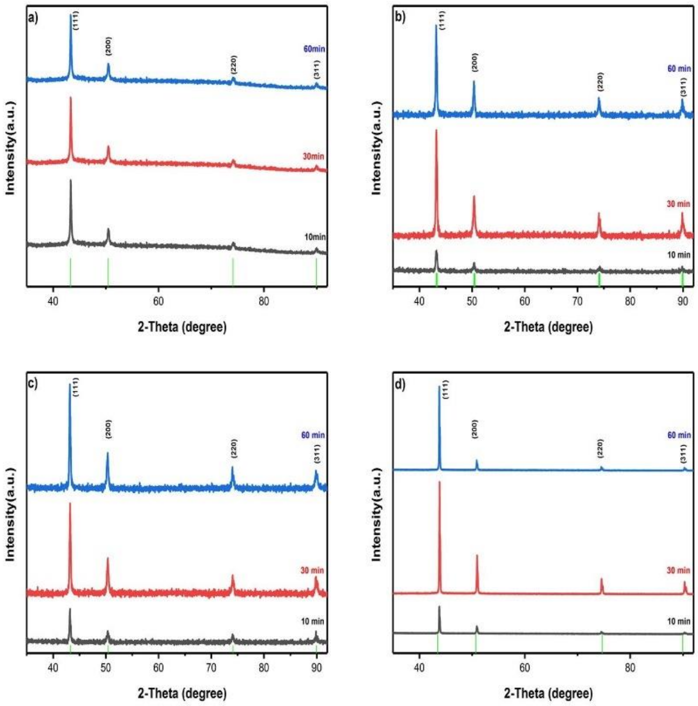

Figure 2.5. *p*-XRD pattern of powders derived from the thermal decomposition of; (a) *cis*–[Cu(gly)$_2$.H$_2$O] (b) *trans*–[Cu(L-Ala)$_2$] (c) *cis*–[Cu(L-Val)$_2$ .H$_2$O] (d) *trans*–[Cu(pic)$_2$], in oleylamine, grown at different time, standard patterns of cubic Cu (PDF no.00-004-0836).

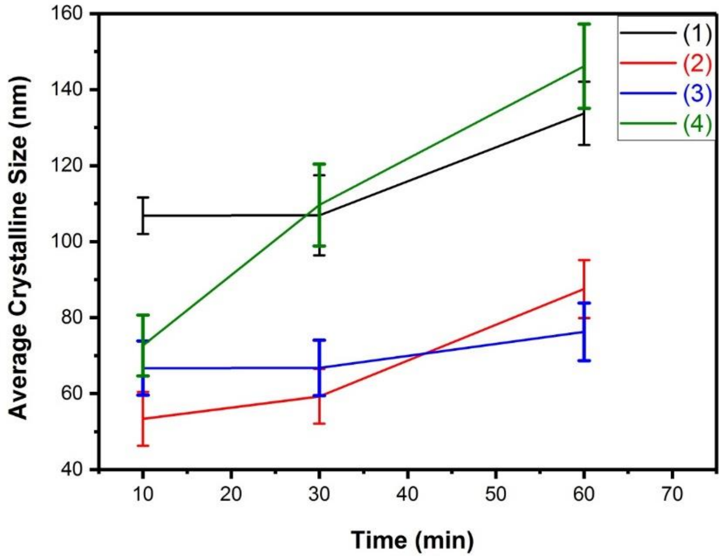

Figure 2.6 Crystallite size of the Cu prepared from the thermal decomposition of complexes (1-4) against time, at 270°C.

Raman spectroscopy is usually used to investigate the presence of carbon contamination in the samples by the presence of two major peaks centred at near 1345 and 1580 cm^{-1}, which correspond to the D and G peaks of disordered carbon materials, respectively.[72-74] The as-prepared Cu products resulting from the solid-state synthesis of complexes **(1-4)** were examined by Raman spectroscopy. The presence of carbon was confirmed in some samples Figure 2.8. Also, the elemental analysis of the samples shows that the carbon contamination increased as numbers of carbon atoms on the complex increased. For example, glycine shows less carbon contamination followed by alanine, valine and finally picolinic acid Figure 2.7. Upon increasing the reaction temperature, the carbon contamination in the product derived from complex (**4**) was increased, where the percentage of the carbon resulting from the thermal decomposition of complex (**3**) was decreased. However, there is no significant change in the carbon present on the products derived from the thermal decomposition of complexes (**1**) and (**2**).

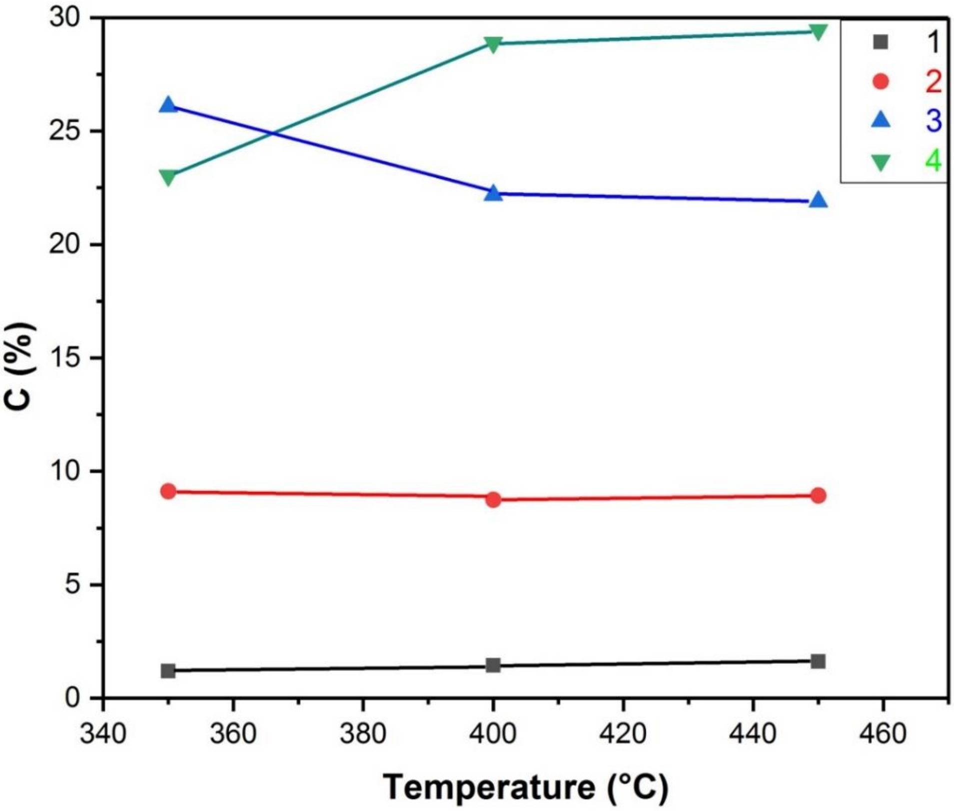

Figure 2.7 Carbon percentage against temperature for the products resulting from the thermal decomposition of complexes (**1**-**4**).

The presence of amorphous carbon is also witnessed by other studies. Shu-Hong Yu and co-workers reported the synthesis of Cu/C by one-step hydrothermal carbonization process of glucose copper solution with the assistance of polyvinyl alcohol (PVA).[76] Another study conducted by the Liu team represented the synthesis of carbon-coated Cu nanoparticles (C/Cu) with an average size between 50-80 nm by a simple solid-state reduction of glucose ($C_6H_{12}O_6 .H_2O$) and cupric carbonate ($CuCO_3.Cu(OH)_2.xH_2O$).[75]

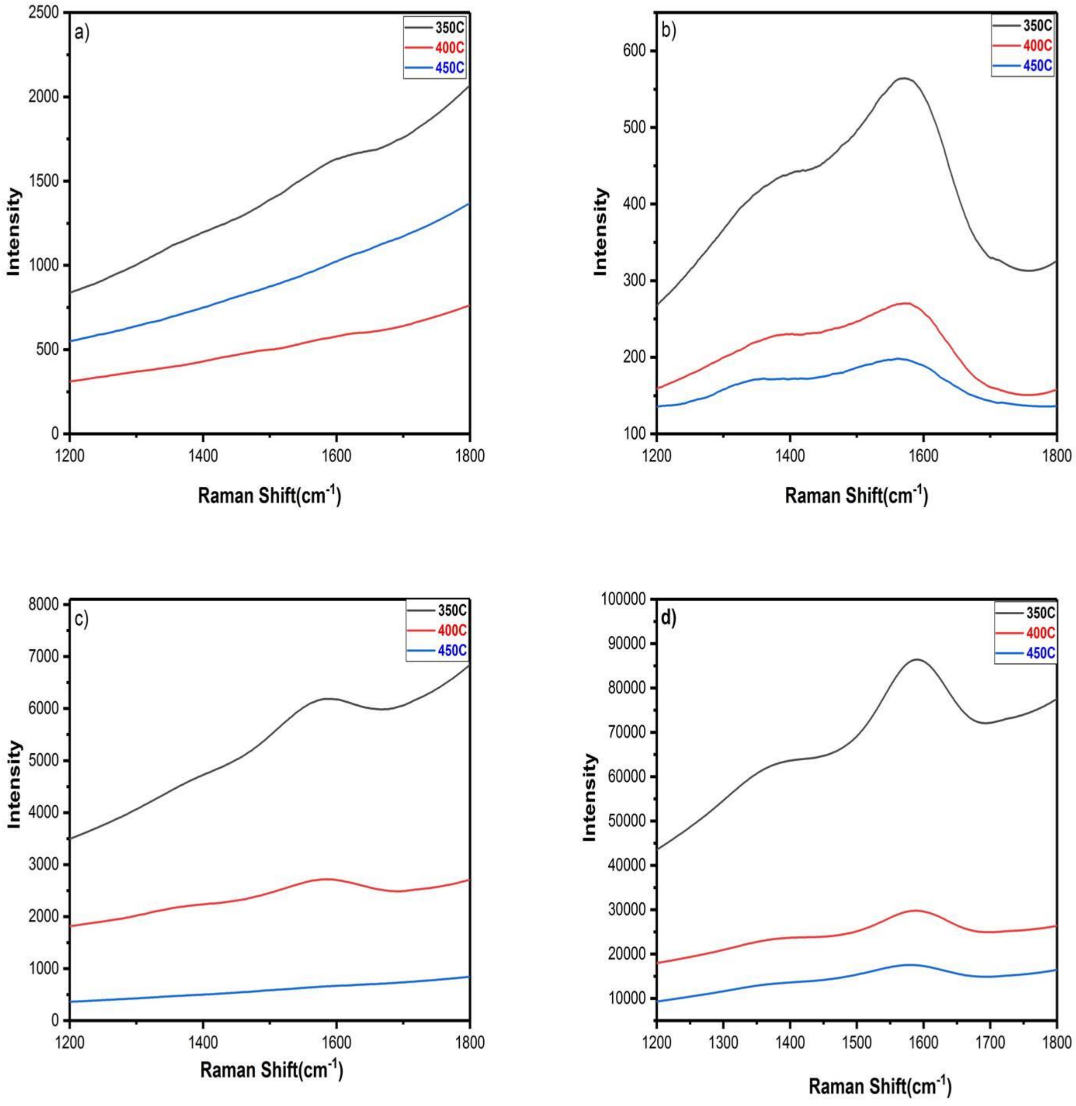

Figure 2.8 The Raman spectrum of powders derived from the thermal decomposition of copper complexes; a) glycine, b) L-alanine, c) L-valine, d) picolinic acid, at different reaction temperatures 350,400 and 450 °C.

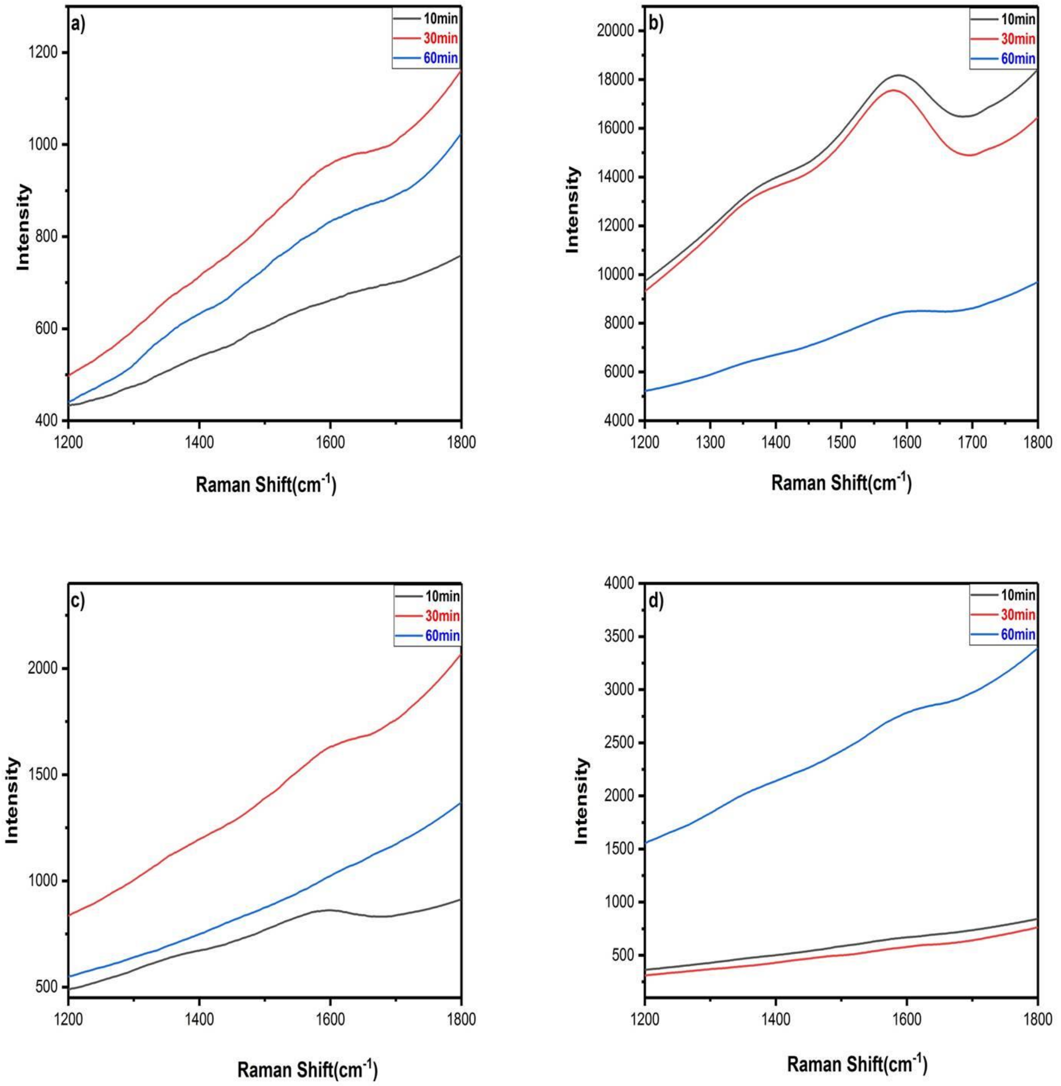

Figure 2.9 The Raman spectrum of powders derived from the thermal decomposition of copper complexes, a) glycine, b) L-alanine, c) L-valine, d) picolinic acid, at different reaction times 10, 30and 60 min °C.

The morphology of crystalline Cu products resulting from the solid phase synthesis of complexes **(1-4)** was investigated by SEM. The materials appeared as coarse powders in all cases. From SEM images Figure 2.10 it is observed that there is no significant effect of changing the precursor or reaction condition on product morphology. Agglomeration was evident in SEM images of products prepared at different conditions, which is indicative of the native surfaces of the particles; there are no capping ligands employed in this procedure and as a result as the crystalline materials formed of tend to agglomerate because they have no capping ligand at their surface. This is potentially advantageous because electrical conduction is unimpeded by an insulating ligand shell and secondly that there would potentially be good electrical contact between particles upon deposition. The size of the particles would make them potentially advantageous for flexible electronics e.g. in contacts for polymer solar cells.

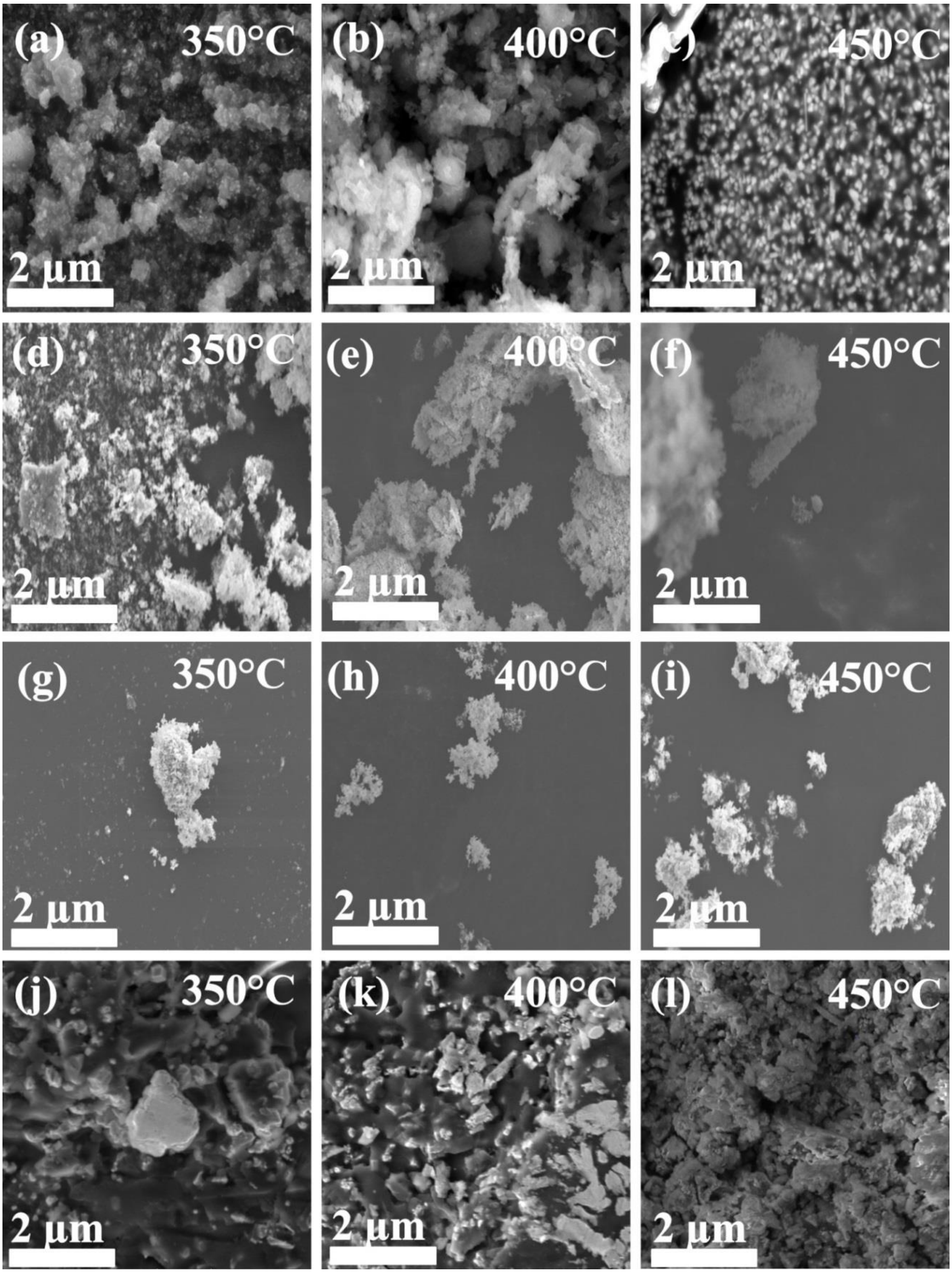

Figure 2.10 SEM images of Cu powder derived from the thermal decomposition of complexes (**1-4**) prepared at 350 °C, 400 °C and 450 °C, (a-c) *cis*–[$Cu(gly)_2.H_2O$]; (d-f) *trans*–[$Cu(L\text{-}Ala)_2$] (g-i) *cis*–[$Cu(L\text{-}Val)_2$ .H_2O]; (j-l) *trans*–[$Cu(pic)_2$], scale bars represent: 2 µm.

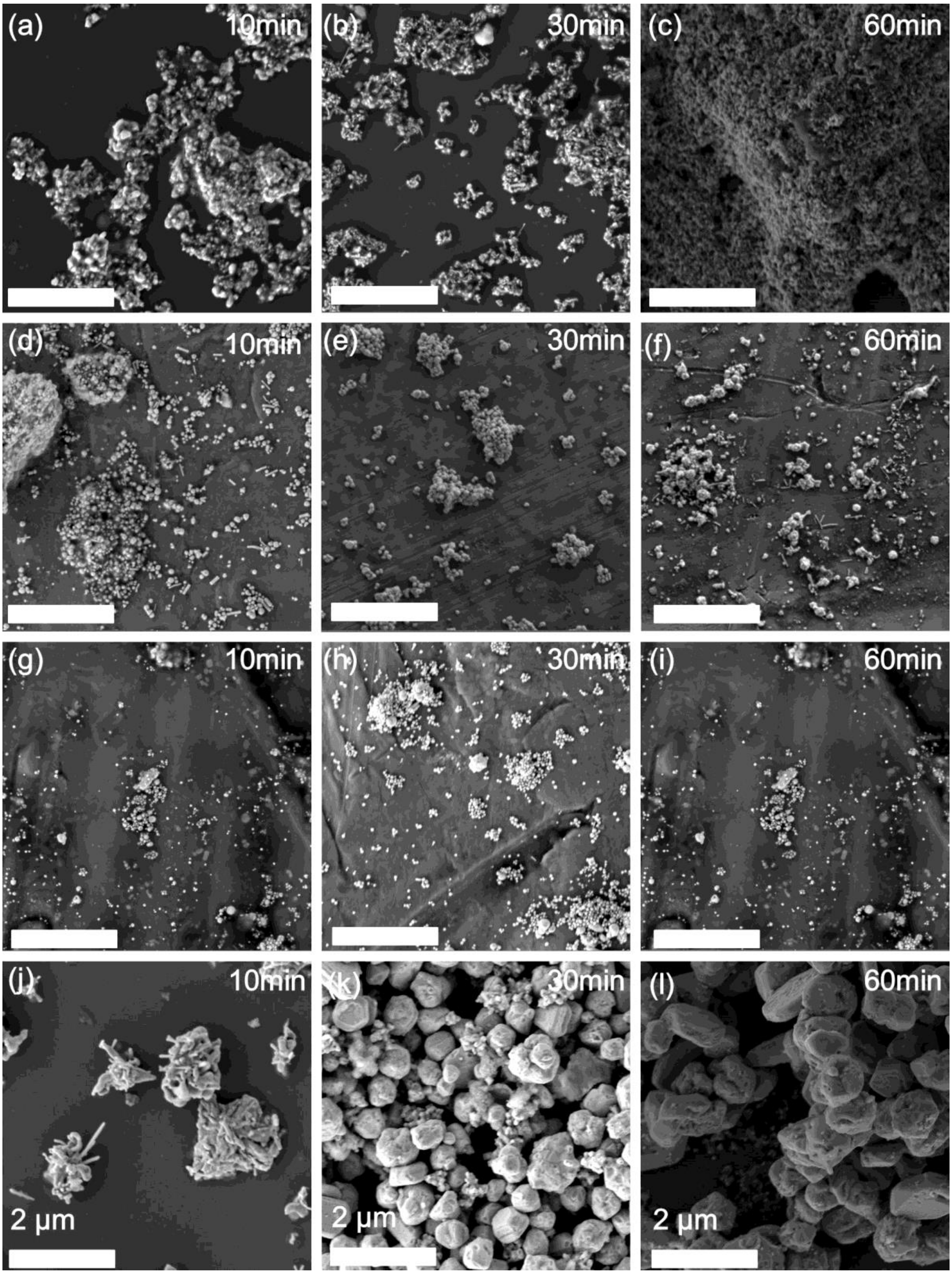

Figure 2.11 SEM image of oleylamine capped Cu nanoparticles from complexes (**1-4**) prepared after 10, 30 and 60 min at 270 °C, (a-c) *cis*–[Cu(gly)$_2$.H$_2$O]; (d-f) *trans*–[Cu(L-Ala)$_2$] (g-i) *cis*–[Cu(L-Val)$_2$ .H$_2$O]; (j-l) *trans*–[Cu(pic)$_2$], scale bars represent: 2 μm.

Oleylamine capped Cu nanoparticles derived from the thermal decomposition of complex (**1- 4**) in oleylamine prepared after 10, 30 and 60 min at 270 °C have slightly different morphologies upon changing the time of the reactions and the ligands Figure **2.11**. Firstly, complexes (**1-3**) present small particles at different reaction times, where products from complexes (**1**) at 30 min and complex (**2**) at 10 min are a mixture of small particles and rods. The products resulting from thermal decomposition of complex (**4**) also exhibit slightly different shapes depending on reaction time. For instance, leaf-like morphologies are observed after 10 min reaction time, where those after 30 min growth in small particles. Disk-like particles are observed after 60 min Figure **2.12**. No significant relationship between the nanoparticles size and reaction time was observed and the particles produced are quite large. This may suggest that the crystal growth becomes uncontrolled during the reaction conditions, i.e. oleylamine did not successfully arrest growth of nucleates and that careful control of temperature would be required during this reaction if smaller particles were to be produced with greater monodispersity.

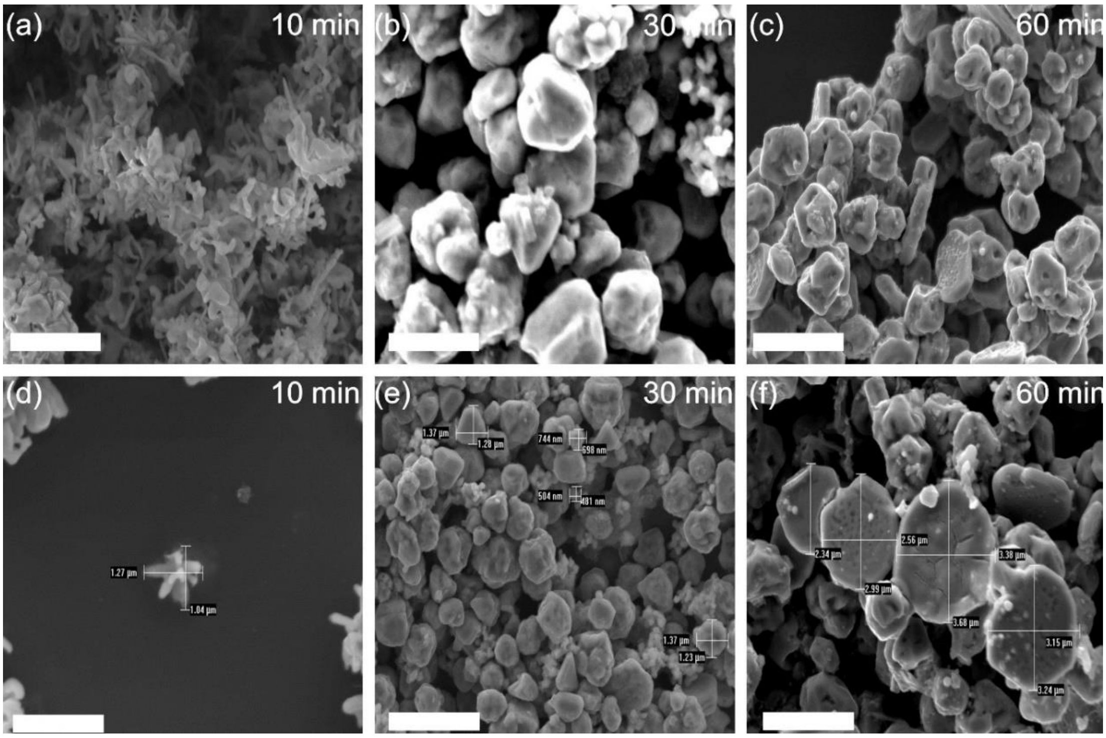

Figure 2.12 SEM image of oleylamine capped Cu nanoparticles from complex (**4**) prepared after (a,d)10 min, (b,e)30 min and (c,f) 60 min at 270 °C, Scale bars represent: 2 µm.

Both methods demonstrate a simple, fast, low toxicity and economical procedure to prepare Cu with high purity and in some cases produced Cu/carbon products. Solventless thermolysis of copper precursors (**1-4**) under inert conditions is successful in producing elemental copper and without contamination from common oxide species. The major challenge in this work was the carbon contamination resulting from the decomposition processes of the precursors. In order to improve the quality of copper product, it's important to select precursors that contain less carbon atoms. However, copper/carbon products could be useful in different applications as they exhibit better chemical stability than single copper nanoparticles because of the existence of carbon shell layers, [25,77] and they also display antibacterial and photocatalytic activity which could be an advantage of these products.[57]

Agglomeration is observed which has been described as disadvantageous for colloidal systems[72]. However, the fact that the copper particles produced are essentially ligand-free means that conduction can occur potentially only impeded by percolation of charge between particles, the fact the particles are in contact by agglomeration would make even the latter barrier somewhat mitigated.

The use of oleylamine as a capping agent was also unable to hinder colloidal particle growth in this case, suggesting that this reaction was under thermodynamic control and the growth of large Cu nanoparticles, which would essentially have bulk-like properties, is very fast under the conditions employed.[78] There are some suggestions to resolve this problem; changing the reaction conditions (time or temperature) might decrease particle size. Another solution could be to introduce an adequate amount of polyvinyl pyrrolidone (PVP) as a polymeric stabilizer.[80]

2.4.5. Conclusion

In summary, four different complexes of copper; glycine (gly), alanine (Ala), valine (Val) and picolinic acid (pic) have been synthesised and characterised by elemental analysis, FTIR spectroscopy and thermogravimetric analysis (TGA) techniques. The use of those complexes as a precursor to prepare crystalline Cu has been investigated utilizing two different methods: hot injection and thermal decomposition. Both methods afford an inexpensive, simple and efficient approach to synthesis metallic Cu nanoparticles and Cu/ carbon products. The prepared crystalline products were characterized by *p*-XRD and SEM analysis. The route proposed here may produce nanostructured copper metal and Cu/ carbon products without resort to power processing or milling, or colloidal synthesis techniques. The use of precursor chemistry to produce high-quality nanostructured copper, free from oxide contaminants is interesting and could be explored as a way to produce conductive copper inks in future for inkjet printing of precursors. The Cu/ carbon products could also be promising candidates as an antibacterial and photocatalytic agent.

2.4.6. References

1. H. Zazo, C. I. Colino and J. M. Lanao, *J. Controlled. Release*, 2016, **224**, 86-102.
2. R. V. Gonçalves, R. Wojcieszak, H. Wender, C. Sato B. Dias, L. L. Vono, D. Eberhardt, S. R. Teixeira and L. M. Rossi, *ACS Appl. Mater. Interfaces*, 2015, **7**, 7987-7994.
3. P. Zijlstra and M. Orrit, *Rep. Prog. Phys.*, 2011, **74**, 106401.
4. A. Kamyshny, J. Steinke and S. Magdassi, *The Open Appl. Phy. J.*, 2011, **4**, 19-36.
5. R. Gréget, G. L. Nealon, B. Vileno, P. Turek, C. Mény, F. Ott, A. Derory, E. Voirin, E. Rivière and A. Rogalev, *ChemPhysChem*, 2012, **13**, 3092-3097.
6. R. R. Letfullin, C. B. Iversen and T. F. George, *Nanomedicine*, 2011, **7**, 137-145.
7. G. Doria, J. Conde, B. Veigas, L. Giestas, C. Almeida, M. Assuncao, J. Rosa and P. V. Baptista, *Sensors*, 2012, **12**, 1657-1687.
8. J. P. Wilcoxon and B. L. Abrams, *Chem. Soc. Rev.*, 2006, **35**, 1162-1194.
9. B. L. Cushing, V. L. Kolesnichenko and C. J. O'Connor, *Chem. Rev.*, 2004, **104**, 3893-3946.
10. K. Philippot and B. Chaudret, *CR CHIM*, 2003, **6**, 1019-1034.
11. A. Roucoux, J. Schulz and H. Patin, *Chem. Rev.*, 2002, **102**, 3757-3778.
12. H. Bönnemann and R. M. Richards, *Eur. J. Inorg. Chem.*, 2001, **2001**, 2455-2480.
13. J. D. Aiken and R. G. Finke, *J. Mol. Catal. A: Chem.*, 1999, **145**, 1-44.
14. G. Schmid and L. F. Chi, *Adv. Mater.*, 1998, **10**, 515-526.
15. M. Reetz, W. Helbig and S. Quaiser, *Wiley-VCH, Weinham*, 1996, **158**, 339.
16. M. T. Reetz and W. Helbig, *J. Am. Chem. Soc.*, 1994, **116**, 7401-7402.
17. M. Faraday, *Philos. Trans. R. Soc. London*, 1857, **147**, 145.
18. M. Salavati-Niasari, Z. Fereshteh and F. Davar, *Polyhedron*, 2009, **28**, 126-130.
19. M. Salavati-Niasari, N. Mir and F. Davar, *Appl. Surf. Sci.*, 2010, **256**, 4003-4008.
20. D. Wang and Y. Li, *Inorg. Chem.*, 2011, **50**, 5196-5202.
21. S. Mourdikoudis and L. M. Liz-Marzan, *Chem. Mater.*, 2013, **25**, 1465-1476.
22. L. Argueta-Figueroa, R. A. Morales-Luckie, R. J. Scougall-Vilchis and O. F. Olea-Mejía, *Prog. Nat. Sci.*, 2014, **24**, 321-328.
23. M. I. Din and R. Rehan, *Anal. Lett.*, 2017, **50**, 50-62.

24. E. K. Athanassiou, R. N. Grass and W. J. Stark, *Nanotechnology*, 2006, **17**, 1668-1673.

25. Z. P. Liu, Y. Yang, J. B. Liang, Z. K. Hu, S. Li, S. Peng and Y. T. Qian, *J. Phys. Chem. B*, 2003, **107**, 12658-12661.

26. S. Panigrahi, S. Kundu, S. K. Ghosh, S. Nath, S. Praharaj, S. Basu and T. Pal, *Polyhedron*, 2006, **25**, 1263-1269.

27. Y. Takeda, O. A. Plaksin, K. Kono and N. Kishimoto, *Surf. Coat. Tech.*, 2005, **196**, 30-33.

28. M. Salavati-Niasari, F. Davar and N. Mir, *Polyhedron*, 2008, **27**, 3514-3518.

29. M. Tada, R. Bal, S. Namba and Y. Iwasawa, *Appl. Catal., A*, 2006, **307**, 78-84.

30. A. K. Verma, R. Kumar, P. Chaudhary, A. Saxena, R. Shankar, S. Mozumdar and R. Chandra, *Tetrahedron Lett.*, 2005, **46**, 5229-5232.

31. M. B. Gawande, A. Goswami, F. X. Felpin, T. Asefa, X. Huang, R. Silva, X. Zou, R. Zboril and R. S. Varma, *Chem. Rev.*, 2016, **116**, 3722-3811.

32. B. C. Ranu, R. Dey, T. Chatterjee and S. Ahammed, *ChemSusChem*, 2012, **5**, 22-44.

33. Z. Liu, J. Xu, D. Chen and G. Shen, *Chem. Soc. Rev.*, 2015, **44**, 161-192.

34. Y. Liu, Z. Liu, N. Lu, E. Preiss, S. Poyraz, M. J. Kim and X. Zhang, *Chem. Commun.*, 2012, **48**, 2621-2623.

35. S. Poyraz, Z. Liu, Y. Liu, N. Lu, M. J. Kim and X. Y. Zhang, *Sensor. Actuators, B*, 2014, **201**, 65-74.

36. Y. H. Wei, S. Chen, B. Kowalczyk, S. Huda, T. P. Gray and B. A. Grzybowski, *J. Phys. Chem. C*, 2010, **114**, 15612-15616.

37. Z. Liu, Y. Liu, L. Zhang, S. Poyraz, N. Lu, M. Kim, J. Smith, X. Wang, Y. Yu and X. Zhang, *Nanotechnology*, 2012, **23**, 335603.

38. D. Zhang, R. Wang, M. Wen, D. Weng, X. Cui, J. Sun, H. Li and Y. Lu, *J. Am. Chem. Soc.*, 2012, **134**, 14283-14286.

39. M. Hakimi and T. S. Aliabadi, *catena*, 2012, **2**, 431-443.

40. S. M. Moussa, R. R. Fenton, B. J. Kennedy and R. O. Plitz, *Inorg. Chem. Acta*, 1999, **288**, 29-34.

41. N. Judas and N. Raos, *Inorg. Chem.*, 2006, **45**, 4892-4894.

42. M. Yokota, S. Kikuchi, J. Sen, T. Kamei and N. Doki, *Adv. Mater. Sci. Eng.*, 2015, **6**, 62.

43. T. Soon-Beng, N. Chew-Hee and E. R. Tiekink, *Inorg. Chem. Acta*, 1989, **163**, 129-130.

44. B. Delf, R. Gillard and P. O'Brien, *J. Chem. Soc., Dalton Trans.*, 1979, 1301-1305.

45. F. H. A. Al-Jeboori and T. A. M. Al-Shimiesawi, *J. Chem. Phar. Res*, 2013, **5**, 318-321.

46. K. Waizump, M. Takuno, N. Fukushima and H. Masuda, *J. Coord. Chem.*, 1998, **44**, 269-279.

47. N. Ndosiri, M. Agwara, A. Paboudam, P. Ndofon, D. Yufanyi and C. Amah, *RJPBCS*, 2013, **4**, 1370-1381.

48. T. D. Thangadurai and K. Natarajan, *Transition Met. Chem.*, 2002, **27**, 485-489.

49. J. E. Weder, C. T. Dillon, T. W. Hambley, B. J. Kennedy, P. A. Lay, J. R. Biffin, H. L. Regtop and N. M. Davies, *Coord. Chem. Rev.*, 2002, **232**, 95-126.

50. S. M. Moussa, R. R. Fenton, B. A. Hunter and B. J. Kennedy, *Aust. J. Chem.*, 2002, **55**, 331-341.

51. I. Oladipo, I. Adeoye and A. Adeyemo, *Am. J. of Food and Nutrition*, 2013, **3**, 53-57.

52. C. Papatriantafyllopoulou, C. P. Raptopoulou, A. Terzis, J. F. Janssens, E. Manessi-Zoupa, S. P. Perlepes and J. C. Plakatouras, *Polyhedron*, 2007, **26**, 4053-4064.

53. H. C. Lukaski, W. A. Siders and J. G. Penland, *Nutrition*, 2007, **23**, 187-195.

54. D. Li, G.-Q. Zhong and Q. Zang, *Iran. J. Chem. Chem. Eng.*, 2016, **35**, 21-29.

55. M. Kalinowska, M. Borawska, R. Swislocka, J. Piekut and W. Lewandowski, *J. Mol. Struct.*, 2007, **834**, 419-425.

56. F. A. Mautner and S. S. Massoud, *J. Mol. Struct.*, 2007, **871**, 108-113.

57. F. Gao, H. Pang, S. Xu and Q. Lu, *Chem. Commun.*, 2009, 3571-3573.

58. X. W. Liu, B. Y. Geng, Q. B. Du, J. Z. Ma and X. M. Liu, *Maert. Sci. Eng., A*, 2007, **448**, 7-14.

59. L. Daróczi, M. Beck, D. L. Beke, M. Kis-Varga, L. Harasztosi and N. Takacs, *Maert. Sci. Fourm*, 1998, **269**, 319-326

60. A. G. Nasibulin, P. P. Ahonen, O. Richard, E. I. Kauppinen and I. S. Altman, *J. Nanopart. Res.*, 2001, **3**, 385-400.

61. Y. H. Kim, D. K. Lee, B. G. Jo, J. H. Jeong and Y. S. Kang, *Colloid Surf., A*, 2006, **284**, 364-368.

62. J. Ramyadevi, K. Jeyasubramanian, A. Marikani, G. Rajakumar and A. A. Rahuman, *Mater. Lett.*, 2012, **71**, 114-116.
63. E. Ye, S. Y. Zhang, S. Liu and M. Y. Han, *Chem. Eur.J.*, 2011, **17**, 3074-3077.
64. T. Togashi, M. Nakayama, A. Hashimoto, M. Ishizaki, K. Kanaizuka and M. Kurihara, *Dalton Trans*, 2018, **47**, 5342-5347.
65. R. B. Nasir Baig and R. S. Varma, *Green Chem.*, 2012, **14**, 625.
66. D. Haase, S. Hampel, A. Leonhardt, J. Thomas, N. Mattern and B. Büchner, *Surf. Coat. Technol.*, 2007, **201**, 9184-9188.
67. P. O'Brien, *J. Chem. Educ*, 1982, **59**, 1052.
68. R. Bikas, B. Soltani, H. Sheykhi, M. Korabik and M. Hossaini-Sadr, *J. Mol. Struct.*, 2018, **1168**, 195-201.
69. A. Colette, A. M. Ondoh, D. M. Yufanyi and D. S. Y. Gaelle, *Int. J. Chem*, 2015, **7**, 10.
70. M. Markovic, N. Judas and J. Sabolovic, *Inorg. Chem.*, 2011, **50**, 3632-3644.
71. Z. Haitao, Z. Canying and Y. Yansheng, *Nanotechnology*, 2005, **16**, 3079.
72. A. Ilie, C. Durkan, W. I. Milne and M. E. Welland, *Phys. Rev. B: Condens. Matter*, 2002, **66**, 045412.
73. Y. Li, E. J. Lee, W. Cai, K. Y. Kim and S. O. Cho, *ACS nano*, 2008, **2**, 1108-1112.
74. Y. Wang, F. B. Su, C. D. Wood, J. Y. Lee and X. S. Zhao, *Ind. Eng. Chem. Res.*, 2008, **47**, 2294-2300.
75. J. Li and C. Y. Liu, *New J. Chem.*, 2009, **33**, 1474-1477.
76. J.-Y. Gong, S.-H. Yu, H.-S. Qian, L.-B. Luo and T.-W. Li, *J. Phys. Chem. C,* 2007, **111**, 2490-2496.
77. Y. Chang, M. L. Lye and H. C. Zeng, *Langmuir*, 2005, **21**, 3746-3748.
78. G. Cheng and A. R. Hight Walker, *Anal. Bioanal. Chem.*, 2010, **396**, 1057-1069.
79. D. Thi My Dung, L. Thi Thu Tuyet, F.-B. Eric and D. Mau Chien, *Adv.Nat. Sci.:Nanosci. Nanotechnol.*, 2011, **2**, 025004.

2.4.7. Electronic Supporting information

Table.S.2-1 Decomposition data of complex (1) *cis*–[Cu(glyO)$_2$.H$_2$O], (2) *trans*–[Cu(L-Aln)$_2$], (3) *cis*–[Cu(L-Val)$_2$ .H$_2$O], (4) *trans*–[Cu(pic)$_2$].

Complex	**Decomposition temperature (°C)**	**Final residue**	**Final residue (%)**	
			Calculated	**Found**
1	240-300	CuO	43.3	42.8
2	260-310	CuO	31.6	31.3
3	250-300	Cu	20.4	20.5
4	285-320	CuO	32.7	31.6

Table S.2-2 Average crystallite size of nanostructured Cu powders.

complex	**Temperature**	**Crystallite size (nm)**
1	350	48.49± (6.0)
	400	53.33± (6.1)
	450	145.82± (6.6)
2	350	103.9± (6.0)
	400	59.31± (5.8)
	450	70.24± (6.2)
3	350	133.45± (5.4)
	400	106.8± (5.7)
	450	76.25± (6.0)
4	350	43.50± (7.3)
	400	87.65± (6.5)
	450	109.52± (8.8)

Table S.2-3 Average ecrystallite size of Cu nanoparticles from hot injection.

Complex	**Time(min)**	**Crystallite size (nm)**
1	10	106.83 ± (4.8)
	30	106.92± (10.5)
	60	133.75± (8.3)
2	10	53.35± (7.1)
	30	59.27± (7.2)
	60	87.52± (7.6)
3	10	66.72± (7.1)
	30	66.74± (7.3)
	60	76.23± (7.6)
4	10	72.96± (8.0)
	30	109.62± (10.8)
	60	146.17± (11.14)

Chapter 3. The Synthesis of Bismuth Sulfide Powders by Pyrolysis of New Xanthate Precursors.

3.1. Introduction

The synthesis and fabrication of nanoscale semiconductor materials with different structures have received a great deal of attention in the past few years because their properties can be tuned by changing the size, shape and chemical composition.[1-6] The earth-abundance and low toxicity of bismuth sulfide Bi_2S_3 is an important inorganic semiconductor material. The tunable direct band gaps between (1.3–1.7 eV) and large visible-light absorption coefficient (in the order of 10^4 to 10^5 cm^{-1})[7-9] make Bi_2S_3 promising candidate for various potential applications including: optoelectronic, sensors and thermoelectric devices, electrochemical energy storage, photothermal therapy,[10-16] as well as absorber layers in solar cells.[17, 18] The aim of this work is the preparation metal sulfide nanoparticles using bismuth (III) xanthate complexes as single-source precursors. Bi_2S_3 is an excellent candidate for use as absorber layers in the PV cell.

Bismuth (III) xanthate complexes with the formula $[N(C_2H_5)_4][Bi(S_2COR)_4]$ where R = alkyl methyl, ethyl, n-propyl, iso-propyl, n-butyl, iso-butyl, pentyl, and hexyl have been synthesised and characterised. The crystal structures of these complexes have been investigated. The potential use of the as-prepared complexes as single-source precursors for the formation of bismuth sulfide nanoparticles have been also investigated by the thermal decomposition of bismuth (III) xanthate complexes at three different temperatures 250, 300 and 350 °C under nitrogen for 1h.

3.2. Authors distribution

In this work, the project idea provided by Paul O'Brien and all the experimental work was done in his the laboratory. The synthesis and characterisation of bi(III) xanthate complexes via IR, NMR, elemental analysis and TGA, as well as the preparation and characterisation of Bi_2S_3 products by the pX-ray diffraction, scanning electron microscope (SEM), energy-dispersive X-ray spectroscopy (EDS) and UV spectroscopy were carried out by me. Mousa Hossin synthesised and characterised some of the xanthate ligand namely hexyl and butyl xanthate. The crystal structure of the Bi(III) xanthate complexes were studied by George Whitehead and Inigo Vitorica-yrezabal. Firoz Alam and David Lewis edited the draft.

3.3. References

1. A. Kis, G. Csanyi, D. Vrbanic, A. Mrzel, D. Mihailovic, A. Kulik and L. Forro, *Small*, 2007, **3**, 1544-1548.
2. S. J. Lee, A. R. Morrill and M. Moskovits, *J. Am. Chem. Soc.*, 2006, **128**, 2200-2201.
3. J. Ma, J. Lian, X. Duan, X. Liu and W. Zheng, *J. Phys. Chem. C*, 2010, **114**, 10671-10676.
4. J. Ma, Y. P. Wang, Y. J. Wang, P. Peng, J. B. Lian, X. C. Duan, Z. F. Liu, X. D. Liu, Q. Chen, T. Kim, G. Yao and W. J. Zheng, *CrystEngComm*, 2011, **13**, 2369-2374.
5. J. M. Ma, Y. P. Wang, Y. J. Wang, Q. Chen, J. B. Lian and W. J. Zheng, *J. Phys. Chem. C*, 2009, **113**, 13588-13592.
6. M. S. Park, G. X. Wang, Y. M. Kang, D. Wexler, S. X. Dou and H. K. Liu, *Angew. Chem. Int. Ed. Engl.*, 2007, **46**, 750-753.
7. L. M. Peter, K. G. U. Wijayantha, D. J. Riley and J. P. Waggett, *J. Phys. Chem. C*, 2003, **107**, 8378-8381.
8. Y. Li, F. Wei, Y. Ma, H. Zhang, Z. Gao, L. Dai and G. Qin, *CrystEngComm*, 2013, **15**, 6611-6616.
9. A. A. Tahir, M. A. Ehsan, M. Mazhar, K. G. U. Wijayantha, M. Zeller and A. D. Hunter, *Chem. Mater.*, 2010, **22**, 5084-5092.
10. W. Huang, C. Xing, Y. Wang, Z. Li, L. Wu, D. Ma, X. Dai, Y. Xiang, J. Li, D. Fan and H. Zhang, *Nanoscale*, 2018, **10**, 2404-2412.
11. Y. Cheng, Y. Chang, Y. Feng, H. Jian, Z. Tang and H. Zhang, *Angew. Chem. Int. Ed.*, 2018, **57**, 246-251.
12. L. Jiao, Q. Li, J. Deng, N. Okosi, J. Xia and M. Su, *Nanoscale*, 2018, **10**, 6751-6757.
13. J. Jin and T. He, *Appl. Surf. Sci.*, 2017, **394**, 364-370.
14. H. Liang, J. Ni and L. Li, *Nano Energy*, 2017, **33**, 213-220.
15. C. Lu, Z. Li, L. Yu, L. Zhang, Z. Xia, T. Jiang, W. Yin, S. Dou, Z. Liu and J. Sun, *Nano Res.*, 2018, **11**, 4614-4626.
16. M. Wang, H. Yin, N. Shen, Z. Xu, B. Sun and S. Ai, *Biosens. Bioelectron.*, 2014, **53**, 232-237.
17. S. ten Haaf, H. Sträter, R. Brüggemann, G. H. Bauer, C. Felser and G. Jakob, *Thin Solid Films*, 2013, **535**, 394-397.
18. A. J. MacLachlan, F. T. F. O'Mahony, A. L. Sudlow, M. S. Hill, K. C. Molloy, J. Nelson and S. A. Haque, *ChemPhysChem*, 2014, **15**, 1019-1023.

3.4. Manuscript: The Synthesis of Bismuth Sulfide Powders by Pyrolysis of New Xanthate Precursors.

Thamer S Alraddadi,[a] Mousa Hossin,[a] Firoz Alam, [a,b] George Whitehead, [a] Inigo Vitorica-Yrezabal,[a] Paul O'Brien[a,b] and David Lewis[b*]

3.4.1. Abstract

We report the synthesis of new series of tetraethylammonium tetrakis(O-alkylxanthato)Bi(III) complexes with different alkyl group (alkyl = methyl, ethyl, n-propyl, iso-propyl, n-butyl, iso-butyl, pentyl, and hexyl). The single-crystal X-ray structures have been investigated. Some of these complexes were used as single-source precursors for producing bismuth sulfide (Bi_2S_3) nanostructured powders utilizing melt method. Also, we reported the structures, morphology and the elemental composition of the products employing the *p*-X-ray diffraction, scanning electron microscope (SEM) and energy-dispersive X-ray spectroscopy (EDS). The estimated optical bandgap of as-prepared Bi_2S_3 varied between 1.13-1.19 V.

---

[a]School of Chemistry, The University of Manchester, Oxford Road M13 9PL, UK.

[b]School of Materials, The University of Manchester, Oxford Road M13 9PL, UK, UK

*Corresponding author: david.lewis-4@manchester.ac.uk ; Tel: +44 (0)1613063561.

3.4.2. Introduction

Over the past decade, significant efforts have been made to develop photoelectrochemically active semiconductor nanoparticles and thin films.[1, 2] Metal chalcogenide $A_2^{V}B_3^{VI}$ (A=Sb, Bi, As and B=S, Se, Te) group compounds are important semiconductor materials because of their excellent thermoelectric properties, photosensitivity and photoconductivity. In fact, they are promising candidates for many potential applications including thermoelectric devices,[3, 4] television cameras,[5] electronic and optoelectronic devices[6-10] and in IR spectroscopy.[11-13] Amongst these materials, bismuth sulfide is a nontoxic n-type semiconductor. Because of the high absorption coefficient (10^5 cm^{-1}) along with direct bandgap, which lies between 1.2 to 1.7 eV, Bi_2S_3 received immense scientific and technological interest in the area of solar cells,[14, 15] thermoelectric coolers,[16-18] hydrogen storage,[19, 20] lithium-ion batteries,[21] medicine contrast agent,[22, 23] and biomolecule detector.[24] The nanostructure of Bi_2S_3 is highly sensitive to synthesis parameters like the temperature, sulfur precursor and synthesis time.[25, 26] The most commonly reported Bi_2S_3 morphology are nanowires,[27-29] nanorods[30, 31] and there are some reported of more complex structures including nanoflowers[32-34] and snowflakes.[19] All of these structures have been obtained using different techniques such as microwave irradiation,[35, 36] ultrasonic methods,[37, 38] hydrothermal synthesis,[39-41] solvothermal decomposition,[42, 43] chemical deposition,[44-46] thermal evaporation[44] and reactive evaporation.[47] However, these methods are time-consuming and require a high-temperature reaction, complex multi-step process and not easily adapted for large scale.[43, 48] Alternatively, the absence of the solvent in the melt reaction is an economic and environmental advantage over other techniques such as hot-injection and heating-up methods where the high boiling point solvent often used. Another interesting benefit of these reactions is that they are usually self-capping. The products produced during the precursor’s decomposition act as capping agent and play a significant role in nanoparticle synthesis: passivating the particle’s surface, controlling of the growth rate and, in some cases in the shape of formed particles, wherein the hot-injection the solvent act as capping ligand.

The use of single source precursors (SSPs) is an efficient approach to produce high-quality crystalline nanoparticles.[49-51] It also has an advantage of tuning the size and size distribution of the products by controlling the reaction conditions.[26] For example; Lewis *et al.* reported the use of Pb(II) xanthate and dithiocarbamate complexes as SSPs in the synthesis of PbS-polymer hybrid films.

They also conclude that the size and shape can be controlled by changing the reaction conditions and the precursors[52].

Several groups have noted some meaningful procedures on the preparations of Bi_2S_3 using different single source precursors including bismuth (III) complexes of dithiocarbamates, thiosulfates, xanthate and other[32,53-64] Metal xanthates are favourable SSPs for producing nanoparticles and thin films of metal sulphide,[65] because of their relatively low melting point and decomposition temperatures (below 250°C) compared to other precursors. Besides that, the decomposition process formed volatile by-products which play an important role in stabilizing the growth of the nanoparticles.[65,66] Most of the reported Bi(III) xanthates complexes usually coordinated by three by chelating xanthate ligands with the formula of $[Bi(S_2COR)_3]$ where R is different alkyl group.[67-70] Some of these complexes have been used as precursors for the preparation of Bi_2S_3 nanoparticles.[32,58-60] There are only two reports on the synthesis of bi(III) xanthates complexes when four xanthate ligands coordinated to the bismuth $[NEt_4][Bi(S_2COEt)]_4$[71] and $[NMe_4]$ $[Bi(S_2CO\text{iso-pro})]_4$[72]. However, they have not been used as precursors to prepared bismuth sulfide nanoparticles. Therefore, we report the synthesis and crystal structures of eight bismuth (III) xanthates complexes and investigate the potential use of these as precursors to produce Bi_2S_3 nanomaterial using melt method.

3.4.3. Experimental

3.4.3.1. Chemicals

Chemicals and solvents used in these experiments were purchased from Sigma-Aldrich or Fisher and were used without further purification. Potassium ethyl xanthogenate (96%, SigmaAldrich), potassium hydroxide (>85%, Fisher Scientific), methanol (99.7%, Sigma-Aldrich), ethanol (99.8%, Sigma-Aldrich), 1-propanol (99.7%, Sigma-Aldrich), 1-butanol (99.8% Sigma-Aldrich), 2-propanol (99.7%, Sigma-Aldrich), 2-butanol (99.5%, Sigma-Aldrich), 1-pentanol (99.5%, Sigma-Aldrich), 1-hexanol (reagent grade 98%, Sigma-Aldrich), carbon disulfide (low benzene ≥99.9%, Sigma-Aldrich), bismuth (III) chloride (reagent grade 98%, Sigma-Aldrich) and tetraethylammonium bromide (reagent grade 98%, Sigma-Aldrich).

3.4.3.2. Characterizations

Elemental analysis (EA) and thermogravimetric analysis (TGA) were collected by the University of Manchester Microanalytical Laboratory. The TGA studies were performed under nitrogen atmosphere from room temperature to 600 °C at a heating rate of 10 $°C\ min^{-1}$. NMR spectrum were collected using a Bruker AVANCE III 400 MHz spectrometer. Raman spectrum were conducted using a Renishaw 1000 microscope system equipped with laser excitation of 514 nm. UV-spectrum were collected using a Shimadzu UV-1800. Powder X-ray diffraction (p-XRD) patterns were acquired with a Bruker Xpert diffractometer using a Cu Kα source ($\lambda = 0.15418$ nm). The surface morphology of the as-formed powders was studied using TESCAN Mira3 scanning electron microscope (SEM). The energy dispersive X-ray (EDX) spectrometers were obtained using TESCAN Mira3 LC FEG-SEM + OI EBSD + EDS.

3.4.3.3. Synthesis of Bi(III) xanthate complexes

3.4.3.3.1. Synthesis of tetraethylammonium tetrakis(methylxanthato)Bi(III) (1)

The tetraethylammonium tetrakis(methylxanthato)Bi(III) was prepared according to modified literature method.[72] Potassium hydroxide (17.0 g, 0.3 mol) was dissolved in 100 mL of a 1:4 mixture of de-ionised (DI) water and methanol, with stirring for 1 h at room temperature. Then the solution was cooled to 0 °C and carbon disulfide (18.62 mL, 0.3 mol) was added dropwise. The resulting yellow solution was stirred for an hour. The yellow precipitate was filtered and then washed with a small amount of water, to give potassium methylxanthate [$K(S_2COMe)$]. Tetraethylammonium bromide (1.9 g, 9.0 mmol) and potassium methylxanthate (4.39 g, 30.0 mmol) were dissolved in methanol (50 ml) and added dropwise to a solution of bismuth (III) chloride (1.74 g, 5.50 mmol) in methanol (50 ml). A precipitate formed directly and the solution was stirred for further 60 min. Insoluble inorganic salts were separated out by filtration and the filtrate allowed to crystallise at -10 °C to yield the product as a yellow crystalline solid. Yield 5.2g, 82%, m.p.149-150 °C. Microanalysis, found (calc for $C_{16}S_8O_4NH_{32}Bi$): C 24.65 (25.0), H 3.99 (4.20), N 1.77 (1.80)%. ^{1}H NMR (400 MHz, [$(CD_3)_2CO$]) δ ppm: 1.40 (tt, J= 7.2 Hz, 3 H) 3.50 (q, J= 7.2 Hz, 2 H) 4.04 (s, 3 H). ^{13}C NMR, [$(CD_3)_2CO$]) δ ppm 7.57 (CH_3), 52.92 (CH_2N), 59.53 (CH_3O) 231.75 (s, CS_2).

3.4.3.3.2. Synthesis of tetraethylammonium tetrakis(Ethylxanthato)Bi(III) (2)

Complex (**2**) was prepared as compound (**1**) with (4.8 g, 30 mmol) of commercially available potassium ethylxanthate used in place of methylxanthate. Yield 4.7g, 70%, m.p. 124-125 °C. Microanalysis, found (calc for $C_{20}S_8O_4NH_{40}Bi$): C 29.46 (29.16), H 4.88 (4.90), N 1.72 (1.70)%. ^{1}H NMR (400 MHz, [$(CD_3)_2CO$]) δ ppm: 1.35 - 1.43 (m, 6 H) 3.49 (q, *J*=7.28 Hz, 2 H) 4.53 (q, *J*=7.03 Hz, 2 H).^{13}C NMR, [$(CD_3)_2CO$]) δ ppm 7.57 (CH_3), 14.09 (CH_3), 52.76 (CH_2N), 69.53 (CH_2O) 230.65 (CS_2).

3.4.3.3.3. Synthesis of tetraethylammonium tetrakis(n-propylxanthato)Bi(III) (3)

Complex (**3**) was prepared as compound (**1**) with (5.30 g, 30 mmol) n-propylxanthate used in place of methylxanthate. Yield 5.1g, 70 %, m.p. 135-137 °C. Microanalysis, found (calc for $C_{24}S_8O_4NH_{41}Bi$): C 32.90 (32.76), H 5.49 (5.50), N 1.60 (1.59)%. ^{1}H NMR (400 MHz, [$(CD_3)_2CO$]) δ ppm: 0.98 (t, *J*=7.40 Hz, 3 H) 1.40 (tt, *J*=7.28, 1.88 Hz, 3 H) 1.81 (sxt, *J*=7.13 Hz, 2 H) 3.50 (q, *J*=7.28 Hz, 2 H) 4.45 (t, *J*=6.65 Hz, 2 H). ^{13}C NMR [$(CD_3)_2CO$]) δ ppm 7.80 (CH_3), 10.85 (CH_3), 22.71(CH_2) 53.14 (CH_2N) 75.43 (CH_2O) 230.65 (CS_2).

3.4.3.3.4. Synthesis of tetraethylammonium tetrakis(O-isopropylxanthato)Bi(III) (4)

Complex (**4**) was prepared as compound (**1**) with (5.30 g, 30 mmol) isopropylxanthate used in place of methylxanthate. Yield 5.1g, 72%, m.p. 150-152 °C. Microanalysis, found (calc for $C_{24}S_8O_4NH_{41}Bi$): C 32.80 (32.67), H 6.04 (5.50), N 1.55 (1.59)%. ^{1}H NMR (400 MHz, [$(CD_3)_2CO$]) δ ppm 1.34 - 1.43 (m, 9 H) 3.50 (q, *J*=7.28 Hz, 2 H) 5.59 (spt, *J*=6.19 Hz, 1 H).^{13}C NMR, [$(CD_3)_2CO$]) δ ppm 6.84 (CH_3), 21.00 (CH_3), 52.17 (CH_2N), 76.43 (CHO) 229.16 (CS_2).

3.4.3.3.5. Synthesis of tetraethylammonium tetrakis(n-butylxanthato)Bi(III) (5)

Complex (**5**) was prepared as compound (**1**) with (5.65 g, 30 mmol) n-butylxanthate used in place of methylxanthate. Yield 6.2g, 82%, m.p. 124-126 °C. Microanalysis, found (calc for $C_{28}S_8O_4NH_{56}Bi$): C 36.10 (35.93), H 6.00 (6.04), N 1.51 (1.50)%. ^{1}H NMR (400 MHz, [$(CD_3)_2CO$]) δ ppm 0.95 (t, *J*=7.40 Hz, 3 H) 1.37 - 1.49 (m, 5 H) 1.70 - 1.83 (m, 2 H) 3.50 (q, *J*=7.28 Hz, 2 H) 4.50 (t, *J*=6.65 Hz, 2 H). 13C NMR, [$(CD_3)_2CO$]) δ ppm 7.23 (CH_3), 13.53 (CH_3), 19.42 (CH_2), 30.89 (CH_2), 52.59 (CH_2N), 73.19 (CH_2O), 230.53 (CS_2).

3.4.3.3.6. Synthesis of tetraethylammonium tetrakis(O-isobutylxanthato)Bi(III) (6)

Complex (**6**) was prepared as compound (**1**) with (5.65 g, 30 mmol) isobutylxanthate used in place of methylxanthate. Yield 6.0g, 80%, m.p. 126-128 °C. Microanalysis, found (calc for $C_{28}S_8O_4NH_{56}Bi$): C 29.0 (29.2), H 4.21 (4.86), N 1.51 (1.70)%. ^{1}H NMR (400 MHz, $[(CD_3)_2CO]$) δ ppm 0.92 (t, *J*=7.53 Hz, 3 H) 1.33 (d, *J*=6.27 Hz, 3 H) 1.40 (tt, *J*=7.28, 1.88 Hz, 3 H) 1.57 - 1.88 (m, 2 H) 3.50 (q, *J*=7.28 Hz, 2 H) 5.45 (sxt, *J*=6.27 Hz, 1 H). ^{13}C NMR, $[(CD_3)_2CO]$) δ ppm 8.28 (CH_3), 10.64 (CH_3), 19.89 (CH_2), 30.00 (CH_3), 19.89 (CH_2),53.61 (CH_2N), 82.71 (CH_3O) 230.99 (CS_2).

3.4.3.3.7. Synthesis of tetraethylammonium tetrakis(pentylxanthato)Bi(III) (7)

Complex (**7**) was prepared as compound (**1**) with (6.0 g, 30 mmol) pentylxanthate used in place of methylxanthate. Yield 6.2g, 79%; m.p. 123-125 °C. Microanalysis, found (calc for $C_{32}S_8O_4NH_{64}Bi$): C 29.0 (29.2), H 4.21 (4.86), N 1.51 (1.70)%. ^{1}H NMR (400 MHz, $[(CD_3)_2CO]$) δ ppm 0.86 - 0.98 (m, 3 H) 1.33 - 1.45 (m, 7 H) 1.74 - 1.87 (m, 2 H) 3.51 (q, *J*=7.28 Hz, 2 H) 4.50 (t, *J*=6.78 Hz, 2 H) ^{13}C NMR, $[(CD_3)_2CO]$) δ ppm 7.21 (CH_3), 13.74 (CH_3), 22.53 (CH_2), 28.43 (CH_2), 28.54 (CH_2), 52.55 (CH_2N), 73.43 (CH_3O) 230.51 (CS_2).

3.4.3.3.8. Synthesis of tetraethylammonium tetrakis(Hexylxanthato)Bi(III) (8)

Complex (**8**) was prepared as compound (**1**) with (6.50 g, 30 mmol) hexylxanthate used in place of methylxanthate. Yield 6 g, 71%, m.p. 118-120 °C. Microanalysis, found (calc for $C_{36}S_8O_4NH_{72}Bi$): C 29.0 (29.2), H 4.21 (4.86), N 1.51 (1.70) %. ^{1}H NMR (400 MHz, $[(CD_3)_2CO]$) δ ppm 0.86 - 0.98 (m, 3 H) 1.33 - 1.45 (m, 7 H) 1.74 - 1.87 (m, 2 H) 3.51 (q, *J*=7.28 Hz, 2 H) 4.50 (t, *J*=6.78 Hz, 2 H) ^{13}C NMR, ($CDCl_3$) δ ppm 8.15 (CH_3), 14.31 (CH_3), 22.84 (CH_2), 25.97 (CH_2), 28.86 (CH_2), 31.78 (CH_2), 53.20 (CH_2N), 74.45 (CH_3O) 230.15 (CS_2).

3.4.3.4. Synthesis of bismuth sulfide powders

The solventless thermolysis method was used to produce Bi_2S_3 powder. Approximately 0.3 g of the precursors of the complexes **2**, **3**, **5** and **8** were placed into a ceramic boat in a tube furnace and annealed at 250, 300, and 350 °C under an inert atmosphere. After 60 min the furnace switched off and then allowed to cool down to room temperature and the powders was collected for further analysis.

3.4.4. Results and discussion

Eight tetraethylammoniumtetrakis(O-alkylxanthato)Bi(III) complexes, $[NEt_4][Bi(S_2COMt)]_4$ (1), $[NEt_4][Bi(S_2COEt)]_4$ (2),$[NEt_4][Bi(S_2CO^nPr)]_4$(3), $[NEt_4][Bi(S_2CO^iPr)]_4$ (4), $[NEt_4][Bi(S_2CO^nBt)]_4$ (5), $[NEt_4][Bi(S_2CO^iBt)]_4$ (6), $[NEt_4][Bi(S_2COPe)]_4$ (7), $[NEt_4][Bi(S_2COHex)]_4$ (8), were synthesised by the dropwise addition of ethanolic solution of bismuth (III) chloride to a mixture of alkylxanthate salt and tetraethylammonium bromide dissolved in methanol. Single crystals suitable for X-ray diffraction were grown by storing the resulting filtrate solutions at -10 °C for 24 h. All complexes were soluble in common organic solvents such as chloroform, tetrahydrofuran (THF) and acetone. These complexes were stored at -10 °C to avoid decomposition.

3.4.4.1. Single-crystal X-ray structure

The single crystal X-ray structures of complexes (1-8) are shown in (Figure 3.1) The structure consists of discrete $(Et_4N)^+$ cations and $(Bi(S_2COR)_4)^-$ anions. All complexes adopt a dodecahedral molecular geometry around the central bismuth ion, the coordination arrangement arising from four S,S chelating of the alkylxanthate ligands. Complex (4) possesses an orthorhombic crystal system with a space group of (Pbca), where complexes (2), (3), (5) and (8) crystallised in the monoclinic system with space group (C2),($P2_1/n$), ($P2_1/c$) and ($P2_1/n$) respectively. On the other hand, complexes (1), (6), and (7) have a triclinic crystal system with (P-1) space group. The bond lengths between Bi-S1 for 1, 2, 3, 5, 7 and 8 are ranged between 2.819(2) and 2.9442(6). The angles between S1-Bi-S2 for complexes 1, 2, 3, 5, 7 and 8 are in the range of 60.64(8) and 62.72(14). Selected bond lengths and angles are reported in ESI Table S.3-5. The refinement data is shown in ESI Table S1. Bond lengths and angles are reported in Table S.3-6 and Table S.3-7.

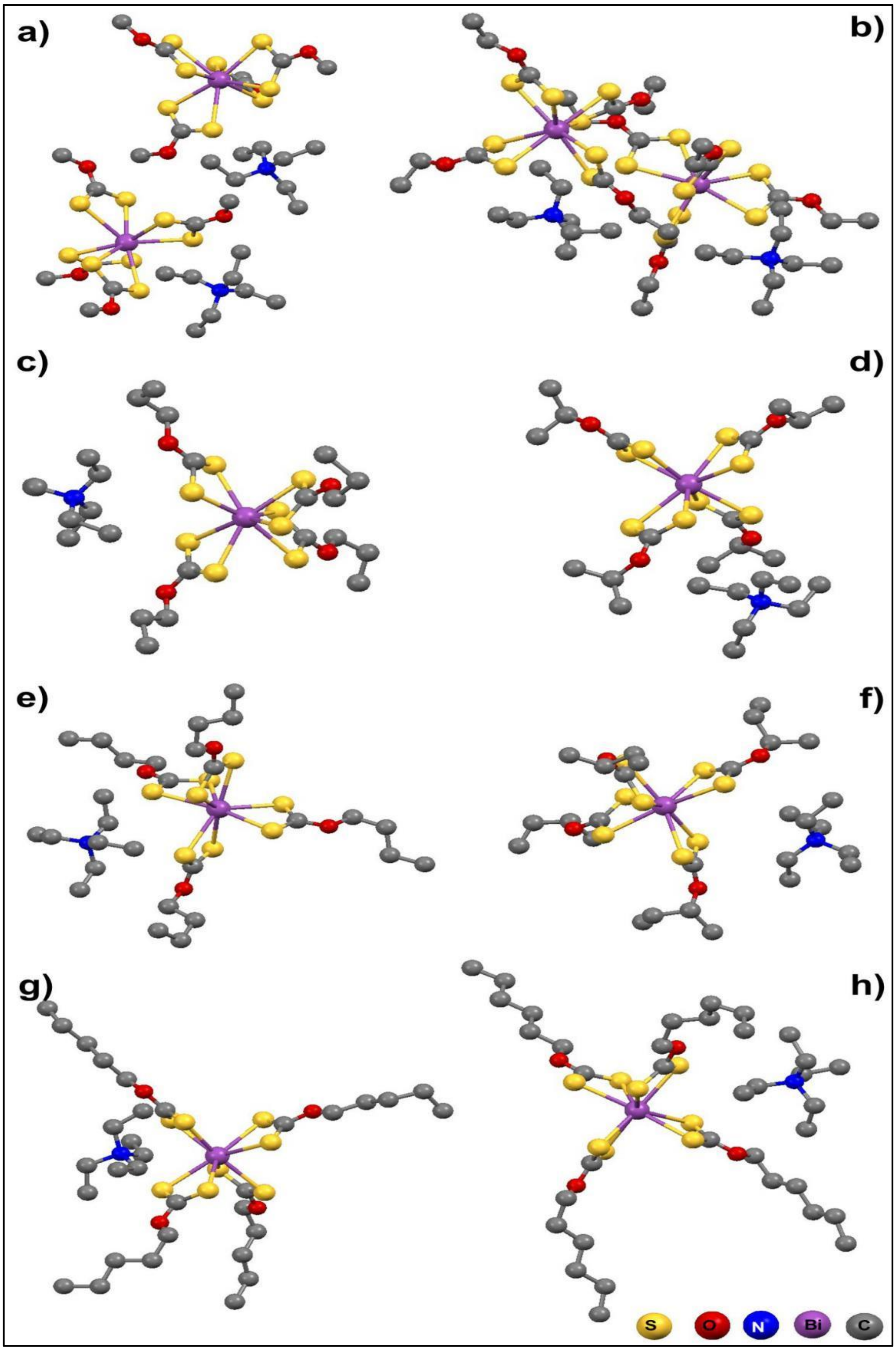

Figure 3.1 Structures of (a) tetraethylammonium tetrakis(Methylxanthato)Bi(III), (b) tetraethylammonium tetrakis(Ethylxanthato)Bi(III), (c) tetraethylammonium tetrakis(n-propylxanthato)Bi(III), (d) tetraethylammonium tetrakis(O-isopropylxanthato)Bi(III), (e) tetraethylammonium tetrakis(n-butylxanthato)Bi(III), (f) tetraethylammonium tetrakis(O-isobutylxanthato)Bi(III), (g) tetraethylammonium tetrakis(pentylxanthato)Bi(III), (h) tetraethylammonium tetrakis(Hexylxanthato)Bi(III).

3.4.4.2. Thermogravimetric analysis (TGA)

Thermogravimetric analyses were performed on the bismuth complexes to determine the decomposition temperature range and the final resulting product. A comparison of TGA profiles for the complexes **2**, **3**, **5** and **8** are shown in Figure 3.2. Investigation of the TGA profiles of these compounds revealed multistep decomposition processes. The product weights at the end of thermolysis are in agreement with the calculated values of bismuth sulfide (Bi_2S_3). Investigation of the TGA profiles for (2), and (3) suggests that the first decomposition step involves loss of $[(Et_4N)][(S_2COR)_2]$, where R is ethyl, and propyl in the range of 115-135 °C. Subsequently, the remaining precursor is decomposing in the range of 130-310 °C to produce Bi_2S_3. On the other hand, the first decomposition step in the TGA profiles of complexes (5) and (8) indicate the elimination of (Et_4N) in the range of 96-128 °C. Following that is the exclusion of residual precursor in the range of 120-300 °C to produce Bi_2S_3. All complexes decomposed to formed final solid residues amounts that matched with the calculated value for Bi_2S_3. TGA results of the final residues are summarised in ESI Table S.3-3.

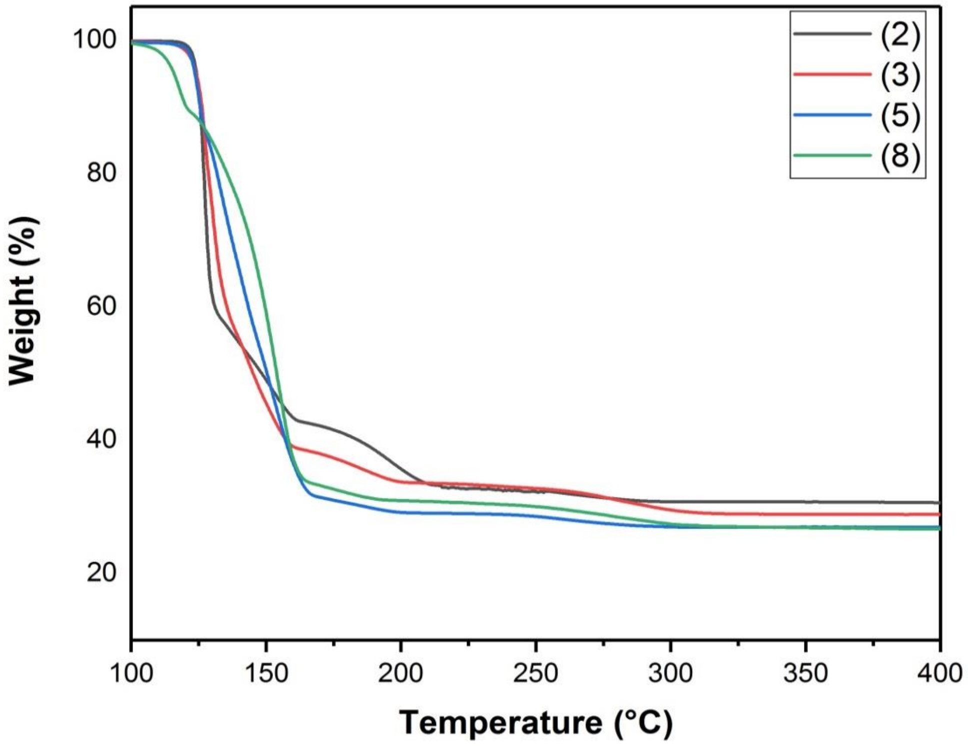

Figure 3.2 TGA profiles for complexes (2), (3), (5) and (8).

Most of the previously reported techniques are requiring harsh reaction conditions such as longer pyrolysis time and high-temperature, and in some cases the addition of surfactant and capping is applied to control the growth and morphology of Bi_2S_3 nanoparticles.[43, 48] Interesting results reported by Sun *et al.*, they described a simple scheme to synthesise Bi_2S_3 nanoflowers by the reaction of bismuth (III) ethylxanthate and ethylenediamine at room temperature, however the reaction time extended for 5 days.[73] Also, in another study, bismuth (III) ethylxanthate has been used as molecular single precursors to prepared Bi_2S_3 nanorods via solventless thermolysis at three different temperatures.[59] Bismuth (III) xanthate complexes are a strong candidate for synthesis of Bi_2S_3 because they show low to moderate reaction conditions. The bismuth (III) xanthate complexes presented in this work show relatively low pyrolysis temperature (250 - 350 °C). A comparison of some bismuth precursors that have been used to prepared Bi_2S_3 nanoparticles are illustrated in Table 3-1.

Table 3-1 Comparison of some bismuth precursors that have been used to prepared Bi_2S_3 nanoparticles.

Precursor	Thermolysis conditions	Product information	Ref
$Bi(S_2COEt)_3$	Melt method, 200 - 300 °C for 1 h	Nanorod	59
$[Bi(S_2COC_4H_9)_3(C_5H_5N)_2]$ $[Bi(S_2COC_4H_9)_3(C_{12}H_8N_2)]$	PVP/Water 180 °C for 16 h	Nanorod	58
$Bi(S_2COEt)_3$	Ethylene diamine, room temperature, 5 days	Flower-like Bi_2S_3	73
$Bi(S_2CNMe\mathit{n}Hex)_3$	TOPO/TOP 150 °C for 2 h	Mixture of Bi_2S_3 and Bi	56
	2-ethoxyethanol, 132 °C for 2 h.	Bi_2S_3 nanoparticles	
	Ethylene glycol, 197 °C for 2 h.	Bi_2S_3 nanoparticles	
	4-ethylpyridine, 168 °C for 2 h.	Bi_2S_3 nanoparticles	
	p-Xylene, at 140 °C for 2 h	Bi_2S_3 nanoparticles	
$Bi(S_2CNEt_2)_3$	1-dodecylamine (DDA), 220 °C for 150 min	Nanosheets	74
	Oleylamine, (OAM), 220 °C for 150 min	Low yield nanosheets	
$Bi((S_2CN(CH_3)(C_6H_{13}))_3$	Ethylene glycol, 132 °C for 2 h	Nanofibers Bi_2S_3	75
Catena-(μ_2-nitrato-O,O')bis(piperidinedithiocarbamato) bismuth(III)	DDA,190,230, 270 °C for 2 h	Nanorod with various lengths	76
Tetrakis(μ-nitrato)tetrakis[bis (tetrahydroquinolinedi-thiocarbamato)bismuth(III)]	HAD, 190,230, 270 °C for 2 h		
	OLA, 190,230, 270 °C for 2 h		
	TOPO, 190,230, 270 °C for 2 h		
$[Bi(SCOPh)_3]$	Dodecanethiol/TOPO 150 °C for 2 h	Bi_2S_3 nanorods	32
	Ethylene glycol/PVP, 150 °C for 1h	Dandelion-like Bi_2S_3	
	Cysteine/H2O room temperature	Bi_2S_3 nanoleaves	
$[MeBi(S_2Ctol)_3]$ $[PhBi(S_2Ctol)_2]$	Diphenylether 260 °C for 3 h	Nanoparticles	77
$[PhBi(S_2Ctol)_2]$	AACVD at 450 °C	Micron-sized fibers	
$[Bi(dtc)_3]$ (dtc = 4-hydroxypiperdine dithiocarbamate)	Melt method, 550 °C for 6 h	Mixture of Bi– Bi_2S_3	78
	ethylene glycol 250 °C for 3 h	Aggregated nanorods	
	ODA 200 °C for 3 h		
$Bi(S_2COR)_4(N(C_2H_5)_4$ R= Ethyl,n-propyl, n-butyl and n-hexyl	Melt method, 250 - 350 °C for 1h	Aggregated nanoparticles	This work

The phase structure and purity of the products from thermal decomposition of complexes (2), (3), (5) and (8) were studied by powder XRD. The *p*-XRD pattern of the as-prepared powder corresponded to orthorhombic phase bismuth sulfide Bi_2S_3 crystal structure (JCPDS card 01-089-8965). No impurity peaks are found in Figure 3.3, suggestion that the Bi_2S_3 crystals obtained via the thermal decomposition of the precursor at 250, 300 and 350 °C consist of a pure phase. The grain sizes have been estimated from the Debye-Scherrer equation.

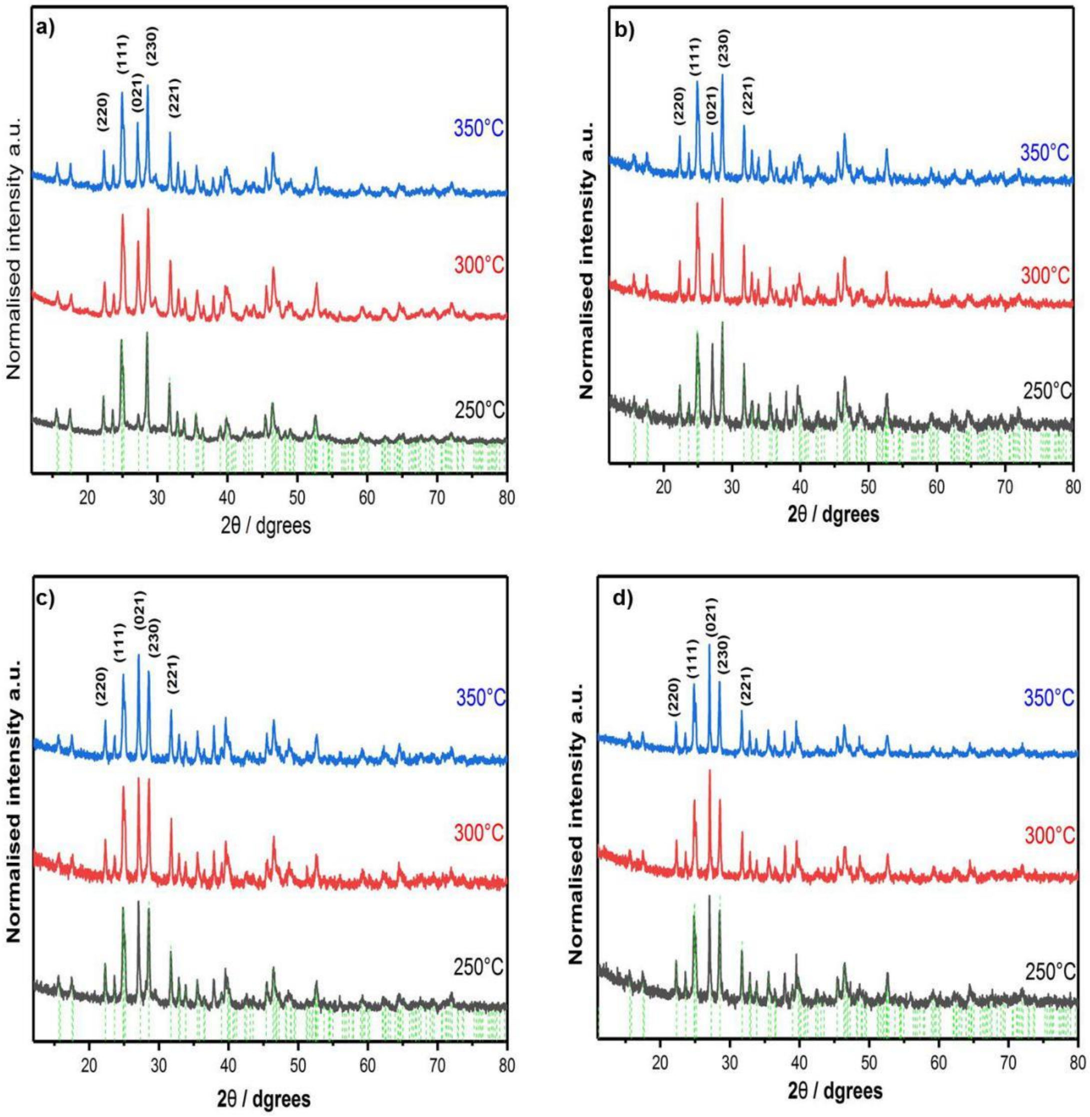

Figure 3.3 XRD pattern of Bi_2S_3 (NPs) from the thermal decomposition of bismuth (III) alkylxanthate; (a) ethyl, (b) propyl, (c) butyl and (d) hexyl at 250, 300 and 350 °C under nitrogen. The reference peak positions for bismuth sulfide Bi_2S_3 crystal structure (JCPDS card 01-089-8965) are shown with green dashed lines.

Table 3-2 The average crystallite size of Bi_2S_3 formed from the thermal decomposition of complexes (2, 3, 5 and 8).

R	Temp (°C)	Crystallite size (nm)
Ethyl	250	32.68 ± (2.3)
	300	33.70± (2.5)
	350	49.65± (3.0)
n-propyl	250	27.39± (3.1)
	300	38.50± (3.2)
	350	34.63± (2.3)
n-butyl	250	59.98± (3)
	300	45.82± (2.5)
	350	35.92± (3.1)
Hexyl	250	29.63± (4.0)
	300	48.47± (5.1)
	350	43.95± (3.3)

The crystalline size of Bi_2S_3 (NPs) from the thermal decomposition of complexes (2), (3), (5) and (8) are shown in Figure 3.4. It is observed that the crystallite size for Bi_2S_3 nanocrystals formed from the thermal decomposition of complex (2) increased as the temperature increased, where products from complex (5) show a decrease in the size with incrementing of the reaction temperature. On the other hands, the Bi_2S_3 nanocrystals prepared from the thermal decomposition of complex (3) and (8) shows an increase in the size when the temperature is increased to 300 °C, then a decrease in the size when the temperature increased to 350 °C.

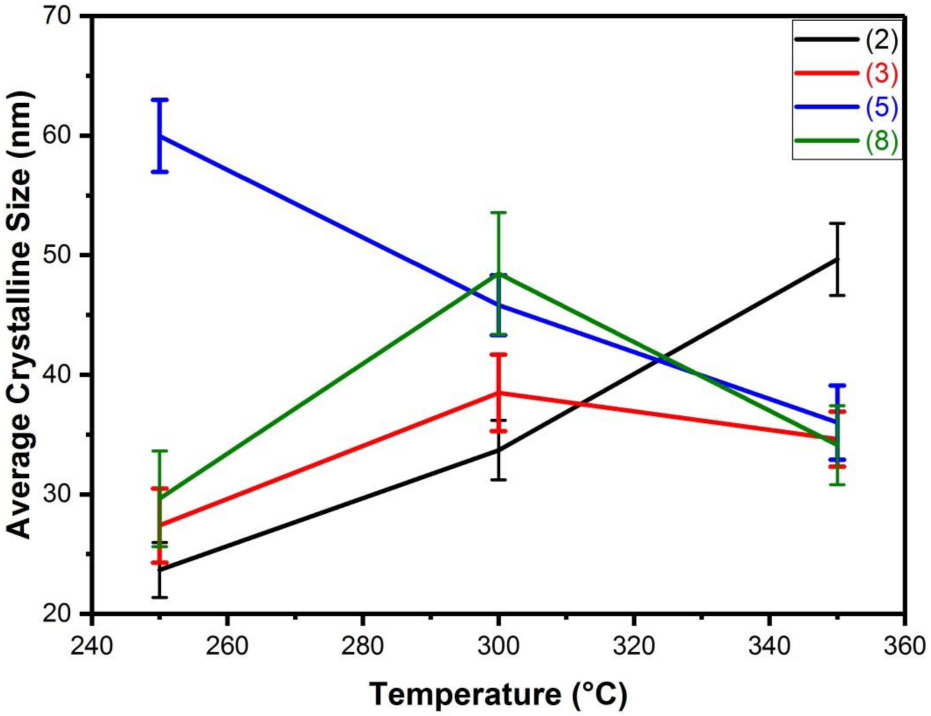

Figure 3.4 The average crystallite size of Bi_2S_3 formed from the thermal decomposition of complexes (2, 3, 5 and 8) against the decomposition temperatures; 250, 300 and 350 °C under nitrogen.

Raman spectroscopy is a powerful method for investigation materials structure.[79, 80] Therefore, it is useful to study the surface structure of as-synthesised Bi_2S_3 nanoparticles. The Raman spectrum of the as-synthesised sample exhibits five peaks Figure 3.5 in the range of 100–1200 cm^{-1}, more specifically, 120, 252, 422, 615 and 965 cm^{-1}. The peaks at 252, 422, 615 and 965 cm^{-1} match well to Bi_2S_3 nanocrystals.[22, 81] However, the peak at 120 cm^{-1} this probably resulting from the difference of the surface optical (SO) phonon modes as it reported previously.[37] Xiao *et al.* claimed that there is no detailed discussion addressing the (SO) modes of Bi_2S_3.[81]

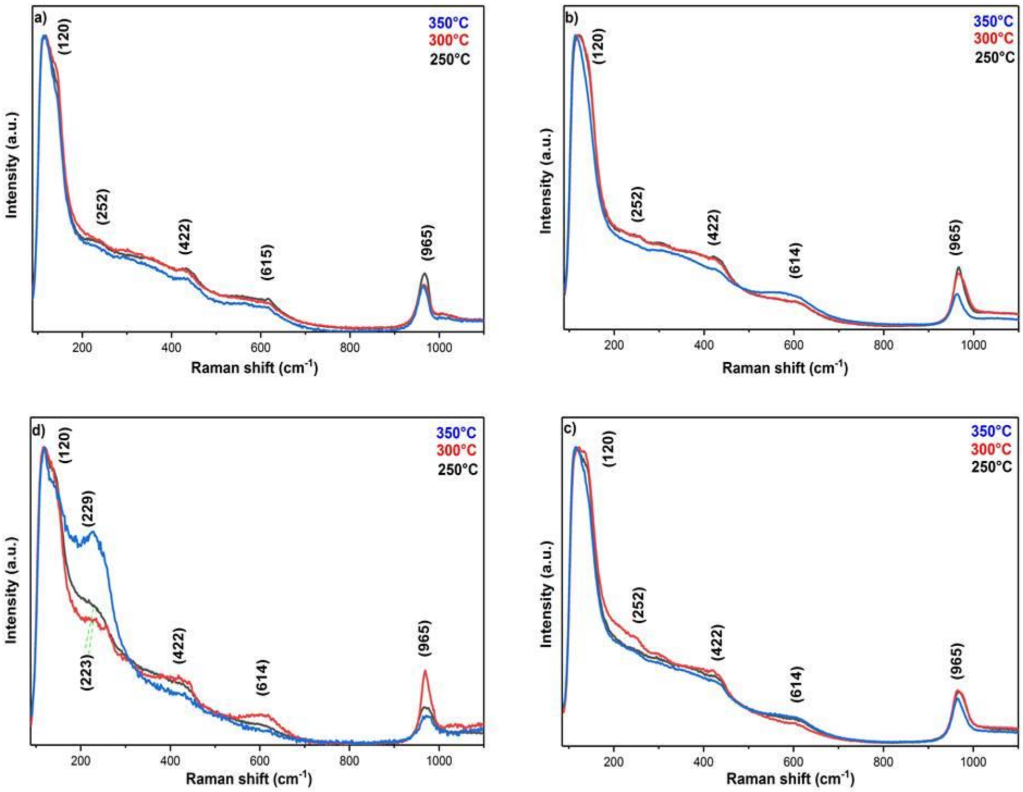

Figure 3.5 Raman spectrum of Bi_2S_3 (NPs) formed the thermal decomposition of bismuth (III) alkylxanthate; (a) ethyl, (b) propyl, (c) butyl and (d) hexyl at 250, 300 and 350 °C under nitrogen.

The UV absorption spectrum of as-synthesised nanocrystal Bi_2S_3 are presented in Figure 3.6. The samples were dispersed in acetone and sonicated for 60 min, then the UV absorption spectrum collected in the wavelength range of 400-1100 nm. The band gaps of Bi_2S_2 nanocrystal were determined using Tauc plot for direct bandgap semiconductor:

$$\alpha h v = A(hv-E_g)^{1/2}$$

where α is the absorption coefficient, h is Planck's constant, v is the frequency of radiation, A is an appropriate constant, E_g is the bandgap. The bandgap was calculated from Tauc plots. The plot of $(\alpha hv)^2$ against hv with a straight line fitting, demonstrating the direct bandgaps between 1.15-1.19 eV, Figure **3.7**. and Table S.3-10. A similar bandgap result has been reported by Grigas *et al.*[82] They reported the optical bandgap of 1.1 and 1.2 eV for Bi_2S_3 crystals grown by melt method. They claimed that the electrical properties of Bi_2S_3 crystals are very sensitive to non-stoichiometry and impurities which result in the large variations in the electrical properties. In a typical solar cell, the absorber layer should be a direct bandgap semiconductor with bandgap around 1.3-1.4eV. The nanocrystal Bi_2S_3 presented in this work is direct bandgap and could be useful as absorber layer in solar cell applications.

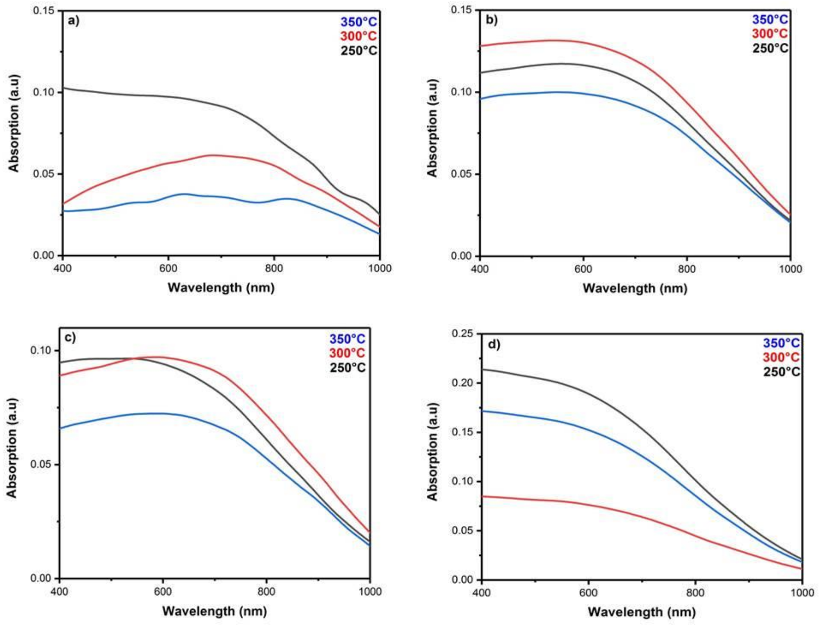

Figure 3.6 The UV absorption spectrum of Bi_2S_3 NPs formed from the thermal decomposition of bismuth (III) alkylxanthate; (a) ethyl, (b) propyl, (c) butyl and (d) hexyl at 250, 300 and 350 °C under nitrogen.

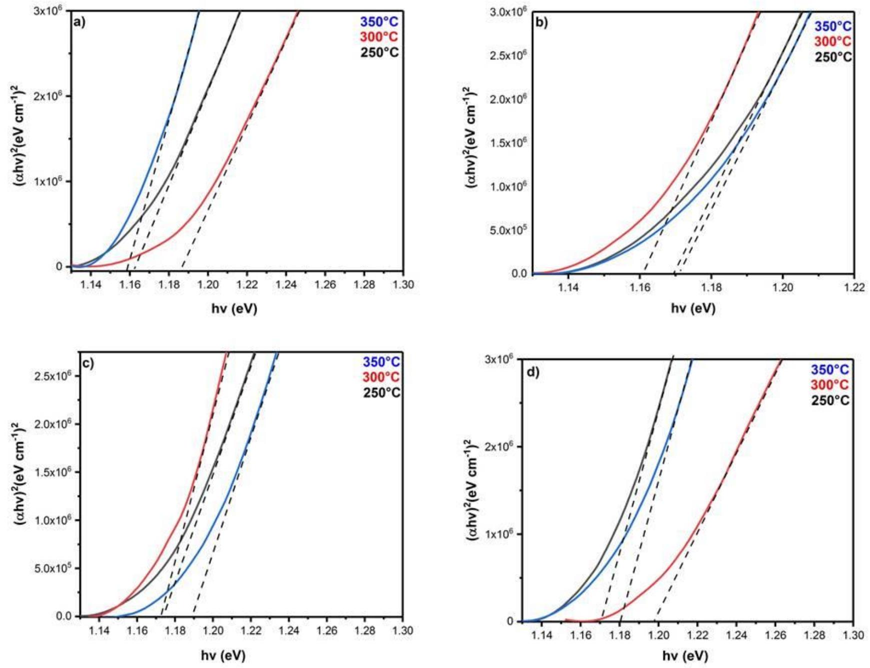

Figure 3.7 Tauc plots of Bi_2S_3 NPs formed from the thermal decomposition of bismuth (III) alkylxanthate; (a) ethyl, (b) propyl, (c) butyl and (d) hexyl at 250, 300 and 350 °C under nitrogen.

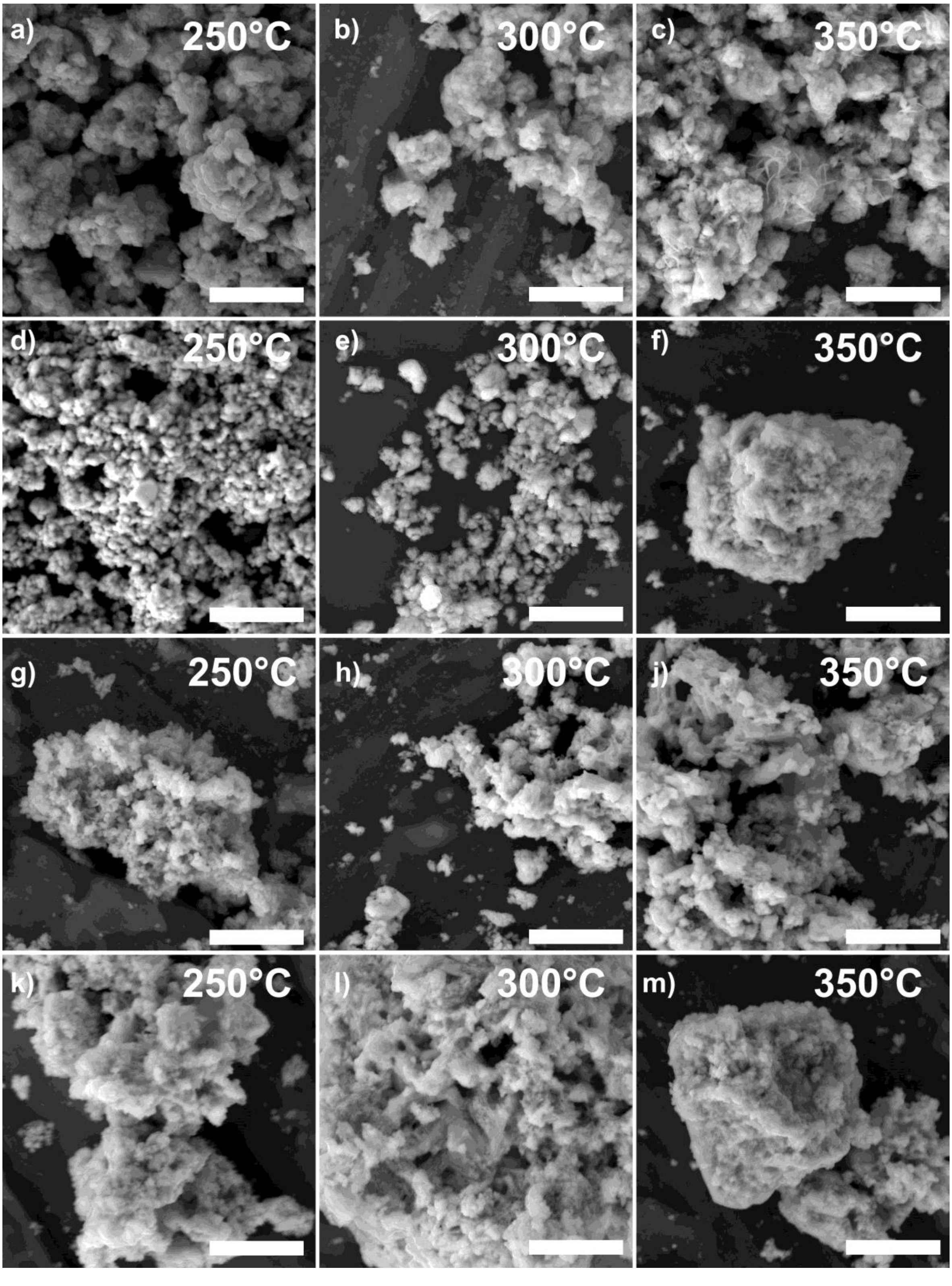

Figure 3.8 SEM of Bi_2S_3 (NPs) produced from the thermal decomposition of bismuth (III) alkylxanthate; ethyl (a-c), propyl (d-f), butyl (g-j) and hexyl (k-m); at 250, 300 and 350 °C under nitrogen, scale bars represent: 2 µm.

The morphology of the as-prepared Bi_2S_3 nanocrystals was studied by SEM Figure 3.8. It clearly observed that the excessive agglomeration results in a bundle of small particles with undefined shape. It is reported in literature that the nanostructure of Bi_2S_3 is influenced by the temperature, precursor, time and temperature of the reaction and the solvent.[25, 26] Therefore, to understand the effect of increasing the reaction temperature and the length of alkyl chain on the morphology of Bi_2S_3 products several experiments were carried out, and the products obtained at different stages were inspected by SEM techniques. Three different temperatures (250, 300, 350 °C) have been chosen based on the TGA profiles which also confirmed by *p*-XRD that the final residuel at those temperatures are pure Bi_2S_3 products. Surprisingly, in this experiment changing reaction temperatures does not have any notable effect on the resulting materials. However, complex (2) showed a mixture of flake-like shape morphology and agglomerated particles when the reaction temperature increased to 350 °C. It's also noted that changing the length of alkyl chain doesn't play any role in either size or shape of Bi_2S_3 nanocrystals.

Melt reaction method used in this experiment represents a simple method to synthesis Bi_2S_3 nanostructures at relatively low temperatures. Unfortunately, in this method the changing of the precursor and the reaction temperature were not sufficient to control the size and the shape of the formed products, since the agglomerated particles were recognized in all conditions. Such a control on the morphology might require higher temperatures or longer reaction time in solid-state process. Yu *et al.* claimed that preparation of bismuth sulfide from the thermal decomposition of some bismuth complexes usually required high temperature or else the final products contain some impurities.[43]

Therefore, further investigation is needed to address the influence of precursor and reaction temperature on Bi_2S_3 nanostructure. It's also suggested to conduct another extensive study to evaluate the impact of other factors and method on Bi_2S_3 nanostructure. For instant, Miniach *et al.* reported the synthesis of Bi_2S_3 nano-sphere and nanoplate-like particles by solvothermal method utilizing water and mixed solvent systems.[83] Wu *et al.* described a simple and effective heating method using microwave irradiation under various experimental conditions to obtain of Bi_2S_3 nanostructure with different morphology and size.[74] Another group reported the synthesis of single crystalline bismuth sulfide with several morphologies (wires, rods, and flowers) via simple polyol solution route.[84]

3.4.5. Conclusions

The new bismuth xanthate, bismuth (III) tetraethylammonium tetrakis(O-alkylxanthato), is a valuable precursor for the preparation of Bi_2S_3 nanostructure at temperatures below 350°C. The effect of changing the temperature on the morphology needs more investigation. The optical properties of the Bi_2S_3 nanocrystals obtained from this method indicate that the materials are direct bandgap semiconductor with bandgap value between 1.15-1.19 eV, which could be suitable absorber for photovoltaic applications. Despite the fact that the melt method does not have sufficient control over the shape and size of the prepared products, the high solubility of these complexes in non-polar organic solvents and the relatively low pyrolysis temperatures is of particular interest for the preparation of bismuth sulfide nanoparticles and thin films.

3.4.6. References

1. A. Hagfeldt and M. Gratzel, *Chem. Rev.*, 1995, **95**, 49-68.
2. H. Weller and A. Eychmüller, in *Stud. Surf. Sci. Catal.*, eds. P. V. Kamat and D. Meisel, Elsevier, 1997, vol. 103, pp. 5-22.
3. M. Telkes, *J. Appl. Phys.*, 1947, **18**, 1116-1127.
4. G. E. Lee, I. H. Kim, S. M. Choi, Y. S. Lim, W. S. Seo, J. S. Park and S. H. Yang, *J. Korean Phys. Soc.*, 2014, **65**, 1908-1912.
5. P. Kunze and H. Mittenentzwei, *Kernenergie (East Germany)*, 1958, Medium: X; Size: Pages: 337-338.
6. Y. Hirose and H. Hirose, *Proc. IEEE*, 1976, **64**, 378-379.
7. M. Shaw, S. Holmberg and S. Kostylev, *Phys. Rev. Lett.*, 1973, **31**, 542.
8. S. A. Keneman, *Appl. Phys. Lett.*, 1971, **19**, 205-&.
9. N. Goto, *J. Non-Cryst. Solids*, 1970, **4**, 378-379.
10. W. Tokuda, T. Katoh, A. Yasumori and K. Nakamura, *J. Appl. Phys.*, 1974, **45**, 5098-5099.
11. B. Ghosh and G. P. Kothiyal, *Prog. Cryst. Growth Charact. Mater.*, 1983, **6**, 393-413.
12. B. T. Kolomiets and B. V. Pavlov, *Soc. Phys. Solid State, 2*, 1960, **2**, 592-597.
13. R. Frerichs, *J. Opt. Soc. Am.A:*, 1953, **43**, 1153-1157.
14. K. Ramasamy, M. A. Malik, N. Revaprasadu and P. O'Brien, *Chem. Mater.*, 2013, **25**, 3551-3569.
15. G. Hodes, J. Manassen and D. Cahen, *Nat.*, 1976, **261**, 403-404.
16. S. Saito, *Science*, 1997, **278**, 77-78.
17. B. X. Chen, C. Uher, L. Iordanidis and M. G. Kanatzidis, *Chem. Mater.*, 1997, **9**, 1655-1658.
18. Q. Yang, C. G. Hu, S. X. Wang, Y. Xi and K. Y. Zhang, *J. Phys. Chem. C*, 2013, **117**, 5515-5520.
19. B. Zhang, X. Ye, W. Hou, Y. Zhao and Y. Xie, *J. Phys. Chem. B*, 2006, **110**, 8978-8985.
20. Q. T. Wang, X. B. Wang, W. J. Lou and J. C. Hao, *New J. Chem.*, 2010, **34**, 1930-1935.
21. H. Y. Zhou, S. L. Xiong, L. Z. Wei, B. J. Xi, Y. C. Zhu and Y. T. Qian, *Cryst. Growth Des.*, 2009, **9**, 3862-3867.
22. O. Rabin, J. Manuel Perez, J. Grimm, G. Wojtkiewicz and R. Weissleder, *Nat. Mater.*, 2006, **5**, 118-122.

23. K. Ai, Y. Liu, J. Liu, Q. Yuan, Y. He and L. Lu, *Adv. Mater.*, 2011, **23**, 4886-4891.
24. L. Cademartiri, F. Scotognella, P. G. O'Brien, B. V. Lotsch, J. Thomson, S. Petrov, N. P. Kherani and G. A. Ozin, *Nano Lett.*, 2009, **9**, 1482-1486.
25. K. Q. Liang, C. G. Wang, X. J. Xu, J. C. Leng and H. Ma, *Phys. Lett. A*, 2017, **381**, 652-657.
26. W. J. Lou, M. Chen, X. B. Wang and W. M. Liu, *Chem. Mater.*, 2007, **19**, 872-878.
27. M. B. Sigman and B. A. Korgel, *Chem. Mater.*, 2005, **17**, 1655-1660.
28. F. Gao, Q. Lu and S. Komarneni, *Chem. Commun.*, 2005, 531-533.
29. A. D. Schricker, M. B. Sigman Jr and B. A. Korgel, *Nanotechnology*, 2005, **16**, S508.
30. S. Vadivel, A. N. Naveen, V. Kamalakannan, P. Cao and N. Balasubramanian, *Appl. Surf. Sci.*, 2015, **351**, 635-645.
31. P. F. Hu, Y. L. Cao and B. Lu, *Mater. Lett.*, 2013, **106**, 297-300.
32. L. Tian, H. Yao Tan and J. J. Vittal, *Cryst. Growth Des.*, 2007, **8**, 734-738.
33. M. Zhang, D. J. Chen, R. Z. Wang, J. J. Feng, Z. Y. Bai and A. J. Wang, *Mater. Sci. Eng.*, C, 2013, **33**, 3980-3985.
34. R. Mukkabla, M. Deepa and A. K. Srivastava, *Electrochim. Acta*, 2015, **164**, 171-181.
35. X. H. Liao, H. Wang, J. J. Zhu and H. Y. Chen, *Mater. Res. Bull.*, 2001, **36**, 2339-2346.
36. X. H. Liao, J. J. Zhu and H. Y. Chen, *Mater. Sci. Eng., B*, 2001, **85**, 85-89.
37. S. Y. Wang and Y. W. Du, *J. Cryst. Growth*, 2002, **236**, 627-634.
38. H. Wang, J. J. Zhu, J. M. Zhu and H. Y. Chen, *J. Phys. Chem. B*, 2002, **106**, 3848-3854.
39. M. W. Shao, M. S. Mo, Y. Cui, G. Chen and Y. T. Qian, *J. Cryst. Growth*, 2001, **233**, 799-802.
40. W. X. Zhang, Z. H. Yang, X. M. Huang, S. Y. Zhang, W. C. Yu, Y. T. Qian, Y. B. Jia, G. I. Zhou and L. Chen, *Solid State Commun.*, 2001, **119**, 143-146.
41. S. H. Yu, J. Yang, Y. S. Wu, Z. H. Han, Y. Xie and Y. T. Qian, *Mater. Res. Bull.*, 1998, **33**, 1661-1666.
42. S.-H. Yu, L. Shu, J. Yang, Z.-H. Han, Y.-T. Qian and Y.-H. Zhang, *J. Mater. Res.*, 2011, **14**, 4157-4162.
43. S. H. Yu, Y. T. Qian, L. Shu, Y. Xie, L. Yang and C. S. Wang, *Mater. Lett.*, 1998, **35**, 116-119.
44. M. E. Rincon, M. Sanchez, P. J. George, A. Sanchez and P. K. Nair, *J. Solid State Chem.*, 1998, **136**, 167-174.
45. R. S. Mane and C. D. Lokhande, *Mater. Chem. Phys.*, 2000, **65**, 1-31.
46. R. S. Mane, B. R. Sankapal and C. D. Lokhande, *Mater. Res. Bull.*, 2000, **35**, 587-601.

47. J. Lukose and B. Pradeep, *Solid State Commun.*, 1991, **78**, 535-538.

48. D. J. Riley, J. P. Waggett and K. G. U. Wijayantha, *J. Mater. Chem.*, 2004, **14**, 704-708.

49. M. A. Malik, N. Revaprasadu and P. O'Brien, *Chem. Mater.*, 2001, **13**, 913-920.

50. M. Afzaal, M. A. Malik and P. O'Brien, *J. Mater. Chem.*, 2010, **20**, 4031-4040.

51. M. Kemmler, M. Lazell, P. O'Brien, D. J. Otway, J. H. Park and J. R. Walsh, *J. Mater. Sci.-Mater. Electron*, 2002, **13**, 531-535.

52. E. A. Lewis, P. D. McNaughter, Z. Yin, Y. Chen, J. R. Brent, S. A. Saah, J. Raftery, J. A. M. Awudza, M. A. Malik, P. O’Brien and S. J. Haigh, *Chem. Mater.*, 2015, **27**, 2127-2136.

53. O. C. Monteiro, T. Trindade, J. H. Park and P. O'Brien, *Chem. Vap. Deposition*, 2000, **6**, 230-232.

54. J. Waters, D. Crouch, J. Raftery and P. O'Brien, *Chem. Mater.*, 2004, **16**, 3289-3298.

55. W. N. Kun, S. Mlowe, L. D. Nyamen, M. P. Akerman, P. O'Brien, P. T. Ndifon and N. Revaprasadu, *Polyhedron*, 2018, **154**, 173-181.

56. O. C. Monteiro, H. I. S. Nogueira, T. Trindade and M. Motevalli, *Chem. Mater.*, 2001, **13**, 2103-2111.

57. A. Cygański and J. Kobyłecka, *Thermochim. Acta*, 1981, **45**, 65-77.

58. Q. F. Han, J. Chen, X. J. Yang, L. Lu and X. Wang, *J. Phys. Chem. C*, 2007, **111**, 14072-14077.

59. T. Alqahtani, M. D. Khan, D. J. Kelly, S. J. Haigh, D. J. Lewis and P. O’Brien, *J. Mater. Chem. C*, 2018, **6**, 12652-12659.

60. Y. W. Koh, C. S. Lai, A. Y. Du, E. R. T. Tiekink and K. P. Loh, *Chem. Mater.*, 2003, **15**, 4544-4554.

61. G. Xie, Z. P. Qiao, M. H. Zeng, X. M. Chen and S. L. Gao, *Cryst. Growth Des.*, 2004, **4**, 513-516.

62. R. Nomura, K. Kanaya and H. Matsuda, *Bull. Chem. Soc. Jpn.*, 1989, **62**, 939-941.

63. M. Lalia-Kantouri and G. Manoussakis, *J. Therm. Anal.*, 1984, **29**, 1151-1169.

64. P. Boudjouk, M. P. Remington, D. G. Grier, B. R. Jarabek and G. J. McCarthy, *Inorg. Chem.*, 1998, **37**, 3538-3541.

65. M. Al-Shakban, P. D. Matthews, G. Deogratias, P. D. McNaughter, J. Raftery, I. Vitorica-Yrezabal, E. B. Mubofu and P. O'Brien, *Inorg. Chem.*, 2017, **56**, 9247-9254.

66. P. D. McNaughter, S. A. Saah, M. Akhtar, K. Abdulwahab, M. A. Malik, J. Raftery, J. A. M. Awudza and P. O'Brien, *Dalton Trans.*, 2016, **45**, 16345-16353.

67. E. R. Tiekink, *Main Group Met. Chem.*, 1994, **17**, 727-736.
68. M. Snow and E. Tiekink, *Aust. J. Chem.*, 1987, **40**, 743-750.
69. B. F. Hoskins, E. R. Tienkink and G. Winter, *Inorg. Chem. Acta*, 1984, **81**, L33-L34.
70. M. Cox and E. Tiekink, *Zeitschrift für Kristallographie-New Cryst. Struct.*, 1998, **213**, 561-562.
71. C. Raston, A. White and G. Winter, *Aust. J. Chem.*, 1978, **31**, 2207-2212.
72. A. ur Rehman, S. Ali, G. Kociok-Köhn and K. Molloy, *J. Mol. Struct.*, 2009, **937**, 56-60.
73. S. S. Sun, Q. F. Han, X. D. Wu, J. W. Zhu and X. Wang, *Mater. Lett.*, 2011, **65**, 3344-3347.
74. J. L. Wu, F. Qin, G. Cheng, H. Li, J. H. Zhang, Y. P. Xie, H. J. Yang, Z. Lu, X. L. Yu and R. Chen, *J. Alloys Compd.*, 2011, **509**, 2116-2126.
75. O. C. Monteiro and T. Trindade, *J. Mater. Sci. Lett.*, 2000, **19**, 859-861.
76. W. N. Kun, S. Mlowe, L. D. Nyamen, P. T. Ndifon, M. A. Malik, O. Q. Munro and N. Revaprasadu, *Chem. Eur. J.*, 2016, **22**, 13127-13135.
77. K. R. Chaudhari, N. Yadav, A. Wadawale, V. K. Jain and R. Bohra, *Inorg. Chem. Acta*, 2010, **363**, 375-380.
78. R. Chauhan, J. Chaturvedi, M. Trivedi, J. Singh, K. C. Molloy, G. Kociok-Kohn, D. P. Amalnerkar and A. Kumar, *Inorg. Chem. Acta*, 2015, **430**, 168-175.
79. H. Q. Cao, G. Z. Wang, J. H. Warner and A. A. R. Watt, *Appl. Phys. Lett.*, 2008, **92**, 013110.
80. H. Cao, X. Qiu, B. Luo, Y. Liang, Y. Zhang, R. Tan, M. Zhao and Q. Zhu, *Adv. Funct. Mater.*, 2004, **14**, 243-246.
81. Y. J. Xiao, H. Q. Cao, K. Y. Liu, S. C. Zhang and V. Chernow, *Nanotechnology*, 2010, **21**, 145601.
82. J. Grigas, E. Talik and V. Lazauskas, *Phys. Status Solidi B*, 2002, **232**, 220-230.
83. E. Miniach and G. Gryglewicz, *J. Mater. Sci.*, 2018, **53**, 16511-16523.
84. Z. Quan, J. Yang, P. P. Yang, Z. L. Wang, C. X. Li and J. Lin, *Cryst. Growth Des.*, 2008, **8**, 200-207.

3.4.7. Electronic Supporting information

Table S.3-3 Data from TGA profiles of bismuth (III) alkylxanthate; ethyl, propyl, butyl and hexyl at 250, 300 and 350 °C under nitrogen.

Compound	Decomp. range (°C)	Expected percentage weight, %	Found percentage weight, %
(2)	115-295	31.20	30.90
(3)	110-315	29.20	28.78
(5)	120-300	27.50	27.30
(8)	95-311	24.5	27.00

Table S.3-4 Selected bond lengths and angles for complexes 4 and 6.

Bond Length (Å)	4	6
Bi-S1	2.8214(6)	2.9373(9)
Bi-S2	2.8195(6)	2.8240(9)
Bi-S3	2.8532(6)	2.9012(9)
Bi-S4	2.9509(6)	2.8569(10)
Bi-S5	2.8047(6)	2.8536(10)
Bi-S6	3.0353(6)	2.9708(9)
Bi-S7	3.0377(6)	2.8771(10)
Bi-S8	2.8304(6)	2.8969(9)
S1-C1	1.696(2)	1.684(4)
S2-C1	1.689(3)	1.700(4)
O1-C1	1.475(3)	1.470(5)
Bond Angle (°)		
S1-Bi-S2	63.528(17)	62.09(3)
S3-Bi-S4	61.929(17)	62.38(3)
S5-Bi-S6	61.151(17)	61.39(3)
S7-Bi-S8	123.54(15)	62.00(3)
S1-C-S2	122.60(14)	122.9(2)

Table S.3-5 Selected bond lengths and angles for complexes1, 2, 3, 5, 7 and 8.

Bond Length (Å)	**1**	**2**	**3**	**5**	**7**	**8**
Bi-S1	2.856(3)	2.839(5)	2.819(2)	2.8948(11)	2.9442(6)	2.9329(17)
Bi-S2	3.078(3)	2.862(5)	2.890(2)	2.9342(11)	2.8205(6)	2.8559(19)
Bi-S3	2.805(3)	2.871(5)	2.951(4)	2.9747(10)	2.8351(7)	2.854(2)
Bi-S4	2.857(3)	2.895(6)	2.752(7)	2.8709(11)	2.9299(7)	2.9435(18)
Bi-S5	3.078(3)	2.953(5)	2.893(3)	2.8640(10)	2.8742(7)	2.9155(18)
Bi-S6	2.770(3)	2.864(5)	2.987(6)	2.8452(11)	2.9414(7)	2.8529(18)
Bi-S7	2.952(3)	2.970(5)	2.979(6)	2.7765(10)	2.8990(6)	2.9119(18)
Bi-S8	2.817(3)	2.864(5)	2.9104(17)	2.9580(11)	2.8627(6)	2.8741(19)
S1-C1	1.709(12)	1.688(19)	1.682(8)	1.701(4)	1.680(3)	1.680(6)
S2-C1	1.672(12)	1.694(19)	1.677(9)	1.683(4)	1.695(3)	1.699(6)
O1-C1	1.336(14)	1.31(2)	1.337(10)	1.327(5	1.342(3)	1.459(7)
Bond Angle (°)	**1**	**2**	**3**	**5**	**7**	**8**
S1-Bi-S2	60.64(8)	62.72(14)	62.51(6)	61.45(3)	62.294(18)	61.86(5)
S3-Bi-S4	63.45(9)	62.13(16)	62.61(13)	61.38(3)	62.33(2)	61.68(5)
S5-Bi-S6	61.53(8)	61.69(15)	60.40(12)	62.85(3)	61.710(19)	62.14(5)
S7-Bi-S8	62.45(8)	61.21(16)	61.62(10)	62.67(3)	62.489(18)	61.88(5)
S1-C-S2	125.2(7)	122.7(11)	123.8(5)	123.3(3)	124.29(15)	123.5(4)

Table S.3-6 Crystallographic data for complexes (1-4).

Compound		**1**	**2**	**3**	**4**
Empirical formula		$C_{16}H_{32}BiNO_4S_8$	$C_{20}H_{40}BiNO_4S_8$	$C_{24}H_{48}BiNO_4S_8$	$C_{24}H_{48}BiNO_4S_8$
Formula weight		767.88	823.99	880.09	880.09
Temperature (K)		150.02	150.01	150.01	150.01
Crystal system		triclinic	monoclinic	monoclinic	orthorhombic
Space group		P-1	C2	$P2_1/n$	Pbca
Unit cell dimensions	a (Å)	10.4004(6)	19.6815(7)	12.7509(4)	18.4522(2)
	b (Å)	13.1951(6)	11.1950(3)	21.8552(7)	17.9406(2)
	c (Å)	21.1681(9)	21.8091(8)	13.2421(4)	21.8487(2)
	α (°)	92.446(4)	90	90	90
	B (°)	97.454(4)	91.032(3)	93.974(3)	90
	γ (°)	96.475(4)	90	90	90
Volume ($Å^3$)		2857.2(2)	4804.5(3)	3681.36(18)	7232.87(13)
Z		4	6	4	8
Crystal size (mm^3)		0.4 × 0.3 × 0.1	0.3 × 0.2 × 0.08	0.11 × 0.1 × 0.02	0.08 × 0.07 × 0.07
Reflections collected		17475	13744	18886	33103
Independent reflections		17475[R_{int} =0.0442]	13744 [R_{int} = 0.0585]	6746 [R_{int} = 0.0368]	6922 [R_{int} = 0.0207]
Goodness-of-fit on F^2		1.066	1.055	1.034	1.136
R indices (all data)		R_1 = 0.0510, wR_2 = 0.1249	R_1 = 0.0471, wR_2 = 0.1176	R_1 = 0.0468, wR_2 = 0.1002	R_1 = 0.0205, wR_2 = 0.0429
R indices (all data)		R_1 = 0.0613, wR_2 = 0.1296	R_1 = 0.0542, wR_2 = 0.1227	R_1 = 0.0697, wR_2 = 0.1088	R_1 = 0.0222, wR_2 = 0.0436

Table S.3-7 Crystallographic data for complexes (5-8).

Compound		**5**	**6**	**7**	**8**
Empirical formula		$C_{28}H_{56}BiNO_4S_8$	$C_{28}H_{56}BiNO_4S_8$	$C_{32}H_{64}BiNO_4S_8$	$C_{36}H_{72}BiNO_4S_8$
Formula weight		936.19	936.19	992.30	1048.40
Temperature (K)		150.00	150.01	150.00	239.98
Crystal system		monoclinic	triclinic	triclinic	monoclinic
Space group		$P2_1/c$	P-1	P-1	$P2_1/n$
Unit cell dimensions	a (Å)	12.6662(4)	12.7369(3)	12.8750(3)	13.0366(3)
	b (Å)	16.8093(4)	13.2430(3)	13.0923(3)	29.5486(9)
	c (Å)	18.8040(5)	13.2763(3)	13.4876(3)	13.0888(3)
	α (°)	90	77.018(2)	86.102(2)	90
	B (°)	90	68.503(2)	81.637(2)	94.795(2)
	γ (°)	90	88.098(2)	85.026(2)	90
Volume ($Å^3$)		4003.56(19)	2027.36(9)	2237.33(9)	5024.3(2)
Z		4	2	2	4
Crystal size (mm^3)		0.4 × 0.15 × 0.15	0.25 × 0.25 × 0.1	0.241 × 0.127 × 0.033	0.3 × 0.25 × 0.05
Reflections collected		29539	46375	23800	68051
Independent reflections		7333 [$R_{int} = 0.0405$]	7413 [$R_{int} = 0.0282$]	9041 [$R_{int} = 0.0221$]	13158 [$R_{int} = 0.0603$]
Goodness-of-fit on F^2		1.021	1.039	1.103	1.145
Final R indices [$I>2\sigma(I)$]		$R_1 = 0.0304$, $wR_2 = 0.0664$	$R_1 = 0.0239$, $wR_2 = 0.0553$	$R_1 = 0.0207$, $wR_2 = 0.0545$	$R_1 = 0.0763$, $wR_2 = 0.1077$
R indices (all data)		$R_1 = 0.0382$, $wR_2 = 0.0690$	$R_1 = 0.0265$, $wR_2 = 0.0561$	$R_1 = 0.0216$, $wR_2 = 0.0548$	$R_1 = 0.1329$, $wR_2 = 0.1204$

Table S.3-8 Elemental composition of Bi and S in bismuth sulfide powder formed from the pyrolysis of bismuth (III) alkylxanthate; ethyl, propyl, butyl and hexyl at 250, 300 and 350 °C under nitrogen using EDX.

R	Temp (°C)	Bi%	S%	Rato Bi:S
Ethyl	250	39.81 ± 0.5	60.19 ± 0.4	2 : 3
	300	39.69 ± 0.7	60.31 ± 0.8	2 : 3
	350	38.84 ± 1.7	61.16 ± 1.5	2 : 3
n-propyl	250	40.97 ± 0.9	59.03 ± 2.0	2 : 2.8
	300	39.66 ± 1.2	60.34 ± 3.5	2 : 3
	350	40.28 ± 2.7	59.72 ± 1.3	2 : 2.9
n-butyl	250	40.4 ± 1.7	59.6 ± 0.9	2 : 2.9
	300	44.9 ± 1.5	55.1 ± 3.2	2 : 2.5
	350	41.8 ± 0.7	58.2 ± 2.1	2 : 2.8
Hexyl	250	42.1 ± 1.9	57.9 ± 1.7	2 : 2.7
	300	42.2 ± 2.1	57.8 ± 2.3	2 : 2.7
	350	42.5 ± 2.5	57.5 ± 1.5	2 : 2.7

Table S.3-9 Elemental composition of Bi and S in bismuth sulfide powder formed from the pyrolysis of bismuth (III) alkylxanthate; ethyl, propyl, butyl and hexyl at 250, 300 and 350 °C under nitrogen, using ICP-(OES).

R	Temp (°C)	Bi%	S%
Ethyl	250	68.24	17.52
	300	67.87	14.71
	350	70.47	14.92
n-propyl	250	83.23	15.57
	300	80.01	17.21
	350	77.52	16.12
n-butyl	250	81.51	13.92
	300	83.36	13.65
	350	81.97	13.57
Hexyl	250	83.11	14.23
	300	84.29	13.29
	350	83.77	14.37

Table S.3-10 The estimated bandgap of prepared Bi_2S_3 nanoparticles at different conditions.

R	Temp (°C)	Bandgap
Ethyl	250	1.16 ± (0.05)
	300	1.18 ± (0.05)
	350	1.15 ± (0.02)
n-propyl	250	1.16 ± (0.03)
	300	1.16 ± (0.01)
	350	1.17± (0.02)
n-butyl	250	1.17± (0.03)
	300	1.17± (0.01)
	350	1.19± (0.02)
n-Hexyl	250	1.16± (0.01)
	300	1.16± (0.03)
	350	1.17± (0.02)

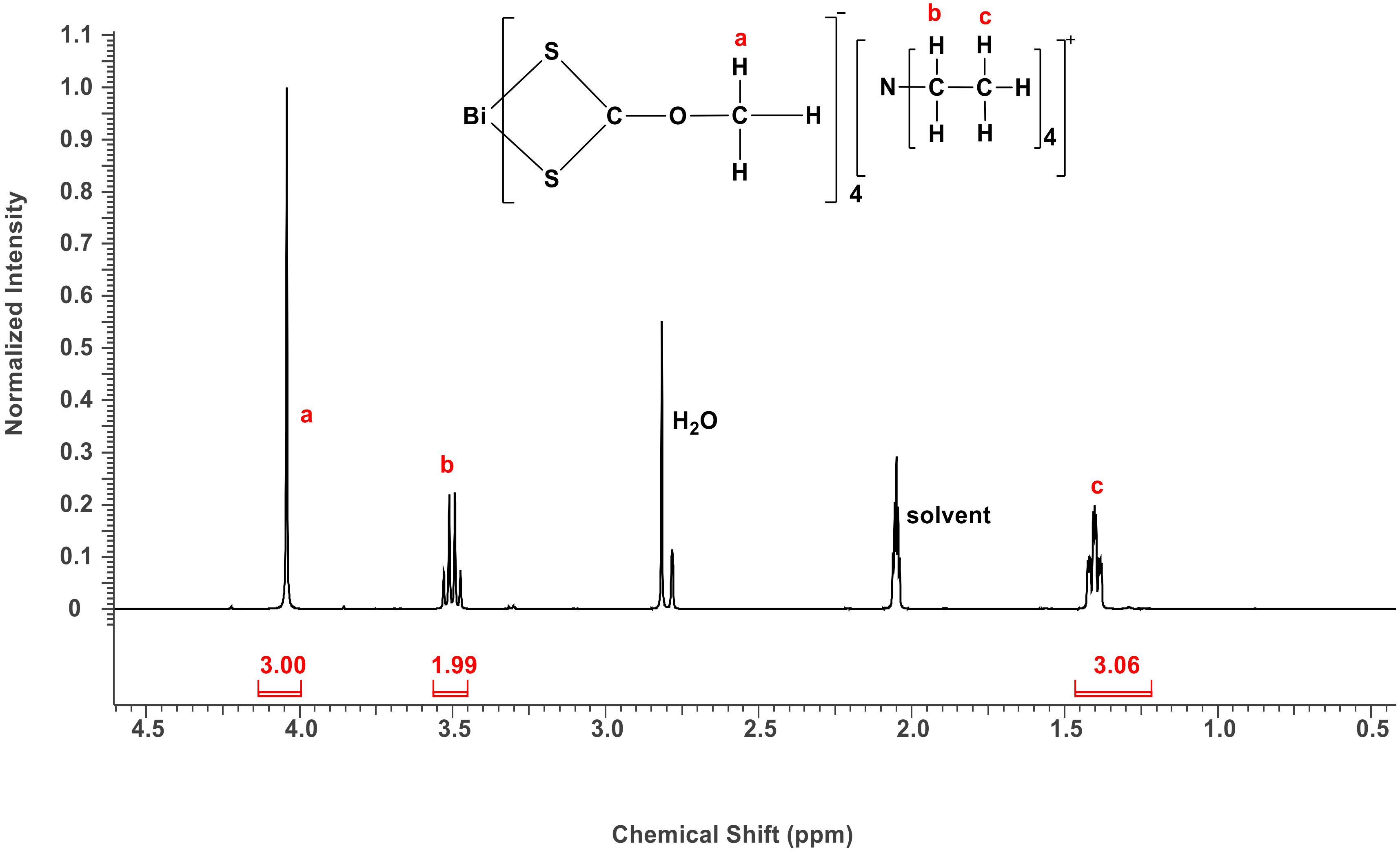

Figure.S.3.9 ^{1}H NMR spectrum of complex (1).

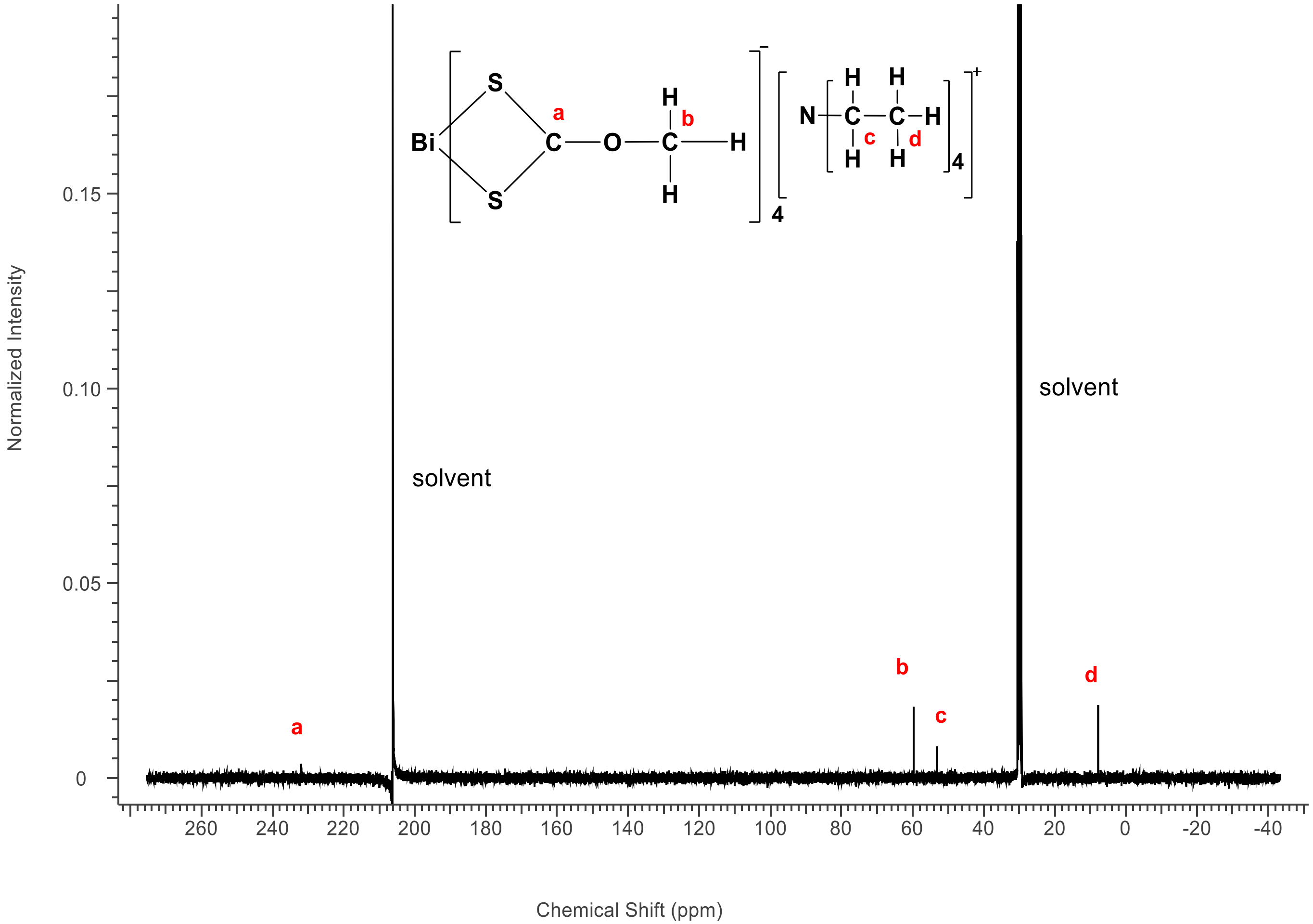

Figure.S.3.10 ^{13}C NMR spectrum of complex (1).

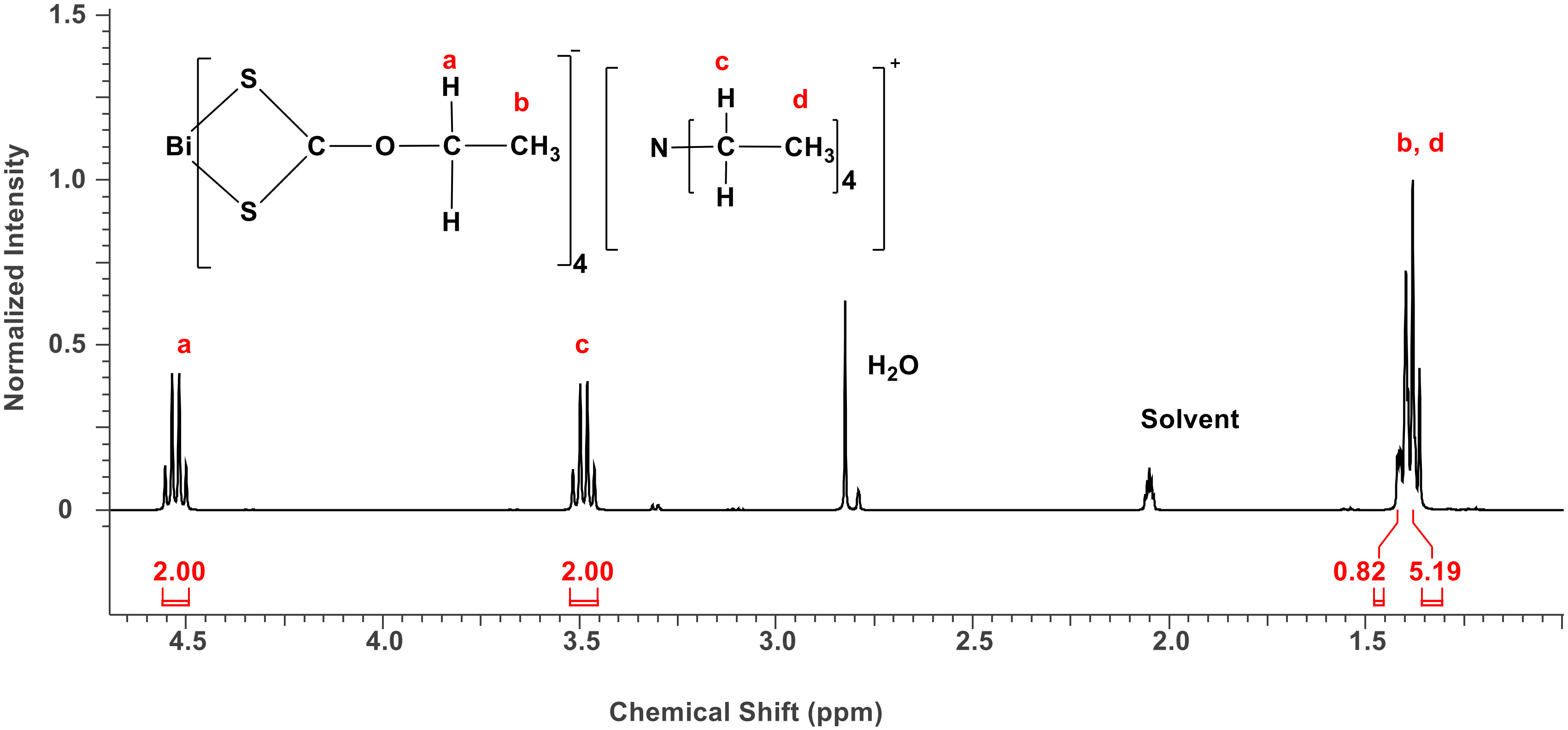

Figure.S.3.11 ^{1}H NMR spectrum of complex (2).

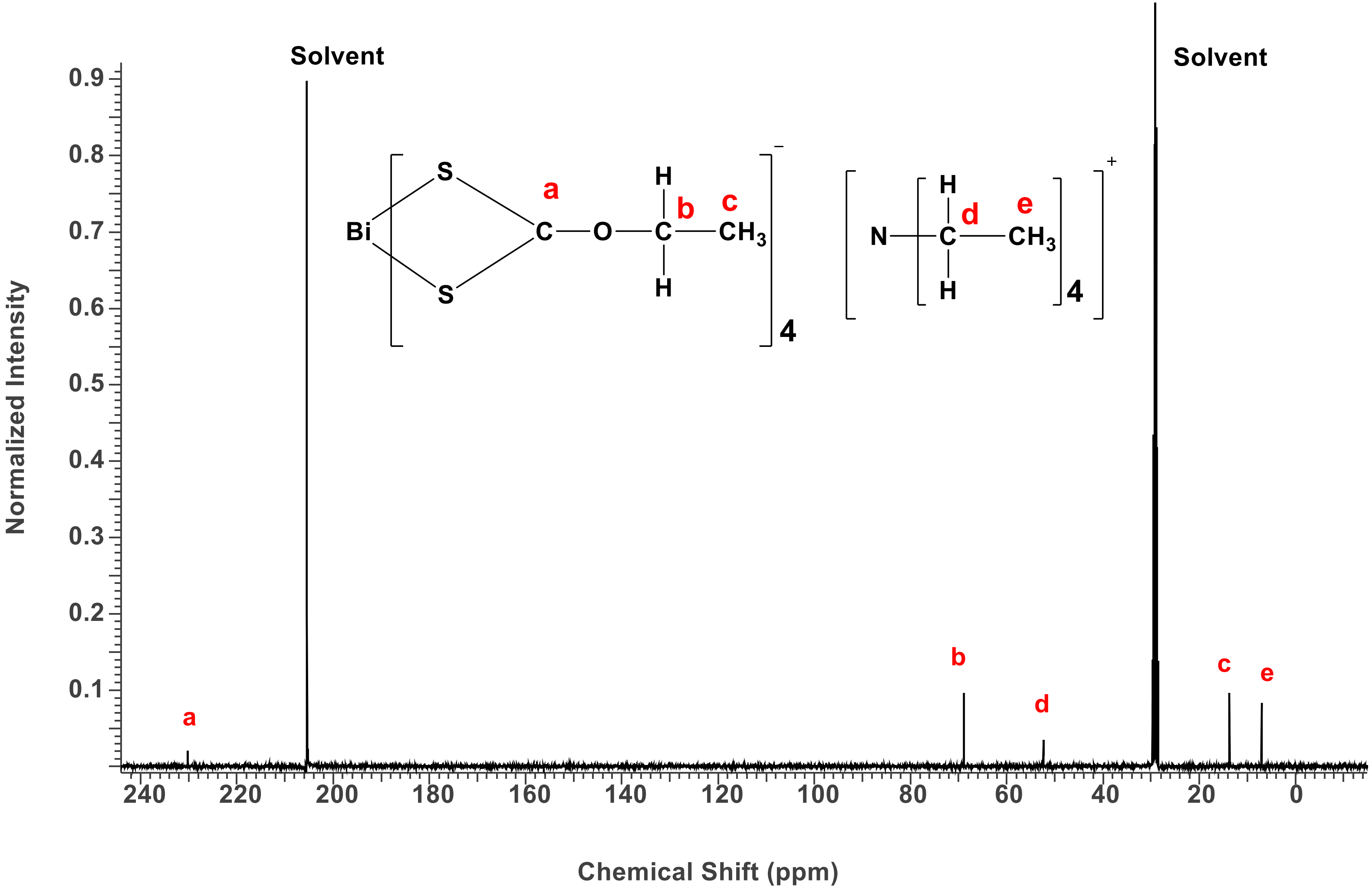

Figure.S.3.12^{13}C NMR spectrum of complex (2).

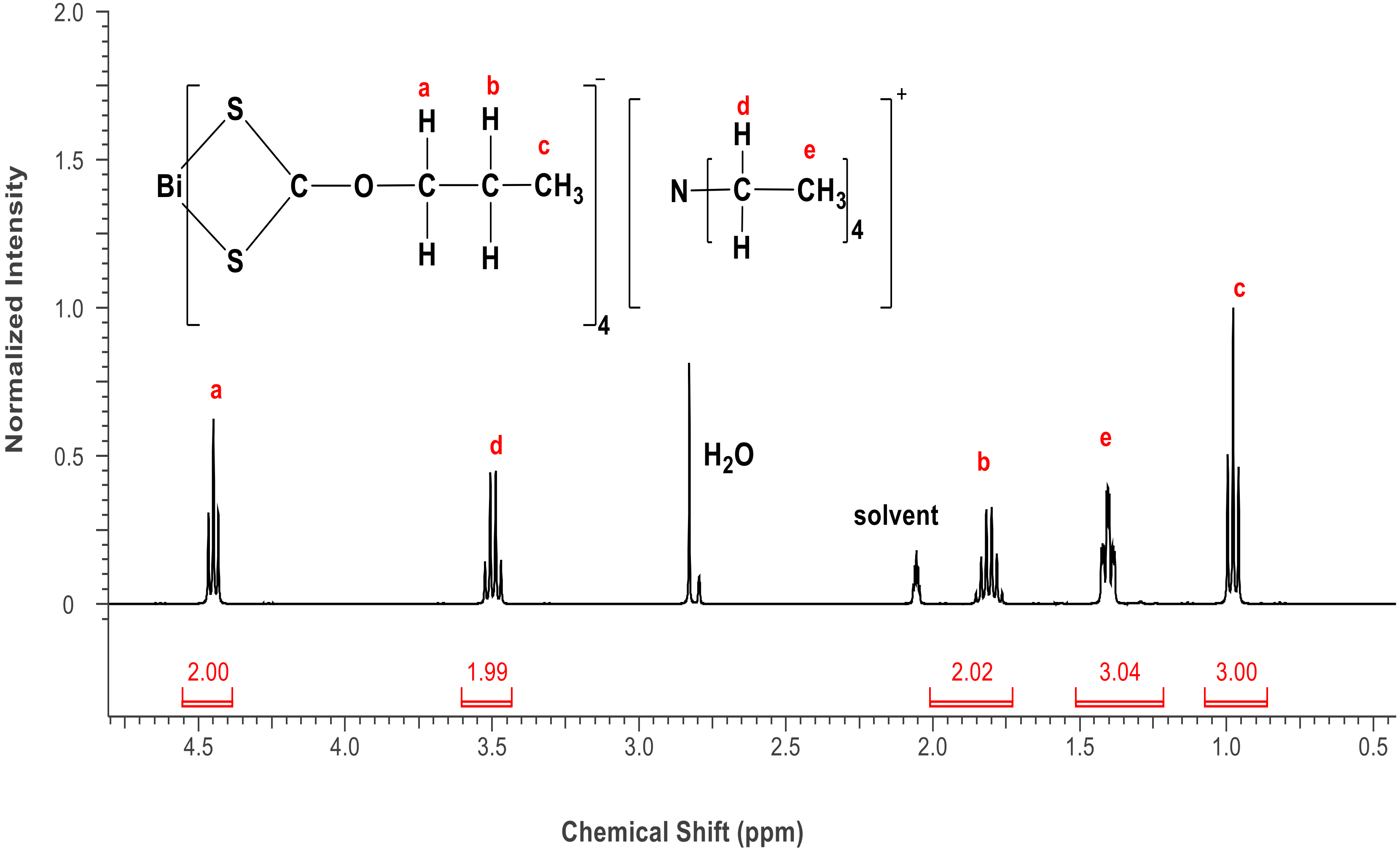

Figure.S.3.13 ^{1}H NMR spectrum of complex (3).

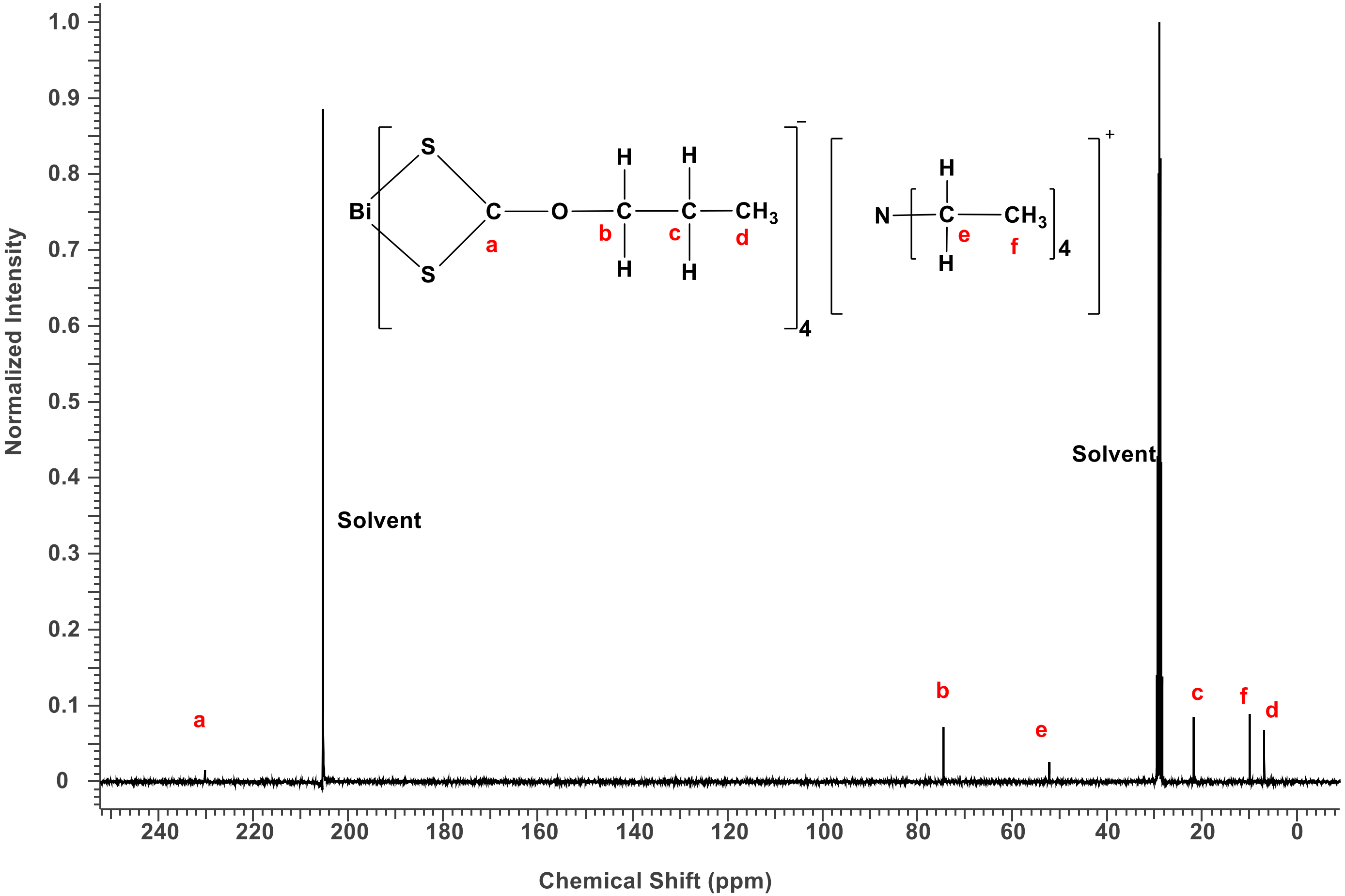

Figure.S.3.14 ^{13}C NMR spectrum of complex (3).

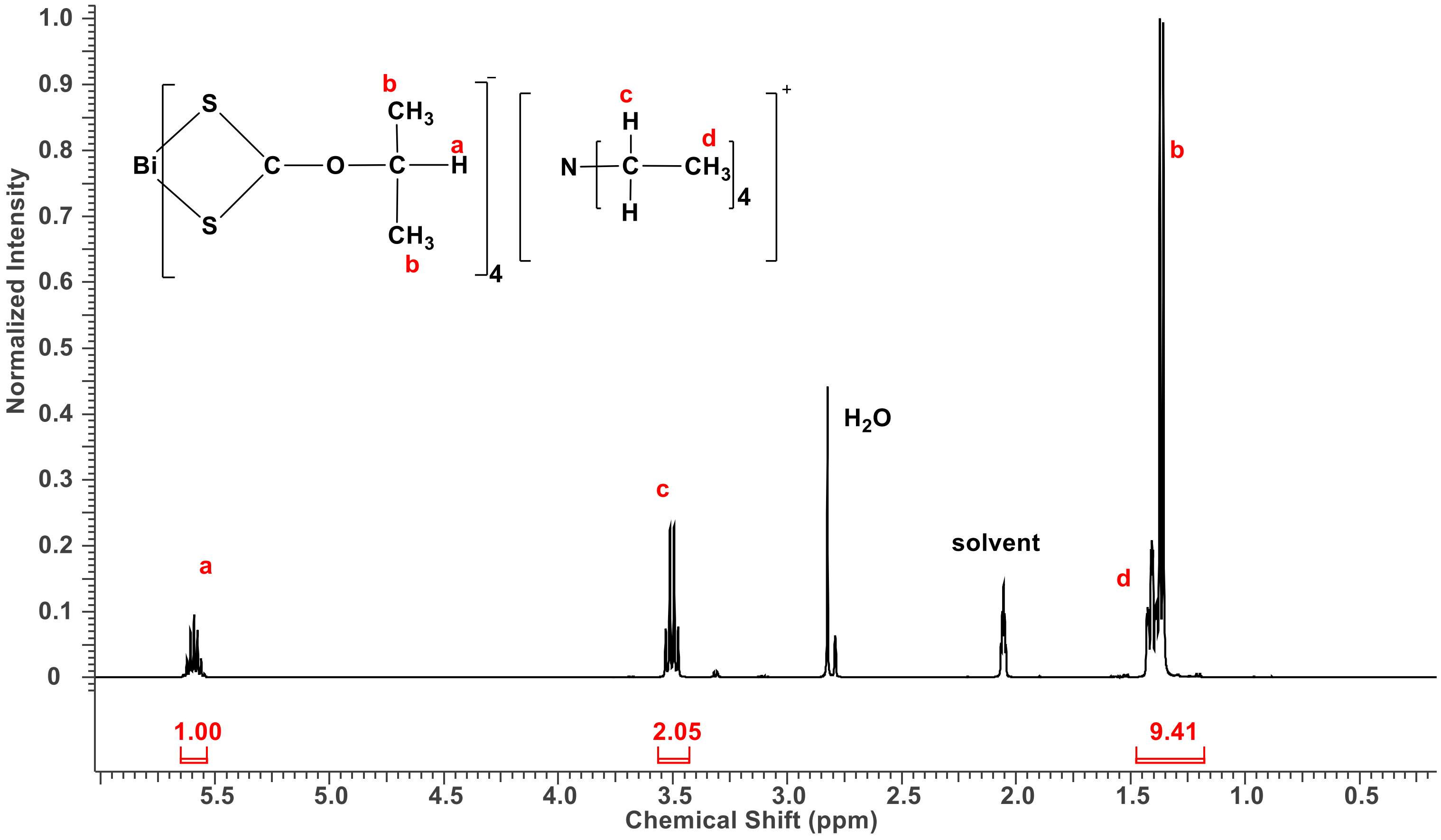

Figure.S.3.15 ^{1}H NMR spectrum of complex (4).

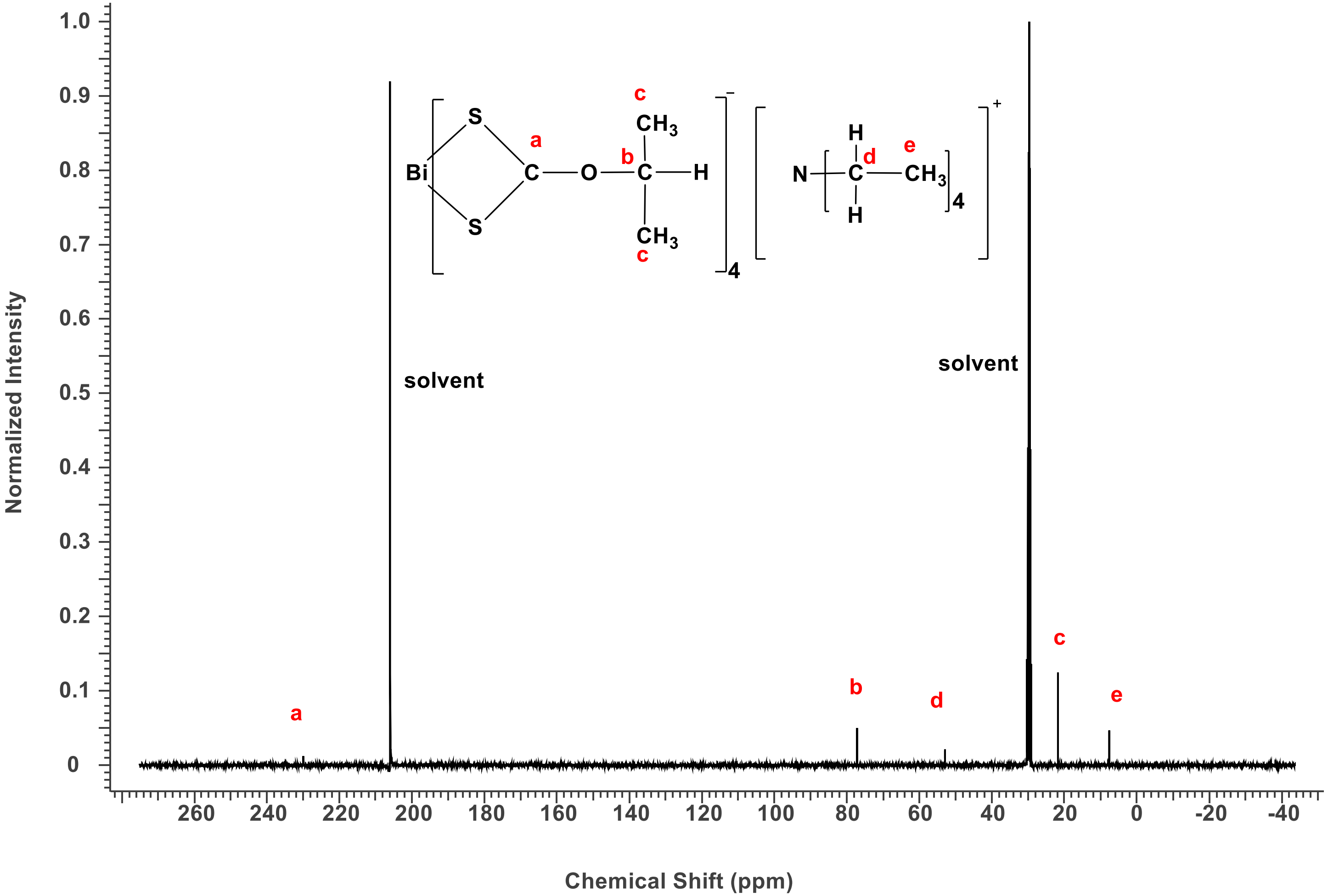

Figure.S.3.16 ^{13}C NMR spectrum of complex (4).

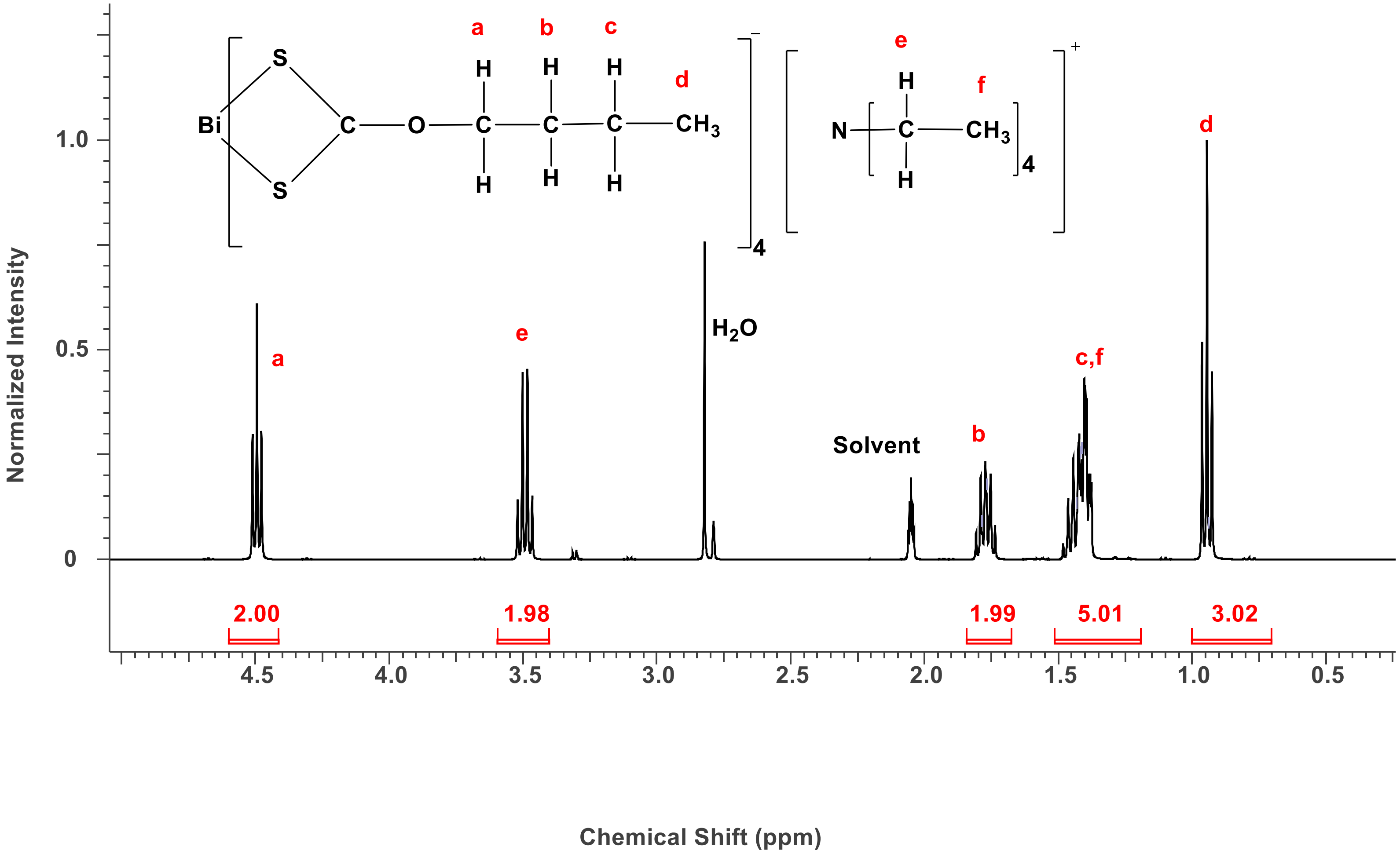

Figure.S.3.17 ^{1}H NMR spectrum of complex (5).

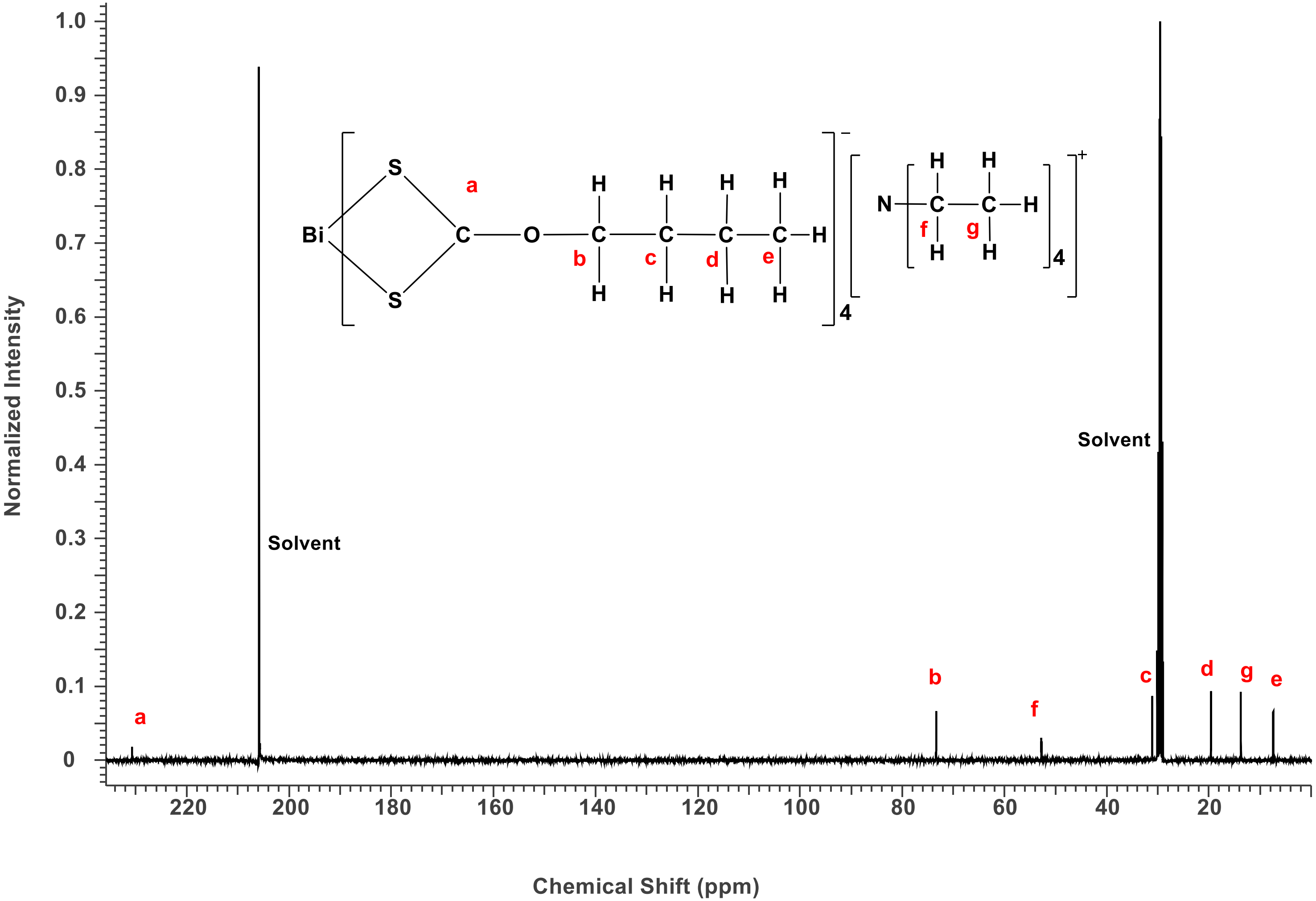

Figure.S.3.18 ^{13}C NMR spectrum of complex (5).

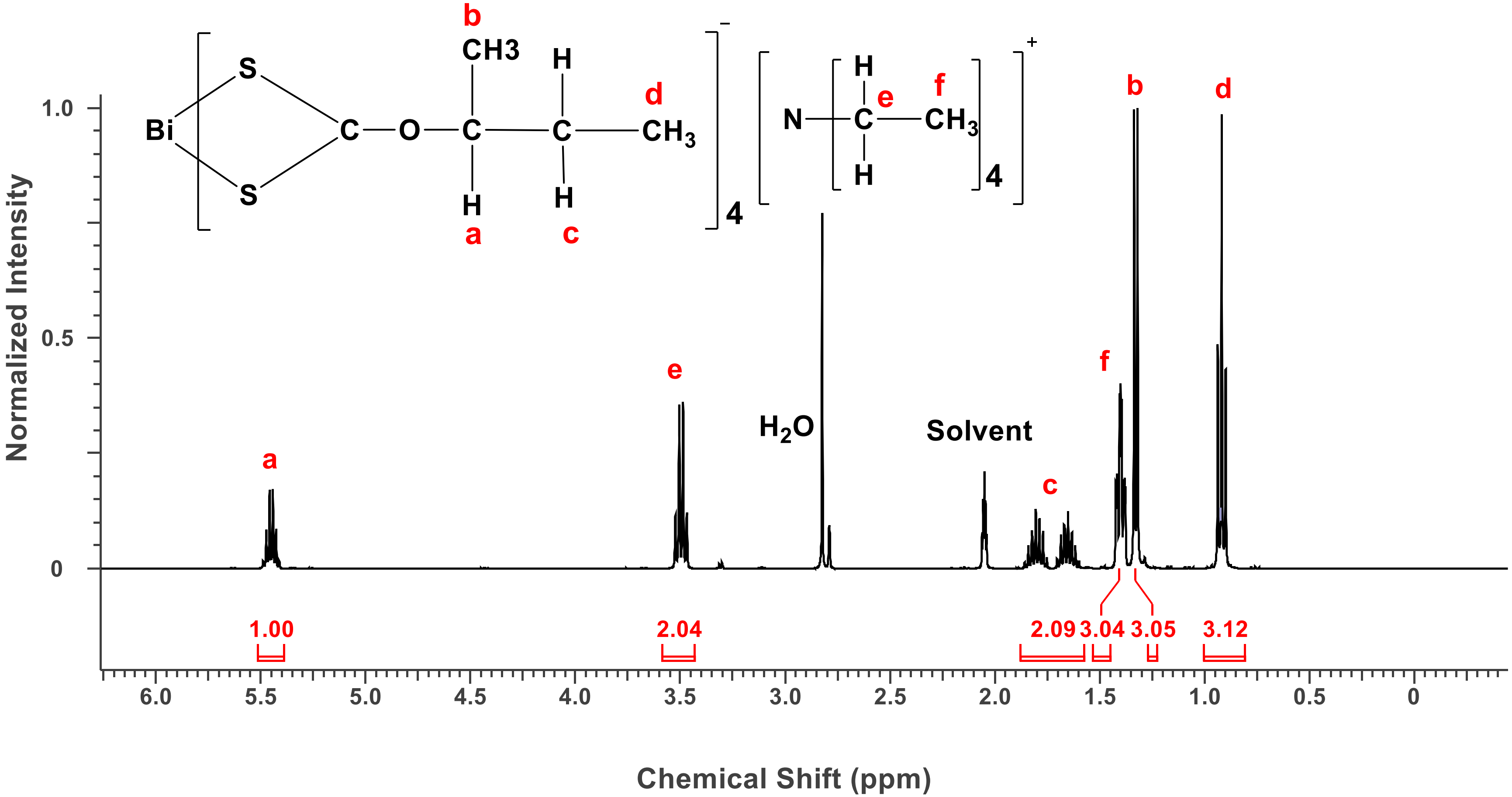

Figure.S.3.19 ^{1}H NMR spectrum of complex (6).

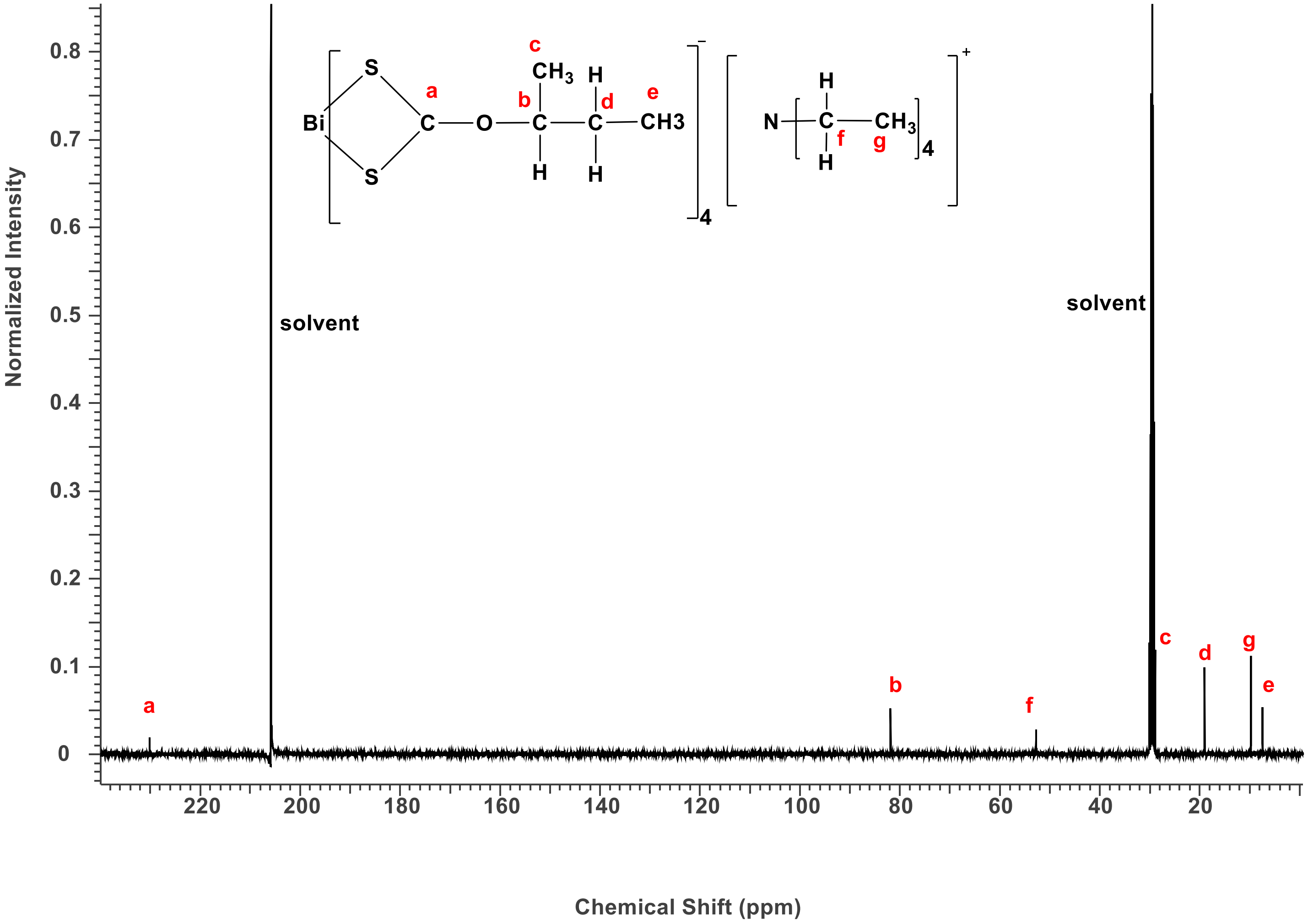

Figure.S.3.20 ^{13}C NMR spectrum of complex (6).

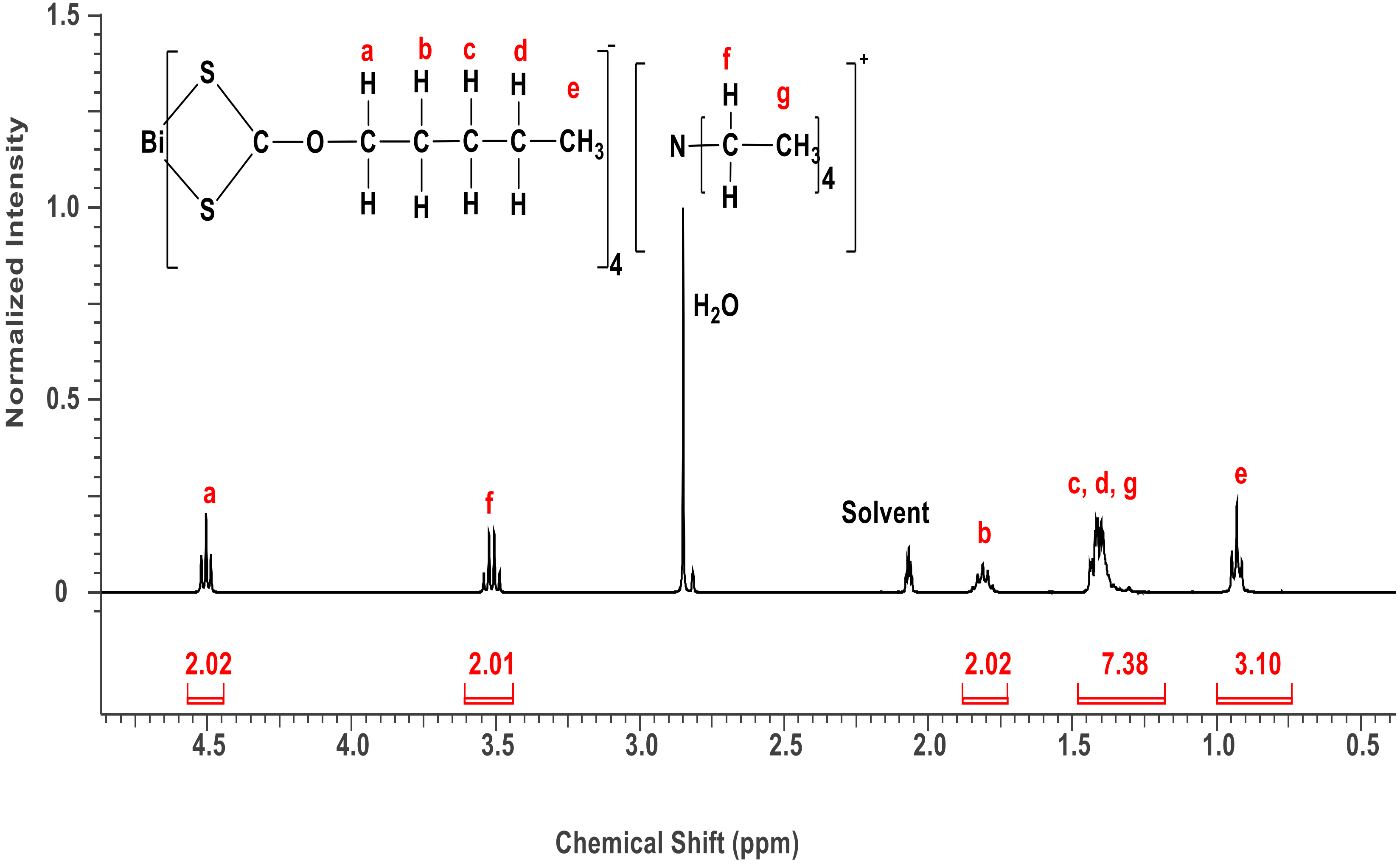

Figure.S.3.21 ^{1}H NMR spectrum of complex (7).

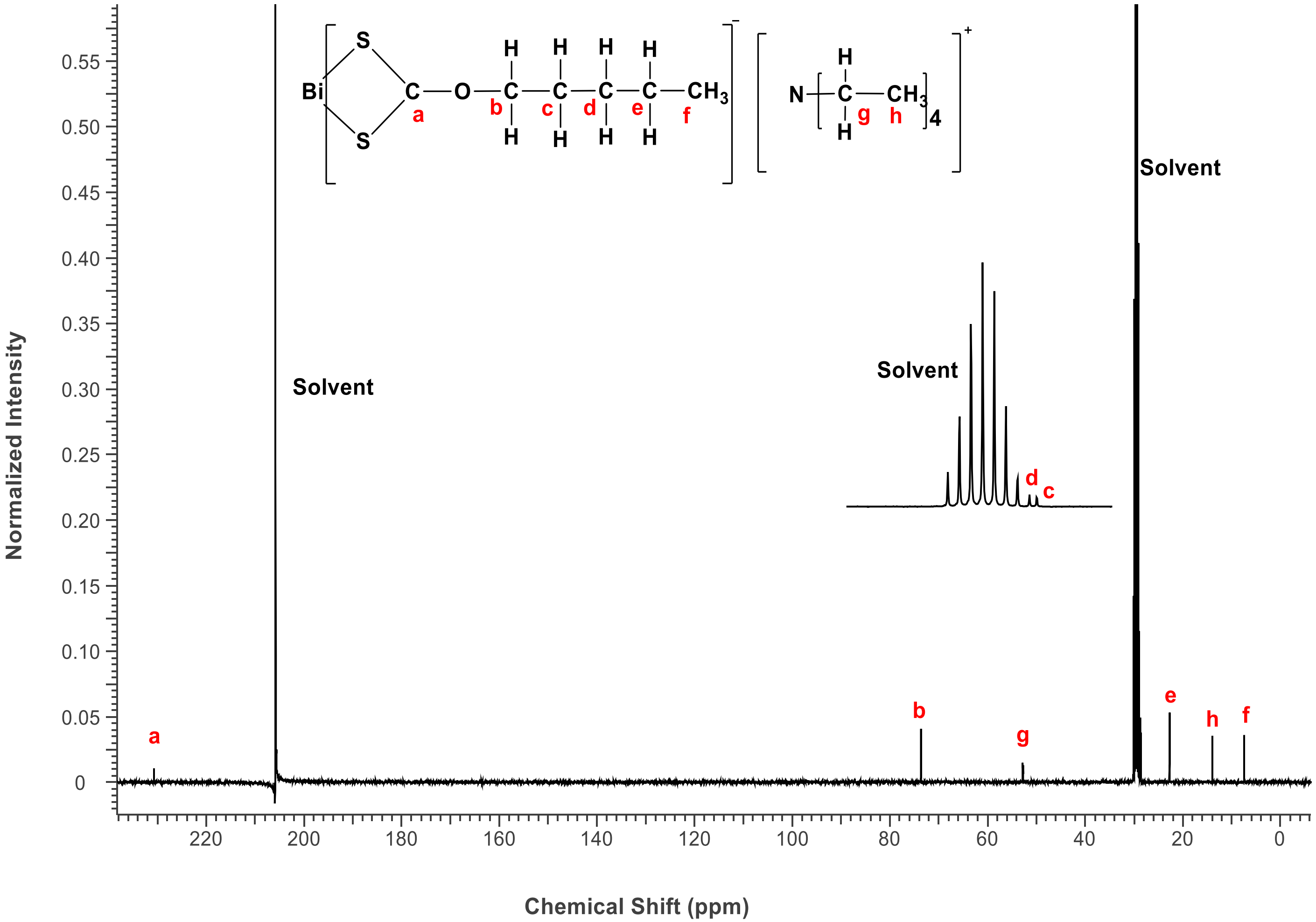

Figure.S.3.22 ^{13}C NMR spectrum of complex (7).

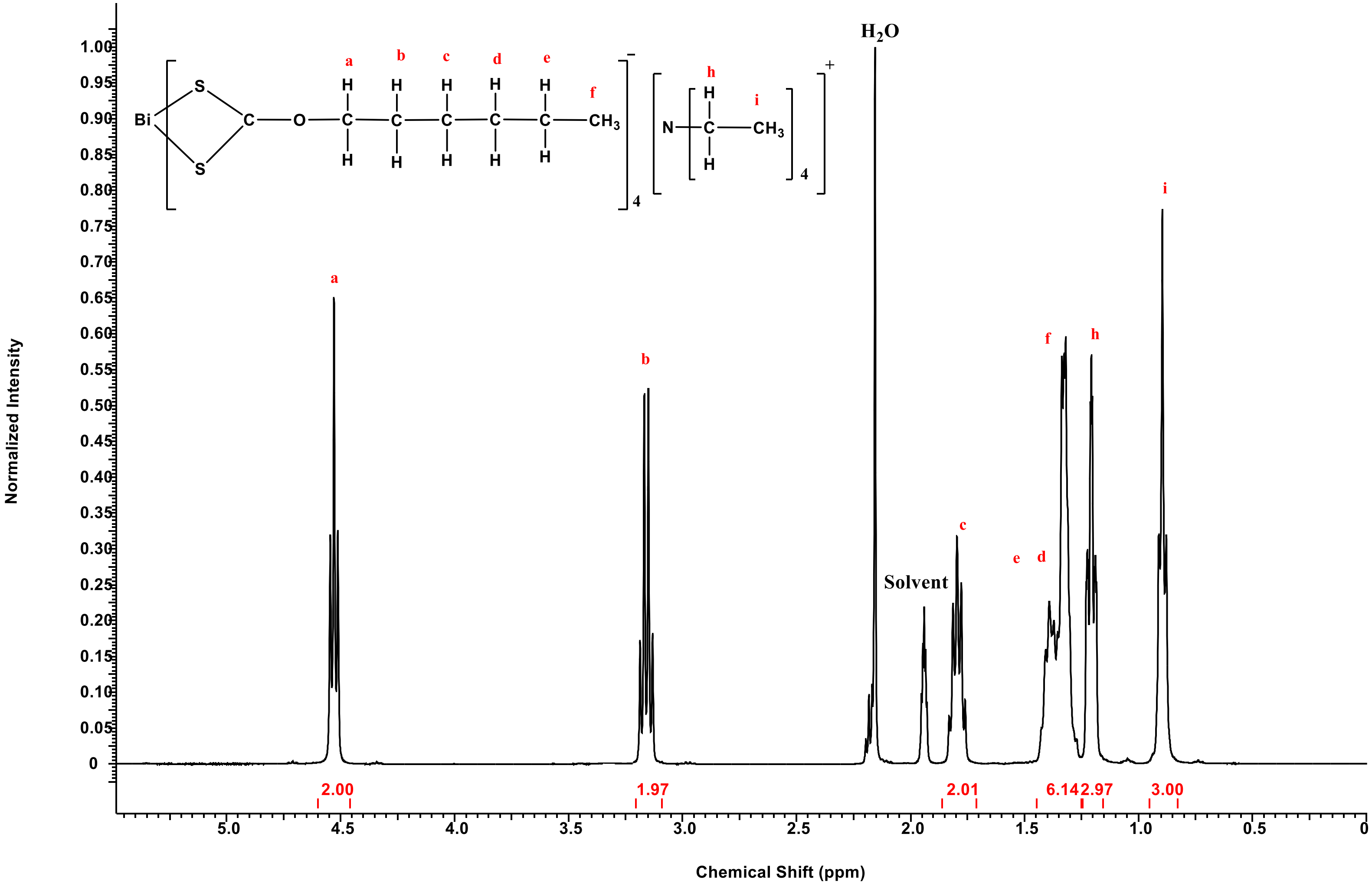

Figure.S.3.23 ^1H NMR spectrum of complex (8).

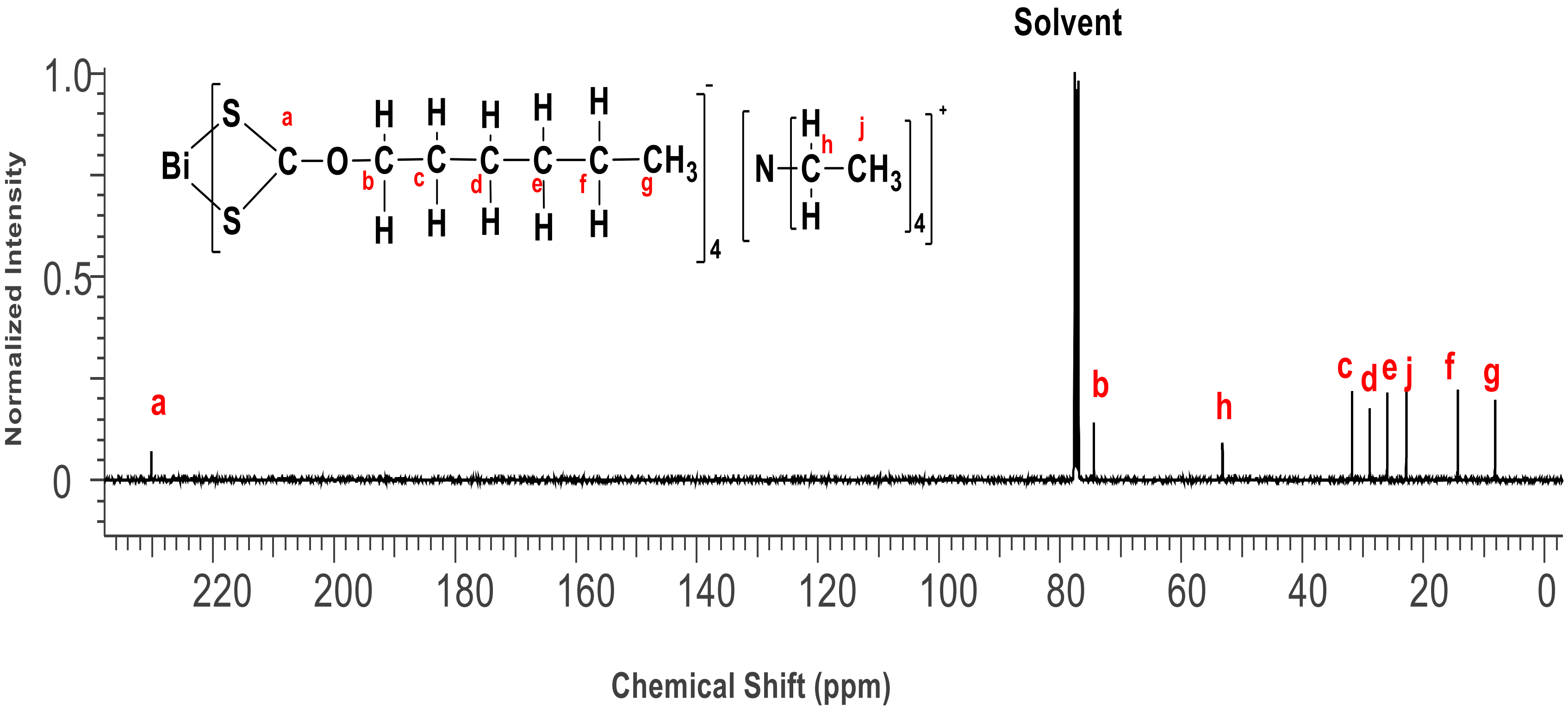

Figure.S.3.24 ^{13}C NMR spectrum of complex (8).

Chapter 4. The Deposition of Lead Sulfide (PbS) on Cellulose Substrates.

4.1. Introduction

The fabricating of solar cells on flexible substrates is not novel. The first flexible solar cell was made in the 1960s for space power applications. The cell was made of thin silicon wafers about (180 mm) on plastic substrates to provide mechanical support. In 2005 Lamprecht *et al*. reported for the first time the deposition of organic photodiodes on ordinary newspaper sheets.[1] Cellulose-based substrates have attracted extensive attention due to biocompatible, biodegradable flexible, foldable and recyclable compared with the most plastic substrates.[2,3] PbS nanoparticles have been used widely in many applications such as sensors, infrared optoelectronic, optical switches and solar cells.[4, 5] Cellulose paper is highly transparent in the IR region, where PbS NPs is highly absorbent into IR zoon. The optical properties of cellulose paper could be changed by the deposition of PbS NPs. The purpose of this work is to present a simple and fast method for the deposition of metal sulfide on cellulose substrate, which could be useful in the construction of flexible solar cell. Lead (III) xanthate complexes with the formula [$Pb(S_2COR)_2$] where R = alkyl, ethyl, n-propyl, n-butyl, and n-hexyl have been synthesised and characterised. The use of these complexes as single-source precursors for the deposition of PbSNPs on cellulose-based substrates was investigated. The optical properties of the deposited film have been studied.

4.2. Author distribution

In this work, the project idea provided by Paul O'Brien and all the experimental work was done in his laboratory. The synthesis and characterise of lead (III) xanthate, and the deposition of PbS NPs on cellulose-based substrates by the thermal decomposition of lead (III) xanthate complexes on 200 °C under nitrogen for 1h was carried out by me. Yasser T Alharbi helps in the synthesis of lead (II) n-propylxanthate. Paul D. Mcnaughter and David Lewis edited the draft.

4.3. References

1. B. Lamprecht, R. Thünauer, M. Ostermann, G. Jakopic and G. Leising, *Phys. Status Solidi A*, 2005, **202**, R50-R52.
2. R. S. Krishnan and R. K. Shankar, *J. Raman Spectrosc.*, 1981, **10**, 1-8.
3. R. Martins, I. Ferreira and E. Fortunato, *Phys. Status Solidi RRL,* 2011, **5**, 332-335.
4. S. A. McDonald, G. Konstantatos, S. Zhang, P. W. Cyr, E. J. D. Klem, L. Levina and E. H. Sargent, *Nat. Mater.*, 2005, **4**, 138-142.
5. K. W. Johnston, A. G. Pattantyus-Abraham, J. P. Clifford, S. H. Myrskog, D. D. MacNeil, L. Levina and E. H. Sargent, *Appl. Phys. Lett.*, 2008, **92**, 151115.

4.4. Manuscript: The Deposition of Lead Sulfide (PbS) on Cellulose Substrates.

Thamer S Alraddadi,[a] Yasser T Alharbi,[a] Paul D. McNaughter, [a] Paul O'Brien[a,b] and David Lewis.[b*]

4.4.1. Abstract

This work demonstrates a fast and low reaction temperature technique as a fabrication method for the deposition of lead sulfide nanoparticles embedded in the cellulose substrates. Using the low-temperature thermal decomposition of lead(II) alky xanthates as single-source precursors (SSPs) it was possible to observe the tuning of the bandgap by variation of the alkyl group length.

---

[a] School of Chemistry, The University of Manchester, Oxford Road M13 9PL, UK.

[b] School of Materials, The University of Manchester, Oxford Road M13 9PL, UK

*Corresponding author: david.lewis-4@manchester.ac.uk ; Tel: +44 (0)1613063561.

4.4.2. Introduction

The research into fabrication and manipulation of flexible electronics is an emerging and exciting research field for many applications, including batteries,[1-4] solar cells,[5-7] sensors,[8-10] displays,[11-13] personal objects and implantable medical devices.[14-17] These developing applications will require materials that possess high conductivities and flexibilities. Plastic materials such as polyethylene terephthalate (PET), polyethylene naphthalate (PEN), polycarbonate (PC), and polyimide (PI) have been developed as the first-generation of substrate materials for a wide range of flexible electronics and have significantly advanced the growth of this area.[18-24] However, there are still limitations of using plastic as substrates, for instance, the probability of irreversible shape changes during the thermal processing due to the high coefficient of thermal expansion (CTE) in most plastics[25]. More importantly, the biodegradability, less environmentally friendly, poor printability, recyclability, and cost-effectiveness of petroleum-based substrates are affecting their development and adding burden to the environment.[26] The rapid development of consumer electronics increased the demand for scalable and environmentally-friendly substrate materials that could be manufactured at low cost.

Cellulose and its derivatives are alternative substrates. Cellulose is long-chain biopolymer consist of β-1,4-glycosidic link D-glucose units Figure 4.1.[27] Cellulose-based materials have received great attention due to good mechanical properties, printability, flexibility, biodegradability biocompatibility and low cost.[28-31] However, there are some disadvantages of using the cellulose as substrate; such as surface roughness and porosity which will require reengineering the cellulose to be compatible with the intended application. Extensive research has been undertaken in the exploratory fabrication of using cellulose materials as substrates.[7, 17, 25, 28, 29, 32, 33] For example, Yei and co-workers reported the fabrication of high-performance green flexible electronics utilizing cellulose nanofibril paper.[28] Another group successfully introduced a new type of cellulose nanofibers as a replacement to ordinary micro-meter sized paper cellulose pulp fibers.[22] Different studies investigated the use of cellulose for energy storage and photovoltaic applications.[34-36]

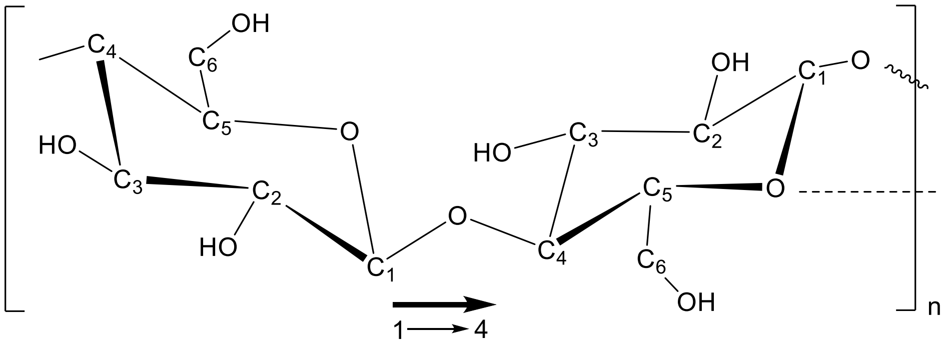

Figure 4.1 Structure of cellulose.

The combinations of polymers with nanoscale inorganic semiconductors has gained great interest recently.[37-39] The flexibility, diversity and processability of organic compounds together with the high performance electronic and optoelectronic properties of inorganic materials make it highly possible to manufacture inexpensive and high-performance electronic and optoelectronic devices in applications such as photovoltaics,[40] lighting,[41, 42] displays,[43] and sensing.[44, 45] Various forms of organic polymers and their derivatives such as poly(*p*-phenylenevinylene) (PPV),[46-49] polythiophene (PT),[50, 51] polyanilines (PANI),[52] and cellulose,[17, 25, 28, 29] have been conjugated with different inorganic materials including Cu, ZnO, CdSe, CdS, TiO_2, ZnS etc. [17, 25, 49-51] There is a considerable amount of literature on combining the cellulose with inorganic materials.[53-57] Yang *et al.* illustrate a simple low cost and scalable solution-processing method to design of highly conductive cellulose paper coated with Cu nanoparticles.[25] Another research team reported the UV-blocking properties of both cotton and silk fabrics coated with gold nanoparticles.[58] In another study, a research group reported the produce a cotton textile with photocatalytic properties by coating cotton with nitrogen-doped titanium dioxide (N-doped TiO_2).[59] A group of scientists also reported for the first time the fabrication of flexible and highly sensitive NO_2 gas sensors by the spin-cast technique of PbS colloidal quantum dots (CQDs) on paper substrate.[60]

Among the semiconductor nanomaterials, lead sulfide (PbS) is an important earth-abundant IV–VI semiconductor material, with cubic crystal structure. The direct narrow bandgap of (0.41 eV) at room temperature and large Bohr radius of 18 nm[61] make lead sulfide nanomaterials possesses a strong quantum size effect resulting in a large confinement energy.[62] PbS nanoparticles have been of great interest due to their unique chemical and physical properties arising from the size-tunable bandgap that covered entire solar spectrum range.[63] Additionally, it’s an attractive candidate for potential uses in a wide range of applications, like sensors, infrared optoelectronic, optical switches, solar cells, and biological imaging.[63-67] Thus, different synthetic routes have been reported the formation of PbS nanocrystals with different size and shape .[68-75]

Another promising scheme is use of single-source precursors (SSPs) to produce semiconductor nanomaterials,[76] such as lead sulfide,[68, 70] iron sulfide,[77, 78] indium sulfide,[79], tin sulfide,[80, 81] molybdenum sulfide,[82] cadmium sulfide,[83] bismuth sulfide[84] and copper sulfide.[85] A wide range of SSPs have been successfully used to synthesize lead sulfide including; xanthates,[68, 70] dithiocarbamates,[70, 86] dialkyldithiophosphates[87] and dichalcogenoimidophosphinates.[88]

Lead (II) xanthate complexes are interesting precursors because of their low melting points and pyrolysis temperatures. McNaughter *et al.* reported that the complete decomposition of lead (II) ethylxanthate to form lead sulfide occurred at 150 °C after 30 minutes.[68] Another advantage of lead (II) ethylxanthate is that the volatile by-products resulting from Chugaev decomposition help to control the growth of the nanocrystals.[68] Akhtar co-group successfully manged to deposited PbS films on plastic substrates (Kapton) at relatively low temperatures by aerosol-assisted chemical vapour deposition (AACVD) using lead (II) butylxanthate complex.[89] Despite the flexible properties offered by the polymer and plastic substrates, the inability to resist high temperatures hinders their usage. More importantly, in flexible solar cells fabrication, it is essential that the precursor decomposes at relatively low temperatures to prevent any damage to the substrates.[90] The capability of cellulose substrates to resist temperatures up to approximately 300 °C make it suitable for the deposition of PbS.[91, 92]

Cellulose substrate for example, filter paper has pores size of 6-20 µm which make this material highly transparent in the IR range. On the other hand, PbS nanoparticles have high absorption in that range. The possibility of changing the optical behaviour of the cellulose substrate by the deposition of PbS on the surface is interesting for the fabrication of flexible electronics that could be used in many application such as sensors and infrared optoelectronic.

This work presents a low cost, simple and fast approach for the growth of PbS nanoparticles on a flexible substrate, employing the thermolysis of lead(II) alkyxanthate as single-source precursor (SSPs). Lead(II) alkyxanthate with different alky group (R= ethyl, propyl, butyl and hexyl) were synthesised and successfully used to deposit PbS on cellulose substrate. The optical properties of the prepared PbS/cellulose films have been investigated.

4.4.3. Experimental

4.4.3.1. Chemicals

All chemicals were used without further purification. Potassium ethyl xanthogenate (96%, Sigma-Aldrich), potassium hydroxide (>85%, Fisher Scientific), ethanol (≥99.8%, Sigma-Aldrich), 1-propanol (anhydrous 99.7%, Sigma-Aldrich), 1-butanol anhydrous (99.8% Sigma-Aldrich), 1-hexanol (reagent grade 98%, Sigma-Aldrich), carbon disulfide (low benzene ≥99.9%, Sigma-Aldrich) and lead(II) acetate trihydrate (≥99.9%, Sigma-Aldrich), Whatman® qualitative filter paper, grade 1, with pore size of ~11µm and thickness of 180 µm. Cotton yarn (Cotton Kings -Cone 500 8/4).

4.4.3.2. Synthesis of precursors

4.4.3.2.1. Synthesis of potassium propylxanthate, [K(S_2CO^nPr)] (1)

Potassium hydroxide (16.83 g, 0.3 mol) was dissolved in 100 mL of a 1:4 mixture of DI water to 1-propanol, with stirring for 1 h at room temperature. Then the solution was cooled to 0 °C, and carbon disulfide (18.62 mL, 0.3 mol) was added dropwise. The resulting yellow solution was stirred for an hour. The yellow precipitate was filtered, washed with a small amount of water, and recrystallized from acetone to give potassium propylxanthate. The yield was (78%). Mp = 128-130 °C. Elemental analysis calcd for [K(S_2CO^nPr)] : C, 27.57; H, 4.5; S, 36.76; K, 22.46, found: C, 27.83; H, 3.99; S, 36.46; K, 22.59. ^{1}H NMR (400 MHz, D_2O): δ ppm 0.89 (t, 3H), 1.68 (m, 2H); 1.21 (t, 2H)

4.4.3.2.2. Synthesis of potassium n-butylxanthate, [K(S_2CO^nBu)] (2)

[K(S_2CO^nBu)] was prepared via the same method as **(1)**, using 75 mL 1-Butanol. The yield was (71%). Mp = 118-120 °C. Elemental analysis calcd for [K(S_2CO^nBu)]: C, 31.90; H, 4.85; S, 33.99; K, 20.50, found: C, 31.81; H, 4.91; S, 33.71; K, 20.79. ^{1}H NMR (400 MHz, D_2O): δ ppm 0.86 (t, 3H), 1.42 (m, 2H), 1.66(m, 2H), 4.42 (t, 2H).

4.4.3.2.3. Synthesis of potassium hexylxanthate, [K(S_2COHex)] (3)

[K(S_2COHex)] was prepared as compound **(1),** using 75 mL 1-Hexanol The yield was (70%). Mp = 130-135 °C. Elemental analysis calcd for [K(S_2COHex)]: C, 38.68; H, 6.06; S, 29.85, K; 18.09, found: C, 38.82; H, 6.03; S, 29.89. ^{1}H NMR (400 MHz, D_2O) δ ppm 0.86 (t, 3 H) 1.25 - 1.42 (m, 7 H) 1.68 - 1.76 (m, 2 H) 4.41 (t, 2 H)

4.4.3.2.4. Synthesis of lead(II) ethylxanthate,[Pb(S_2COEt)$_2$] (4).

Potassium ethyl xanthogenate (6.4 g, 40 mmol) was dissolved in 100 mL of DI water while stirring. To this a solution of lead(II) acetate (6.5 g, 20 mmol) dissolved in 50 mL of DI water was added dropwise and was stirred for a further 60 min. The precipitate which formed was then filtered and washed with ethanol and water. The product was then dried under vacuum overnight. The yield was (70%). Mp = 130-135 °C. Elemental analysis calcd for [Pb(S_2COEt)$_2$]: C, 16.04; H, 2.24; S, 28.47; Pb, 46.12, found: C, 16.02; H, 2.13; S, 28.24; Pb, 46.04. ^{1}H NMR (400 MHz, acetone) δ ppm 1.45 (t, *J*=7.1 Hz, 3 H) 4.65 (q, *J*=7.0 Hz, 2 H).

4.4.3.2.5. Synthesis of lead(II) n-propylxanthate, [Pb(S_2CO^{n}Pr)$_2$] (5).

Potassium propylxanthate (6.9 g, 40 mmol) was dissolved in 100 mL of DI water. An aqueous solution (50ml) of lead(II) acetate (6.5 g, 20 mmol) was added dropwise to the yellow potassium xanthate solution and the mixture was stirred for a further 30 min. A brown precipitate formed which was filtered, washed with a small amount of water and dried under vacuum overnight. The yield was (78.5%). Mp = 85-87 °C. Elemental analysis calcd for [Pb(S_2CO^{n}Pr)$_2$]: C, 20.12; H, 2.96; S, 26.80; Pb, 43.42, found: C, 20.28; H, 2.83; S, 26.55; Pb, 43.69. ^{1}H NMR (400 MHz, acetone) δ ppm 1.00 (t, *J*=7.4 Hz, 3 H) 1.87 (sxt, *J*=7.1 Hz, 2 H) 4.57 (t, *J*=6.65 Hz, 2 H).

4.4.3.2.6. Synthesis of lead(II) n-butylxanthate, [Pb(S_2CO^{n}Bu)$_2$] (6)

Was prepared as compound (**5**) with (7.5 g, 40 mmol) 1-Butanol used in place of n-propanol. The yield was (75.5%). Mp = 90-95 °C. Elemental analysis calcd for [Pb(S_2CO^{n}Bu)$_2$]: C, 23.75; H, 3.59; S, 25.31; Pb, 41.01, found: C, 24.15; H, 3.48; S, 25.29; Pb, 41.09. ^{1}H NMR (400 MHz, acetone) δ ppm 0.96 (t, *J*=7.40 Hz, 3 H) 1.41 - 1.50 (m, 2 H) 1.80 - 1.88 (m, 2 H) 4.62 (t, *J*=6.53 Hz, 2 H)

4.4.3.2.7. Synthesis of lead(II) hexylxanthate [Pb(S_2CO^nHex)] (7)

lead(II) Hexylxanthate (4) was prepared as compound (2) with (8.0 g, 40 mmol) 1-Hexanol used in place of n-propanol. The yield was (76.0%). Mp = 65-67 °C. Elemental analysis calcd for [Pb($S_2COHex)_2$]: C, 29.93; H, 4.67; S, 22.79; Pb, 36.92, found: C, 30.10; H, 4.68; S, 22.84; Pb, 37.16. ^{1}H NMR (400 MHz, acetone) δ ppm 0.90 (t, *J*=1.0 Hz, 3 H) 1.32 - 1.37 (m, 4 H) 1.39 - 1.49 (m, 2 H) 1.81 - 1.90 (m, 2 H) 4.61 (t, *J*=6.53 Hz, 2 H).

4.4.3.3. Deposition of lead sulfide on cellulose

Lead(II) alkyl xanthate solutions (alkyl= ethyl, n-prolyl, n-butyl and n-hexyl) were prepared as following; 0.5 g of the relevant lead(II) xanthate dissolved in 60 ml tetrahydrofuran (THF) 60 ml. Then the cellulose samples were immersed in Petri dishes containing the prepared lead(II) solution. After 15 min the wet samples removed from the solution and dried at room temperature. The thermal decomposition was performed in tube furnace at 200 °C under nitrogen for 30 min.

4.4.3.4. Characterization

Elemental analysis (EA) and thermogravimetric analysis (TGA) were performed by the Microelemental Analysis service at the University of Manchester. EA was performed using a Flash 2000 Thermo Scientific elemental analyzer, and TGA data were obtained with Mettler Toledo TGA/DSC1 stare system in the range of 30−600 °C at a heating rate of 10 °C min^{-1} under nitrogen flow. NMR spectrum were collected using a Bruker Ascend spectrometer operating at 400 MHz. The X-ray diffraction (XRD) patterns were obtained with a Bruker D8 Advance diffractometer using a Cu Kα source (λ = 1.5418 Å). The surface morphology and elemental composition of the nanomaterials were determined using Tescan Mira3 SEM equipped with energy-dispersive X-ray spectroscopy (EDS). UV−vis spectrum were collected on a Perkin Elmer lambda 1050UV/Vis spectrophotometer.

4.4.4. Result and discussion

Lead(II) alkylxanthate precursors 1-4 were prepared by complexing relevant potassium alkylxanthate with lead(II) acetate trihydrate. All complexes were soluble in organic solvents such as chloroform, THF and acetone. The crystal structures of all complexes have been previously reported.[68]

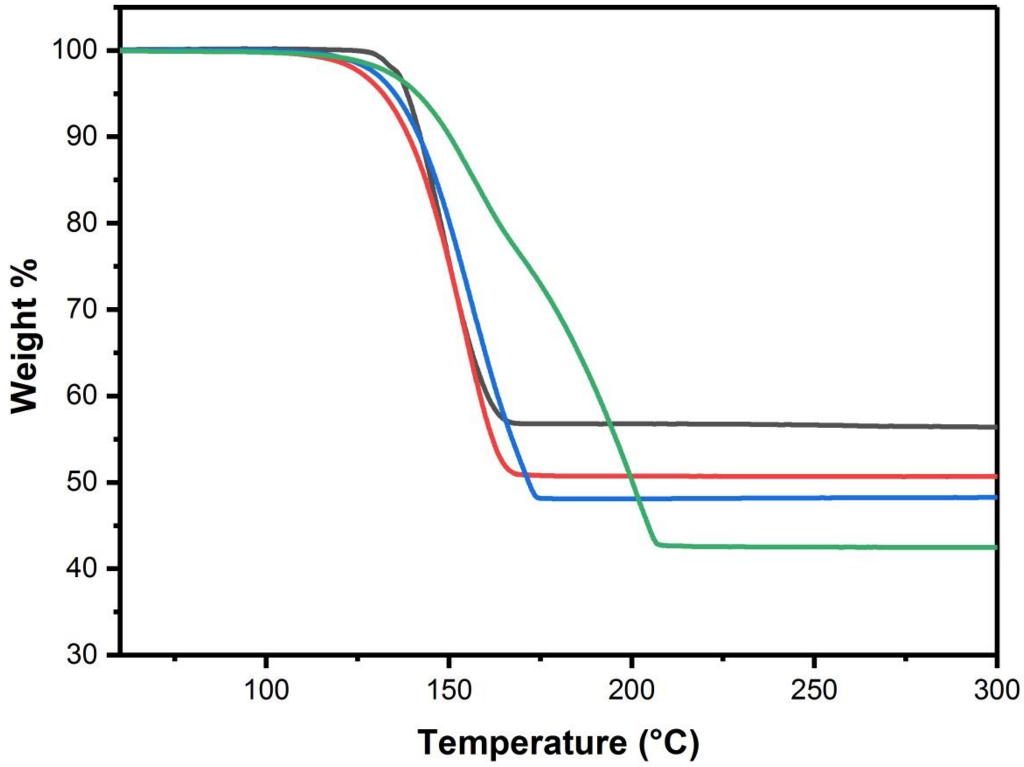

Figure 4.2 TGA of lead(II) alkylxanthate complexes: black = Et, red = Pr, blue = Bu, green = Hex.

The thermal decomposition behaviours of all lead (II) alkylxanthate complexes (4-7) were investigated by TGA in the range of 30 to 300 °C under nitrogen Figure 4.2 The suggested mechanism of lead xanthate decomposition is *via* Chugaev elimination process resulting in the formation of PbS. These complexes displayed similar TGA profiles.

Single-step decomposition with a rapid mass loss within the temperature range of 110 to 220 °C, except lead (II) hexylxanthate complex exhibited two-step breakdown. In fact, the effect of increased alkyl chain length on change the TGA profile from a single-step breakdown to two-step decomposition is clearly observed. For example, the first decomposition step for [Pb(S_2COHex)$_2$] is at about 160 °C which is close to the single decomposition for shorter chain xanthate complexes, implying the similarity of pyrolysis mechanism. The second decomposition step happens at approximately 200 °C indicating the breakdown of stronger bond. The change in bonding system could be responsible for changes in the decomposition behaviours resulting in the appearance of two-step pyrolysis. This behaviour was also reported previously with TGA profiles of [Pb(S_2COHex)$_2$] and [Pb(S_2COOct)$_2$].[68] The decomposition onset temperature ranged between 93-125 °C, for R = ethyl, propyl, butyl and hexyl, but shown no clear trend with alkyl chain length. The lead(II) ethylxanthate complex exhibited a clearly higher onset at 125 °C. The melting point for the complexes display a decrease as the alkyl chain is increased: 130, 85.3, 81.7 and 64.5 °C for complexes ethyl, propyl, butyl and hexyl,Table 4-1. TGA results of the final residues are shown in Table 4-1. All four complexes broke down cleanly to give expected final solid residue amounts that matched with the calculated value for PbS. The thermal decomposition of cellulose substrates (filter paper and cotton yarn) are shown in Figure 4.3; both substrates are demonstrating acceptable heat resistance up to 300 °C.

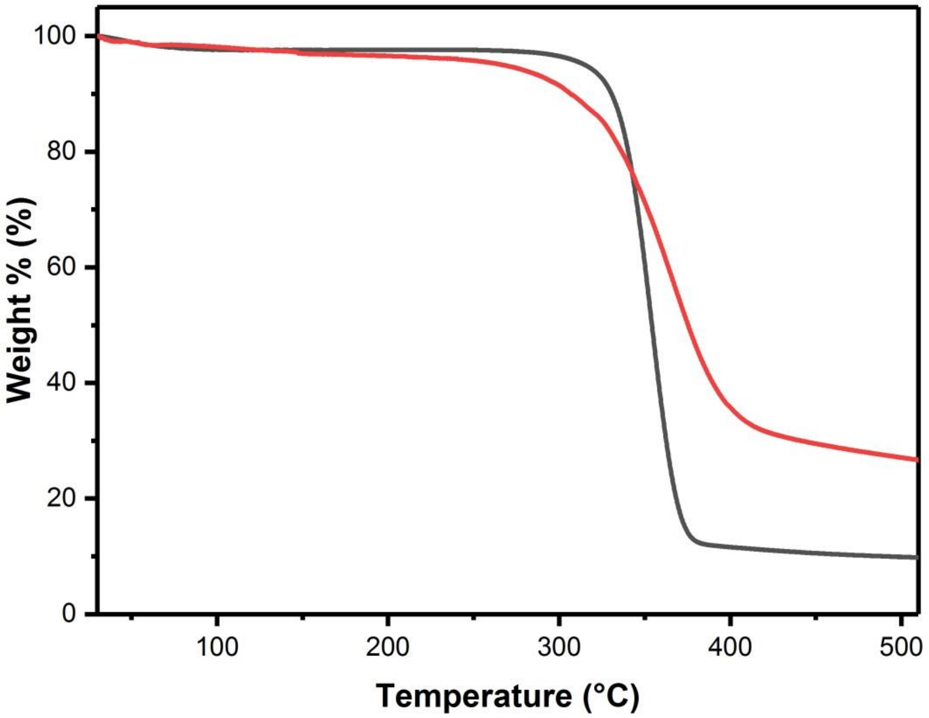

Figure 4.3 TGA of cellulose samples; black = filter paper, red = cotton yarn**.**

Table 4-1 Data from TGA profiles of TGA of lead(II) alkylxanthate complexes: Et, Pr, Bu and Hex.

R group of complex	Decomposition onset / °C	Decomposition offset / °C	Expected percentage weight, %	Found percentage weight, %	m.p. / °C
Et	125	170	53.2	56.6	130
Pr	93	167	50.2	50.6	85.3
Bu	100	174	47.3	47.7	81.7
Hex	107	207	44.8	42.8	64.5

4.4.4.1.1. Growth of PbS nanoparticles (NPs) on a cellulose substrate:

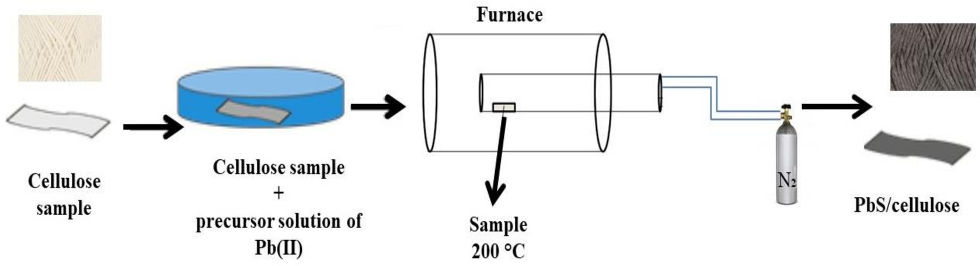

Figure 4.4 Synthetic scheme of growth of PbS on cellulose substrates.

The fabrication process is illustrated in Figure 4.4. Starting with distribution of the precursor into the substrates by immersing the samples into a volatile solution containing the lead(II) complex. The thermal decomposition of the precursor at 200 °C under nitrogen causes the growth of PbS NPs. The using of the volatile solution in this method during the dipping step helps to prevent cellulose paper from wrinkling. For example, Voggu *et al.* notified that the crispiness is one of the problems associated with the adsorption of water on paper during the deposition of CdS, which prevenst the fabrication of PVs.[93] One advantage of this synthetic scheme that it doesn't require any additional agents, since the by-products formed from the single source lead(II) alkylxanthate via Chugaev decomposition act as capping agents helping to stabilize nanocrystals growth.[68]

The successful deposition of PbS on the cotton yarn substrates were confirmed by the X-ray diffraction (XRD) pattern of the composite shown in Figure 4.5, with the peaks at 25.988°, 30.108°, 43.100°, 51.026°, 53.740° assigned to the diffraction planes of (111), (200), (220), (311), (222) of PbS (JCPDS file no. 03-65-0135). Additionally, the well-defined diffraction peaks located at $2\theta = 14.80°$, 16.50°, 22.62°, and 34.25° are assigned to the diffraction planes of (101), (101), (200), and (040), respectively, of crystalline cellulose.[94] In the case of PbS coated filter paper the X-ray diffraction, Figure 4.6, show peaks at 26.033°, 30.149°, 43.160°, 51.098°, 53.547° assigned to the diffraction planes of (111), (200), (220), (311), (222) of PbS (JCPDS file no. 019078-18899). Additionally, cellulose diffraction peaks were observed.

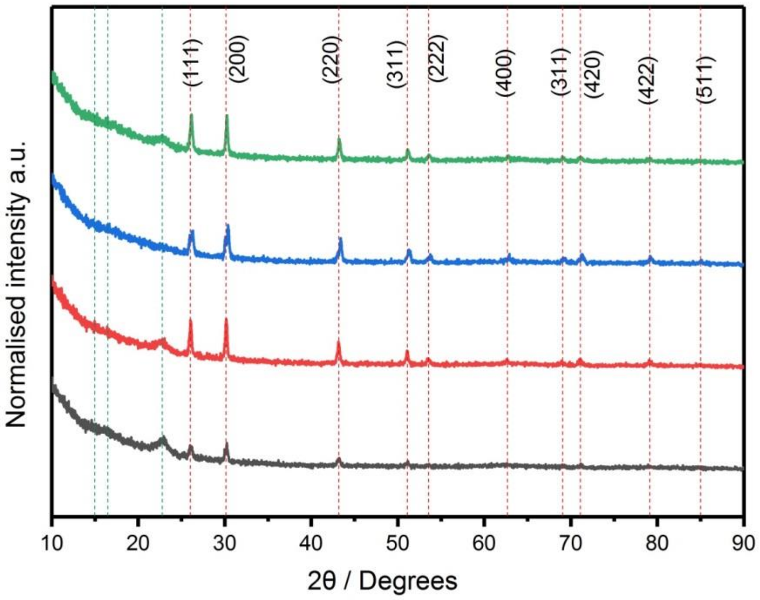

Figure 4.5 XRD pattern of cotton yarn coated with PbS (NPs) from the thermal decomposition of (a) lead(II) ethylxanthate, (b) lead(II) propylxanthate, (c) lead(II) butylxanthate, (d) lead(II) hexylxanthate at 200 °C under nitrogen. The reference peak positions for PbS 03-065-0135 are shown with red dashed lines and cellulose green dashed lines.

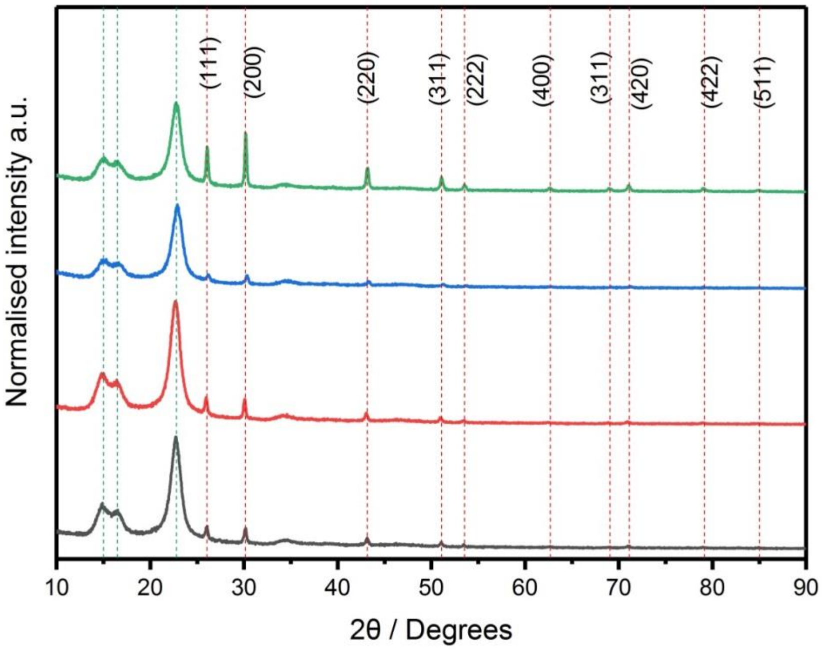

Figure 4.6 XRD pattern of filter paper coated with PbS (NPs) from the thermal decomposition of lead(II) ethylxanthate (black), lead(II) propylxanthate (red), lead(II) butylxanthate (blue), lead(II) hexylxanthate (green), at 200 °C under nitrogen. The reference peak positions for PbS 01-078-1899 are shown with red dashed lines and the cellulose reference is green dashed lines.

The SEM images of the blank cellulose substrates (Figure 4.7 a, b) and (Figure 4.8 a,b) highlighted the surface morphology of filter paper and cotton yarn respectively. Blank filter paper has interconnected as well as isolated fibres of the cellulose with diameters range of 6-20 µm as reported earlier.[95, 96] Where the cotton samples have symmetrical surface and fine porosities with fibres diameters of ~10 µm. The deposition of PbS nanoparticles from the thermal decomposition of lead(II) ethylxanthate on cellulose substrates are shown in Figure 4.7 c, d and Figure 4.8 c,d for filter paper and cotton yarn respectively . Clusters of lead sulfide NPs non-uniformly covered the filter paper substrates. Also, agglomerates of PbS nanoparticles were dispersed in cotton yarn samples. Such agglomeration is very commonly witnessed in nanostructured materials due to their high surface energy.[97, 98] For example, a research team argued that the agglomeration of Ag nanoparticle on filter paper improved the surface-enhanced Raman scattering (SERS) spectrum.[99] Chauhan's group reported the agglomeration of TiO_2 nanoparticles on cellulose paper sheets.[100] They also claimed that no report is available about how to prevent the agglomeration of nanostructures on the cellulose paper.

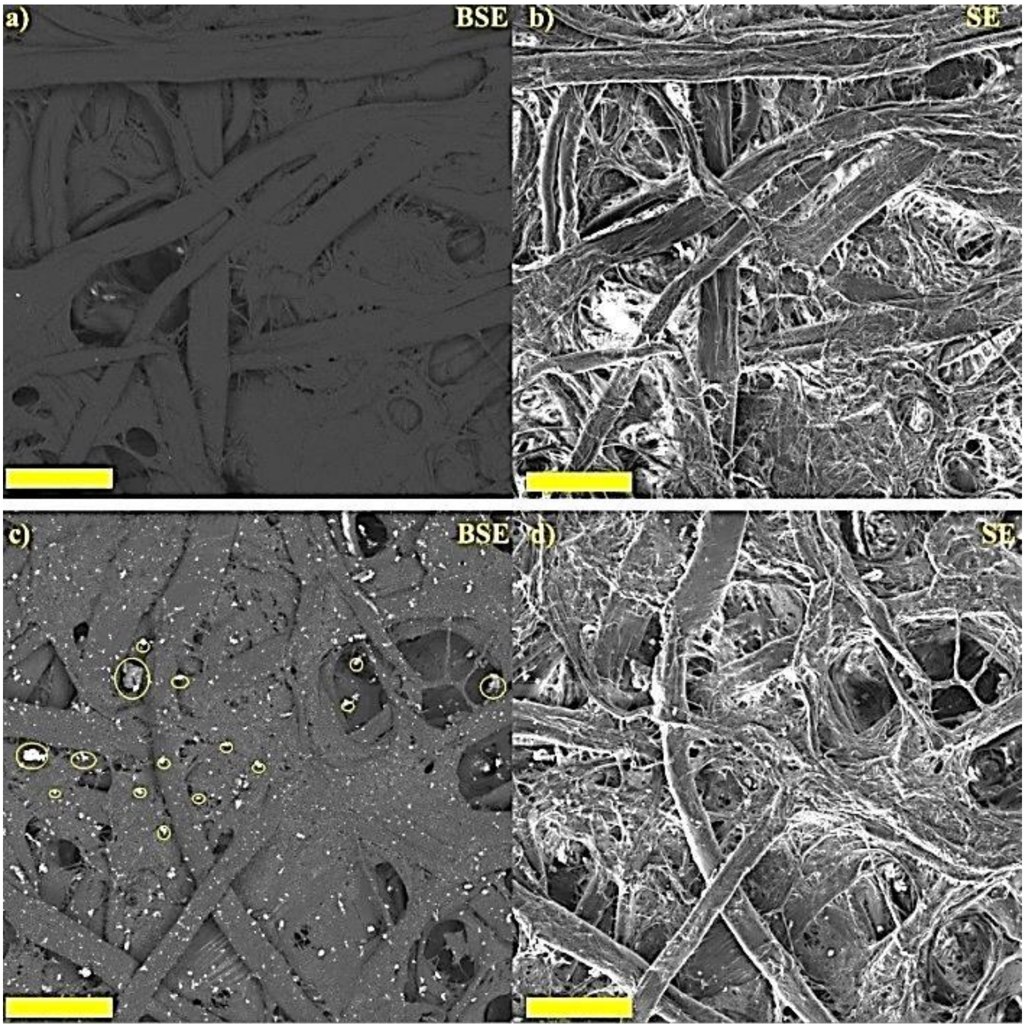

Figure 4.7 SEM of images of blank filter paper (a&b), and PbS (NPs) from the thermal decomposition of lead(II) ethylxanthate at 200 °C under nitrogen on filter paper substrates(c&d). Images (a&c) using BSE detector, where (b&d) using SE detector. Scale bar 100 µ. The yellow circles show the PbS nanoparticles.

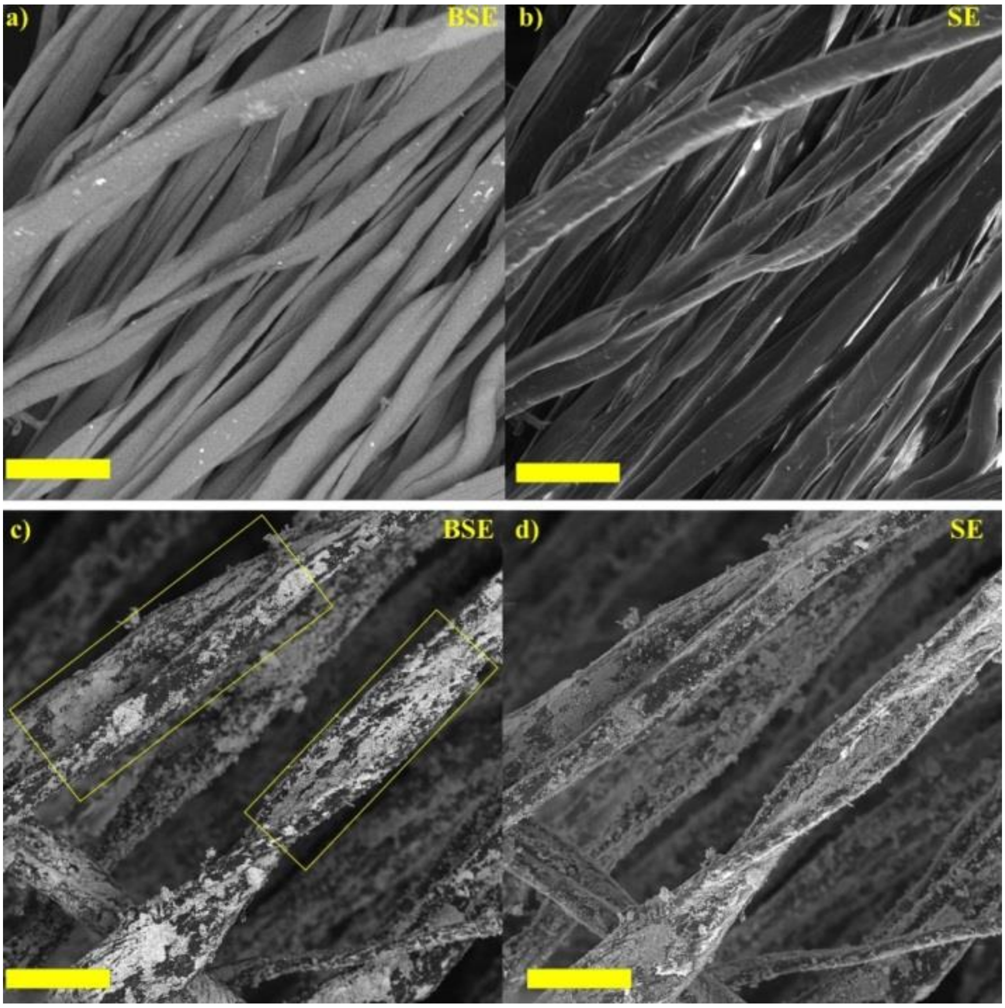

Figure 4.8 SEM of images of blank cotton yarn (a&b), and PbS (NPs) from the thermal decomposition of lead(II) ethylxanthate at 200 °C under nitrogen on cotton yarn substrates(c&d). Images (a&c) using BSE detector, where (b&d) using SE detector. Scale bar 100 µ. The yellow rectangles show the PbS nanoparticles.

Moreover, it was difficult to measure the size of the PbS nanoparticles from the SEM images because of the electrostatic charging on the surfaces of the filter paper substrates as also noted by Zheng *et al.*[58] The platinum coating of the cotton samples helps to reduce electrostatic charging on the surfaces. SEM images of cotton samples at higher magnification of cotton samples Figure **4.9** and Figure 4.10 display cubic lead sulfide (NPs) with average nanoparticle size ranged between 53.1 to 186.3 nm. McNaughter *et al*. investigated the effect of alkyl chain length of lead(II) xanthates on nanocrystal size using the melt reaction method. They claimed that increasing the alkyl chain length will result in reducing the nanocrystal size of PbS.[68]. Lewis group confirmed the control of lead sulfide NPs size by precursor choice. Use of precursors with longer xanthate chain reduces the dimensions of the nanocrystals produced.[70] In this work, it's observed that increasing the xanthate chain length lead to a decrease in the average size of PbS nanoparticles. The cubes average size were 186.3 (±31), 169.7 (±22), 81.0 (±9) and 53.1 (±11) for ethyl, propyl, butyl and hexyl samples respectively. This implies that the nanoparticle size decreases as the number of carbon atoms in the alkyl chain increase Figure 4.11. The size distribution of lead sulfide NPs deposited on cotton samples are presented in Figure 4.10.

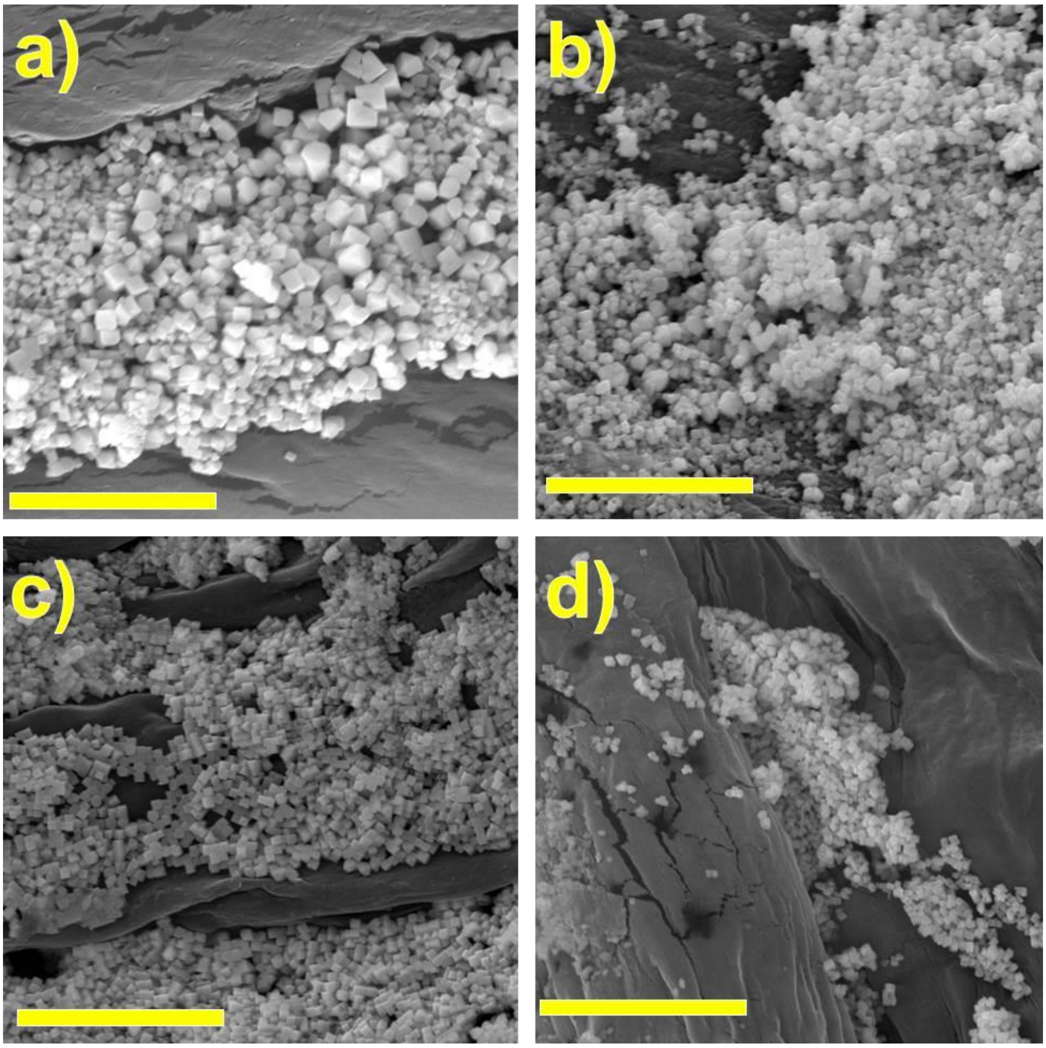

Figure 4.9 SEM of images of cotton yarn coated with PbS NPs from the thermal decomposition of lead(II) alkylxanthate; a) ethyl, b) propyl, c) butyl, d) hexyl. Scale bar is 1 µm.

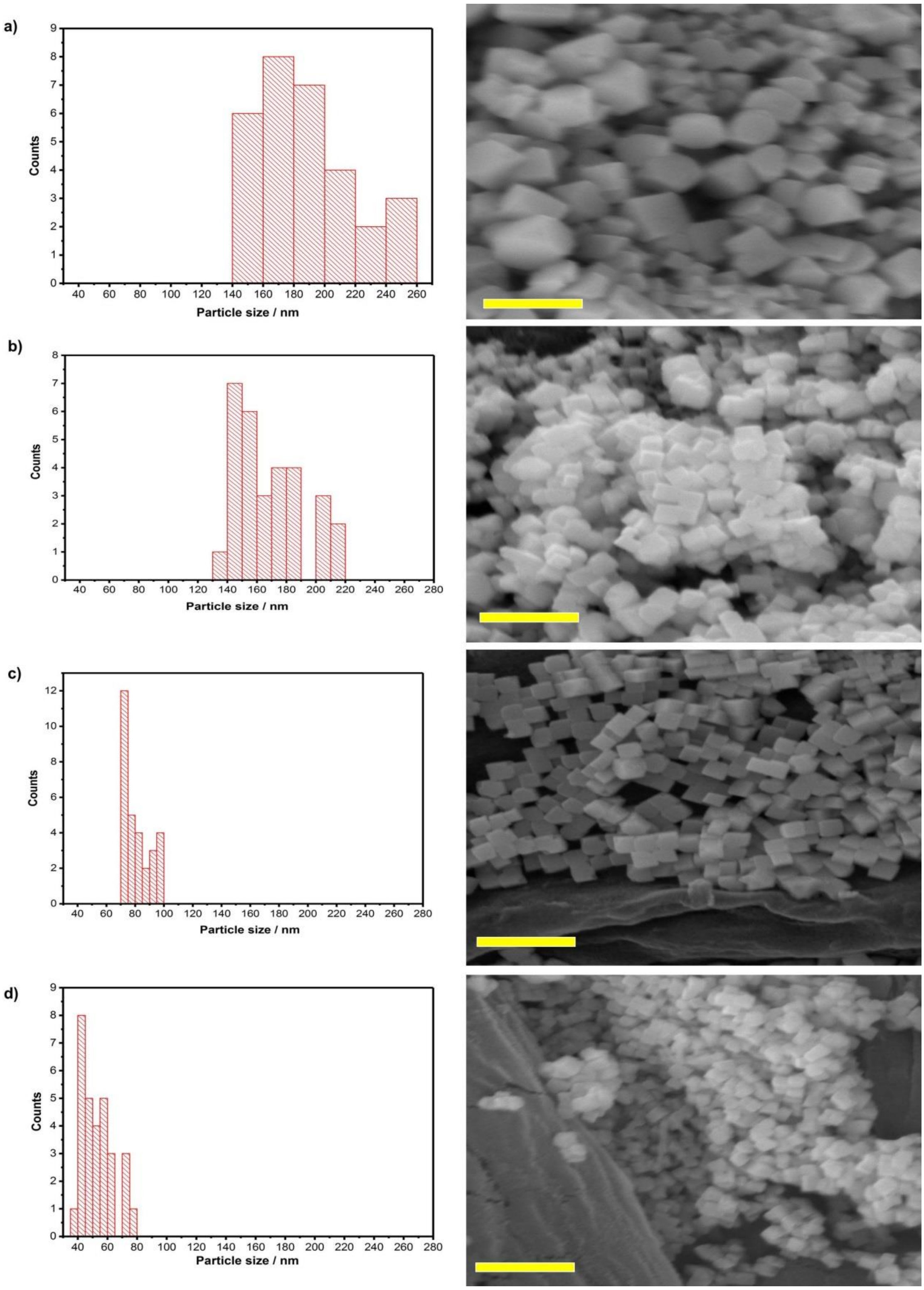

Figure 4.10 The size analysis (left column) and a typical SEM image (right column) , for lead(II) alkylxanthate; a) ethyl, b) propyl, c) butyl, d) hexyl. Scale bar is 500 nm.

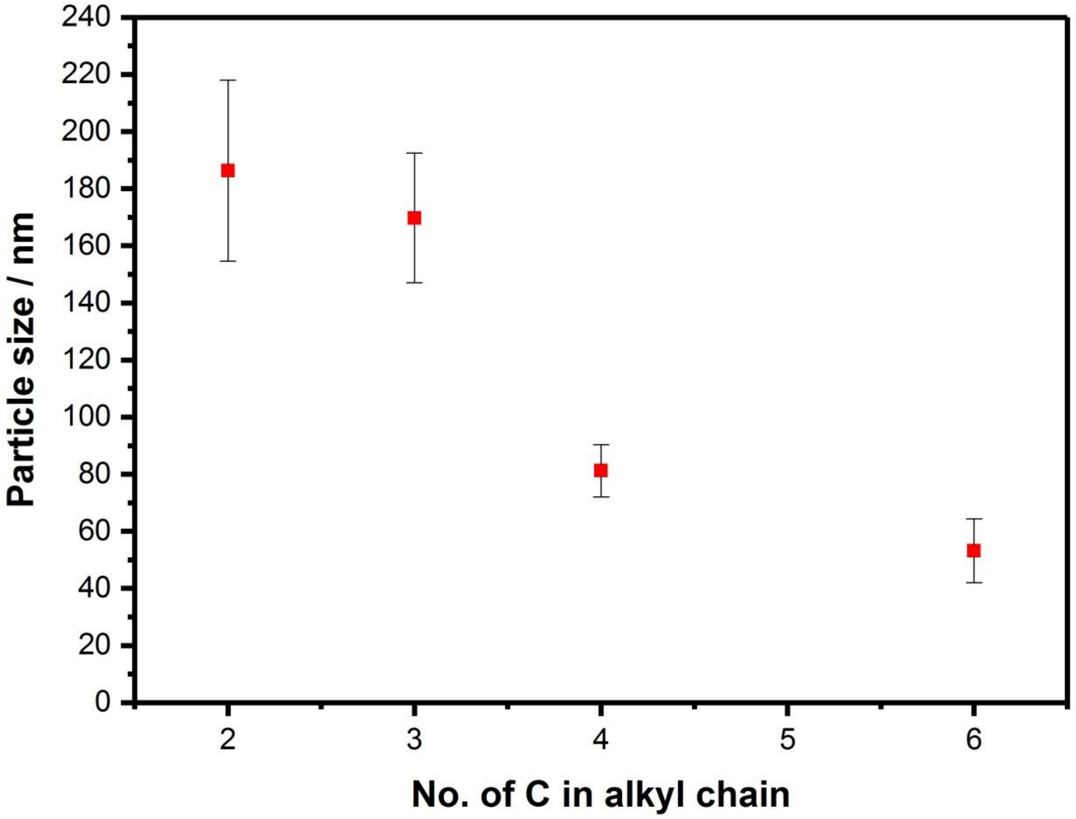

Figure 4.11 Average particle size (with standard errors) against the length of alkyl chain.

The elemental composition of the PbS nanoparticles on the cellulose substrates was determined by energy-dispersive X-ray spectroscopy (EDS),Table S.4-2. The ratio of Pb/S is consistent for all of the nanoparticles produced from the thermal decomposition of (3-6).

The transmittance spectrum of blank filter paper and PbS coated on filter paper are shown in Figure **4.12**. Blank filter paper is highly transparent in the wavelength range of 1000 nm to 2000 nm. However, PbS coated filter papers shows a gradual decrease in transmission in the same region. Since the blank filter paper is transparent in this area, the reduction in transmission is due to absorption by the PbS nanoparticles. The band gaps of the PbS nanoparticles were determined by using Tauc relation for a direct bandgap semiconductor.

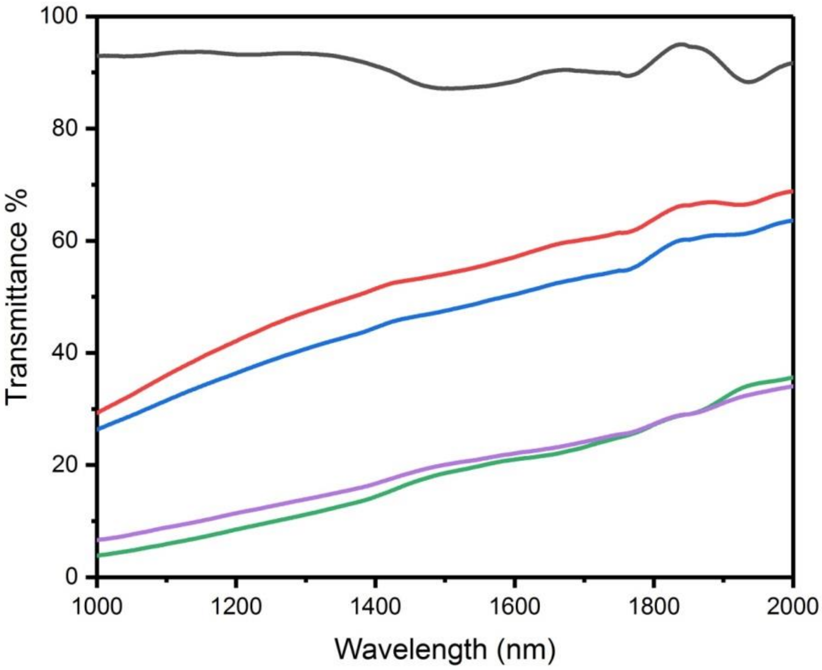

Figure 4.12 The transmittance spectrum of blank filter paper and PbS coated on filter paper from the thermal decomposition of lead(II) alkylxanthate at 200 °C under nitrogen. Black = blanck filter paper, red = ethyl, blue = propyl, purple = butyl, green = hexyl.

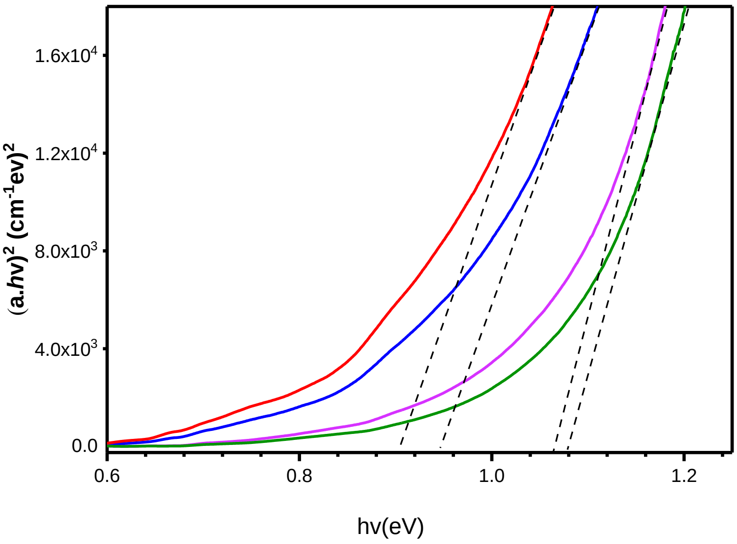

Figure 4.13 Tauc plots of PbS/filter paper nanocomposite from the thermal decomposition of lead(II) akylxanthates at 200 °C under nitrogen. Red = ethyl, blue = propyl, purple = butyl, green = hexyl.

The calculated band gaps are 0.90, 0.94, 1.06, and 1.07 for PbS nanoparticles prepared from the thermal decomposition of lead(II) ethyl, propyl, butyl and hexyl xanthate respectively. The bulk PbS has a bandgap of 0.41 eV at 300 K[101]. Beside that PbS nanoparticles display quantum size effect below Bohr radius of 18 nm[102]. Consequently, the band gaps of PbS NPs increases as the size decreases. The variation in bandgap observed of PbS/ filter paper (Figure 4.13) is due to the changing in PbS nanoparticles size. The calculated particles size from SEM images implies that particles size decreased as the alkyl chain length increased. This is in agreement with a result that has been previously reported for PbS nanoparticles[68, 70]. Therefore, in this experiment, we demonstrate the tunability of the bandgap by changing the alkyl group. The decrease of the particle size by increasing the length of the alkyl chain will result in the increased bandgap Figure 4.14.

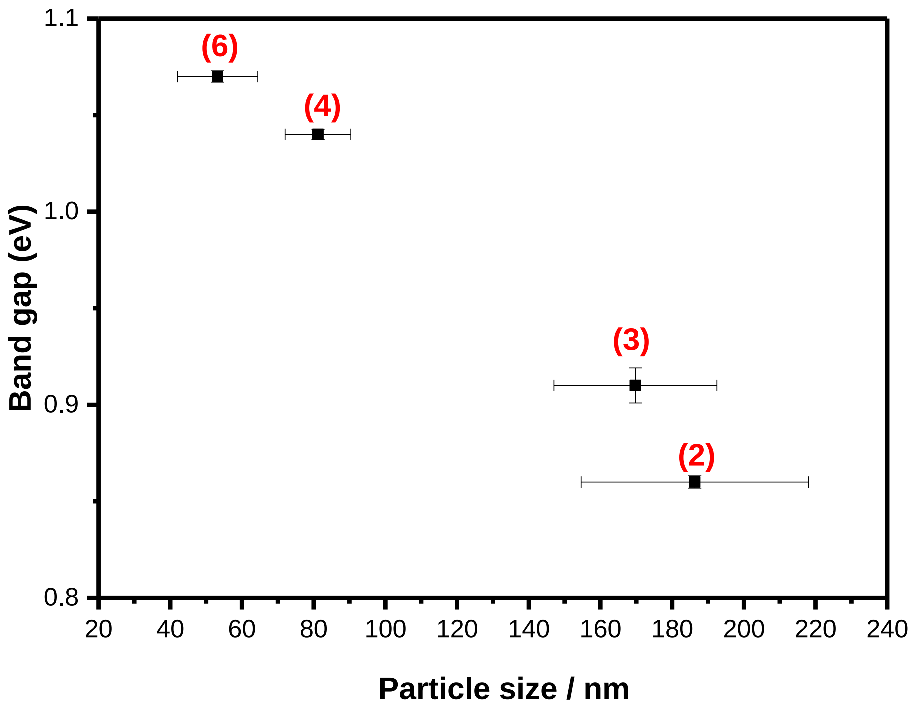

Figure 4.14 The bandgap versus particle size, the red number is the number of carbon atoms on the alkyl chain.

Although this work shows successful deposition of PbS nanoparticles on cellulose substrates, still the quality of deposition from the described approach is unsuitable to use in the fabrication of solar cells, because of the high surface roughness of filter paper used in this method made of cellulose fibers with pore size of ~11 µm. Solar cell devices require a smooth and non-porous substrate to prevent the cracks in the films. In the case of multilayer thin-film solar cells, the excessive surface roughness can lead to non- homogeneous coverage of the different depositions or even permeation of one cell layer into another, making the devices inoperable.[103] Strong candidate substrates are nanostructured celluloses and derivatives such as methyl cellulose (MC), hydroxypropylmethyl cellulose (HPMC), ethyl cellulose (EC), hydroxypropyl cellulose (HPC) and carboxymethyl cellulose (CMC).[104]

Another potential solution is the use of fillers in form of powders to improve smoothness, thermal resistance, gloss, optical, and other properties of paper.[98, 105] Finally, the cast-coating method is another powerful pathway that not only improves the surface roughness but also decreases paper substrates wettability, which could be problematic for aqueous deposition processes like printing.[106]

4.4.4.2. Conclusions

We have successfully demonstrated that PbS nanoparticles can be easily deposited on cellulose substrates by the thermal decomposition of single-source precursors at relatively low temperatures. The optical measurement of the PbS/cellulose substrates shows improvement in the IR absorption since the substrate was highly transparent before the deposition. Additionally, the bandgap also can be tunable by changing the length of alkyl chain. This may be interesting in the fabrication of flexible, light, portable and green substrates. However, filter paper has high surface roughness and porosity; as a result, the lead sulfide NPs were non-uniformly distributed on the substrates. In fact solar cell devices require a smooth and non-porous substrate to prevent cracks, breaks and shunts in the films. Therefore, paper with low porosity and smooth surface could be an alternative candidate. It’s also worth to try different deposition methods like Chemical Vapor Deposition (CVD), spin coating and spray coating.

4.4.4.3. References:

1. W. Li, R. Bi, G. X. Liu, Y. X. Tian and L. Zhang, *ACS Appl. Mater. Interfaces*, 2018, **10**, 26982-26989.
2. K. K. Fu, J. Cheng, T. Li and L. B. Hu, *Acs Energy Lett.*, 2016, **1**, 1065-1079.
3. S. H. Kim, K. H. Choi, S. J. Cho, S. Choi, S. Park and S. Y. Lee, *Nano Lett.*, 2015, **15**, 5168-5177.
4. G. Y. Qian, X. B. Liao, Y. X. Zhu, F. Pan, X. Chen and Y. Yang, *Acs Energy Lett.*, 2019, **4**, 690-701.
5. C. F. Pan, S. M. Niu, Y. Ding, L. Dong, R. M. Yu, Y. Liu, G. Zhu and Z. L. Wang, *Nano Lett.*, 2012, **12**, 3302-3307.
6. G. S. Han, S. Lee, M. L. Duff, F. Qin and J. K. Lee, *ACS Appl. Mater. Interfaces*, 2018, **10**, 4697-4704.
7. Q. Y. Cheng, D. D. Ye, W. T. Yang, S. H. Zhang, H. Z. Chen, C. Y. Chang and L. N. Zhang, *Acs Sustainable Chem. Eng.*, 2018, **6**, 8040-8047.
8. W. Gao, H. Ota, D. Kiriya, K. Takei and A. Javey, *Acc. Chem. Res.*, 2019, **52**, 523-533.
9. T. Li, Y. Li and T. Zhang, *Acc. Chem. Res.*, 2019, **52**, 288-296.
10. X. Liao, Z. Zhang, Q. Liang, Q. Liao and Y. Zhang, *ACS Appl. Mater. Interfaces*, 2017, **9**, 4151-4158.
11. L. Zhou, A. Wanga, S.-C. Wu, J. Sun, S. Park and T. N. Jackson, *Appl. Phys. Lett.*, 2006, **88**, 083502.
12. G. H. Gelinck, H. E. Huitema, E. van Veenendaal, E. Cantatore, L. Schrijnemakers, J. B. van der Putten, T. C. Geuns, M. Beenhakkers, J. B. Giesbers, B. H. Huisman, E. J. Meijer, E. M. Benito, F. J. Touwslager, A. W. Marsman, B. J. van Rens and D. M. de Leeuw, *Nat. Mater.*, 2004, **3**, 106-110.
13. A. Sugimoto, H. Ochi, S. Fujimura, A. Yoshida, T. Miyadera and M. Tsuchida, *IEEE J. Sel. Top. Quantum Electron.*, 2004, **10**, 107-114.
14. Y. Khan, A. E. Ostfeld, C. M. Lochner, A. Pierre and A. C. Arias, *Adv. Mater.*, 2016, **28**, 4373-4395.
15. M. M. Rodgers, V. M. Pai and R. S. Conroy, *IEEE Sens. J.*, 2015, **15**, 3119-3126.
16. C. C. Yang and Y. L. Hsu, *Sensors*, 2010, **10**, 7772-7788.
17. S. Veeralingam, P. Sahatiya, A. Kadu, V. Mattela and S. Badhulika, *ACS Appl. Electron. Mater.*, 2019, **1**, 558-568.

18. V. Zardetto, T. M. Brown, A. Reale and A. Di Carlo, *J. Polym Sci. Pol. Phys.*, 2011, **49**, 638-648.
19. W. J. Yu, S. Y. Lee, S. H. Chae, D. Perello, G. H. Han, M. Yun and Y. H. Lee, *Nano Lett.*, 2011, **11**, 1344-1350.
20. V. Scardaci, R. Coull and J. N. Coleman, *Appl. Phys. Lett.*, 2010, **97**, 023114.
21. A. R. Rathmell and B. J. Wiley, *Adv. Mater.*, 2011, **23**, 4798-4803.
22. M. Nogi, S. Iwamoto, A. N. Nakagaito and H. Yano, *Adv. Mater.*, 2009, **21**, 1595-1598.
23. L. B. Hu, H. Wu and Y. Cui, *MRS Bull.*, 2011, **36**, 760-765.
24. A. Anctil, C. W. Babbitt, R. P. Raffaelle and B. J. Landi, *Prog. Photovoltaics Res. Appl.*, 2013, **21**, 1541-1554.
25. Y. Yang, Q. Huang, G. F. Payne, R. Sun and X. Wang, *Nanoscale*, 2019, **11**, 725-732.
26. H. L. Zhu, Z. G. Xiao, D. T. Liu, Y. Y. Li, N. J. Weadock, Z. Q. Fang, J. S. Huang and L. B. Hu, *Energ Environ. Sci.*, 2013, **6**, 2105-2111.
27. M. S. Islam, L. Chen, J. Sisler and K. C. Tam, *J. Mater. Chem. B*, 2018, **6**, 864-883.
28. Y. H. Jung, T. H. Chang, H. Zhang, C. Yao, Q. Zheng, V. W. Yang, H. Mi, M. Kim, S. J. Cho, D. W. Park, H. Jiang, J. Lee, Y. Qiu, W. Zhou, Z. Cai, S. Gong and Z. Ma, *Nat. Commun.*, 2015, **6**, 7170.
29. P. Cataldi, I. S. Bayer, F. Bonaccorso, V. Pellegrini, A. Athanassiou and R. Cingolani, *Adv. Electron. Mater.*, 2015, **1**, 1500224.
30. Y. Zheng, Z. Z. He, Y. X. Gao and J. Liu, *Sci. Rep-Uk*, 2013, **3**, 1786.
31. H. Tao, L. R. Chieffo, M. A. Brenckle, S. M. Siebert, M. Liu, A. C. Strikwerda, K. Fan, D. L. Kaplan, X. Zhang, R. D. Averitt and F. G. Omenetto, *Adv. Mater.*, 2011, **23**, 3197-3201.
32. E. F. Gomez and A. J. Steckl, *Acs Photonics*, 2015, **2**, 439-445.
33. D. A. Gopakumar, A. R. Pai, Y. B. Pottathara, D. Pasquini, L. Carlos de Morais, M. Luke, N. Kalarikkal, Y. Grohens and S. Thomas, *ACS Appl. Mater. Interfaces*, 2018, **10**, 20032-20043.
34. Z. Fang, H. Zhu, Y. Yuan, D. Ha, S. Zhu, C. Preston, Q. Chen, Y. Li, X. Han, S. Lee, G. Chen, T. Li, J. Munday, J. Huang and L. Hu, *Nano Lett.*, 2014, **14**, 765-773.
35. Z. Gui, H. Zhu, E. Gillette, X. Han, G. W. Rubloff, L. Hu and S. B. Lee, *ACS Nano*, 2013, **7**, 6037-6046.

36. G. Nystrom, A. Razaq, M. Stromme, L. Nyholm and A. Mihranyan, *Nano Lett.*, 2009, **9**, 3635-3639.
37. F. Gao, S. Q. Ren and J. P. Wang, *Energ Environ. Sci.*, 2013, **6**, 2020-2040.
38. A. J. Moule, L. L. Chang, C. Thambidurai, R. Vidu and P. Stroeve, *JMCh*, 2012, **22**, 2351-2368.
39. R. Zhou and J. Xue, *ChemPhysChem*, 2012, **13**, 2471-2480.
40. W. U. Huynh, J. J. Dittmer and A. P. Alivisatos, *Sci.*, 2002, **295**, 2425-2427.
41. V. L. Colvin, M. C. Schlamp and A. P. Alivisatos, *Nat.*, 1994, **370**, 354-357.
42. L. Qian, Y. Zheng, J. G. Xue and P. H. Holloway, *Nat. Photonics*, 2011, **5**, 543-548.
43. T. Rauch, M. Boberl, S. F. Tedde, J. Furst, M. V. Kovalenko, G. N. Hesser, U. Lemmer, W. Heiss and O. Hayden, *Nat. Photonics*, 2009, **3**, 332-336.
44. J. W. Grate, S. N. Kaganove, S. J. Patrash, R. Craig and M. Bliss, *Chem. Mater.*, 1997, **9**, 1201-1207.
45. E. Bescher and J. D. Mackenzie, *Adv. Mater. Sci. Eng.*, 1998, **6**, 145-154.
46. G. Yu and A. J. Heeger, *J. Appl. Phys.*, 1995, **78**, 4510-4515.
47. A. J. Breeze, Z. Schlesinger, S. A. Carter and P. J. Brock, *Phys. Rev. B: Condens. Matter.*, 2001, **64**, 125205.
48. H. Becker, A. Lux, A. B. Holmes and R. H. Friend, *Synth. Met.*, 1997, **85**, 1289-1290.
49. P. A. van Hal, M. M. Wienk, J. M. Kroon, W. J. H. Verhees, L. H. Slooff, W. J. H. van Gennip, P. Jonkheijm and R. A. J. Janssen, *Adv. Mater.*, 2003, **15**, 118-121.
50. C. Y. Kwong, A. B. Djurisic, P. C. Chui, K. W. Cheng and W. K. Chan, *Chem. Phys. Lett.*, 2004, **384**, 372-375.
51. Q. Qiao, J. Beck, R. Lumpkin, J. Pretko and J. T. Mcleskey, *Sol. Energy Mater. Sol. Cells*, 2006, **90**, 1034-1040.
52. S. A. Chen and Y. Fang, *Synth. Met.*, 1993, **60**, 215-222.
53. Y. Li, L. Xu, B. Xu, Z. Mao, H. Xu, Y. Zhong, L. Zhang, B. Wang and X. Sui, *ACS Appl. Mater. Interfaces*, 2017, **9**, 17155-17162.
54. G. Chu, X. Wang, H. Yin, Y. Shi, H. Jiang, T. Chen, J. Gao, D. Qu, Y. Xu and D. Ding, *ACS Appl. Mater. Interfaces*, 2015, **7**, 21797-21806.
55. S. K. Zhou, M. Wang, X. Chen and F. Xu, *ACS Sustainable Chem. Eng.*, 2015, **3**, 3346-3354.
56. E. Lizundia, U. Goikuria, J. L. Vilas, F. Cristofaro, G. Bruni, E. Fortunati, I. Armentano, L. Visai and L. Torre, *Biomacromolecules*, 2018, **19**, 2618-2628.

57. Y. A. Chen, P. Potschke, J. Pionteck, B. Voit and H. S. Qi, *Acs Omega*, 2019, **4**, 5117-5125.

58. Y. Zheng, M. Xiao, S. Jiang, F. Ding and J. Wang, *Nanoscale*, 2013, **5**, 788-795.

59. E. Katoueizadeh, S. M. Zebarjad and K. Janghorban, *J. Mater. Res. Technol.*, 2018, **7**, 204-211.

60. H. Liu, M. Li, O. Voznyy, L. Hu, Q. Fu, D. Zhou, Z. Xia, E. H. Sargent and J. Tang, *Adv. Mater.*, 2014, **26**, 2718-2724, 2617.

61. J. L. Machol, F. W. Wise, R. C. Patel and D. B. Tanner, *Phys. Rev. B: Condens. Matter*, 1993, **48**, 2819-2822.

62. K. Ramasamy, A. O. Nejo, N. Ziqubu, P. V. S. R. Rajasekhar, A. A. Nejo, N. Revaprasadu and P. O'Brien, *Eur. J. Inorg. Chem.*, 2011, **2011**, 5196-5201.

63. S. A. McDonald, G. Konstantatos, S. Zhang, P. W. Cyr, E. J. Klem, L. Levina and E. H. Sargent, *Nat. Mater.*, 2005, **4**, 138-142.

64. K. W. Johnston, A. G. Pattantyus-Abraham, J. P. Clifford, S. H. Myrskog, D. D. MacNeil, L. Levina and E. H. Sargent, *Appl. Phys. Lett.*, 2008, **92**, 151115.

65. S. F. Wang, F. Gu and M. K. Lu, *Langmuir : the ACS J. Surf. Colloids*, 2006, **22**, 398-401.

66. J. Sun, M. Q. Zhu, K. Fu, N. Lewinski and R. A. Drezek, *Int. J. Nanomed*, 2007, **2**, 235-240.

67. T. Mandal, G. Piburn, V. Stavila, I. Rusakova, T. Ould-Ely, A. C. Colson and K. H. Whitmire, *Chem. Mater.*, 2011, **23**, 4158-4169.

68. P. D. McNaughter, S. A. Saah, M. Akhtar, K. Abdulwahab, M. A. Malik, J. Raftery, J. A. Awudza and P. O'Brien, *Dalton Trans.*, 2016, **45**, 16345-16353.

69. C. Y. Zha, C. Pang, Y. Xu, C. Ji, X. Y. Zhang, L. M. Shen, Y. F. Wang, A. Gupta and N. Z. Bao, *Rsc Adv*, 2016, **6**, 62226-62235.

70. E. A. Lewis, P. D. McNaughter, Z. J. Yin, Y. Q. Chen, J. R. Brent, S. A. Saah, J. Raftery, J. A. M. Awudza, M. A. Malik, P. O'Brien and S. J. Haigh, *Chem. Mater.*, 2015, **27**, 2127-2136.

71. Z. Tshemese, M. D. Khan, S. Mlowe and N. Revaprasadu, *Mater. Sci. Eng. B-Adv*, 2018, **227**, 116-121.

72. J. Chen, Y. Kong, W. Wang, H. Fang, Y. Wo, D. Zhou, Z. Wu, Y. Li and S. Chen, *Chem Commun (Camb)*, 2016, **52**, 4025-4028.

73. Y. R. Ma, L. M. Qi, J. M. Ma and H. M. Cheng, *Crystal Growth & Design*, 2004, **4**, 351-354.

74. Y. H. Ni, H. J. Liu, F. Wang, Y. Y. Liang, J. M. Hong, X. Ma and Z. Xu, *Crystal Growth & Design*, 2004, **4**, 759-764.
75. N. Zhao and L. M. Qi, *Adv. Mater.*, 2006, **18**, 359-+.
76. N. L. Pickett and P. O'Brien, *Chemical record*, 2001, **1**, 467-479.
77. L. Almanqur, F. Alam, G. Whitehead, I. Vitorica-yrezabal, P. OBrien and D. J. Lewis, *J. Cryst. Growth*, 2019, **522**, 175-182.
78. L. Almanqur, I. Vitorica-yrezabal, G. Whitehead, D. J. Lewis and P. O'Brien, *Rsc Adv*, 2018, **8**, 29096-29103.
79. S. C. Masikane, P. D. McNaughter, D. J. Lewis, I. Vitorica-Yrezabal, B. P. Doyle, E. Carleschi, P. O'Brien and N. Revaprasadu, *Eur. J. Inorg. Chem.*, 2019, **2019**, 1421-1432.
80. M. Al-Shakban, Z. Q. Xie, N. Savjani, M. A. Malik and P. O'Brien, *J. Mater. Sci.*, 2016, **51**, 6166-6172.
81. M. Al-Shakban, P. D. Matthews, E. A. Lewis, J. Raftery, I. Vitorica-Yrezabal, S. J. Haigh, D. J. Lewis and P. O'Brien, *J. Mater. Sci.*, 2019, **54**, 2315-2323.
82. N. Zeng, D. G. Hopkinson, B. F. Spencer, S. G. McAdams, A. A. Tedstone, S. J. Haigh and D. J. Lewis, *Chem Commun (Camb)*, 2018, **55**, 99-102.
83. K. I. Y. Ketchemen, S. Mlowe, L. D. Nyamen, P. T. Ndifon, N. Revaprasadu and P. O'Brien, *J Mater Sci-Mater El*, 2018, **29**, 14462-14470.
84. W. N. Kun, S. Mlowe, L. D. Nyamen, M. P. Akerman, P. O'Brien, P. T. Ndifon and N. Revaprasadu, *Polyhedron*, 2018, **154**, 173-181.
85. M. D. Khan, M. Akhtar, M. A. Malik, N. Revaprasadu and P. O'Brien, *Chemistryselect*, 2018, **3**, 2943-2950.
86. M. Afzaal, K. Ellwood, N. L. Pickett, P. O'Brien, J. Raftery and J. Waters, *JMCh*, 2004, **14**, 1310-1315.
87. T. P. Duan, W. J. Lou, X. B. Wang and Q. J. Xue, *Colloid Surface A*, 2007, **310**, 86-93.
88. N. O. Boadi, P. D. McNaughter, M. Helliwell, M. A. Malik, J. A. M. Awudza and P. O'Brien, *Inorg. Chem. Acta*, 2016, **453**, 439-442.
89. J. Akhtar, M. Afzaal, M. A. Vincent, N. A. Burton, I. H. Hillier and P. O'Brien, *Chem Commun (Camb)*, 2011, **47**, 1991-1993.
90. C. Fradler, T. Rath, S. Dunst, I. Letofsky-Papst, R. Saf, B. Kunert, F. Hofer, R. Resel and G. Trimmel, *Sol. Energy Mater. Sol. Cells*, 2014, **124**, 117-125.
91. L. Petersson, I. Kvien and K. Oksman, *Compos. Sci. Technol.*, 2007, **67**, 2535-2544.

92. H. Fukuzumi, T. Saito, T. Iwata, Y. Kumamoto and A. Isogai, *Biomacromolecules*, 2009, **10**, 162-165.

93. V. R. Voggu, J. Sham, S. Pfeffer, J. Pate, L. Fillip, T. B. Harvey, R. M. Brown and B. A. Korgel, *Acs Energy Lett*, 2017, **2**, 574-581.

94. Y. Guo, X. Wang, X. Shu, Z. Shen and R. C. Sun, *J. Agric. Food. Chem.*, 2012, **60**, 3900-3908.

95. T. Kamal, S. B. Khan and A. M. Asiri, *Cellulose*, 2016, **23**, 1911-1923.

96. T. Kamal, S. B. Khan and A. M. Asiri, *Environmental pollution*, 2016, **218**, 625-633.

97. R. Dave, R. Gupta, R. Pfeffer, S. Sundaresan and M. S. Tomassone, NSF Science and Engineering Grantees Conference, 2006.

98. H. H. Liu, S. Surawanvijit, R. Rallo, G. Orkoulas and Y. Cohen, *Environ. Sci. Technol.*, 2011, **45**, 9284-9292.

99. L. F. Sallum, F. L. F. Soares, J. A. Ardila and R. L. Carneiro, *Spectrochimica Acta Part A: Molecular and Biomolecular Spectroscopy*, 2014, **133**, 107-111.

100. I. Chauhan, S. Chattopadhyay and P. Mohanty, *Materials Express*, 2013, **3**, 343-349.

101. M. H. Patel, T. K. Chaudhuri, V. K. Patel, T. Shripathi, U. Deshpande and N. P. Lalla, *Rsc Adv*, 2017, **7**, 4422-4429.

102. S. Gallardo, M. Gutierrez, A. Henglein and E. Janata, *Ber Bunsen Phys Chem*, 1989, **93**, 1080-1090.

103. I. Chauhan, S. Aggrawal, Chandravati and P. Mohanty, *Rsc Adv*, 2015, **5**, 83036-83055.

104. A. T. Vicente, A. Araújo, M. J. Mendes, D. Nunes, M. J. Oliveira, O. Sanchez-Sobrado, M. P. Ferreira, H. Águas, E. Fortunato and R. Martins, *J. Mater. Chem. C*, 2018, **6**, 3143-3181.

105. J. Kettle, T. Lamminmaki and P. Gane, *Surf Coat Tech*, 2010, **204**, 2103-2109.

106. H. Aguas, T. Mateus, A. Vicente, D. Gaspar, M. J. Mendes, W. A. Schmidt, L. Pereira, E. Fortunato and R. Martins, *Adv. Funct. Mater.*, 2015, **25**, 3592-3598.

4.4.4.4. Electronic Supporting information

Table S.4-2 Atomic percentage of lead and sulfur from thermal decomposition of lead(II) alkylxanthate, using EDX.

R group of complex	Cotton		Filter paper	
	Atomic percentage of Pb, %	Atomic percentage of S, %	Atomic percentage of Pb, %	Atomic percentage of S, %
Ethyl	50.9	49.1	50.9	49.1
Propyl	51.7	48.3	50.8	49.2
Butyl	50.5	49.5	51.5	48.5
Hexyl	51.2	48.8	50.1	49.9

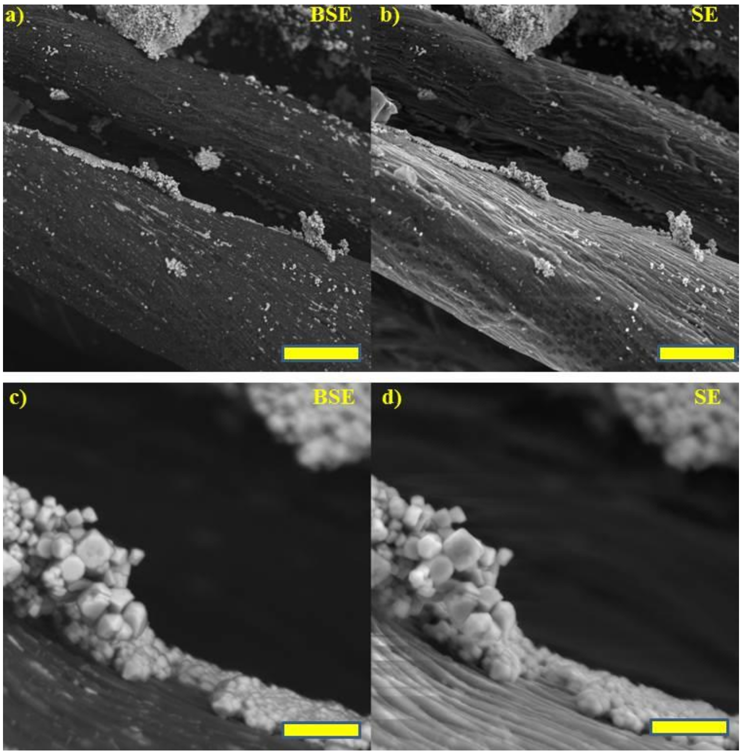

Figure .S4.15 SEM of images of PbS NPs produced from the thermal decomposition of lead(II) propylxanthate at 200 °C under nitrogen on cotton yarn substrates. Images (a & c) using BSE detector (a & c), where (b & d) using SE detector. Scale bar (a & b) 20 µm, (c & d) 2 µm.

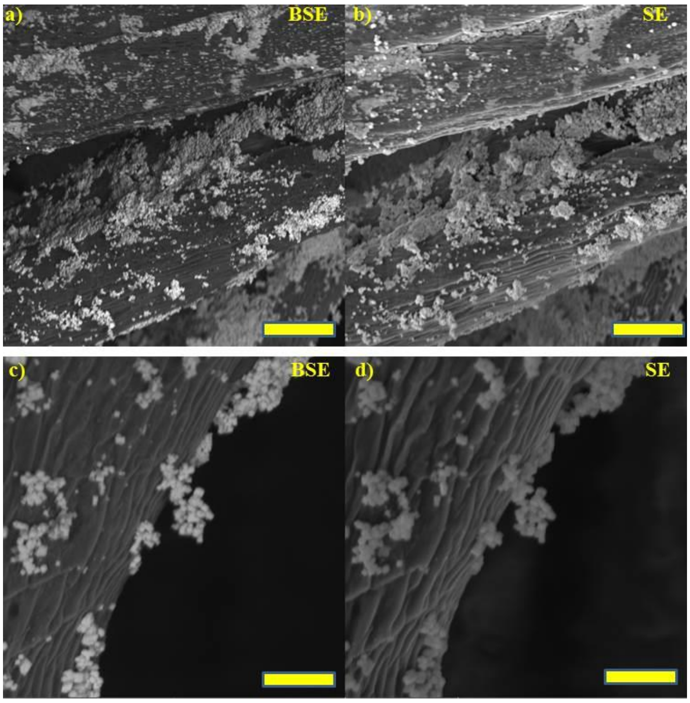

Figure .S.4.16 SEM of images of PbS NPs produced from the thermal decomposition of lead(II) butylxanthate at 200 °C under nitrogen on cotton yarn substrates. Images (a & c) using BSE detector (a & c), where (b & d) using SE detector. Scale bar (a & b) 20 µm, (c & d) 2 µm.

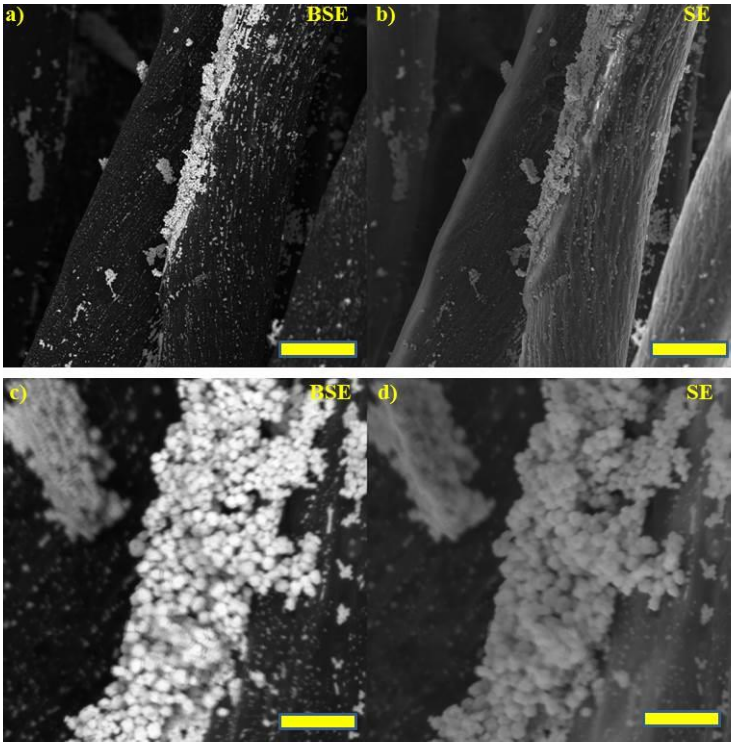

Figure .S.4.17 SEM of images of PbS NPs produced from the thermal decomposition of lead(II) hexylxanthate at 200 °C under nitrogen on cotton yarn substrates. Images (a & c) using BSE detector (a & c), where (b & d) using SE detector. Scale bar (a & b) 20 µm, (c & d) 2 µm.

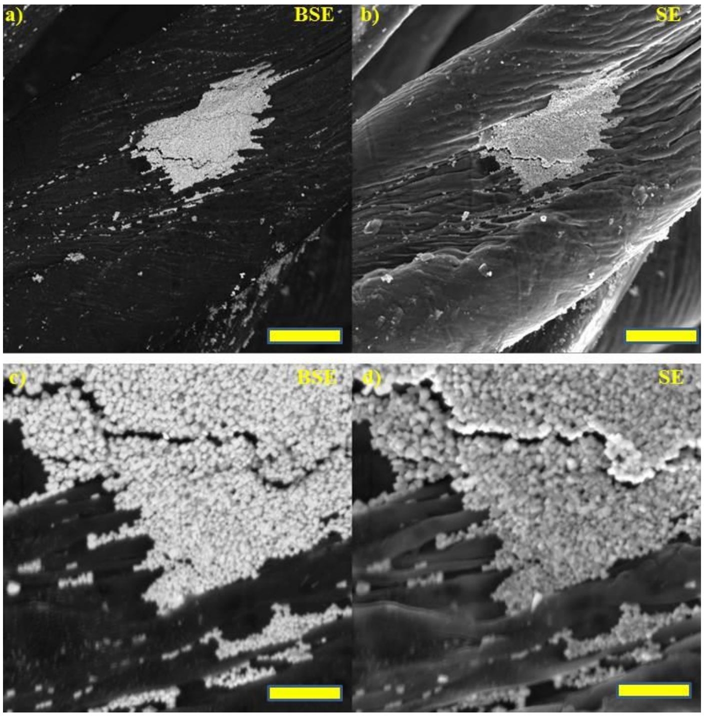

Figure .S.4.18 SEM of images of filter paper (a & b) and cotton yarn (c & d) where BSE (a & c), SE (b & d), coated with PbS NPs from the thermal decomposition of lead(II) ethylxanthate at 200 °C under nitrogen. Scale bar (a & b) 20 µm, (c & d) 5 µm.

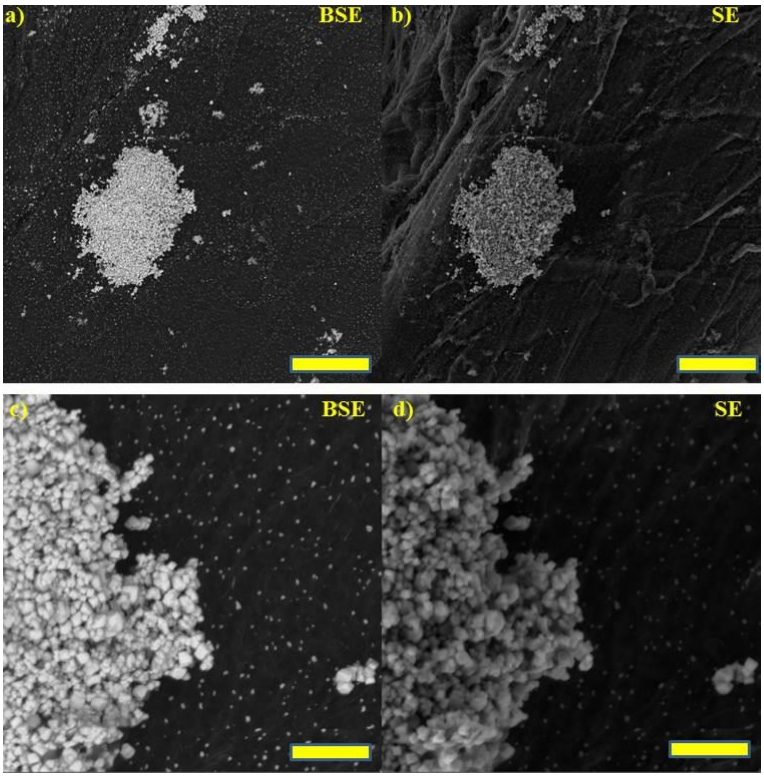

Figure .S.4.19 SEM of images of filter paper (a & b) and cotton yarn (c & d) where BSE (a & c), SE (b & d), coated with PbS NPs from the thermal decomposition of lead(II) propylxanthate at 200 °C under nitrogen. Scale bar (a & b) 20 µm, (c & d) 5 µm.

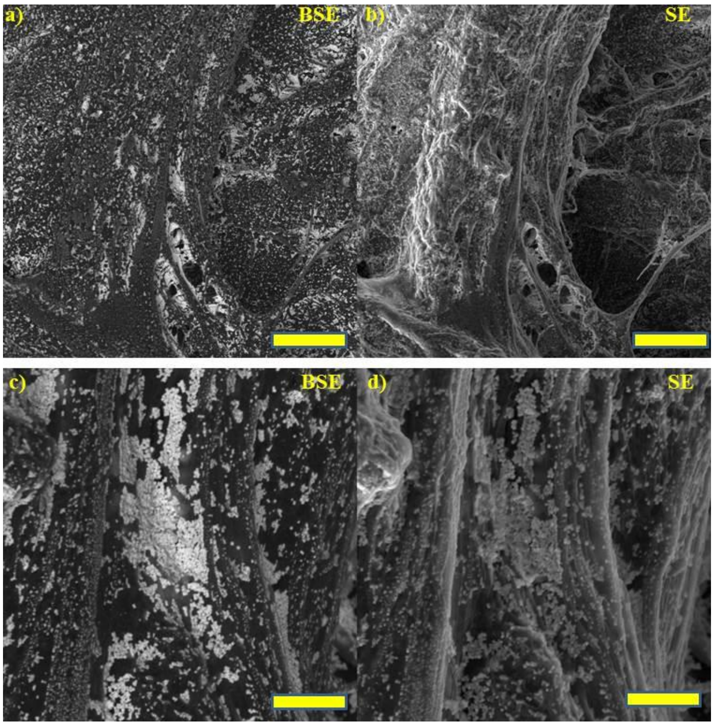

Figure S.4.20 SEM of images of filter paper (a & b) and cotton yarn (c & d) where BSE (a & c), SE (b & d), coated with PbS NPs from the thermal decomposition of lead(II) butylxanthate at 200 °C under nitrogen. Scale bar (a & b) 20 µm, (c & d) 5 µm.

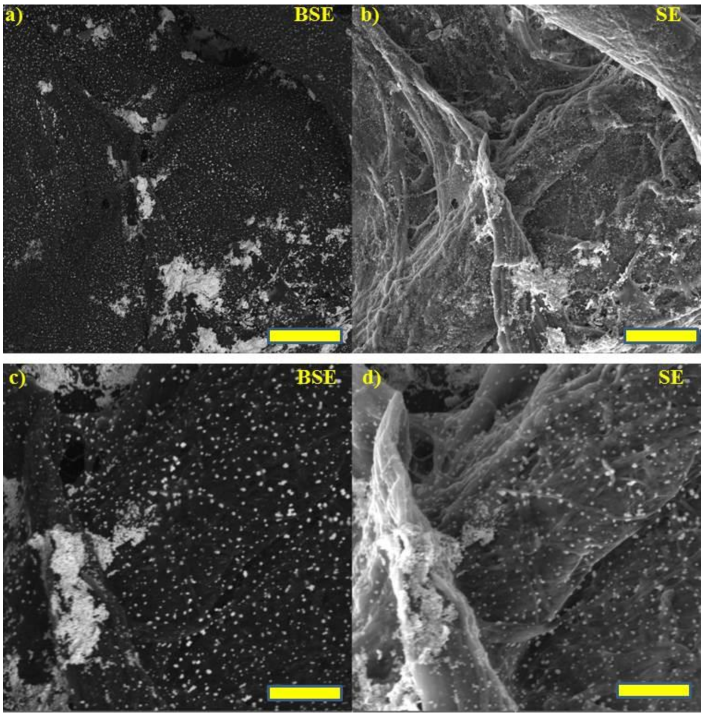

Figure.S.4.21 SEM of images of filter paper (a & b) and cotton yarn (c & d) where BSE (a & c), SE (b & d), coated with PbS NPs from the thermal decomposition of lead(II) hexylxanthate at 200 °C under nitrogen. Scale bar (a & b) 20 µm, (c & d) 5 µm.

Chapter 5. Conclusion and Future work

5.1. Conclusion

Semiconductor materials have great potential in the fabrication of solar cell devices. Solid state and hot injection methods have been widely used to grow high-quality nanostructure material. This project investigated the possibility of producing suitable, inexpensive and high-efficiency materials which could be used in the fabrication of flexible PV devices. This work has explored the possibility of formation of metal conduct electrode and an absorber layer. Also, it's examined the deposition of an absorber layer on a flexible substrate. The project was started by studying the formation of copper nanoparticles by two different methods, the solid-state reaction and colloid method, using copper (II) amino carboxylic acid complexes as a molecular precursor (Chapter 2). To understand the effect of reaction conditions on the morphology and the size of the product, different parameters including; reaction time and temperatures, have been applied. The copper nanostructures were characterized by powder X-ray diffraction, Raman spectrum and scanning electron microscopy. Both methods demonstrated a simple, fast, low-toxicity and economical technique to prepare copper nanostructures free from oxide contaminants. However, agglomeration of the particles and carbon contamination resulting from the decomposition processes of the precursors are the main drawbacks of those methods. Thus, it's vital to select precursors that contain less carbon atoms to improve the quality of Cu nanoparticles.

Bismuth sulfide Bi_2S_3 is an important direct bandgap semiconductor and therefore could be potentially an absorber layer on solar cell device. Chapter three describes the synthesis and single-crystal X-ray characterization of eight novel bismuth (III) xanthate complexes with the formula $[(N(C_2H_5)_4][Bi(S_2COR)_4]$ where R = methyl, ethyl, n-propyl, iso-propyl, n-butyl, iso-butyl, pentyl and n-hexyl. These complexes were used as single-source precursors for the preparation of Bi_2S_3 nanoparticles by solid-state reaction at three different temperatures 250, 300 and 350 °C. This technique is straightforward, solventless and potentially scalable for preparation of Bi_2S_3 nanoparticles. However, the lacking of control over the size and the shape is the main disadvantage of this method. Moreover, the high thermal decomposition of these precursors inhibits the use of them as absorber layer on fixable substrata, like cellulose. In chapter fourth, a fast and straightforward method has been described for the deposition of lead sulfide nanoparticles on two types of cellulose substrates (filter paper and cotton yarn). Cubic shape of PbS nanoparticles with different size has been obtained from the thermal decomposition of lead(II) alkyxanthate complexes where alky are ethyl, n-propyl, n-butyl and n-hexyl. Cubic shape of PbS nanoparticles has been obtained with different size. It’s observed that as the length of alkyl chain increasing the particle size is decreased. The bandgap could be changed by altering the length of the alkyl chain. However, the excessive surface roughness of cellulose (filter paper) reduces the quality of deposition because of the filter paper made of fibres with large pore size.

In summary, the work presented in this thesis shows promising result toward the preparation of nanoparticles that could be used as conduct electrode and an absorber layer. However, improve the quality of these products is essential to use them in the fabrication of flexible PV device.

Future work in this area will be focus on three different scopes. Firstly, it is essential to control the growth of the nanoparticles by controlling the reaction conditions such as temperatures, solvent and reaction time. Using the surfactant and capping agents are promising suggestion to obtain monodisperse nanoparticles. So, it is recommended to study the effect of different surfactant and capping agents such as citric acid, oleic acid, tetramethylammonium hydroxide and octadecylamine on the formation of copper and Bi_2S_3 nanoparticles. It is expected these stabilizers could help in preventing agglomeration and controlling the growth of the nanoparticles. Secondly, conduct extensive studies on the deposition of metal sulfide using different coating techniques such as ACVD, spin coating and air spry to improve the quality of deposition. Third, exploring the ability to use other alternative substrates such as cellophane, glassine paper and cellulose nanopaper.